Solid State Nuclear Magnetic Resonance of Paramagnetic Metal-Organic and -Inorganic Systems

Shashi Kumar Kumara Swamy

Solid State Nuclear Magnetic Resonance of Paramagnetic Metal-Organic and -Inorganic Systems

Shashi Kumar KUMARA SWAMY

Thesis supervisor: Jens DITTMER

Submitted to

École Doctorale 3MPL

10th January 2013, Le Mans

To mom (ಅಮ್ಮ) *and dad* (ಅಪ್ಪಾಜಿ)

Declaration

I hereby declare that the work presented in this thesis is entirely original and carried out by me at the Institut des Molécules et Matériaux du Mans (IMMM), Université du Maine, Le Mans, France. I further declare that this work has not formed the basis for the award of any degree or diploma or any other similar title of any other university or institution of higher learning.

Le Mans

10th January 2013 Shashi Kumar KUMARA SWAMY

Acknowledgement

One of the joys of completion is to look over the past journey of these three years of my PhD. First and foremost I would like to express my heartfelt gratitude to my thesis advisor Prof. Jens Dittmer who has not only been a mentor to me but also a dear friend. He created a friendly and cool atmosphere and has been a guardian angel to me throughout the tough path of my PhD life. I would like to thank him once again for his patience during discussions and in reading my thesis.

I would like to thank Prof. A. Mehdi, Prof S. Chouaib and Prof. A. Ben-Rhaiem for providing samples for investigation in my PhD thesis work. I would like to thanks Agnieszka Karzsmarsca for initiating the metal-cyclam project during her master stage. I thank Prof. A. Kassiba for EPR measurement and useful discussions we had on electron relaxation theory. Further I would like to thank Prof. M. Makowska-Janusik for her guidance on DFT calculations, when I thought I was completely lost. I would like to thank Dr. P. Pelupessy and Prof. C. Legein for the evaluation of my CST reports. I would like to specially thank Dr. Monique Body and Dr. Bholanath Pahari who have constantly motivated me when I gave up in my academic work. I would like to thank Francis Chavanon for his technical assistance for troubleshooting in UNIX.

I would like to thank my colleagues Ludovic Roussille, Gireesh Balakrishna Nair, Mamata Biswal, Venkatesan Rajalingam, Vasanth Kumar, Mounesha, Srikanth Chakaravarthy, Dilbhag Singh Kahlon and Achyutha Prabhu for their help in everything unknown to me. I would like to thank my friend and peer Uday Krishna Ravella for XRD test and some useful discussions we had on crystallography.

I would like to thank the Région Pays de la Loire for funding my project and providing me an opportunity to pursue my PhD research. I would like to thank école doctorale for their assistance during my PhD. I would like to thank all the jury members the referees Prof. M. Makowska-Janusik, Dr. P. Pelupessy, as well as Prof. A. Kassiba, Prof. P. Vasos, and Prof. C Legein, for agreeing to spend the time to evaluate my thesis.

Last but not the least I would like to thank two individuals in my life: my mom and dad who are responsible for shaping my personal and academic life and without whom I would have not stepped into such a stage at what I am right now.

I would like to apologize to anyone whom I have not acknowledged here. Thanks to every missing ones in this acknowledgment who have helped me in many ways in completion of my PhD.

Shashi Kumar KUMARA SWAMY

Abstract

The thesis aims at developing techniques in solid state nuclear magnetic resonance (ssNMR) of paramagnetic metal-organic and inorganic systems in combination with electron paramagnetic resonance (EPR) spectroscopy and quantum chemical methods such as density functional theory (DFT).

Solid state NMR signals of paramagnetic systems suffer from severe loss of sensitivity and resolution due to large hyperfine interactions. Among all the interactions seen in ssNMR, the interaction between the unpaired electron(s) and the observed nucleus leading to hyperfine interaction in paramagnetic solids is large in magnitude. Large broadening due to fast relaxation in paramagnetic systems on the one hand limits the excitation of the nuclei using conventional probes thereby causing severe loss in sensitivity and resolution of ssNMR signals. On the other hand the large shifts due to Fermi-contact interaction mask the diamagnetic chemical shifts (which are rich source of chemical group information) and make signal assignment difficult. The conventional techniques developed for solid state NMR of diamagnetic systems are inefficient for paramagnetic systems. These factors have led ssNMR of paramagnetic systems to be an unexplored topic for decades.

Recently Ishii and co-workers have circumvented some of these problems using very-fast magic angle spinning (VFMAS).[1] Spinning the sample at MAS frequencies >30 kHz drastically enhances the sensitivity and resolution of ssNMR signals in paramagnetic complexes. We have used the VFMAS approach and have shown how to cope with moderate hyperfine interactions in ssNMR of organic (cyclam and acetylacetonate) and inorganic (alkaline-copper pyrophosphates) systems with transition metal ions such as Cu^{II}, Ni^{II} and V^{IV} as paramagnetic center. On the one hand Fermi-contact interaction which is responsible for large shifts up to 100 ppm in ^{1}H and 1000 ppm in ^{13}C and ^{31}P cause severe problems for signal assignment. But on the other hand it also leads to better spectral dispersion and hence improve the resolution of the ssNMR signals. We were able to exploit this idea and a well resolved ^{13}C and even ^{1}H solid state NMR spectrum in paramagnetic metal-organic systems was obtained using a simple Hahn-echo experiment. This is usually not possible, since ^{1}H NMR in diamagnetic solids suffer from large broadening of 100 kHz due to ^{1}H-^{1}H homonuclear dipolar coupling. Furthermore fast relaxation in paramagnetic systems allows one to reduce the interscan delay and thereby repeat the experiments several times in a given time and improve the signal to noise ratio. This compensates for loss in sensitivity more often due to fast relaxation in paramagnetic systems.

Fermi-contact shifts are characteristics of unpaired electron spin density in a molecule. Using quantum chemical methods such as DFT one can calculate the theoretical Fermi-contact shifts.[2] We have compared the experimental ^{13}C ssNMR shifts with shifts from DFT calculation in paramagnetic metal –cyclam and –acetylacetonate complexes and have assigned the ^{13}C signals. For assignment of ^{1}H, a 2D version of dipolar INEPT (insensitive nuclei enhancement by polarization transfer) was used. In some cases such as the Cu-cyclam complex, a very well resolved ^{1}H ssNMR spectrum motivated us to try ^{1}H-^{1}H homonuclear correlation experiment. We obtained several

important cross peaks with a relatively simple pulse sequence. We used the dipolar connectivity information from it to complete the ^{1}H assignment.

One of the important aims of the thesis was to find a way to measure the metal-carbon distances using solid state NMR relaxation rates. In paramagnetic metal-organic complexes the carbon-13 relaxation caused by the dipolar interaction with the unpaired electron depends on the distance of the carbon atoms to the central metal ion, therefore its rates in principle contain structural information. We have measured these relaxation rates in order to assess the suitability of such a method and its range of validity. Limits are given for example by the loss of signals due to extreme broadening and the validity of the point dipole approximation, or the superposition of other interactions. In paramagnetic solids, electron relaxation time T^{e} forms the correlation time τ_{c}.[3] This parameter, critical for the extraction of metal-nucleus distance, was measured using EPR for calculating metal-nucleus distances. For Cu-cyclam we could reach a precision of 0.1 Å in a range of about 2.5 to 4 Å.[4] The applicability of the above techniques was tested on Ni-cyclam (a system with electronic spin S=1), three metal-acetylacetonates, and on ^{31}P solid state NMR of the three inorganic compounds Li_2-, Na_2- and $K_2CuP_2O_7$.

References:

1. Ishii, Y., Wickramasinghe, N. P., Chimon, S., *J. Am. Chem. Soc.*, 2003, **125**, 3438.
2. Wilkens, S. J., Xia, B., Weinhold, F., Markley, J. L., Westler, W. M., *J. Am. Chem. Soc.*, 1998, **120**, 4806.
3. Kervern, G., Steuernagel, S., Engelke, F., Pintacuda, G., Emsley, L., *J. Am. Chem. Soc.*, 2007, **129**, 14118.
4. (a) Solomon, I., *Phys. Rev.*, 1955, **99**, 559; (b) Koenig, S. H., *J. Magn. Reson. (1969)*, 1978, **31**, 1;
   (c) Koenig, S. H., *J. Magn. Reson. (1969)*, 1982, **47**, 441.

Content

Chapter 1: Introduction

"The only possible conclusion science can draw is: Some do, some don't." – **Richard R. Ernst**

Metal-organic and inorganic systems have widespread applications in various branches of science. In a metal-organic or –inorganic system that is paramagnetic, the metal ion often plays a role as reaction center. Many of such paramagnetic metal-organic systems are used in the area of synthetic chemistry,[1] material science,[2-8] and medicinal research.[9] Some of them are used as raw material for synthesizing anti-HIV and anti-cancer drugs.[10] Many of these applications require the paramagnetic systems to be administered in solid form. Synthesis and application of such potential systems require an efficient characterization technique to probe and understand them. Several characterization techniques developed for solids such as X-ray diffraction (XRD), scanning electron microscopy (SEM), and tunneling electron microscopy (TEM)[11] have served successfully in providing physical and chemical insight of such systems.

Solid state nuclear magnetic resonance (ssNMR) is an important technique for characterizing diamagnetic solids.[12-16] Contrarily, solid state NMR of paramagnetic systems has been less explored due to various technical challenges. NMR signals of paramagnetic solids suffer from severe loss of sensitivity and resolution due to the hyperfine interaction. Solid state NMR techniques that are developed for diamagnetic systems are found to be inefficient for paramagnetic systems. Recent developments in the area of solid state NMR of paramagnetic systems have given some hope for researchers to probe paramagnetic systems using solid state NMR.[17] In the following we will discuss some of the challenges encountered, research in the past few years and recent developments in the area of solid state NMR of paramagnetic systems.

1.1 Solid state NMR of paramagnetic systems

Over the years solid state nuclear magnetic resonance has grown into a large and important branch of magnetic resonance spectroscopy with the help of techniques such as magic angle spinning, cross polarization, heteronuclear and homonuclear decoupling and recoupling methods.[18] The broad range

of methods that are available in solid state NMR to characterize the important systems of physics, chemistry, biology and various other branches of science has made it unique among the characterization techniques. The ability of this technique to probe on the atomic or molecular level and provide information on structure, and local environment of systems such as catalysts[19], batteries[20-23], zeolites [12,24], liquid crystals[25-29], polymers[13,30-31], glasses[32-35], ceramics[36-37], membrane proteins[38-41] and pharmaceutical compounds[42] has made it a corner stone technique for characterization.

1.1.1 Research in the yesteryears

Anisotropic nuclear magnetic resonance interactions in solids such as chemical shift anisotropy, dipolar coupling, and quadrupolar coupling on the one hand are deleterious to the characterization because they cause line broadening and loss of coherence during pulse sequence. On the other hand they are rich in atomic or molecular information such as site asymmetry and inter-nuclear distances. Over the years, these interactions have been well exploited with the methods that are developed in solid state NMR for non-crystalline diamagnetic solids.[14-15] Contrarily, NMR of paramagnetic solids are still a challenge due to the hyperfine interaction between the unpaired electron(s) and the observed nucleus (Fermi-contact and pseudocontact interaction)[43] which are often large in magnitude with respect to all other interactions in NMR of solids. The hyperfine interaction between the unpaired electron and the observed nucleus can be defined based on the proximity of the electron to the nucleus. If the unpaired electron is close to the nucleus (5 Å), there is finite probability to find the spin density of the unpaired electron on the nucleus leading to the so-called Fermi-contact interaction. If the unpaired electron is far away from the nucleus, it can still interact with it through space (dipolar interaction), the pseudocontact interaction. In the case of Fermi-contact interaction the nucleus experiences shifts whereas in the case of pseudocontact interaction the nucleus will experience both shift and relaxation. Three major challenges one usually encounters while investigating paramagnetic systems using solid state NMR are: (1) the fast relaxation, (2) the large hyperfine shifts and (3) large inhomogeneous line broadening. Fast nuclear relaxation (due to the dipolar interaction between the unpaired electron and the observed nucleus) in paramagnetic

systems causes severe loss in sensitivity and resolution of NMR signals and hampers data acquisition. Furthermore large hyperfine shifts (Fermi-contact) mask the chemical shift information and make spectral assignment by conventional methods difficult.[44] The conventional techniques that are developed in solid state NMR for diamagnetic systems are found to be inefficient for paramagnetic systems.[45-48]

On the other hand there is considerable amount of work been done in the field of solution state NMR of paramagnetic molecules (both small and large).[49-50] In solution, due to the rapid rotation and tumbling motion of molecules the anisotropic interactions (both diamagnetic and paramagnetic) are averaged and the NMR spectrum is relatively simple to understand. Metallo-proteins, other metallo-biomolecules and small metal-complexes that are paramagnetic have been successfully studied using solution state NMR.[51] In large proteins and biomolecules that accommodate paramagnetic metal complexes the distance between metal and observed nucleus is for most atoms sufficiently large (> 10 Å) and hence the pseudocontact term is the dominant paramagnetic interaction. In solution state especially for bio-macromolecules containing paramagnetic ions the pseudocontact interaction is understood very well. In fact several methods have been developed to exploit pseudo-contact interaction for structural information such as: metal-nucleus distance measurement using nuclear relaxation rates,[52] measuring angles using pseudo-contact shifts,[53] or immersion into a membrane by measuring relaxation.[54-56]

In the past few decades attempts were made to study paramagnetic systems using solid state NMR despite many challenges. ^{1}H and ^{13}C NMR spectra which could provide fundamental information, suffer from severe loss of sensitivity and resolution of signals due to fast relaxation. Also the pulse sequences and techniques that are developed for diamagnetic systems do not work for paramagnetic systems due to loss of coherence from fast relaxation. For example cross polarization (CP) which is a routine experiment in solid state NMR for sensitivity enhancement of insensitive nuclei such as ^{13}C, ^{15}N etc. suffer from loss of sensitivity due to inefficiency of polarization transfer. The fast relaxation in paramagnetic system requires the contact time in CP technique to be very short for exciting broadband ^{1}H resonances thereby imposing very short time for polarization transfer.[57] In spite of such limitations there are some examples of ^{13}C CP in paramagnetic systems. The first solid

state ^{13}C CP MAS in paramagnetic system was demonstrated in paramagnetic praseodymium and lanthanum acetate complexes by Ganapathy *et al.*[45] However they showed that moderate spinning speed of 4.5 kHz is not sufficient for eliminating large anisotropic interactions in paramagnetic systems. Furthermore Brough and coworkers[57-58] have shown that ^{1}H decoupling during acquisition is inefficient for paramagnetic lanthanide complexes and they conclude that only deuteration was the solution. Large spectral dispersion of ^{1}H signals limits the ^{1}H decoupling thereby leading to loss in sensitivity and resolution of ^{13}C signals of paramagnetic systems. Liu *et al.*[44] overcame this problem by deuterating the paramagnetic Cu^{II}(DL-alanine) and $V^{III}(acac)_3$ complexes. Being an expensive technique, deuteration reduces the line width of ^{13}C signals by diluting protons and accounts for the improvement of sensitivity and resolution of ^{13}C signals. They even demonstrate how sensitivity lost due to extreme broadening is recovered by fast repetition of experiments by reducing the inter-scan delay. This advantage is attributed to the fast relaxation in paramagnetic systems.[57] They have demonstrated lanthanide metal-carbon distance determination by measuring the chemical shift anisotropy using sideband analysis. However they experience problem in assigning deviated ^{13}C shifts (methyl, carbonyl) due to Fermi-contact interaction.

1.1.2 The breakthrough and recent developments

A breakthrough in the field of solid state NMR of paramagnetic systems was seen with the application of very-fast MAS by Ishii *et al.*[17] They have shown that spinning the sample at MAS frequencies > 25 kHz drastically improves the sensitivity and resolution of ^{1}H and ^{13}C solid state NMR signals in paramagnetic metal-organic complexes. They observe natural abundance ^{13}C solid state NMR spectra of Cu^{II}(DL-alanine) and $V^{III}(acac)_3$ employing very-fast MAS, in contrast to Liu *et al.*,[44] who successfully worked on the same samples by deuterium and ^{13}C labeling. Using the very-fast MAS approach Ishii and co-workers have shown that one pulse/Hahn-echo experiments are nearly sufficient to obtain a decent ^{13}C solid state NMR spectrum[59-60] unlike CP which results in severe loss of sensitivity due to the reasons mentioned before. For assignment of the ^{13}C signals in both complexes, they use a REDOR type recoupling sequence for ^{13}C signal editing to distinguish between $^{13}CO_2$, $^{13}CH_3$ and ^{13}CH groups in $V^{III}(acac)_3$. They even extend to ^{1}H-^{13}C 2D correlation

experiment and were successful to produce the first solid state NMR 2D correlation spectra of paramagnetic complex.

Kerven *et al.*[61] have used very fast MAS approach in solid state NMR to study paramagnetic DIAD-Fe^{II} catalyst. Using some of the 2D correlation techniques such as ^{1}H-^{13}C 2D dipolar INEPT demonstrated by Wickramasinghe *et al.*,[60] Kerven *et al.*[61] have done the assignment of ^{1}H and ^{13}C signals by solid state NMR with the DFT calculations in DIAD-Fe^{II} catalyst.

One can see that in solid state NMR of paramagnetic systems, many disadvantages are converted to advantages. For example fast relaxation in paramagnetic systems causes broadening of the signals leading to severe loss in sensitivity and resolution. But the former is partially compensated by gain in sensitivity through fast signal averaging due to shorter inter-scan delay compared to diamagnetic solids where the nuclear relaxation times can be long and one has to wait for several seconds to minutes for repeating the experiment. Furthermore the Fermi contact shifts which can range from 100 ppm to 1000 ppm shift the ^{1}H and ^{13}C signals away from the normal (diamagnetic) chemical shift range and make signal assignment difficult. But on the other hand Fermi contact shifts can cause large spectral dispersion of signals and provide excellent resolution of ^{13}C solid state NMR spectra. Furthermore the ^{1}H-^{1}H homonuclear dipolar coupling which is very strong due to the homonuclear flip-flop term in diamagnetic systems is weaker in paramagnetic complexes due to the large spectral dispersion. Now VFMAS sufficiently removes all the anisotropic interactions including ^{1}H-^{1}H homonuclear, thereby reducing the line widths of ^{1}H signal and makes even ^{1}H NMR feasible for paramagnetic metal-organic solids.

1.2 Goal of the thesis

The thesis aims at developing techniques in solid state NMR of paramagnetic metal-organic and –inorganic complexes. The focus will be on small systems. The work done in the last decade meant a major breakthrough in the treatment of paramagnetic systems, but the study of such systems is still far from being routine. There are still only few studies published. The present work intends to be a further step in the technical development for such systems. With the help of electron paramagnetic resonance spectroscopy (EPR) and quantum chemical calculation methods such as density

functional theory (DFT), we are in the quest of making solid state NMR as a routine technique for probing small metal-organic and –inorganic systems.

Recent developments in the area of solid state NMR of paramagnetic metal-organic systems such as results from the work of Ishii et al.[17] and Kerven et al.[61] form the major inspiration of this work. The paramagnetic complexes of metal-cyclam with Cu (II) and Ni (II) ions as metal center and metal-acetylacetonate complexes with Cu (II) and VO (IV) ions as metals center are the model systems studied in the metal-organic section. Alkaline metal (Li^{2+}, K^{2+} and Na^{2+})-pyrophosphates with Cu (II) ion as metal center are the model systems studied in the metal-inorganic section.

1.2.1 Paramagnetic metal-organic systems: metal-cyclam and metal-acetylacetonate complexes

In our investigation of solid state NMR of paramagnetic metal-organic systems the first model systems we have studied are paramagnetic metal-cyclam complexes. Paramagnetic Cu- and Ni-cyclam complexes are well known systems in the field of coordination chemistry.[6,10,62-71] Metal-cyclam complexes have potential applications in pharmaceutical industries, for example as raw material for anti-HIV and anti-cancer drugs.[72] They can also be used as active groups in mesoporous structures leading to functional materials with applications in electronics and optics[6] or chemical sensing with high sensitivity.[73] The tetradentate cyclam ligand binds with transition metal ions such as Cu (II) and Ni (II) with some halides (such as chlorine in our case) as axial ligand to form stable paramagnetic coordination complex. In case of Cu-cyclam a single chloride ion forms as counter ion leading to five coordinated Cu-cyclam monochloride complex. In the case of Ni-cyclam two chloride ions forms as counter ions leading to six coordinated Ni-cyclam dichloride complex. There is no X-ray structure available for Cu-cyclam monochloride complex studied here. However, we found the X-ray structure of Cu-cyclam sulphocyanide complex investigated by Lu *et al.*[67] to have similar coordination as that of Cu-cyclam monochloride complex studied here. Ni-cyclam dichloride complex however is a very well known complex. We found some X-ray structures[74-76] and some examples of solution state ^{1}H NMR including assignments for Ni-cyclam complex in the literature.[66,77-78]

In case of Cu-cyclam the distances to the central ion are between 2.0 Å for the ligating nitrogen atoms and 4.4 Å for two of the equatorial hydrogens. In this distance range, electron-nuclear dipolar coupling can cause an extremely fast relaxation which not only introduces additional line broadening, but also makes the conventional NMR experiments developed for solids unusable. Cu^{2+} ions have an effective electronic spin S_e = ½ and therefore represent examples where the perturbation by hyperfine interactions is not too extreme.[44] For such systems, there are even benefits from hyperfine interactions, in particular for metal-organic complexes. We start with applying the techniques developed in previous work to our model system Cu-cyclam, a system with moderate difficulty.

Assignment of such broad and largely shifted signals is difficult using convention assignment technique and one has to rely on quantum chemical calculations such as density functional theory (DFT) for ^{1}H and especially ^{13}C signal assignment.

In past few decades the DFT calculation of open shell systems has grown into important branch of theoretical chemistry. The need of experimentalists for theoretical spectroscopic parameters of a system under study has driven theoreticians of quantum chemistry and physics to focus on developing new and robust methods to calculate these parameters. The parameter associated with NMR of paramagnetic systems is the Fermi-contact shift. Knowing this parameter is equivalent of the assignment of paramagnetic NMR spectra. The total shift in any NMR spectrum of paramagnetic complex is the sum of chemical shift (diamagnetic) and Fermi-contact shift (paramagnetic). Normally we can have information of chemical shift of respective nucleus under study from the database, which is routine NMR assignment procedure. Some contemporary researchers in this field have used DFT calculation for assignment of ^{1}H and ^{13}C signals in Fe(III)-Rubredoxin protein reported by Wilkens *et al.*,[79-80] in paramagnetic metallo-porphyrins reported by Zhang *et al.*[81-82] and in DIAD-Fe^{II} catalyst reported by Kerven *et al.*[61] Using some of these reported DFT methods, we use Gaussian 09[83] program to performing DFT calculation on our model systems.

In NMR one uses 2D experiments to resolve the signals which are complicated to understand through a one dimensional spectrum. The main use of it is to know heteronuclear connectivity

information in the molecule. For example in solid state 2D ^{1}H-^{13}C correlation experiment such as HETCOR (Heteronuclear Correlation), one has information of ^{1}H-^{13}C dipolar connectivity and henceforth can assign the ^{1}H signals. For assignment of ^{1}H signals in Cu-cyclam complex a 2D version of dipolar INEPT experiment similar to the one by Kervern *et al.*[61] will be used. Dipolar INEPT is a coherent polarization technique similar to INEPT[84] (Insensitive nuclei polarization transfer) in liquids. The MAS averaged dipolar coupling is reintroduced into the systems by using a TEDOR[85] (transferred echo double order resonance) type dipolar recoupling sequence. Since the pulse sequence is rotor-synchronized a very short transfer time ($2\tau_r$ = 66.7 μs) was used.

A 2D correlation experiment can in principle be done in two ways, with the signal of either the one or the other nucleus being acquired. In solid state NMR of organic systems the signal is always acquired on ^{13}C due to the poor resolution of ^{1}H (due to large ^{1}H-^{1}H homonuclear dipolar couplings). This is in contrast to liquid state NMR, where one benefits of the excellent sensitivity of ^{1}H, for example in the HSQC experiment using *J*-coupling. Fair resolution in ^{1}H spectra of Cu-cyclam complex motivated us to try a ^{1}H-^{13}C dipolar HSQC with ^{1}H acquisition.

The ^{13}C-^{1}H correlation spectrum is not sufficient for complete ^{1}H assignment. For example in the case of Cu- and Ni- cyclam complex distinction of equatorial and axial hydrogen attached to the same carbon has to be done. One solution is to distinguish the signals based on Karplus relation.[50,86] The other solution is ^{1}H assignment by ^{1}H-^{1}H correlation experiment. The very well resolved ^{1}H solid state NMR spectrum observed in Cu-cyclam complex motivated us to try some Homonuclear correlation type of experiment similar to Correlation spectroscopy (COSY) and Nuclear Overhauser spectroscopy (NOESY) in solution state NMR. The pulse sequence is similar to NOESY with a very short mixing time (~150 μs) and a presaturation pulse during interscan delay and mixing time to avoid evolution of diamagnetic signal which influenced other signals. The correlation obtained with such type of experiment can be used to understand dipolar connectivity of ^{1}H and hence one can use it for assigning the ^{1}H signals.

One of the important and main goals of the thesis is to determine metal-carbon distances using relaxation rates. In paramagnetic metal-organic complexes the carbon-13 relaxation caused by

dipolar interaction between the unpaired electron and the nucleus depends on the distance of the carbon atoms to the central metal ion. Hence these rates in principle contain structural information as seen from Solomon's rate equation.[50,87-89] In NMR, the nucleus relaxation is caused by fluctuation of NMR interactions. In paramagnetic solid complexes electron-nucleus dipolar interaction is the dominant mechanism by which nucleus relaxes. So here in our case the correlation time τ_c in Solomon's rate equation can be approximated by the electron relaxation time T^e. This is an unknown parameter which is not accessible by NMR techniques and which inhibits the determination of metal-nucleus distances from the measured relaxation rates. We therefore measure the electron relaxation time T^e in Cu-cyclam complex by EPR. Further we see that Wickramasinghe *et al.*[90] have already tried this approach with longitudinal rates R_1 and have observed only relative distance with the help of a reference distance from XRD. So here we therefore try to use transverse relaxation rates R_2 for measuring metal-nucleus distance. We use Carr Purcell Meiboom Gill (CPMG)[91-92] pulse sequence to measure spin-spin relaxation rate R_2 of ^{13}C signals in Cu-cyclam complex The ^{13}C nuclear relaxation rates R_2 and the electron relaxation time T^e are inserted in the Solomon's rate equation and the carbon-copper distances in Cu-cyclam complex is determined.

In the second part of our investigation on paramagnetic metal-organic complexes we investigate paramagnetic copper-, vanadyl-, and nickel- acetylacetonate complexes using the same methods established for Cu-cyclam complex. Acetylacetonate (acac) is a very well known ligand and has oxygen as donor atoms for coordinating with metal ions and forms paramagnetic metal-acetylacetonate complex. One dimensional ^1H and ^{13}C solid state NMR Hahn-echo served as basic solid state NMR experiments for the investigation. Due to the hyperfine shift the assignment of ^{13}C signals in $Cu[acac]_2$ and $VO[acac]_2$ are done using the spin density from DFT calculation. However due to complex trimerization in $Ni[acac]_2$ which is reflected in the ^{13}C Hahn-echo spectra the ^{13}C assignment from DFT calculation are not straight forward. For assignment of ^1H signals a 2D dipolar INEPT experiment is used for Cu-acac and VO-acac complexes.

1.2.2 Paramagnetic metal-inorganic systems: Alkali metal [Li^{2+}/K^{2+}/Na^{2+}]-copper pyrophosphate

Some of the interesting and successful results seen in solid state NMR of paramagnetic metal-organic systems motivated us to extend the solid state NMR investigation on metal-inorganic systems. The anions of pyrophosphoric acid ($H_4P_2O_7$) are generally called pyrophosphates $[P_2O_7]^{4-}$. They are very important in biochemistry, often encountered with the abbreviation PP_i during the hydrolysis of adenosine tri-phosphate (ATP) to adenosine mono-phosphate (AMP). Pyrophosphates find importance in inorganic chemistry as well, they form stable metal pyrophosphates with transition metal ions such as copper, nickel and cobalt. Furthermore these transition metal-pyrophosphates combine with alkali metal ions such as Li^{2+}, Na^{2+} and K^{2+} and form stable alkaline transition metal-pyrophosphates which are paramagnetic. Alkaline transition metal-pyrophosphates have wide range of applications as prospective materials in technology, viz. in electronic device, as solid electrolytes, ceramics, solid state lasers and magnetic materials.

Here phosphorus isotope ^{31}P is the subject of NMR interest in alkaline metal (Li^{2+}, K^{2+} and Na^{2+})-copper pyrophosphate systems. Due to 100% natural abundance of ^{31}P nuclei in nature the sensitivity of the phosphorus-31 signal was appreciably good. Due to the presence of paramagnetic metal ion of copper we observe severely shifted phosphorus signals away from diamagnetic range [250 ppm to -200 ppm] in all the three copper-pyrophosphates. However all the three samples show a single broad ^{31}P signal which corresponds to single phosphorus site.

Furthermore we tried to test the feasibility of method of determining metal-nucleus distances in these alkali metal-copper pyrophosphates as done in the case of Cu-cyclam complex. The ^{31}P spin-spin relaxation rates are measured using CPMG in solid state NMR. Since the EPR experiment of alkaline metal-copper pyrophosphates were not straight forward we have no reference for the electron relaxation time T^e. Hence we use the Cu-cyclam electron relaxation for testing purpose. These measured rates are compared with the expected rates calculated using copper-phosphorus distances from XRD.[93-95]

Chapter 2: Solid state NMR principles and techniques

"It is wrong to think that the task of physics is to find out how Nature is. Physics concerns what we say about Nature." – **Niels Bohr**

2.1 Nuclear Magnetic Resonance

Spectroscopy is a branch of physics which deals with the study of interaction between the incident radiation and the matter. For the radiation to interact with matter the energy levels of the matter should be in match with the wavelength of the incident radiation, which is termed as *'Resonance'*. The term resonance was first termed in classical systems which vibrate or oscillate and experience large amplitude oscillations when they are driven at their resonant frequency. In quantum mechanics, resonance is seen in case of coupling between a 'photon' and an 'electron', famously described by Planck-Einstein's equation $E = h\nu$, where frequency ν of the photon is in resonance with the energy difference between the two electron states. This idea forms the basic underlying principle for nuclear magnetic resonance (NMR) spectroscopy except that the matter is in the magnetic field. The electromagnetic spectrum which is distributed over broad range of frequencies right from 10 KHz to 10 EHz has several spectroscopic techniques associated with respective range of frequency. One such range of frequency (radio frequency) in the electromagnetic spectrum is associated with the nuclear magnetic resonance spectroscopy. The range of NMR frequency in the electromagnetic spectrum is between 2 KHz to 1 GHz which is equivalent to the Larmor's frequency of a proton (^{1}H): in earth's magnetic field of 0.5×10^{-4} T, and the state of the art NMR spectrometers equipped with superconducting magnets of field strength 25 T respectively.

Nuclear magnetic resonance was first observed in 1938 by I. I. Rabi in molecular beams[96] and later in 1945 by E. M. Purcell[97] in solids at Stanford, and in 1946 by F. Bloch[98-100] in liquids at Cambridge. Both Bloch and Purcell shared a Noble prize in physics in 1952 for their development of method to measure nuclear magnetic precision. Rabi, Purcell, and Bloch observed that nuclei such as ^{1}H, ^{31}P and ^{19}F when placed in magnetic field and excited with RF field responded uniquely i.e. each nucleus having specific frequency of absorption. This gave them the feeling that the magnetic resonance technique would later turn out to be a very strong and powerful spectroscopic

technique which can be applied to various branches of science. Until 1966, Nuclear magnetic resonance was studied under the so-called continuous wave (CW) technique which resulted in severe loss of sensitivity of the NMR signals due to low signal to noise ratio. In 1991 R. R. Ernst was awarded the noble prize for his discovery of pulsed Fourier transform nuclear magnetic resonance (FTNMR) technique,[101] which overcame the loop holes that existed in CW NMR technique. This discovery paved way for a revolutionary branch of spectroscopy using which the physicists, the chemists, and the biologists around the world could extract structural information about the systems they have been working on. Initially NMR technique was developed to understand magnetism of materials in physics, later it was found to be of great use in understanding the environment of a chemical, and after a good amount of success in studying small organic molecules to as large as proteins, it grew to a greater field in magnetic resonance spectroscopy. After the discovery of the pulse FTNMR, research in the development of techniques and methodology in nuclear magnetic resonance took a quantum leap and is still continuing until this day for better understanding of physical, chemical and biological systems. In spite of being a relatively insensitive spectroscopic technique, NMR has played an important role in understanding the chemical structure of the molecules.

2.2 Nuclear -spin, -magnetic moment, and -magnetism

Matter is composed of atoms; atoms consist of nucleus (protons and neutrons) and electrons. The electrons orbiting the nucleus possess orbital angular momentum, in terms of quantum mechanics it is termed as the orbital quantum number *L*. Furthermore, electrons also possess intrinsic angular momentum or in other words spin *S*. Spin is abstract term and one cannot think of geometrical revolution if we are speaking in terms of quantum mechanics. Nevertheless, this idea of geometrical imagination of intrinsic angular momentum or spin is widely accepted. Now, this spin is what is responsible for magnetic moment μ_s of an electron. Similarly, the nucleus also possesses the spin *I* and hence the magnetic moment μ_I, given by,

$$\vec{\mu}_I = \gamma\vec{I} \qquad \textbf{2.2.1}$$

Here the proportionality constant γ is known as gyromagnetic ratio and is characteristic of the individual isotope of nucleus. Table 1.1 shows a list of nuclei with their NMR properties and in which one of them is gyromagnetic ratio. The value of γ is negative when $\vec{I}$ and $\vec{\mu}$ are in opposite direction, and is positive when $\vec{I}$ and $\vec{\mu}$ are in same direction.

Isotope	**Nuclear spin state**	**Natural Abundance *in %***	**Gyromagnetic ratio γ *in* 10^6 rad s^{-1} T^{-1}**	**NMR frequency *in MHz* (at 300 MHz or 7.05 T magnetic field)**
^{1}H	½	99.9	267.52	300
^{6}Li	1	7.4	39.371	44.15
^{7}Li	3/2	92.6	103.975	116.59
^{13}C	½	1.1	67.283	75.43
^{31}P	½	100	108.41	121.44

Table 2.2.1: Some nuclei of NMR interest with their magnetic properties

When a system containing nuclei with non-zero spin are placed in a magnetic field the magnetic moment arising from the nuclei interacts with external magnetic field, this is nuclear magnetism. The degeneracy in the energy level is lifted due to '*Zeeman interaction*'. This results in the distribution of single state into $2I+1$ non-degenerate state. For example in an isolated system: a spin ½ nuclei according to $2I+1$ leads to 2 x ½ +1 = 2 states as shown in Figure 2.2.1.

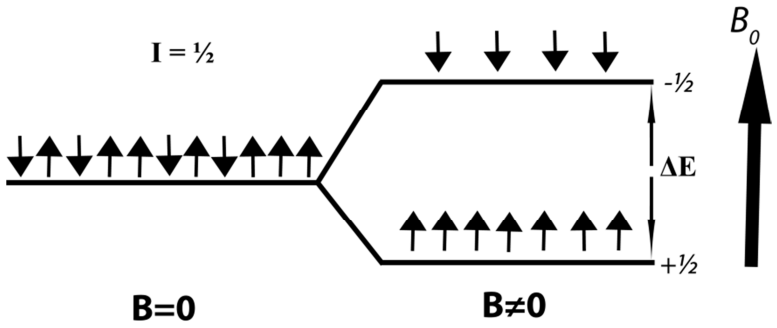

Figure 2.2.1: Zeeman interaction of spin ½ nuclei under external magnetic field

Mathematically, the nuclear *Zeeman interaction* is written as:

$$\hat{H}_{Nuclear\ Zeeman} = -\vec{\mu} \cdot \vec{B} \qquad \textbf{2.2.2}$$

$$E = -\gamma m_I \hbar B_0 \qquad \textbf{2.2.3}$$

For I = ½, the energy difference between the states <½,-½> is given by

$$\frac{1}{2}\hbar\gamma B_0 - \left(-\frac{1}{2}\hbar\gamma B_0\right) = \hbar\gamma B_0 \qquad \textbf{2.2.4}$$

When a electromagnetic radiation of energy

$$\hbar\omega = \hbar\gamma B_0 \qquad \textbf{2.2.5}$$

interacts with such a system, the nuclear spin changes their state undergoing resonant absorption.

Here $\omega = -\gamma B_0$ is termed as '*Larmor Frequency*'[102] (see Figure 2.2.2).

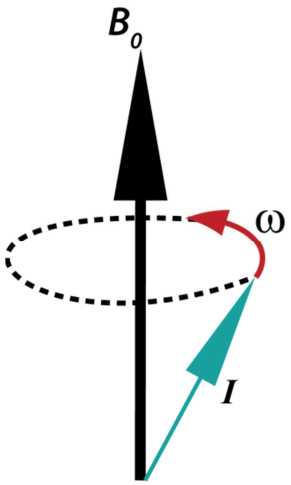

Figure 2.2.2: Larmor precession of a nuclear spin in magnetic field B_0

2.3 Interactions in NMR

Nuclei can interact with the fields arising from its surroundings especially from bonding electrons. The magnetic field induced by the bonding electrons shields nucleus from the external field and give rise to an interaction called *Chemical shift*.[103-107] This is one of the important NMR interactions which renders chemical group information in a molecule. The nucleus can also interact with the immediate neighboring nucleus through bonding electrons. This coupling between two nuclei

commonly studied in liquids is called the *J-coupling*.[108-110] *J-coupling* serves information about the spin system of nuclei in a molecule. The *Chemical shift* and *J-coupling* are the two interactions which are commonly used as source of information in NMR of liquids. *Chemical shift* is what which makes NMR a powerful tool to understand biological, chemical and physical systems. It provides a unique signature of particular nucleus (more commonly ^{1}H, ^{13}C, and ^{15}N) due to its surrounding in a molecule. Besides, *J*-coupling renders information about the connectivity of spin system in a molecule and helps in betters understanding of the structure of a molecule. There are several other interactions in NMR which one encounters during their investigation such as dipolar coupling, chemical shift, quadrupolar coupling, and hyperfine coupling, which are prominent in solids and are explained in detail in upcoming units.

2.4 Solid state nuclear magnetic resonance

Over past few decades there has been a significant increase in the research of solid materials such as ceramics, glasses, polymers, fibers etc. due to their unique physical and chemical properties. The potential application of such solid materials is foreseen in various branches of science. Therefore for researchers to have an insight into structure and properties, it is very important to have a successful characterization technique. X-ray diffraction (XRD), scanning electron microscopy SEM, tunneling electron microscopy (TEM), atomic force microscopy (AFM) and many more techniques are used to understand the structure of such potential solid materials.

Solid state nuclear magnetic resonance is one of the important spectroscopic techniques to study solid materials. Application of solid state NMR as characterization technique, ranges from inorganic solids,[111] glasses,[32] ceramics,[36] polymers,[30] and membrane proteins.[40] Development of methodology in solid sate NMR has increasingly grown over past few decades due to its potential use as a characterization technique for systems in physics, chemistry and biology. Initially the techniques in solid state NMR were applied to few physical systems; due to their broad line features as a consequence of large anisotropic interactions such as chemical shift anisotropy and dipolar coupling. Over years, development of methods such as magic angle spinning (MAS), cross polarization (CP), decoupling (heteronuclear and homonuclear) and recoupling techniques have

made solid state NMR a successful technique for organic, inorganic, and biological solids. One important advantage of solid state NMR is that it does not demand the system under study to be highly ordered unlike XRD. Apart from structural insight of a system, it also renders information on molecular dynamics. The recoupling techniques in solid state NMR which are explained in the later unit demonstrates that the anisotropic interactions in spite of being annoyances in solid state NMR are rich source of local information of a system under study. Recent investigations have shown how successfully solid state NMR can be applied to extract structural information in insoluble proteins.[41,112-113] Accordingly solid state NMR is most widely used technique in structure determination after XRD technique. The next unit gives a brief introduction to various interactions that one encounters during their investigation of the system using solid state NMR.

2.5 NMR interactions in solids

Interactions in NMR are always spoken in terms of interaction energy or Hamiltonians. The NMR interaction Hamiltonian gives a mathematical picture of the particular interaction influencing a system. The total NMR Hamiltonian is the sum of internal and external interactions. Mathematically written as,

$$\hat{H}_{total} = \hat{H}_{\text{int}} + \hat{H}_{ext} \qquad \textbf{2.5.1}$$

In general, an NMR experiment involves an external static magnetic field with which the nuclear spin magnetic moments interact and then we have a time dependent oscillating field or radio frequency r.f. field generated by the NMR spectrometer that causes transition between nuclear Zeeman energy levels. Mathematically one can write NMR experiment as:

$$\hat{H}_{ext} = \hat{H}_{Zeeman} + \hat{H}_{rf}(t) \qquad \textbf{2.5.2}$$

The Zeeman and the r.f. Hamiltonian forms the external Hamiltonian and all other interactions in NMR form the internal Hamiltonians. The interactions in NMR of solids are quite complicated due to anisotropic terms. On the other hand contain useful information about the system under investigation. The internal Hamiltonian of NMR in solids can be mathematically written as,

$$\hat{H}_{\text{int}} = \hat{H}_{CSA} + \hat{H}_{D} + \hat{H}_{J} + \hat{H}_{Q} + \hat{H}_{Hyp} \qquad \textbf{2.5.3}$$

The first two terms are $\hat{H}_{CSA}$ and $\hat{H}_{D}$ i.e. chemical shift anisotropy (CSA) and dipolar coupling Hamiltonians, respectively, and are the most common interactions studied in NMR of solids. The third term *J-coupling* Hamiltonian $\hat{H}_{J}$ is usually ignored solids since CSA and dipolar coupling are overwhelming. The quadrupolar coupling Hamiltonian $\hat{H}_{Q}$ is a special type of interaction found in integer and half integer spin nuclei (I >½). The last term is the hyperfine interaction term $\hat{H}_{Hyp}$ which is due to the eventual interaction of an unpaired electron and the observed nucleus. Shown in Figure 2.5.1 is a comparison of typical magnitudes of NMR interactions in solids. If we have hyperfine interaction in a system it would overwhelm all other interactions. The four NMR interactions in solids: chemical shift anisotropy, dipolar coupling, quadrupolar coupling and the hyperfine interaction are considered to be the most important interactions and are well explained in the later unit with the theory involving each one of them.

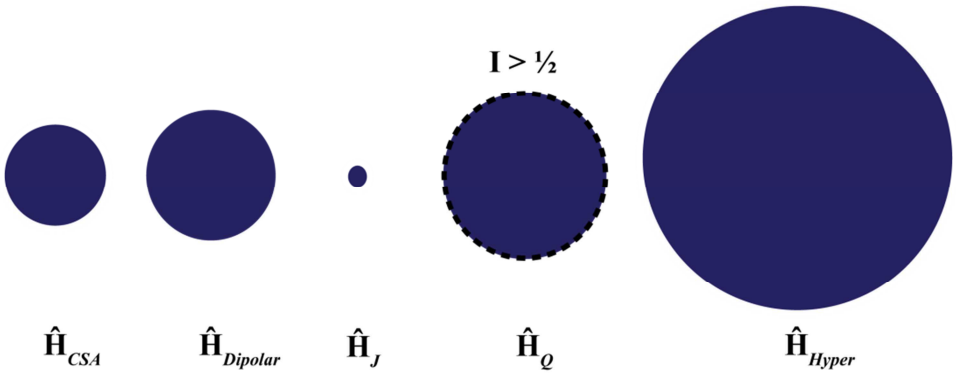

Figure 2.5.1: Comparison of magnitude of NMR interactions in solids

2.5.1 Chemical shift anisotropy

In NMR, nuclei in a sample experience the local magnetic field which is the sum of applied magnetic field and the induced magnetic field due to bonding electrons so,

$$\vec{B}_{Local} = \vec{B}_0 + \vec{B}_{induced} \qquad \textbf{2.5.4}$$

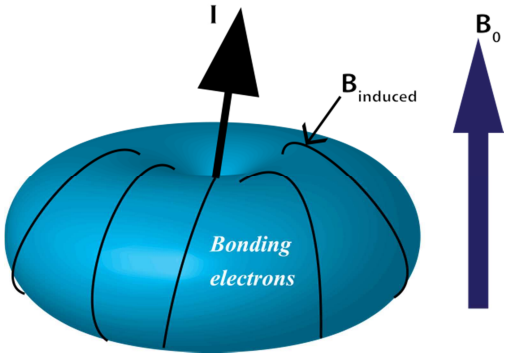

Figure 2.5.2: Nucleus engulfed by the induced field $B_{induced}$ due to the circulation of bonding electrons

The induced magnetic field $B_{induced}$ is due to the quantum mechanical behavior of the electrons. There are two terms of induced field identified: (1) field induced due to the circulation of bonding electrons leading to diamagnetic term as shown in Figure 1.3 and (2) field induced due to the unpaired electron leading to paramagnetic term. The latter term will be discussed in the *hyperfine interaction* unit of this chapter, and the present unit would only focus on the diamagnetic term. Diamagnetic chemical shift of a nucleus is the characteristic of its electronic environment in a molecule and are distinctive with respect to chemical group. They have magnitude only 10^{-4} times the external field B_0 which is small but large enough to give rise to observable chemical shifts in the spin frequencies of precession. The interaction of the magnetic moment with the induced field due to bonding electrons can be written as,

$$\hat{H}_{CS} = -\vec{\mu} \cdot \vec{B}_{induced} \qquad \textbf{2.5.5}$$

$$B_{induced} = \delta_{ij} \cdot B_0 \qquad \textbf{2.5.6}$$

Here induced field can be easily approximated to $\delta_{ij} \bullet B_0$ since it is linearly dependent on the applied field. The δ_{ij} is a 3 x 3 matrix of real numbers, called the *chemical shift tensor* of the site of the nuclei *I*. Hence equation 2.5.7 can be written as,

$$\hat{H}_{CS} = -\gamma \vec{I} \cdot \left(\delta^{ij} \cdot \vec{B}_0\right) \qquad \textbf{2.5.7}$$

In isotropic liquids, the motional averaged chemical shift Hamiltonian can be written as,

$$\hat{H}_{CS} = -\gamma B_0 \delta^{iso} I_z \qquad \textbf{2.5.8}$$

It is convenient to combine external Hamiltonian with the chemical shift term and we have

$$\hat{H}_0 = \hat{H}_{ext} + \hat{H}_{CS} \qquad \textbf{2.5.9}$$

$$\hat{H}_0 = \omega_0 I_z \qquad \textbf{2.5.10}$$

Here ω_0 is the chemically shifted Larmor frequency which depends on the isotropic chemical shift δ^{iso}, according to

$$\omega_0 = -\gamma B_0 \left(1 + \delta^{iso}\right) \qquad \textbf{2.5.11}$$

In solids, the atomic motion is restricted. The chemical shift Hamiltonian in equation 2.1 depends on the chemical shift tensor element δ_{ij} which is dependent on the orientation angle θ of the atomic framework with respect to magnetic field B_0. Now in solids, the chemical shift Hamiltonian has two parts the isotropic and the anisotropic part which is given by,

$$\hat{H}_{CS} = -\gamma B_0 I_z \left[\delta_{iso} + \delta_{CSA} \frac{\left(3\cos^2\theta - 1\right)}{2} \right] \qquad \textbf{2.5.12}$$

$$\text{With } \delta_{iso} = \frac{(\delta_{11} + \delta_{22} + \delta_{33})}{3} \text{ and } \delta_{CSA} = \delta_{33} - \delta_{iso}$$

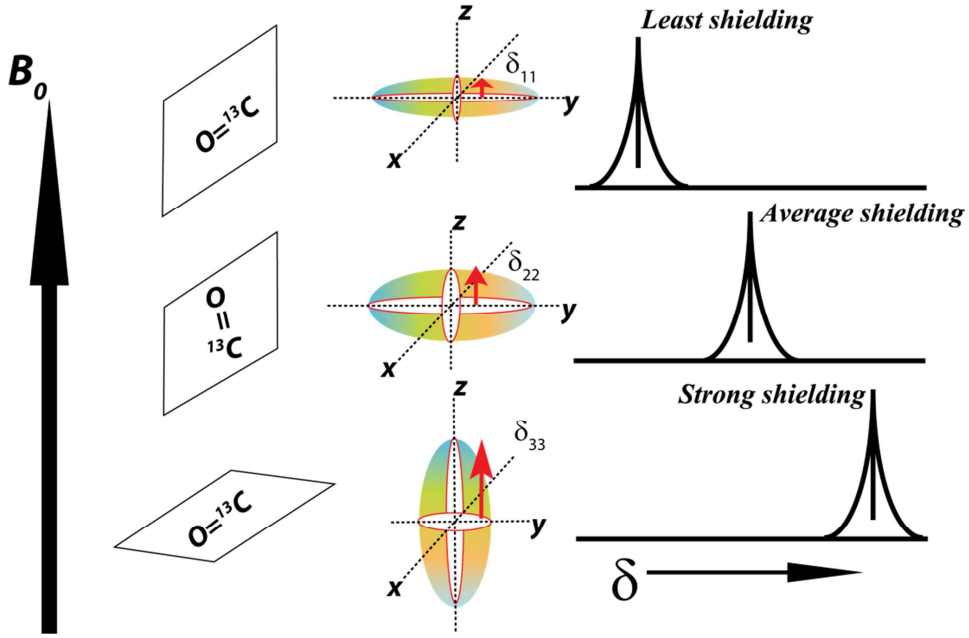

Figure 2.5.3: Orientation dependence of chemical shift in a crystal

To understand the chemical shift in solids let us see an example. Consider a ^{13}C NMR spectrum of a solid crystal sample. For the sake of simplicity we have only one chemical group i.e. Carbonyl

group $^{13}C=O$. Figure 1.5 demonstrates the orientation dependency of the δ_{ij} leading to three shielding terms in a single molecule. The ellipsoid in the Figure 2.5.3 is the representation of the chemical shift tensor δ_{ij}, the three terms δ_{11}, δ_{22}, and δ_{33} are the possible orientation of the crystallites with respect to magnetic field B_0 leading to least, average and strong shielding respectively in a solid. This is clearly depicted in the ^{13}C spectrum with variable chemical shift. In isotropic liquids the three orientations are averaged out due to the rapid tumbling and rotation.

On the other hand the powder sample has many crystals with many different possible orientations. The solid state NMR spectrum of powder sample has a typical broad shape as shown in Figure 2.5.4. The line shape of the NMR spectra of a solid sample is determined by the asymmetry parameter η

$$\eta = \frac{(\delta_{22} - \delta_{11})}{\delta_{CSA}} \qquad \textbf{2.5.13}$$

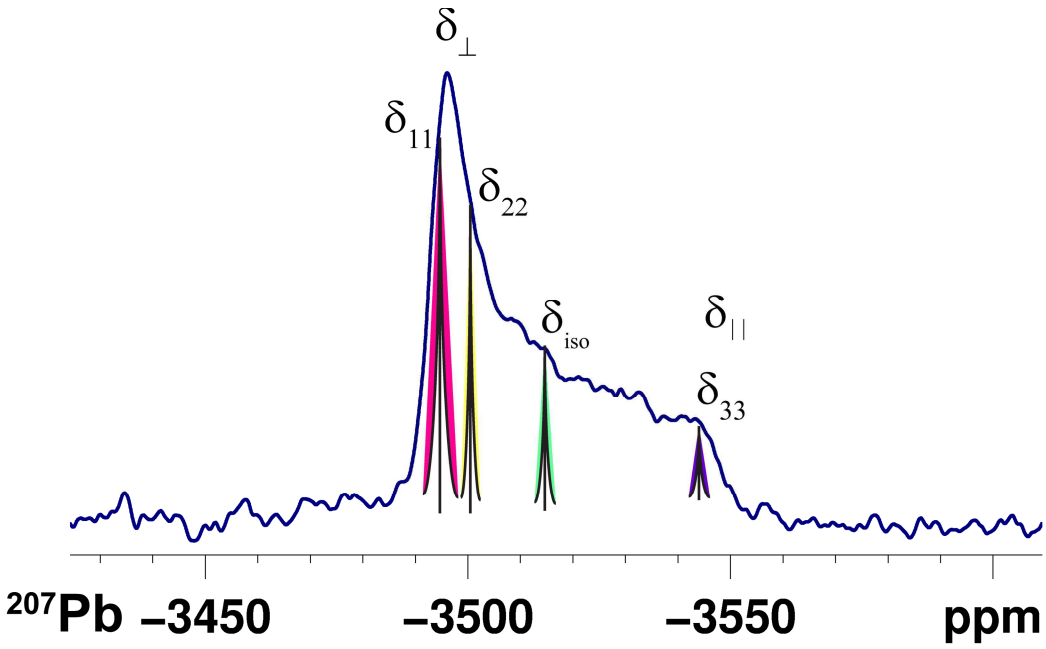

Figure 2.5.4: Solid state NMR spectra (static) of ^{207}Pb in Lead nitrate $Pb(NO_3)_2$

Figure 2.5.4 shows a ^{207}Pb solid state NMR spectrum of Lead nitrate $Pb(NO_3)_2$ at 7.05 T magnetic field. The line shape of the spectrum indicates that the sample is almost axially symmetric, with

perpendicular component δ_{11}, and δ_{22} being large and almost equal to each other and, the parallel component δ_{33} is small as shown in Figure 2.5.4. The distribution of the signals from all possible crystallite orientations give rise to *powder pattern* as shown in Figure 2.5.4.

^{207}Pb solid state NMR spectra show a broad feature which is due to the anisotropy term δ_{CSA} in the Equation 2.5.12. It has a value of 1.5 kHz or 100 ppm at 7.05 T or 300 MHz magnetic field. The line width in solid is almost 3 orders of magnitude large compared to solution state spectra (5 Hz). The chemical shift anisotropy is a serious menace for the analysis of a solid state NMR spectrum. In spite of being annoyance, the chemical shift anisotropy contains important information of the local environment of the solid under study.

Nucleus	**δ_{CSA} in ppm**	**δ_{CSA} in kHz (at 18.8 T magnetic field / 800 MHz)**
^{1}H (Amide)	12-14	11.2
^{13}C (Aliphatic)	30	6
^{13}C (Aromatic)	150	30
^{15}N	160	20
^{207}Pb	50	8

Table 2.5.1: Typical values of δ_{CSA} of some nuclei of NMR interest

Table 2.5.1 shows typical values of δ_{CSA} normally one encounters during their investigation using solid state NMR.

2.5.2 Dipolar coupling

Sample containing non-zero nuclear spin (I > 0) in a magnetic field generates a looping field around the surrounding space and this field influences the looping field generated by the neighboring nuclei. Vaguely, this interaction can be termed as inter-nuclear Zeeman interaction: the magnetic field generated by one nucleus influencing the other nucleus through space. Figure 2.5.5 shows a vector picture of dipolar interaction of two identical nuclei in a magnetic field.

The dipolar interaction Hamiltonian for two identical nuclei is given by,

$$\hat{H}_{DD}^{ij} = d_{ij}\frac{\left(3\cos^2\theta_{ij}-1\right)}{2}\left[3I_iI_j - \vec{I}_i \bullet \vec{I}_j\right] \qquad \textbf{2.5.14}$$

Here $d_{ij} = -\frac{\mu_0}{4\pi}\frac{\gamma_i\gamma_j\hbar}{r_{ij}^3}$ **2.5.14b**

is the dipolar coupling between the two nuclei $\boldsymbol{I}_i$ and $\boldsymbol{I}_j$. 'r_{ij}' is the inter-nuclear distance between the nuclei $\boldsymbol{I}_i$ and $\boldsymbol{I}_j$ and the γ_i, γ_j are the gyromagnetic ratio of the two nuclei involved. The dipolar coupling d_{ij} depends on the inter-nuclear distance, where as the dipolar interaction Hamiltonian depends on orientation due to $3cos^2\theta$-1 term. The term $\vec{I}_i \cdot \vec{I}_j$ in the Equation 2.5.14 can be furthermore written as,

$$I_{i+}I_{j-} + I_{i-}I_{j+} \qquad \textbf{2.5.15}$$

The term in equation 2.5.15 is a homonuclear flip-flop term, which causes energy-neutral exchange of magnetization between spin pair and its effect is clearly seen in a ^{1}H (or any other high abundant nuclei) solid state NMR spectrum.

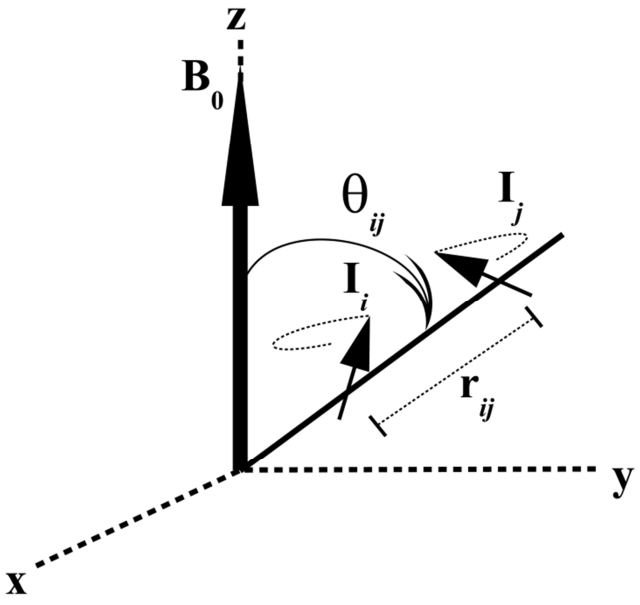

Figure 2.5.5: Dipolar interaction of two nuclei $\boldsymbol{I}_i$ and $\boldsymbol{I}_j$ in a magnetic field $\boldsymbol{B}_0$

In the case of dipolar interaction between two different nuclei $\boldsymbol{I}$ and $\boldsymbol{S}$ i.e. heteronuclear, the Hamiltonian is given by,

$$\hat{H}_{DD} = d\left(3\cos^2\theta - 1\right)\vec{I}\,\vec{S} \qquad \textbf{2.5.16}$$

Similar to the chemical shift anisotropy, the dipolar interaction also causes broadening of the solid state NMR signals due to the orientation dependent term. The magnitude of the homonuclear dipolar interaction is much larger compared to the heteronuclear case due to the extra flip-flop term present in homonuclear dipolar coupling Hamiltonian (see 2.5.15). Later in this chapter we will see how one can simplify the solid state NMR spectra by using some of the technique like magic angle spinning to average both CSA and dipolar coupling.

2.5.3 Hyperfine coupling

The interaction between electrons and the nucleus in a molecule as seen from NMR point of view has been discussed in previous units. In diamagnetic molecules, the bonding electrons produce a local field due to their magnetic moment around the observed nucleus, which adds or subtracts the applied field and hence one observes a chemical shift which is a characteristic of a nuclear surrounding. This information is very important in NMR to analyze a given molecule. Now, if a molecule contains an unpaired electron then the observed nucleus senses at least two types of local fields: one by the valence and bonding electrons and the other by the unpaired electron as shown in Figure 2.5.6. If we consider a nuclear spin I and electron spin S_e in a magnetic field then the Zeeman energy levels are given by their M_I and M_S values, respectively. The nucleus and electron spins continuously change the magnetic energy levels but the population distribution remains constant at a given temperature.

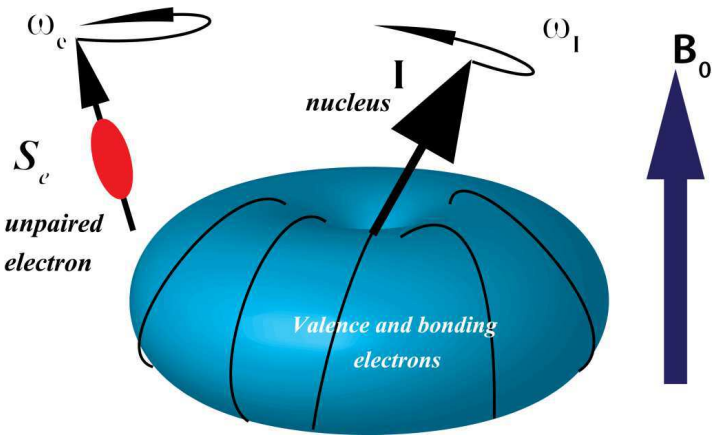

Figure 2.5.6: Interaction between an unpaired electron and a nucleus in a magnetic field

The electron relaxes several orders of magnitude faster than the nucleus. As a result the nucleus on its M_I level sees one electron rapidly changing its orientation in M_S energy level. Hence the nucleus experiences an average magnetic moment of electron. In contrary, in paramagnetic systems the average magnetic moment $\langle\mu\rangle$ felt by the nucleus is proportional to $\langle S_z\rangle$ and is negative (due to excess population in M_S = -½). The interaction of the unpaired electron and the nucleus in a molecule is called the hyperfine interaction. This interaction is often large in magnitude (see Figure 2.5.1) compared to all other NMR interactions in solids. The general Hamiltonian of the hyperfine coupling of a system is given by

$$\hat{H}_{Hyp} = \hat{I} \cdot \tilde{A} \cdot \hat{S} \qquad \textbf{2.5.17}$$

where $\tilde{A}$ is the hyperfine coupling tensor, $\hat{I}$ is the nuclear spin and $\hat{S}$ is the electron spin operator.

The hyperfine interaction is commonly resolved into: (a) The Fermi contact interaction - the unpaired electron has a non-zero probability of finding itself on the position of the nucleus, (b) pseudocontact interaction - a magnetic dipolar interaction between the nucleus and of the unpaired electron. The total Hamiltonian of the hyperfine interaction hence is a sum of Fermi and pseudocontact interaction

$$\hat{H}_{Hyp} = \hat{H}_{FC} + \hat{H}_{PC} \qquad \textbf{2.5.18}$$

Fermi-contact interaction

The Fermi contact interaction can be approximated as a scalar interaction (when g is isotropic) similar to the J-coupling. However, if spin-orbit coupling constant cannot be neglected, it is often treated by replacing the electronic gyromagnetic ratio g_e by a tensor. The total Fermi contact interaction then becomes anisotropic. The fractional unpaired electron spin distribution on the nucleus in a molecule is explained by two mechanisms: (1) delocalization and (2) spin polarization. The contact interaction leads to contact shifts (upfield and or downfield) which are dominant in small paramagnetic metal complexes, where the proximity of the paramagnetic metal center to the observed nucleus is very close. The contact shift masks the chemical information. In the isotropic case the interaction Hamiltonian of Fermi contact interaction is given by

$$\hat{H}_{FC} = A\,\hat{I}\cdot\hat{S} \qquad \textbf{2.5.19}$$

where, A is Fermi contact coupling constant. The energy difference obtained by evaluating the Equation 2.5.19 gives us the Fermi contact shift contribution which is given by

$$\delta_{FC} = \frac{A g_e \mu_B S(S+1)}{\hbar \quad 3\gamma_I kT} \qquad \textbf{2.5.20}$$

where $A = \frac{\mu_0}{3S} h\gamma_I g_e \mu_B \sum_i \rho_i(\vec{r})$ is the contact coupling constant. The Fermi contact shift δ_{FC} is characteristic of the unpaired electron spin density $\rho(\vec{r})$. For zero electron-nucleus distance,

$$\rho(\vec{r}) = \psi_{-\frac{1}{2}}(\vec{r})^2 - \psi_{\frac{1}{2}}(\vec{r})^2 \qquad \textbf{2.5.21}$$

where $\psi(\vec{r})$ is the value of the molecular orbital wave function at the nucleus for the -½ and ½ states. By grouping physical constants in Equation 2.5.20 the expression for δ_{FC} can be written as[81-82]

$$\delta_{FC} = m\frac{(S+1)}{T}\rho(r) \qquad \textbf{2.5.22}$$

Here $m = 2.35 \times 10^7$ $K^{-1}au^{-1}ppm$ is collection of constants. From Equation 2.5.22 (in atomic units) it is clear that Fermi contact shift δ_{FC} depends primarily on unpaired electron spin density $\rho(\vec{r})$, total electronic spin S (for example S = ½ for doublet state) and the temperature T.

Pseudocontact interaction

In a molecule if the unpaired electron is sufficiently far away from the observed nucleus, then it will interact with the nucleus through space (similar to dipolar coupling). This electron – nuclear dipolar interaction is termed as pseudocontact interaction. The pseudocontact interaction is an orientation dependent term and hence anisotropic in nature similar to the nuclear dipolar coupling. The interaction Hamiltonian for pseudocontact interaction is given by,

$$\hat{H}_{PC} = S\cdot\tilde{D}\cdot I \qquad \textbf{2.5.23}$$

At high field approximation,

$$\hat{H}_{PC} = D\frac{1}{2}\left(3\cos^2\theta - 1\right) I_z S_z \qquad \textbf{2.5.24}$$

with coupling constant,

$$D \propto \frac{\gamma_N g_e \mu_B}{r^3} \qquad \textbf{2.5.25}$$

where, r is the electron-nuclear distance. In small molecules the pseudocontact interaction is less dominant. Due to the anisotropic nature of this interaction, it can in principle be averaged by magic angle spinning in solids. It is in many cases responsible for very fast relaxation of the nucleus in a paramagnetic system under study.

2.6 Techniques in solid state NMR

NMR interactions in solids are quite large and complicated to understand compared to interactions in liquids. In liquids, the anisotropic interactions such as chemical shift anisotropy, dipolar coupling and quadrupolar coupling are averaged out due to the rotation and tumbling of molecules. Even though NMR signals were first observed in solids[97] the fair sensitivity and resolution of the NMR signals in liquids relative to solids led to the rapid growth in the development of techniques in solution state NMR. NMR of solids remained as a tool only for physicists working in material magnetism until the development of spatial averaging technique like magic angle spinning (MAS)[114-117] which simplified the solid state NMR spectra. In a solid powder sample the NMR signals are broad, distribution of signals from individual crystallite orientation giving rise to anisotropic interactions. Magic angle spinning allows one to mimic the motion of molecules in solids with respect to liquids and averages out anisotropic interactions such as chemical shift anisotropy, dipolar coupling, and first order quadrupolar coupling.[115-116] The solid state NMR spectra obtained using magic angle spinning is free of anisotropic interaction to some extent and gives room for ease signal assignment. Most of the solid state NMR experiments nowadays employ the MAS technique to obtain spectra consisting of narrow signals.

One of the major drawbacks of NMR spectroscopy is the sensitivity. Due to low natural abundance major set of NMR active nuclei under study fail to give a descent NMR spectrum, among them is Carbon-13 isotope of carbon. The natural abundance of ^{13}C is 1.1 % with respect to ^{1}H which is 99 % abundant. In solids the low natural abundance of less sensitive nuclei adds on to the problem of

broadening due to anisotropic interaction and causes severe loss of sensitivity and resolution. Cross polarization[118] is one of the important sensitivity enhancement techniques in solid state NMR similar to its counterpart technique INEPT[84] (Insensitive Nuclei Enhancement by Polarization Transfer) in solution state NMR. On the one hand large amount of polarization from ^{1}H is transferred to ^{13}C or other insensitive nuclei. On the other hand ^{1}H abundance is a menace to the sensitivity and resolution of ^{13}C or other less abundant nuclei due to heteronuclear and homonuclear dipolar coupling. During acquisition of the NMR signal of ^{13}C, one can apply pulses on ^{1}H and try to decouple the interaction between the two spins ^{1}H and ^{13}C; this technique is called as heteronuclear decoupling. Heteronuclear decoupling[119] would improve the sensitivity and resolution of ^{13}C signal by reducing the residual line broadening due to ^{1}H dipolar coupling in MAS experiments.

Magic angle spinning renders one to control the anisotropic interaction by reducing the spinning speed and invoking back the interactions. One can also reintroduce the interactions in spin space by applying r.f. pulses during magic angle spinning into the system for various applications, this is called recoupling. The general interaction one uses in recoupling technique is the dipolar coupling and hence the experiments are called dipolar recoupling experiments. There are number of recoupling pulse sequence developed for various uses in solid-state NMR such as dipolar coupling measurement[120] and determination of inter nuclear distance measurement[121-122] and polarization transfer.[123-128]

Important techniques such as magic angle spinning (MAS), cross-polarization (CP), heteronuclear decoupling, and some recoupling sequence such as Transferred-echo double order resonance (TEDOR) which forms the basis for the 2D dipolar INEPT pulse sequence (used in this work) in solid state NMR are briefly explained in this section.

2.6.1 Magic angle spinning (MAS)

Major breakthrough in research in the field of solid state NMR was seen after the invention of magic angle spinning (MAS) technique in the 1950's by Lowe[129] and Andrew *et al.*[115] Broad features in NMR spectra originating from the static solids due to anisotropic interactions such as

chemical shift anisotropy and dipolar coupling could be narrowed down using this technique. The technique involves the spinning of powdered sample in zirconium rotor rapidly at an angle θ_m equal to 54.7° called magic angle with respect to magnetic field B_0 as shown in Figure 2.6.1. This process of spinning eventually aligns all the possible orientation of the crystallites to the axis titled to magic angle with respect to magnetic field B_0. One can see that in the Equation 2.5.12 and 2.5.14 i.e. the Hamiltonians of CSA and dipolar coupling both contain $3cos^2\theta$-1 term. This term averages to zero with the magic angle θ_m. The sample with relatively less magnitude of anisotropy gives a very well resolved solid state NMR spectrum and the higher ones gives signals with lot of sidebands.

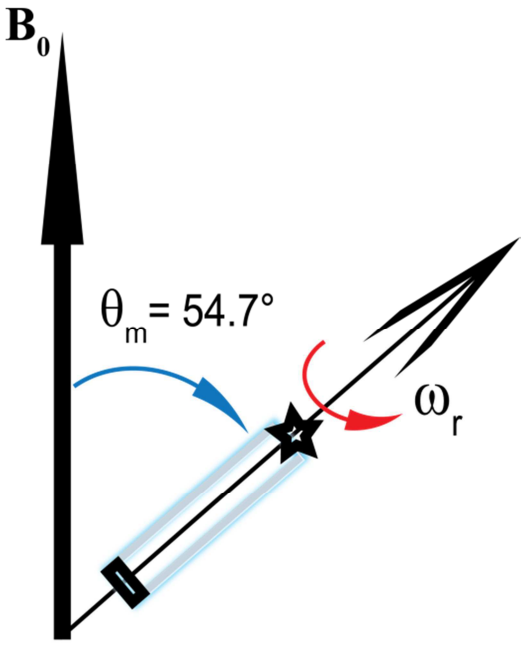

Figure 2.6.1: Sample rotation at magic angle 54.7° with respect to magnetic field $\boldsymbol{B_0}$ in MAS technique

During early 1960's the MAS unit provided several hundred hertz to few kilo hertz of spinning speed. Present state of the art MAS probes (1.6 mm) can render up to 66 kHz of spinning speed, a typical value of ^{1}H-^{13}C dipolar coupling. All modern solid state NMR experiments employ MAS technique to have high resolution. Figure 2.6.2 demonstrates a difference in sensitivity and resolution of ^{207}Pb solid state NMR spectra in $Pb(NO_3)_2$ sample at static and MAS condition. Various orientations of the lead nitrate crystallites give rise to broad feature of the NMR signal as seen in ^{207}Pb solid state NMR spectrum at static condition.

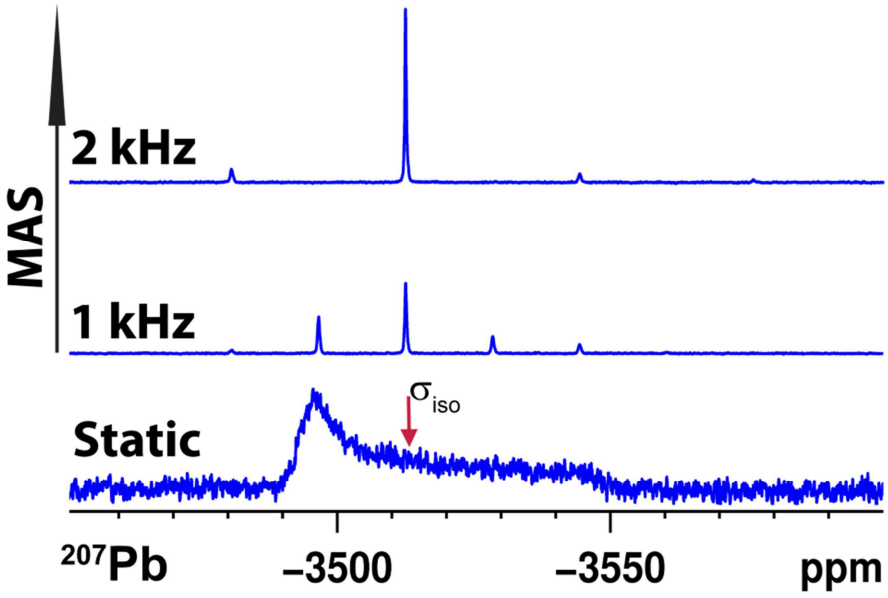

Figure 2.6.2: ^{207}Pb 1D solid state NMR spectra at static and MAS (1 and 2 kHz) condition

In Figure 2.6.2 shown is the 1D solid state NMR spectra of ^{207}Pb, at 1 kHz MAS condition the system undergoes a transformation where the chemical shift anisotropy (which is dominant in this case) is partially averaged out and results in the distribution of side bands separated 1 kHz away from the central intense peak. Now increasing the MAS speed to 2 kHz shifts the side bands 1 kHz more. The intensity of the central intense peak is amplified and thereby reduces the line width to almost 30 Hz, which improves both the sensitivity and resolution of the signal. The value of the central peak which is invariant under the increment in the MAS frequency is called the isotropic chemical shift σ_{iso}.

2.6.2 Cross polarization (CP)

Another routine and a very important technique in solid state NMR is cross polarization (CP). Similar to INEPT[84] in solution state NMR where the magnetization from the more abundant nuclei such as proton is transferred to less abundant nucleus (such as ^{13}C, ^{15}N etc.) through *j*-coupling, here CP uses dipolar coupling between two spins *I* and *S*. The basis of cross polarization experiment is the nuclear double resonance experiments which were developed and explained through thermodynamics and quantum mechanics by Hartmann and Hahn[130] in 60's. Initially cross polarization experiment was developed by Pines, Gibby, and Waugh[118] for static samples and later modified by Schafer and Stejskal for rotating solids[131]. Figure 2.6.3 demonstrates a simple version

of pulse sequence of cross polarization experiment with heteronuclear decoupling (explained in next unit) in solid state NMR. A 90° pulse on more abundant nuclei *I* (such as protons) creates fair amount of magnetization. This is followed by a spin lock field on both *I* and *S* (such as ^{13}C, ^{15}N etc.) channel to certain time called contact-time. For magnetization to be transferred from *I* to *S* the spin lock fields on both the channel have to fulfill the Hartmann-Hahn condition[130] given by,

For static condition, $$\omega_1^I = \omega_1^S \Rightarrow \gamma_I B_1^I = \gamma_S B_1^S \qquad \textbf{2.6.1}$$

and for MAS, $$\omega_1^I = \omega_1^S + n\omega_r \Rightarrow \gamma_I B_1^I = \gamma_S B_1^S + n\omega_r \qquad \textbf{2.6.2}$$

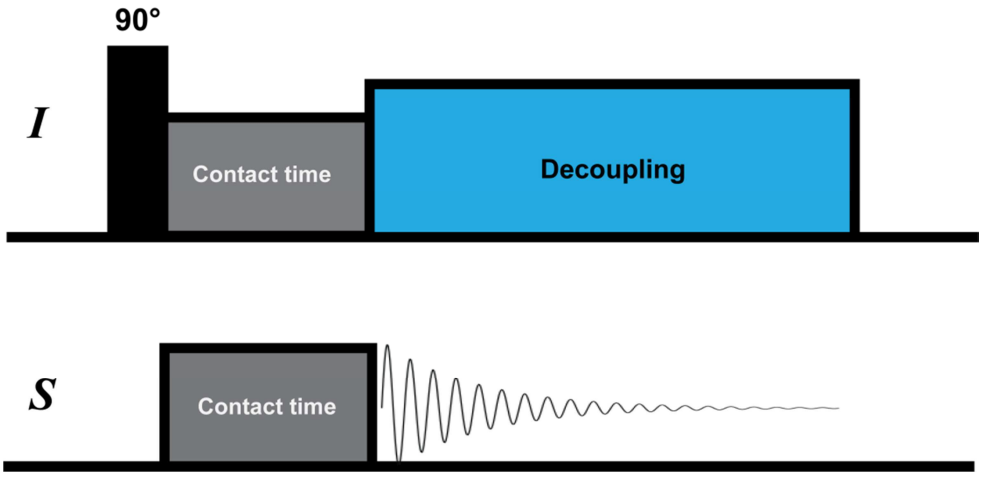

Figure 2.6.3: Pulse sequence of cross polarization with Heteronuclear decoupling

where ω_r is the MAS frequency, B_1^I and B_1^S are r.f. field strengths of contact pulses on *I* and *S* channel respectively and '*n*' is the integer. Using CP, theoretically the signal enhancement is expected to be proportional to γ_I/γ_S depending on the proportion of *I* and *S* pair in a system. Various version of CP experiments are used to get better signal enhancement one such is ramp-CP.[132] In this version, the amplitude of contact pulse on either one of the channel is steadily increased. This version is very effective for optimum polarization transfer in systems containing different types of ^{13}C groups (CH, CH_2, and CH_3). Figure 2.6.4 demonstrates the drastic gain in signal in a CP experiment of an organic group functionalized mesoporous silica material with respect to one pulse excitation experiment.

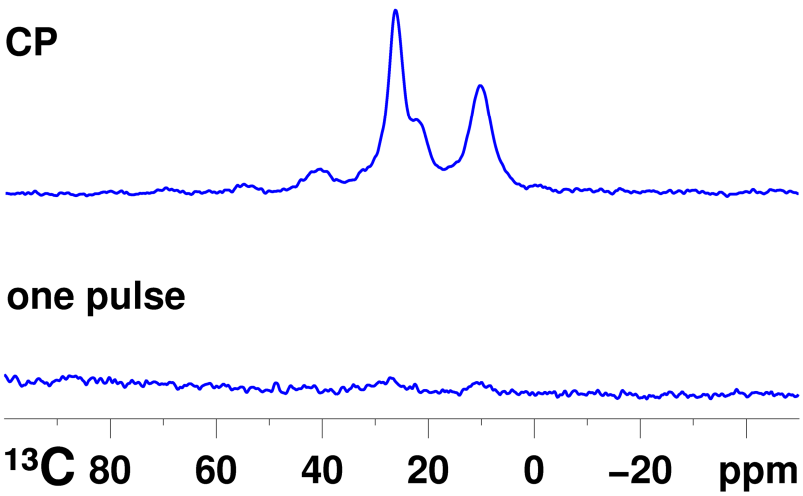

Figure 2.6.4: ^{13}C one pulse and CP experiment in organic group functionalized mesoporous silica material

2.6.3 Heteronuclear Decoupling

Magic angle spinning partially averages the dipolar coupling between *I-S* pairs such as ^{1}H-^{13}C. The limit of averaging the anisotropic interactions using MAS depends on the factors such as the spinning speed (slow, moderate and fast) and strength of dipolar coupling between ^{1}H and ^{13}C (how much the system is rich in protons). The moderate (10 kHz) and fast (<25 kHz) is sometimes not sufficient to obtain well resolved ^{13}C spectra, especially in organic and biological solids which are rich in protons. In such cases one has to average the residual interactions in spin space by applying r.f. pulses in combination with MAS which is called as Heteronuclear decoupling in the case of *I-S* pair (such as ^{1}H-^{13}C or ^{1}H-^{15}N). During the acquisition a continuous r.f. irradiation on abundant spin *I* (say ^{1}H) decouple the interaction between *I* and *S* as shown in Figure 2.6.5.

In solid state NMR the simplest method of heteronuclear decoupling is *continuous wave* (CW) decoupling similar to the technique developed for solution state NMR.[133-135] CW decoupling works by rotating the spin state of ^{1}H spins, thus the interactions are averaged every 2π rotation while the spin state of the ^{13}C are not modified as shown in Figure 2.6.5. Under MAS condition, the sample rotation and the CW decoupling can interfere with each other if their timescales are comparable, leading to inefficient decoupling. Therefore there are two different ways by which the CW decoupling can be efficient.[136]

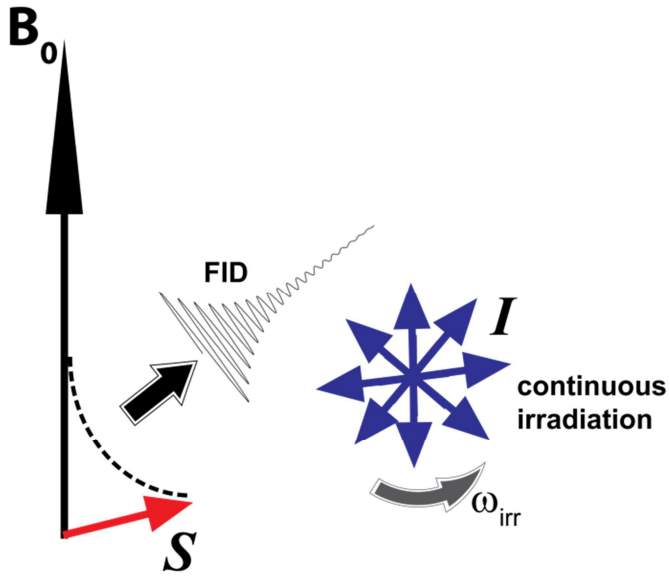

Figure 2.6.5: Heteronuclear decoupling in *I-S* system by continuous irradiation on *I*

-high power CW decoupling and low power CW decoupling.[137] In high power CW decoupling the sample is spun at relative low or moderate spinning (<25 kHz) and a high power r.f. of 50-250 kHz is irradiated and in the low power decoupling an r.f. of 50 kHz is irradiated while spinning sample at

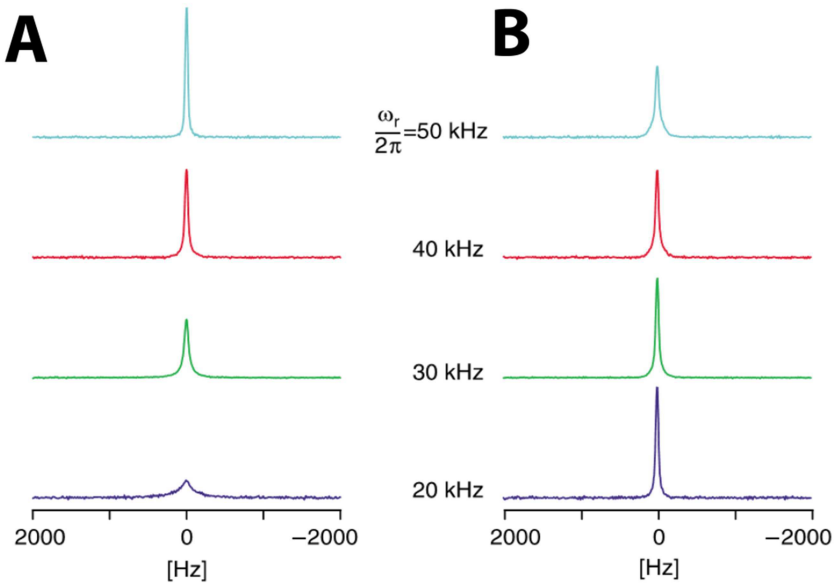

Figure 2.6.6: ^{13}C spectra of 8 % labeled 2-^{13}C alanine at MAS frequency of 20, 30, 40, and 50 kHz with (A) low power CW decoupling (ω_1=21 kHz) and (B) high power decoupling (ω_1=215 kHz)

frequency more than 30 kHz. Figure 2.6.6 referred from Ernst *et al.*[137] demonstrate the performance of CW decoupling in a ^{13}C CP-MAS experiment on 8 % labeled 2-^{13}C alanine sample. At 50 kHz MAS and 21 kHz CW irradiation power a narrow line width of 40 Hz was obtained, on contrary 215

kHz of CW r.f. irradiation power is required to obtain a narrow line width at 20 kHz MAS speed. Technique such as composite pulse decoupling (CPD)[138] has paved way for many family of CPD decoupling sequences such as WALTZ-16,[139] TPPM,[119] and SPINAL-64[25] which have shown better performance over traditional CW decoupling.

2.6.4 Recoupling techniques

Reintroducing MAS averaged anisotropic interactions back into the system by application of pulses to gain access to some useful information such as dipolar coupling and inter-nuclear distances is called as *recoupling*. Generally recoupling is used to bring back dipolar interaction into the system and hence the technique associated with it is called as *dipolar recoupling*. The principle behind dipolar recoupling is to apply *rotor synchronized pulse sequences* which are known as *recoupling sequences*, while maintaining high resolution achieved by MAS. In the case of dipolar recoupling one can distinguish the recoupling technique based on the nuclei pair under study i.e. *Homonuclear* and *Heteronuclear recoupling*. Here in this unit only *Heteronuclear dipolar recoupling* technique would be emphasized since the thesis deals with the usage of a heteronuclear dipolar recoupling technique TEDOR[85](transferred echo double order resonance).

Dipolar recoupling techniques are used basically for the two major purposes:

1. **Measure dipolar coupling and hence inter-nuclear distances:**

   In the simplest case the NMR signal intensity is measured as a function of time interval in which the dipolar recoupling sequence is applied. One such dipolar recoupling sequence is REDOR[140] (rotational echo double order resonance) introduced by Gullion *et al.* in late 80's. Figure 2.6.7 demonstrates the measurement of ^{15}N-^{13}C distance in glycine (from ref. 54) by recoupling the dipolar interaction between ^{15}N-^{13}C using the REDOR pulse sequence applied on ^{15}N channel (shown in Figure 2.6.7 A). Here the experiment follows a simple ^{1}H-^{13}C CP followed by rotor synchronized REDOR pulse sequence on ^{15}N channel. The intensity of the ^{13}C is measured as a function of time during which the application of REDOR pulse sequence is monitored on ^{15}N. A plot of dephasing time 'τ' versus the signal intensity of ^{13}C with and without recoupling pulses on ^{15}N channel gives a curve. By fitting the decay of ^{13}C

magnetization (see Figure 2.6.7 D), the dipolar coupling value of 195 Hz between ^{13}C-^{15}N was determined. Inserting the value of ^{13}C-^{15}N dipolar coupling in Equation 2.5.14.b a distance of ~2.5 Å was obtained. There are some early examples of ^{13}C-^{17}O dipolar coupling measurement[140] and ^{13}C-^{15}N distance measurement[122] in alanine reported by Gullion *et al.* using REDOR recoupling technique.

2. Coherent polarization transfer: TEDOR

Another important use of dipolar recoupling technique is coherent polarization transfer between *I-S* (like ^{1}H-^{13}C) using technique such as REPT (recoupled polarization transfer)[125,127-128] under fast MAS condition (>30 kHz) unlike the counterpart technique CP which is incoherent in nature. At high spinning speeds the ^{1}H-^{1}H homonuclear and ^{1}H-X (where X=^{13}C, ^{15}N, ^{31}P etc.)

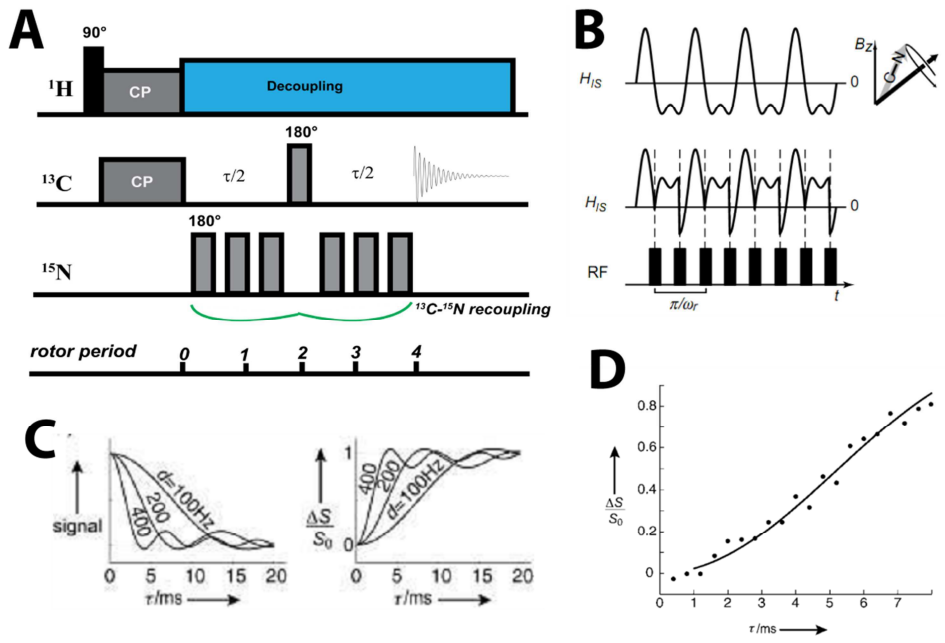

Figure 2.6.7: (A) ^{13}C-^{15}N dipolar recoupling using REDOR recoupling sequence. (B) Recoupling of dipolar interaction between ^{13}C-^{15}N by application of rotor synchronized 180° r.f. pulses. (C) ^{13}C-^{15}N Dephasing curves obtained as a function of the dephasing time. (D) ^{13}C magnetization in ^{13}C-^{15}N labeled glycine as a function of length of dephasing time τ. $\Delta S/S_0$ (the REDOR difference) is the normalized difference between ^{13}C signal intensities with and without pulses on ^{15}N[141].

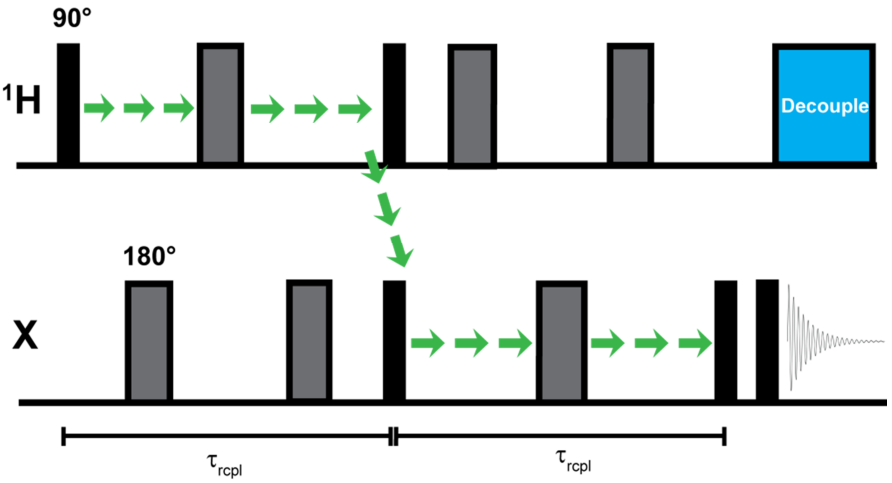

Figure 2.6.8: Pulse sequence of ^{1}H-X TEDOR recoupled polarization transfer under fast MAS. (Arrows indicate the pathway of polarization)

dipole-dipole coupling is efficiently reduced and gives room for heteronuclear dipolar recoupling schemes to be used for coherent and distance selective polarization transfer between ^{1}H and X. A well known REPT scheme is TEDOR (transferred echo double order resonance) which was introduced by Hing *et al.*[85] and uses REDOR-type Heteronuclear recoupling to accomplish polarization transfer. Shown in Figure 2.6.8 is a recoupled polarization transfer based pulse sequence scheme employing TEDOR. Since REPT schemes are rotor synchronized, they have very short transfer period $\tau_r = \tau_{rcpl}$ (~66.7 μs for two rotor period) under fast MAS condition (>30 kHz). The TEDOR pulse sequence shown in Figure 2.6.8 can be modified for advanced 2D experiment and a correlation between ^{1}H-X can be obtained similar to HETCOR (Heteronuclear correlation) which employs CP for polarization transfer.

We have used dipolar INEPT, a TEDOR based recoupling polarization technique to obtain 2D correlation between ^{1}H-^{13}C in our present work which can be seen in the result and discussion part of the thesis.

Chapter 3: Materials and methods

"The only possible conclusion science can draw is: Some do, some don't." – **Richard R. Ernst**

3.1 Materials

3.1.1 Paramagnetic metal-cyclam and –acetylacetonate complex

The paramagnetic metal-cyclam (Cu-cyclam and Ni-cyclam) complexes used in this work were provided by Prof. Ahmad Mehdi, Institut Charles Gerhardt of University of Montpellier, France. The cyclam (1, 4, 8, 11-tetraazacyclotetradecane) compound of 99% purity was purchased from Sigma Aldrich®, France.

The paramagnetic metal-acetylacetonate (Cu-acac, VO-acac and Ni-acac) complexes of 99% purity used in this work were purchased from Sigma Aldrich®, France.

3.1.2 Paramagnetic alkaline metal-copper pyrophosphates

The paramagnetic metal-inorganic systems of alkaline metal (Na^{2+}, K^{2+}, and Li^{2+})-copper pyrophosphates used in this investigation were provided by Prof. Souhir Chouaib and Prof. Abdullah Ben-Rhaiem, University of Sfax, Tunisia.

3.2 Methods

In this section we describe the experimental (Solid state NMR, EPR and XRD) and theoretical methods (DFT calculations) used in this work. We also provide the information of other supporting programs used in this work for processing, visualizing and graphical fitting.

3.2.1 Solid state NMR spectroscopy

Solid state NMR spectra were acquired on a Bruker Avance III 300 MHz spectrometer equipped with a double-resonance 2.5 mm VTN probe. All experiments were performed under magic angle spinning (MAS) with a frequency of 30 kHz at room temperature. The sample temperature was 58°C due to friction. The spectra were referenced to TMS. In the case of paramagnetic metal-

cyclam and –acetylacetonate complexes the ^{1}H and ^{13}C, and in the case of paramagnetic alkaline metal-copper pyrophosphates the ^{31}P one dimensional spectrum were acquired by means of a Hahn echo experiment. Hard pulses with nutation frequencies of 136 kHz for ^{1}H, 143 kHz for ^{13}C and 107 kHz for ^{31}P (excitation pulse p_{90} = 1.84 μs for ^{1}H, 1.75 μs for ^{13}C, and 2.34 μs for ^{31}P) were used. The carbon-13 CP-MAS experiment was performed with ^{1}H hard pulse of nutation frequency 113 kHz, a ramp amplitude pulse was used during the contact time (contact pulse p_{CT} = 105 μs). For all experiments in the case of paramagnetic metal-organic complexes an inter-scan delay between 40 and 55 ms was set. In the case of metal-inorganic system the inter-scan delays was 1 s for paramagnetic alkaline metal-copper pyrophosphate and 60 s for sodium pyrophosphate (diamagnetic reference). No ^{1}H decoupling was applied during the indirect evolution or during the acquisition period of any 1D (including ^{13}C CP) or 2D experiment. ^{13}C transverse relaxation rates (R_2) were measured by means of the CPMG[91-92] experiment.

For 2D ^{1}H-^{13}C correlation, a variation of dipolar INEPT or TEDOR[60-61,85] was applied with a mixing time of two rotor periods (66.7 μs). Pulse sequences for dipolar HSQC and ^{1}H-^{1}H correlation are described in the Results section (see section 5.4 of Chapter 5). For 1D ^{1}H and ^{13}C spectra 128 K and 1024 K scans were accumulated, respectively, for the ^{13}C relaxation spectra 128 K scans, for the dipolar INEPT 64 complex data points with 32 K scans each, incremented by 16.67 μs, for the dipolar HSQC 16 complex data points with 16 K scans, incremented by 33.33 μs, and for the ^{1}H-^{1}H correlation experiment 148 increments with 512 scans, incremented by 8.33 μs. For all 2D experiments, the States-TPPI quadrature detection scheme was applied.

3.2.2 EPR spectroscopy

EPR experiments were obtained with the courtesy of Prof. Abdelhadi Kassiba, Institut des Molécules et des Matériaux du Mans (IMMM) at Université du Maine, Le Mans, France.

CW-EPR experiments were performed on a Bruker EMX spectrometer working with X-Band (9.5 GHz). The spectra were recorded at RT by using low micro-wave power (20 mW), modulation field (5 G), and 100 kHz as a standard modulation frequency. The spectral parameters (g-tensor, line width) were determined with the Bruker software SimFonia.

3.2.3 DFT calculations

Quantum chemical calculations of paramagnetic systems often referred as open-shell systems calculation is a separate branch of quantum chemistry. There has been numerous amounts of research done in the past and going on in this area to develop robust and optimum techniques to obtain parameters associated with many spectroscopic techniques.[142] Some of the pioneering works of Walter Kohn and Lu sham in the field of open-shell quantum chemical calculations[143] has significantly contributed to the progress of Quantum chemistry branch. We have found some of the works in literature pertaining to quantum chemical calculation of transition metal-complexes such as and have used similar approach to obtain required parameter. Some of the quantum chemical calculation methods mentioned in the works of Wilkens *et al.*,[79-80] Rastrelli *et al.*,[144] Bühl *et al.*,[145] Mao *et al.*,[82,146] Zhang *et al.*,[81] Hrobárik *et al.*,[147] Kervern *et al.*,[61] Adams *et al.*,[148] and Carlier *et al.*[149] have significantly been used during our investigation of paramagnetic metal-organic and –inorganic systems. There are numerous and advanced programs to run quantum chemical calculations that have been developed since several decades such as GAMESS, GAUSSIAN, ADF, CASTEP, Quantum ESPRESSO, TURBOMOLE etc. We have used GAUSSIAN 09 package to perform DFT calculations on our systems.

The calculations of Fermi-contact shifts and diamagnetic chemical shifts of paramgneitc metal-cyclam and -acetylacetonate were performed with density functional theory (DFT) using generalized gradient approximation (GGA) applying hybrid potential implemented in the program GAUSSIAN 09 (G09).[83] Two Opteron 2.3 GHz processors with 16 GB RAM of a Beowulf-type parallel computing facility were used provided at Université du Maine, Le Mans, France.

The structures of the Cu-/ Ni-cyclam and Cu-/ VO-acetylacetonate complexes were constructed by means of the program GaussView 5.0 purchased from GAUSSIAN Inc.

A full geometry optimization of these structures were performed (using *OPT* command) at unrestricted Hartree-Fock method (UHF) applying B3LYP potential.[150-151] A basis set of 6-311G in case of metal (Cu- and Ni-)-cyclam and Vanadyl-acetylacetonate complex.A basis set of Wacters-f on Cu, 6-31G(d) on hydrogen and 6-311G(d) on other atoms were set in the case of Copper-

acetylacetonate complex. The self consistent field (SCF) convergence was equal to 10^{-6} Hartree or up to 64 iterations in all the cases.

Frequency calculations were performed to check for false minima. (using *FREQ* command) on these optimized structures using the same method and basis set (used during optimization). The vibration frequencies showed no imaginary modes. The output of the frequency calculation was visualized using the program GaussView 5.0.

Upon calculations in UHF approximation, G09 generates a list of the unpaired electron spin densities and the Fermi contact couplings at the positions of all nuclei of NMR interest, out of which the Fermi-contact shifts were determined. The optimized structure of paramgnetic Cu/Ni-cyclam and Cu/VO–acetylacetonate complexes were furthermore used for the chemical shift calculation (using NMR=GIAO command) with the 6-311+G(2d,p) basis set. These shifts were referenced to TMS (calculated with the same theory and basis set) and added to the hyperfine shifts. Furthermore, the optimized structures were used for molecular orbital calculation (using *POP gfinput = full* command) using same method and basis set used during optimization job.

3.2.3 Details of the processing, graphical, and data analysis programs

The output of the molecular orbital calculation from G09 was visualized using the graphical program CHEMCRAFT. The contour level diagrams of the molecular orbitals used in the thesis were plotted with the same program.

The data from ^{13}C relaxation experiments of paramagnetic Cu-cyclam complex were processed using a joint-fit program written in MATLAB (see Appendix II). The procedure of the joint-fit is described in the Results part (see section 5.7 of Chapter 5) of the thesis. Furthermore the graphic program SIGMA PLOT 12.0 was used for plotting the decay curves and to perform the non-linear curve fitting.

RESULTS AND DISCUSSION

SECTION I

PARAMAGNETIC METAL-ORGANIC SYSTEMS

Chapter 4: Paramagnetic metal-cyclam complexes

"I believe that a scientist looking at nonscientific problems is just as dumb as the next guy."

– Richard P. Feynman

4.1 Introduction

Coordination complexes of cyclam with transition metal ions such as Cu^{2+}, Ni^{2+}, Cr^{3+}, Co^{2+} etc. as metal centers have been extensively studied in coordination chemistry.[152-153] High thermodynamic and kinetic stability[154-155] exhibited by metal-cyclam complexes especially with Cu^{2+} and Ni^{2+} ions as metal centers makes them unique among the group of coordination complexes. Hence these transition metal-cyclam complexes are extensively used for various applications in physical, chemical, biological, and pharmaceutical sciences.[10,72,156-159] Many of such applications require the metal-cyclams to be administered in solid form.[6-8,157,160] Synthesis of such potential systems requires efficient characterization techniques such as XRD, SEM, TEM, etc. Solid state NMR is one of the important characterization techniques for diamagnetic metal-organic complexes, where ^{1}H and ^{13}C chemical shifts serve as the fundamental and most basic information of the ligand. Furthermore one can have physical insight into the system by exploring the NMR interactions using advanced 2D experiments in solid state NMR.[14-15] However, in metal-organic complexes with transition metal ions such as Cu- and Ni-cyclam which exhibit paramagnetic behavior, the hyperfine interaction between the unpaired electron and the observed nucleus causes serious hindrance for the analysis of solid state NMR signals. The NMR signals resulting from such paramagnetic complexes show severe loss of sensitivity and resolution due to broadening by enhanced nuclear relaxation rates. Furthermore, the spin density of unpaired electron on the observed nucleus causes large shifts by the Fermi-contact interaction. These shifts masks diamagnetic chemical shifts and make signal assignment difficult using conventional methods. The paramagnetic interaction is more pronounced in solids and it requires novel and unconventional methods to probe such systems using solid state NMR.

Recent development in the area of solid state NMR of paramagnetic complexes by Ishii *et al.*[17] has been a main motivation of the work presented here. Ishii and coworkers observed that by very fast magic angle spinning (VFMAS, >25 kHz) sensitivity and resolution enhancement in paramagnetic metal-organic complexes can be achieved. We show here in this section that, one can obtain well resolved ^{1}H and ^{13}C solid state NMR spectra in paramagnetic Cu- and Ni- cyclam complexes by using VFMAS as shown by Ishii and Wickramasinghe *et al.*[17,60] and Kervern *et al.*[61] Furthermore, we use spin densities (and hence Fermi contact shifts) from DFT calculation for assignment of ^{13}C signals in paramagnetic Cu- and Ni-cyclam complexes. For assignment of ^{1}H signals we use ^{1}H-^{13}C 2D dipolar INEPT in paramagnetic Cu-cyclam complexes. Furthermore, with the help of the good sensitivity achieved in ^{1}H solid state NMR we show the possibility of a ^{1}H-^{13}C 2D dipolar HSQC with ^{1}H acquisition. Also, we show how a ^{1}H-^{1}H 2D correlation experiment was useful in completion of ^{1}H assignment in Cu-cyclam complex.

One of the main goals of this thesis is to measure metal-carbon distances using solid state NMR nuclear relaxation rates in paramagnetic metal-organic complexes. We have discussed here some of the results obtained in the case of the paramagnetic Cu-cyclam complex.

4.1.1 Chemical composition, crystal structure, and coordination chemistry of paramagnetic Cu- and Ni-cyclam complexes

Cyclam (1, 4, 8, 11-tetraazacyclotetradecane) is a fourteen membered tetramine macrocyclic ligand with chemical composition $C_{10}H_{24}N_4$ (Figure 4.1.1 A). Cyclam comes under the group of azamacrocyclic chelated ligands. The four nitrogen atoms in the cyclam arm serve as donor atoms for the binding of the ligand to the metal ion. Especially with transition metal cations such as Co^{2+}, Cr^{3+}, Cu^{2+}, Ni^{2+} etc. cyclam provides enhanced thermodynamic and kinetic stability of the metal-cyclam through its macrocyclic effect[161] (Figure 4.1.1 B). These transition metal-cyclam complexes so formed show various configurations in solution state as shown in Figure 4.1.1 C. But in solid state the stable *Trans-III* configuration is mostly favored[10,162] which makes it an ideal model system for the development of methods in solid state NMR. The paramagnetic Cu- and Ni-cyclam complex

used in the investigation have one and two chlorine anion as axial ligand (counter ion) forming five and six coordination type respectively. The cyclam ligand coordinates with the Cu^{2+} and Ni^{2+} metal ion and forms first coordination sphere of $[metal\text{-}cyclam]^{2+}$ complex cation as shown in Figure 4.1.1 B. Then there are one chlorine ion for Cu-cyclam and two chlorine ions for Ni-cyclam acting as counter ion. The geometry of the final coordination of the

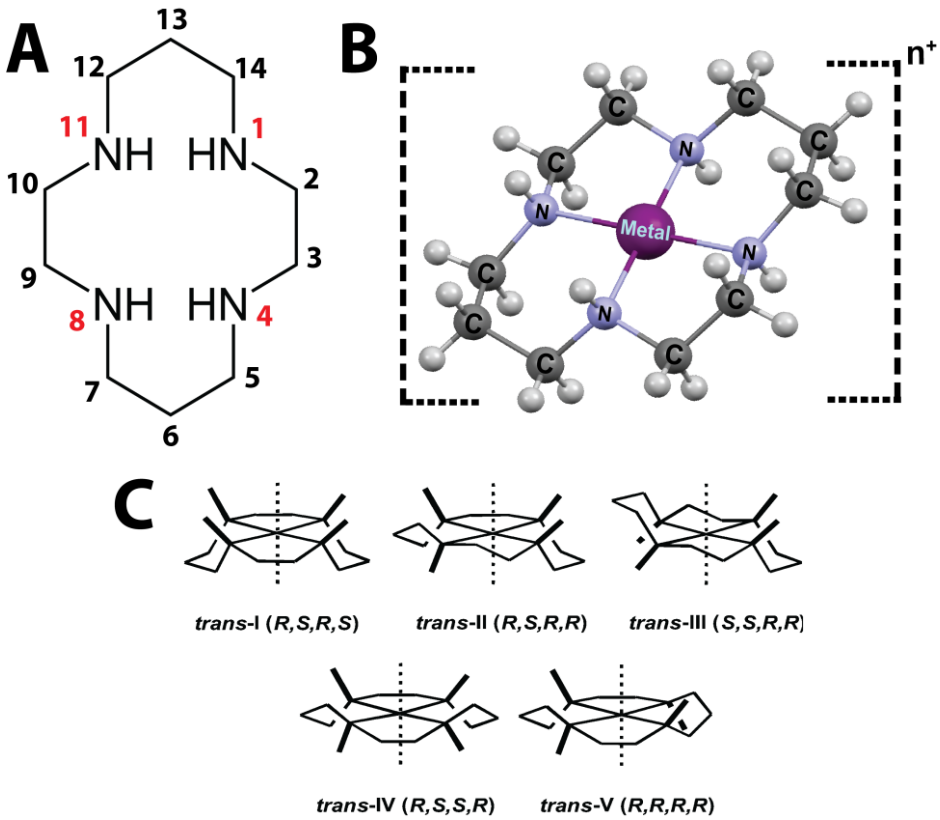

Figure 4.1.1: (A) Structure of cyclam (1, 4, 8, 11-tetraazacyclotetradecane) ligand with IUPAC numbering. (B) The metal-cyclam coordination complex shows (C) various configurations in solution state.

metal-ligand complex is crucial for the understanding of the magnetic property exhibited by the coordinating complexes.

In general the metal-organic and -inorganic complexes involving transition metal ion can exhibit paramagnetic behavior. The coordination complex involving transition metals can be diamagnetic or paramagnetic depending on two factors: (1) oxidation state of the metal ion and (2) the electrostatic field strength of the ligand (strong field or weak field ligand) coordinating the transition metal ion. According to crystal field theory, when a ligand binds to a *d*-block transition metal ion such as Cu^{2+},

Ni^{2+} etc. the degeneracy in the energy of the *d*-orbital is lifted based on the strength of the ligand and the geometry of the complex. The unpaired electron in the *d*-orbital of a transition metal ion is relocated after coordination based on the crystal field stabilization energy Δ (CFSE). The range of Δ from small to large of few known ligands are listed below (spectrochemical series). The ligands in the left are considered to be weak field ligands and the ones in the right are strong.

$I^- < Br^- < S^{2-} < SCN^- < Cl^- < NO_3^- < N_3^- < F^- < OH^- < C_2O_4^{2-} \approx H_2O < NCS^- < CH_3CN <$ py(pyridine) $< NH_3 <$ en (ethylenediamine) < cyclam < CN^-

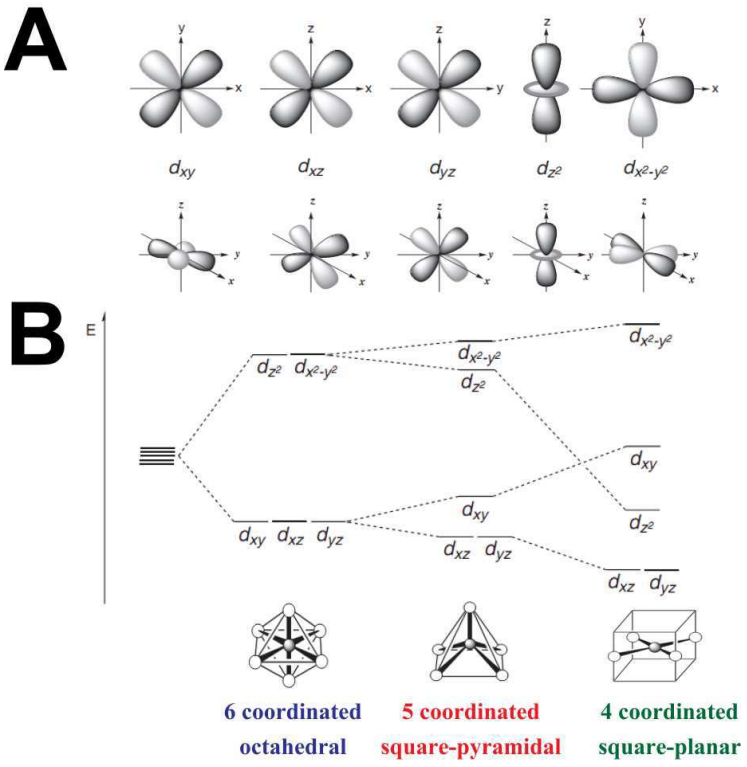

Figure 4.1.2: (A) Overview of five *d*-orbital shapes. (B) Energy level splitting of *d*-orbital in six-, five- and four-coordinated complexes (pictures from reference 161).[163]

Strong field ligands bind to the transition metal cations and shift the *d*-orbital energy levels largely producing low spin complexes. Conversely weak field ligands shift *d*-orbital energy levels with relatively low CFSE (Δ) value resulting in high spin complexes. Figure 4.1.2 (B) demonstrates the energy levels of the five *d*-orbital shown in Figure 5.1.2 (A): $d_{xz}, d_{yz}, d_{xy}, d_{x^2-y^2}$, and d_{z^2} six-, five- and four-coordinated complexes. The geometry of coordination becomes crucial for the

location of the unpaired electron in the complex and thereby becomes important for magnetic property of the complex.

The paramagnetic Cu-cyclam and the Ni-cyclam complexes investigated have one and two chlorine ion as counter ion, respectively.[6] The structure of Cu-cyclam is therefore square-planar with some distortion of the Cu-cyclam coordination plane due to the chlorine ion which binds axially. The structure can be vaguely termed as five coordinated square based pyramidal. We have found some example of X-ray structure of Cu-cyclam binding with diperchlorato ion $(ClO_4)^{2-}$,[64] bromine ion (Br^-),[164] isothiocyanate ion (SCN^-),[67] and copper tetrachloride ion $(CuCl_4)^{2-}$ [165] in literature which are shown in Figure 5.1.3.

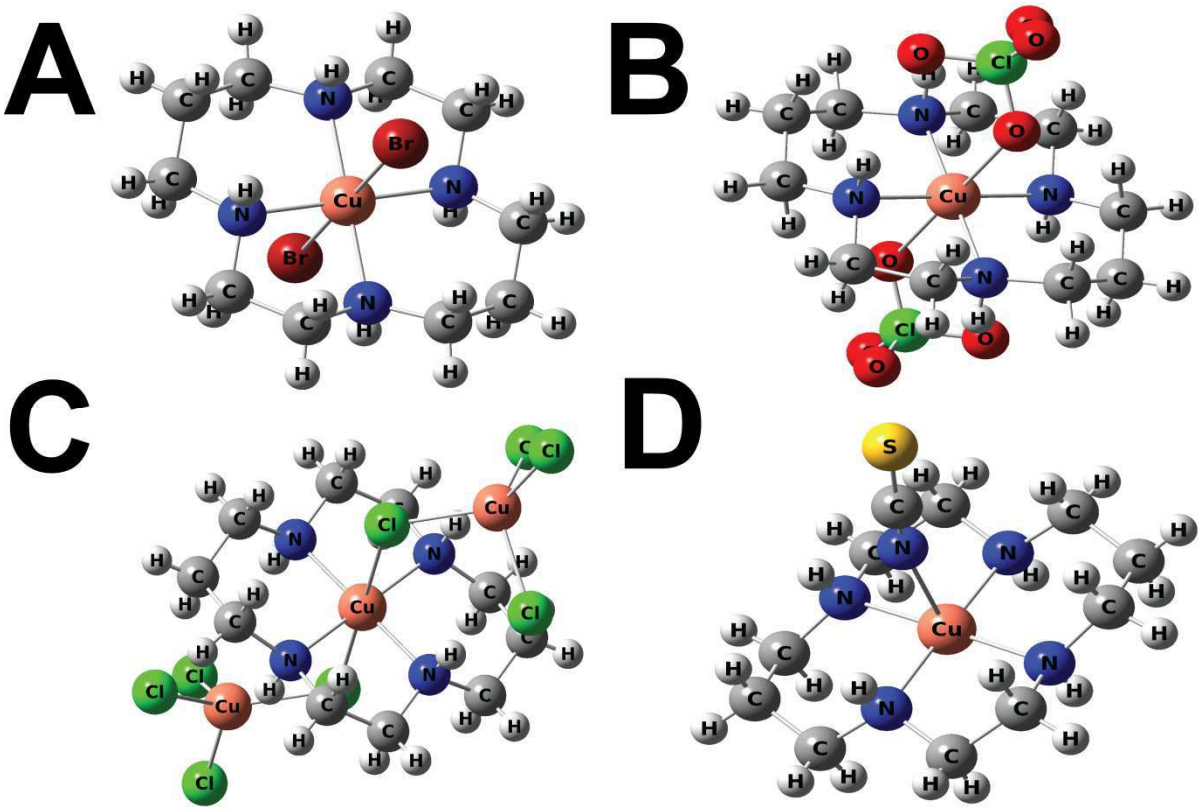

Figure 4.1.3: X-ray structure of Cu-cyclam coordinating with (A) bromide ion $(Br)^-$,[164](B) diperchlorato ion $(ClO_4)^{2-}$,[64] (C) copper tetrachloride ion $(CuCl_4)^{2-}$,[165] and (D) isothiocyanato ion $(SCN)^-$.[67]

For Ni-cyclam complex we found XRD structures such as Ni-cyclam coordinating with diperchlorato ion $(ClO_4)^{2-}$ reported by Prasad *et al.*[166], dichloride reported by Ito *et al.*[76] and Bosnich *et.al.*[74-75] (Figure 4.1.4 A and B).

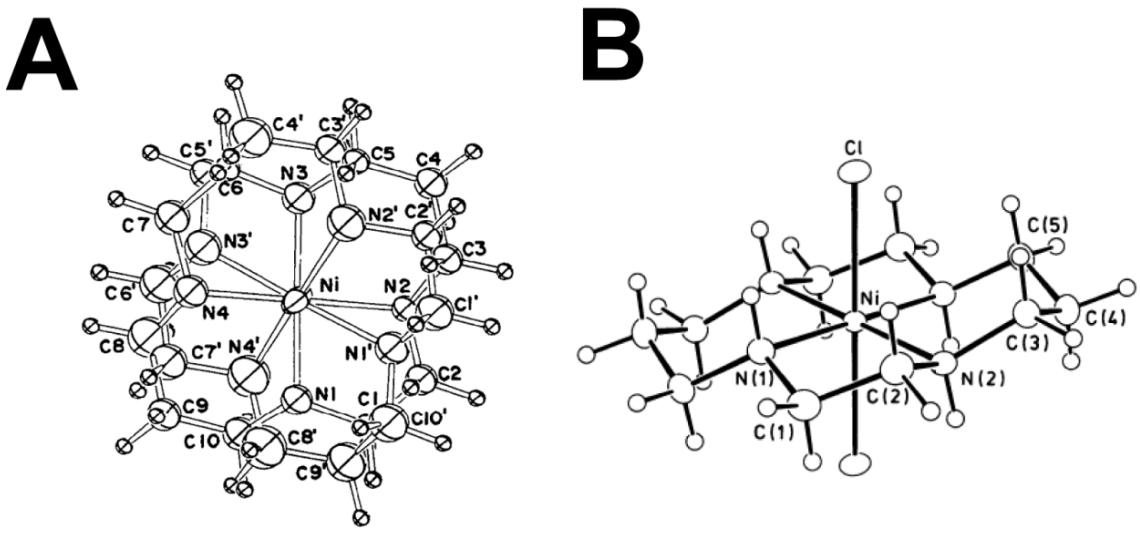

Figure 4.1.4: X-ray structure of Ni-cyclam coordinating with (A) diperchlorato ion (ClO_4), (B) dichloride

4.1.2 ^{1}H and ^{13}C NMR of cyclam and a diamagnetic metal-cyclam complex

In diamagnetic metal-organic systems the ^{1}H and ^{13}C chemical shifts provide information of the chemical groups that are present in the ligand coordinating with the metal. This helps to understand the structure of the metal-organic complexes under study. Applications which require metal-organic complexes to be administered in solid form are usually characterized by solid state NMR. It is routine in solid state NMR to use the cross polarization experiment to study the less sensitive nucleus such as carbon-13 which forms the fundamental entity of the metal-organic complex. The cyclam ligand used in our investigation shows very simple ^{13}C CP spectrum due to only one carbon group -CH_2. The ^{13}C chemical shift of –CH_2 carbon group is distributed over three different chemical environment positions in cyclam i.e. (see Figure 4.1.5 A): (a) –CH_2-CH_2-CH_2- (**29.6** ppm), (b) -CH_2-CH_2-NH- (**49.5** ppm), and (c) –NH-CH_2-CH_2-NH- (**50.7** ppm). Figure 4.1.5 C demonstrates ^{13}C CP MAS spectra of pure cyclam sample acquired at 10 kHz MAS frequency under ^{1}H decoupling. The three carbon-13 signals represent the three sites of carbon –CH_2 in cyclam. The solid and solution state ^{13}C NMR chemical shifts of cyclam ligand are compared in Figure 4.1.5 B and C which shows no difference. Furthermore we have found solution state

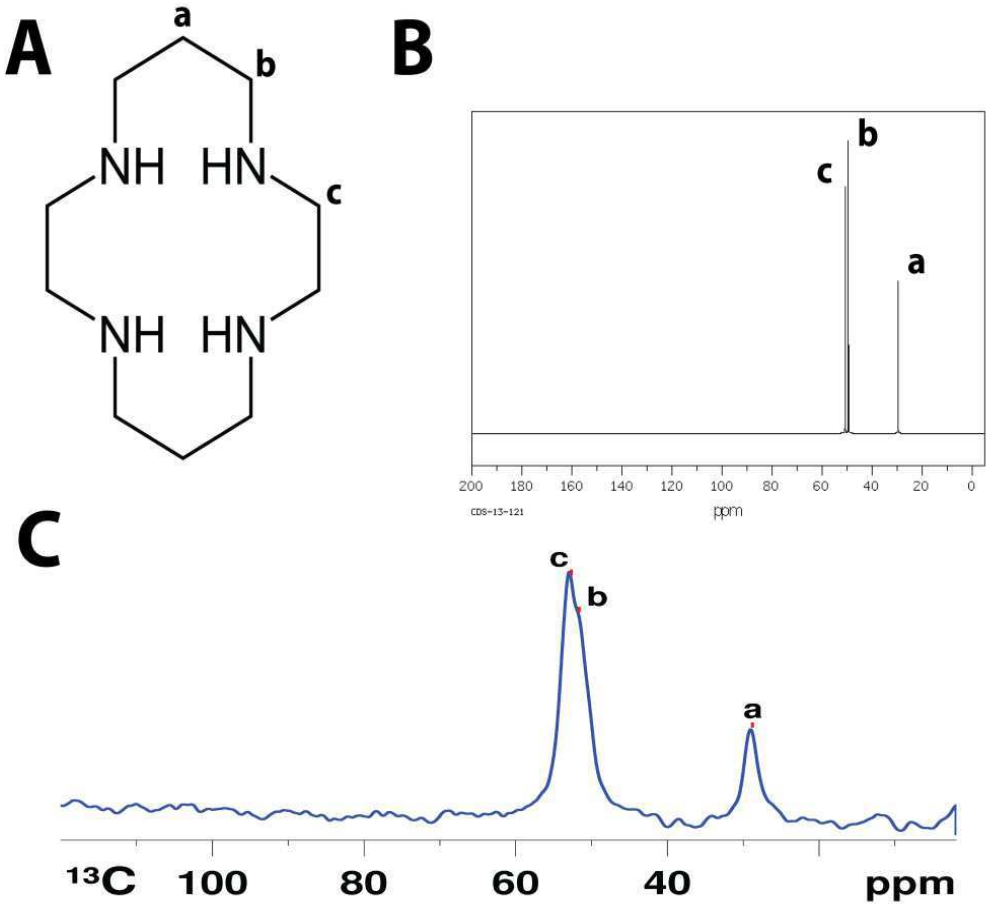

Figure 4.1.5: (A) Position of $-CH_2$ group in three different environments. (B) ^{13}C solution state NMR spectrum of cyclam from Japanese database (SDBS No. 9378CDS-13-121) (C) Solid state NMR ^{13}C CP MAS spectra of pure cyclam.

^{13}C NMR example of diamagnetic zinc-cyclam reported by Alcock *et al.*[156] which was used to compare the ^{13}C NMR chemical shifts from pure cyclam and we have found no change in the shifts.

4.2 One dimensional ^{1}H and ^{13}C solid state NMR of paramagnetic Cu- and Ni-cyclam complex

In 2003 Ishii *et al.*[17] have demonstrated that when samples of paramagnetic metal-organic complexes are spun at a magic angle spinning frequency greater than 23-26 kHz drastic enhancement in sensitivity and resolution of ^{1}H and ^{13}C signals are seen. We have observed the same in ^{1}H and ^{13}C solid state NMR of Cu-and Ni-cyclam complex when spun at MAS frequency of 30 kHz.

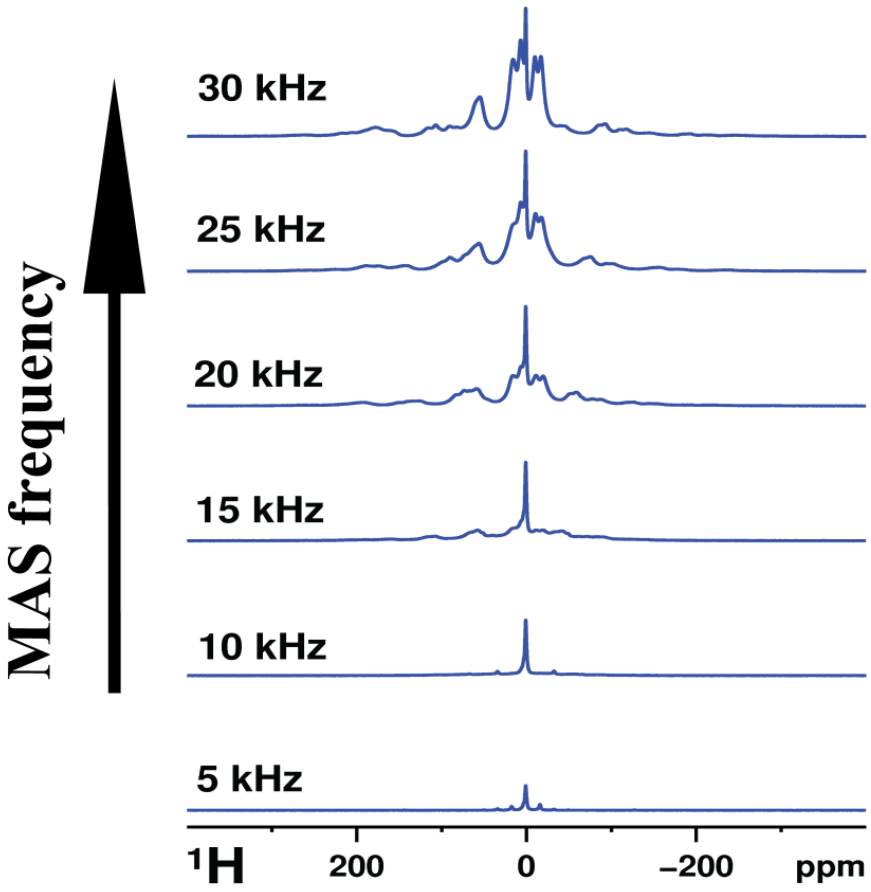

Figure 4.2.1: ^{1}H Hahn-echo spectra of Cu-cyclam complex acquired at various MAS speed

Figure 4.2.1 demonstrates a ^{1}H Hahn-echo spectra of Cu-cyclam complex acquired under various magic angle spinning speeds from 5 kHz – 30 kHz with an interval of 5 kHz. The experiment here demonstrates how VFMAS technique is efficient in resolving solid state NMR signals in paramagnetic metal-organic complex. At 5 kHz MAS there is a single signal near to 0 ppm, with sidebands separated at 5 kHz on both sides of this isotropic peak. As the MAS speed is increased to 10 kHz we observe an increase in the intensity of the isotropic signal near 0 ppm and few other signals close to this signal surfaces. Later a strong appearance of many new signals is seen at 15 and 20 kHz MAS. These signals are quite broad compared to the signals near 0 ppm which is a characteristic of a paramagnetic NMR signal. When spun at 30 kHz there is a drastic enhancement of intensity and the signals are relatively free of sidebands and have relatively high sensitivity and resolution.

Sensitivity and resolution enhancement of the ^{1}H and ^{13}C solid state NMR signals using VFMAS technique forms the basic idea for all the solid state NMR experiments demonstrated in this work. The enhanced ^{1}H signals in Cu-cyclam complex at 30 kHz are spread over +200 ppm to -20 ppm. We observe here that large Fermi contact shifts cause spectral dispersion and are advantageous in separating the signals thereby accounting for resolution of solid state NMR spectra. The Fermi contact shifts are so large that broad ^{1}H signals are also relatively well resolved. Furthermore sample spinning at 30 kHz is sufficient to essentially average all the anisotropic interactions which reduces the line width of the signal and improves for the spectral resolution. Using simple experiment such as Hahn-echo we show here that even ^{1}H NMR is possible in solid state NMR without any advanced techniques.[167]

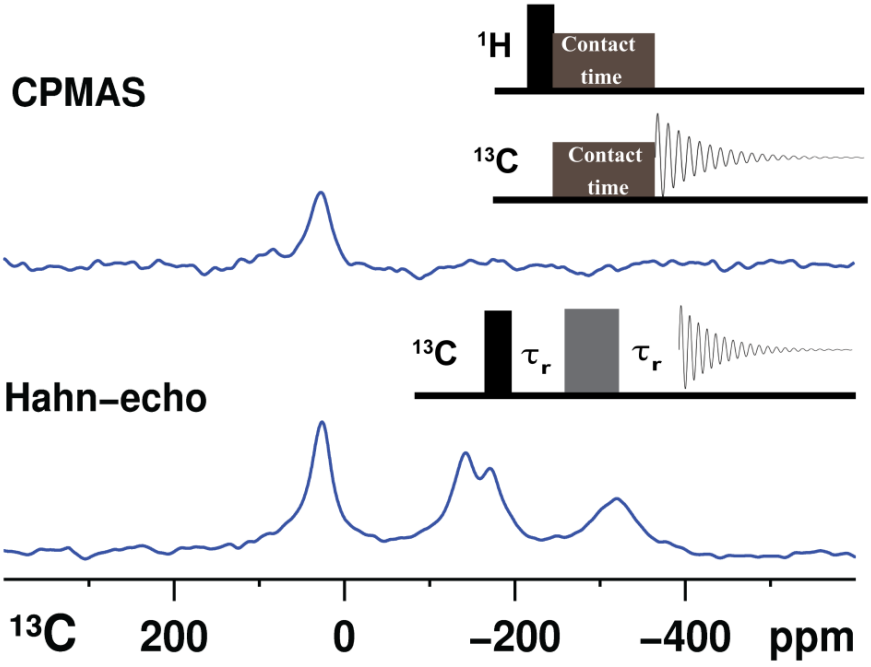

Figure 4.2.2: Comparison of ^{13}C CPMAS and Hahn-echo spectra of Cu-cyclam complex

It is a common practice to use cross polarization technique to acquire ^{13}C spectra of organic complexes in solid state NMR. But for paramagnetic systems CP technique has its limitation due to the hyperfine interaction. Large spectral dispersion in paramagnetic systems leads to relatively weak ^{1}H-^{1}H dipolar network (poor ^{1}H-^{1}H spin diffusion) and poor Hartmann-Hahn matching in CP. Moreover fast relaxation in paramagnetic system requires the contact time in CP to be very short.

This limits the ^{1}H-^{13}C polarization transfer and makes cross polarization technique inefficient for paramagnetic systems. We have observed that ^{13}C Hahn-echo is more efficient than cross polarization for paramagnetic metal-organic complexes. Figure 4.2.2 demonstrates a comparison between simple ^{13}C Hahn-echo and a cross polarization experiment in Cu-cyclam complex acquired under 30 kHz MAS. The ^{13}C CPMAS spectra of Cu-cyclam show a single signal at 29 ppm with relatively low sensitivity compared to Hahn-echo spectra. In ^{13}C Hahn-echo we see three more signals which are shifted upfield with relatively high sensitivity. The upfield shifted signals are broad compared to intense narrow signal at 29 ppm, and are expected to arise from carbon close to paramagnetic center. Hence these signals are not detected in CP experiment.

4.2.1 Comparative studies of one dimensional ^{1}H and ^{13}C solid state NMR in paramagnetic Cu- and Ni-cyclam complex

Using very-fast MAS we were able to acquire well resolved ^{1}H and ^{13}C solid state NMR spectra in paramagnetic Cu- and Ni-cyclam complexes using just a Hahn-echo experiment.

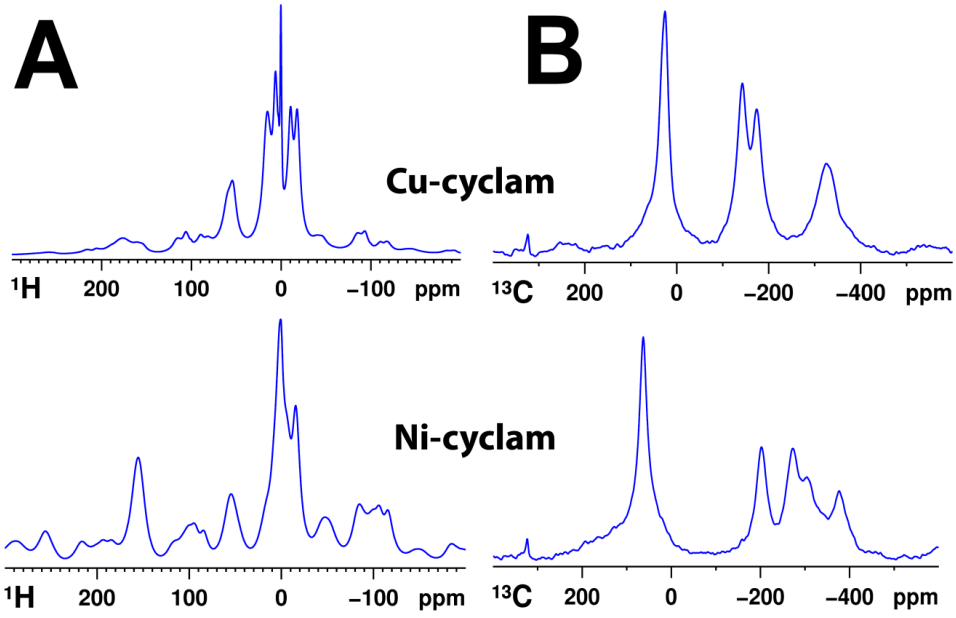

Figure 4.2.3: Comparison of (A) ^{1}H Hahn-echo and (B) ^{13}C Hahn-echo solid state NMR spectra in Cu- and Ni-cyclam complex acquired at 30 kHz MAS

Figure 4.2.3 A & B demonstrates a comparison of ^{1}H and ^{13}C Hahn-echo solid state NMR spectra in paramagnetic Cu- and Ni-cyclam complex acquired under 30 kHz MAS. In ^{1}H Hahn-echo spectra of

both the complexes the signals are spread over +200 ppm to -20 ppm which is a deviation from normal ^{1}H NMR chemical shift range of 0-14 ppm. Both the spectra have common high intense signal at almost 0 ppm which has less line width compared to other signals. Furthermore observation in ^{1}H Hahn-echo spectra of both Cu- and Ni-cyclam complexes reveal some overlapped signals (including strong signal near 0 ppm) near 0-10 ppm range, these are attributed to the signals arising from the uncoordinated cyclam units (without metal centers) which are considered to be diamagnetic in nature.

There are five ^{1}H signals identified in both the complexes which are deviated from the ^{1}H chemical shift range (0-14 ppm) and are broad suggesting that they are from paramagnetic metal-cyclam units. Three out of these five signals are found in the downfield and two upfield of the chemical shift. In ^{1}H Hahn-echo spectra of both the complex the intense signal is found between 0-10 ppm which is attributed to diamagnetic cyclam unit. The similarities in ^{1}H spectra of both the complexes reflect that the ^{1}H chemical environment is not so much different in both complexes and hence the structure too must be almost the same. The ^{1}H Hahn-echo spectra of Ni-cyclam complex is very well dispersed compared to Cu-cyclam; however there is relatively large number of sidebands in it. Even though the chemical shift dispersion is large in Ni-cyclam the overlap of the signals with the sidebands compromise the resolution, making ^{1}H spectra of Cu-cyclam complex better resolved compared to Ni-cyclam.

Figure 4.2.3 B shows a comparison of ^{13}C Hahn-echo spectra of Cu- and Ni-cyclam complex. The ^{13}C Hahn-echo in Cu- and Ni-cyclam shows 4 and 5 distinct signals respectively. Three out of four ^{13}C signals in Cu-cyclam and four out of five signals in Ni-cyclam are upfield shifted. The five distinct ^{13}C signals in Ni-cyclam represent the five different sites of carbon (chemical environment) in metal-cyclam complex as shown in Figure 4.2.4. Large signal dispersion in Ni-cyclam due to the presence of two unpaired electron can be strongly seen through well resolved five distinct signals in ^{13}C Hahn-echo spectra of Ni-cyclam unlike in ^{13}C Hahn-echo of Cu-cyclam which still shows four signals. A single downfield shifted signal at 29 ppm in Cu-cyclam and 65 ppm in Ni-

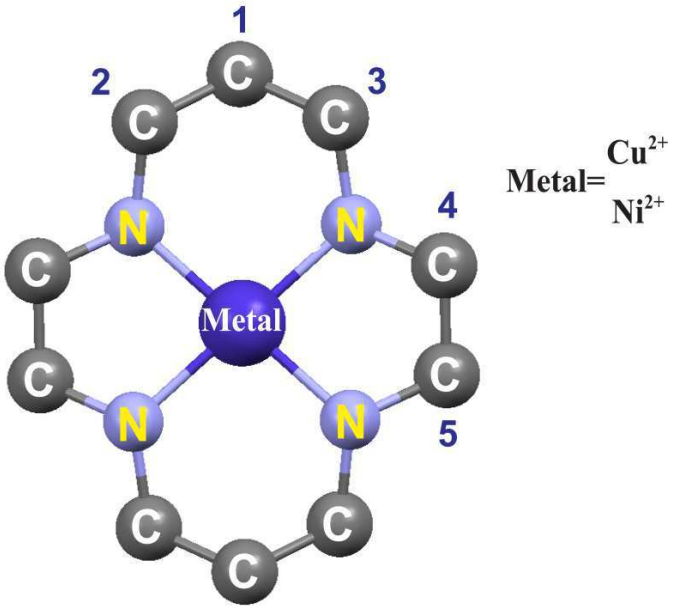

Figure 4.2.4: Five different chemical environments of carbon in metal-cyclam complexes

cyclam appears in the ^{13}C diamagnetic range (0-220 ppm) and has highest intensity in both the complexes. The upfield shifted signals in ^{13}C Hahn-echo spectra of Cu- and Ni-cyclam complex are broadened and shows clear influence of relaxation from paramagnetic metal-center. We hypothesize that the signals shifted to extreme negative end of the chemical shift scale stem from the carbon atoms that are close to the metal-centre and the one at the extreme positive end is far from the metal-center.

Hyperfine shifted ^{1}H and ^{13}C signals in paramagnetic Cu- and Ni-cyclam complexes cannot be assigned easily; but due to large spectral dispersion they certainly contribute for the resolution of ^{1}H and ^{13}C Hahn-echo spectra.

4.3 Carbon-13 signal assignment from spin densities using DFT calculations in Cu- and Ni-cyclam complexes.

NMR spectroscopy is very powerful due to its capability of identifying the chemical groups present through chemical shifts of any system. For organic chemists ^{1}H and ^{13}C NMR chemical shifts provide major and fundamental information of the organic groups that are present in their respective systems under investigation. In NMR of small molecules one compares chemical shifts of respective nucleus of a diamagnetic system under study with the database and to identify the chemical groups

present in it. On contrary paramagnetic systems experience large NMR shifts that deviates away from normal chemical shift range due to hyperfine interaction. The paramagnetic shifts masks the diamagnetic chemical shifts that are rich in chemical group information. Hence this breaks down the whole idea of assignment of NMR signals using the information from NMR database. This makes the paramagnetic system a challenging topic to study using NMR.

4.3.1 Geometry optimization, Vibration frequency analysis and molecular orbital analysis of the Cu-cyclam complex

Geometry optimization of structures of paramagnetic metal-organic complexes of Cu- and Ni-cyclam was performed using hybrid density functional theory (Hartree-Fock DFT) methods. For the

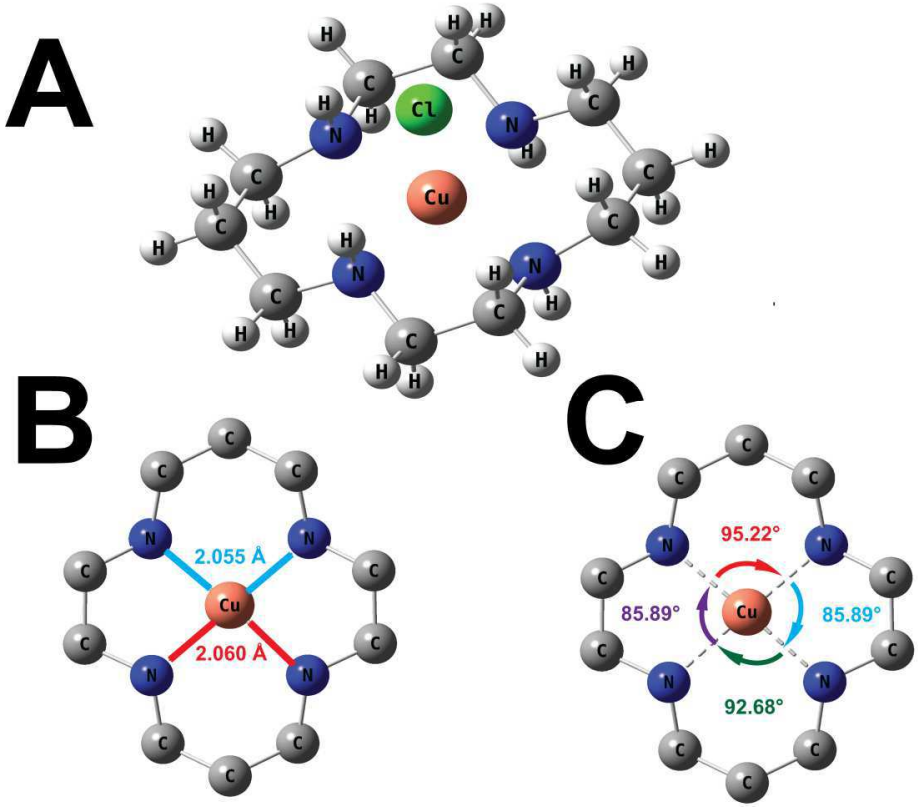

Figure 4.3.1: (A) DFT optimized Cu-cyclam monochloride structure with (B) Cu-N bond distances and (C) N-Cu-N bond angles.

sake of comparison of the optimized geometry of the complexes a series of X-ray structures of Cu-cyclam and Ni-cyclam were used. In the case of Cu-cyclam complex used in our investigation the Cu-cyclam unit is coordinated to one chlorine ion leading to a 5-coordianted square pyramidal type

complex as shown in Figure 4.1.3 D. In the literature we have found several X-ray structures (see Figure 4.1.3) of [Cu-cyclam]$^{2+}$ coordinating with diperchlorato ion $(ClO_4)^{2-}$,[64] bromine ion $(Br)^{2-}$,[164] isothiocyanato $(SCN)^-$ ion,[67] and copper tetrachloride ion $(CuCl_4)^{2-}$.[165] Among the four Cu-cyclam complexes in the literature we have found only Cu-cyclam coordinating with isothiocyanato ion complex to have closed similarities in terms of structure and hence it was used for the comparison.

Bond distance and bond angle	**DFT data of Cu-cyclam coordinating with chloride ion (Cl^-)**	**X-ray data of the Cu-cyclam coordinating with:**			
		Diperchlorato ion $(ClO_4)_2^{2-}$ **Tasker *et al.*[64]**	**Bromide ion $(Br)^-$** **Chen *et al.*[164]**	**Isothiocyanato ion $(SCN)^-$** **Lu *et al.*[67]**	**Cu-Cl_4 ion $(CuCl_4)^{2-}$** **Wang *et al.*[165]**
Cu-N	2.055	2.020	2.016	2.011	2.016
Cu-N`	2.060	2.020	2.023	2.016	2.025
N-Cu-N	95.22	94.00	94.8	94.08	94.3
N`-Cu-N`	92.68	94.00	94.8	93.88	94.3

Table 4.3.1: Comparison of Cu-N bond distance and N-Cu-N bond angle from DFT optimization of Cu-cyclam monochloride structure with the X-ray data of Cu-cyclam coordinated with various ions.

The X-ray analysis of Ni-cyclam dichloride was first performed in 1965 by Bosnich *et al.*[74] There are even some examples of solution state ^1H NMR analysis done on the paramagnetic Ni-cyclam dichloride complex by Dei *et al.*,[77] Billo and Connolly *et al.*[66,78] The structures of Cu-cyclam with one chlorine ion and Ni-cyclam with dichloride ion were constructed using GAUSSVIEW 5 graphic software. Geometry optimization of these structures was performed with density functional theory (DFT) using generalized gradient approximation (GGA) applying hybrid potential implemented in the program Gaussian 09. The X-ray structure of Cu-cyclam with isothiocyanato $(SCN)^-$ ion was adapted manually using GAUSSVIEW 5 graphic program as a primary structure for the calculation. The SCN^- ion was replaced with chloride ion $(Cl)^-$ and the geometry optimization job was initialized

using B3LYP[150-151,168] potential with 6-311G[169] basis set. Since the total charge of the Cu-cyclam with one chloride ion is +1 the charge parameter in the Gaussian job setup was changed from 0 to +1 giving the spin state of complex to be doublet. The optimization of the structure was performed at unrestricted mode since the system is open-shell type.[144-145] The optimized structure of the Cu-cyclam complex was subject to frequency calculation (FREQ) job and we observed only positive frequencies thereby confirming that optimization has reached stationary state. Figure 4.3.1 (A) shows the DFT optimized structure of Cu-cyclam monochloride complex with (B) Cu-N bond distances and (C) N-Cu-N angles. These distances and angles were compared with the X-ray data of the four structures (see Figure 4.1.3) of Cu-cyclam complexes found in literature. Table 4.3.1 shows a comparison of Cu-N bond distance and N-Cu-N bond angle of DFT optimized Cu-cyclam monochloride structure with the X-ray data of the four Cu-cyclam complex structures found in literature (see Figure 4.1.3). The three structures among the four found in the literature have six coordinated octahedral geometry except for Cu-cyclam coordinating with isothiocyanato ligand. Cu-cyclam SCN^- complex shows a five coordinated distorted square pyramidal geometry. The N-Cu-N bond angle of this complex measured from XRD is in relatively close agreement with the N-Cu-N bond angle of our model system (Cu-cyclam monochloride complex). The optimized structure of Cu-cyclam monochloride complex was subjected to FREQ job (vibration frequency calculation) using the same DFT method.

The frequency calculation resulted in an output with positive frequency values. Using GAUSSVIEW 5 graphic editor the theoretical IR spectra of the Cu-cyclam monochloride were plotted. For the sake of comparison we found experimental IR spectra of Cu-cyclam complex in literature by Diaz *et al.*[160] Figure 5.3.2 shows a comparison of (A) theoretical IR spectra of Cu-cyclam monochloride from DFT calculation and (B) experimental IR spectra of Cu-cyclam complex from Diaz *et al.* In spite of testing for positive frequencies from the output of vibration frequency calculation we did the analysis of the IR spectra by comparing it with the experimental IR data. In Figure 4.3.3 A, shown is the DFT generated theoretical IR spectra of Cu-cyclam monochloride complex with the full range of spectrum from 400 cm^{-1} to 4000 cm^{-1}.

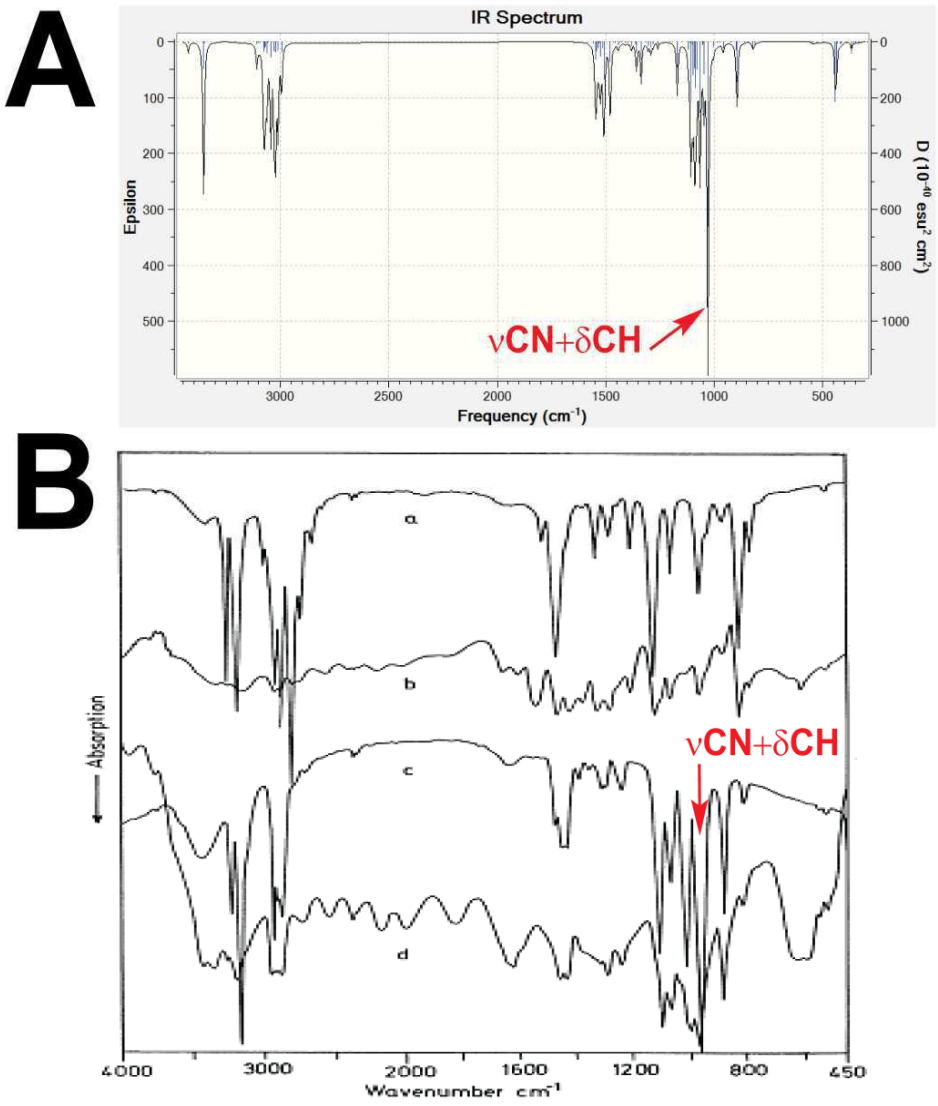

Figure 4.3.2: comparison of (A) theoretical IR spectra of Cu-cyclam monochloride from DFT calculation and (B) experimental IR spectra of Cu-cyclam complex from Diaz *et al.*[160] with red arrows indicating the prominent strong signal of the C-N vibration and C-H rotation in Cu-cyclam complex

Figure 4.3.3 B shows experimental IR spectra of (a) pure cyclam and (c) Cu-cyclam complex reported by Diaz *et al.*[160] In this work (the study of effects of ligands on smooth copper surface) the goal was to assign the vibration frequency signals of the Cu-cyclam complex by comparing with IR spectra of pure cyclam (see Figure 4.3.2 B (a) pure cyclam and (c) Cu-cyclam). Therefore, in Figure 4.3.2 B only (a) and (c) are relevant for your discussion. In the work of Diaz *et al.*[160] it is emphasized that the signal at 1110 cm^{-1} (see Figure 4.3.3 B red arrow) which is a combined stretching and bending of CN and CH pair (νCN+δCH) is significant for confirmation of the fact that Cu-cyclam complexation is formed.

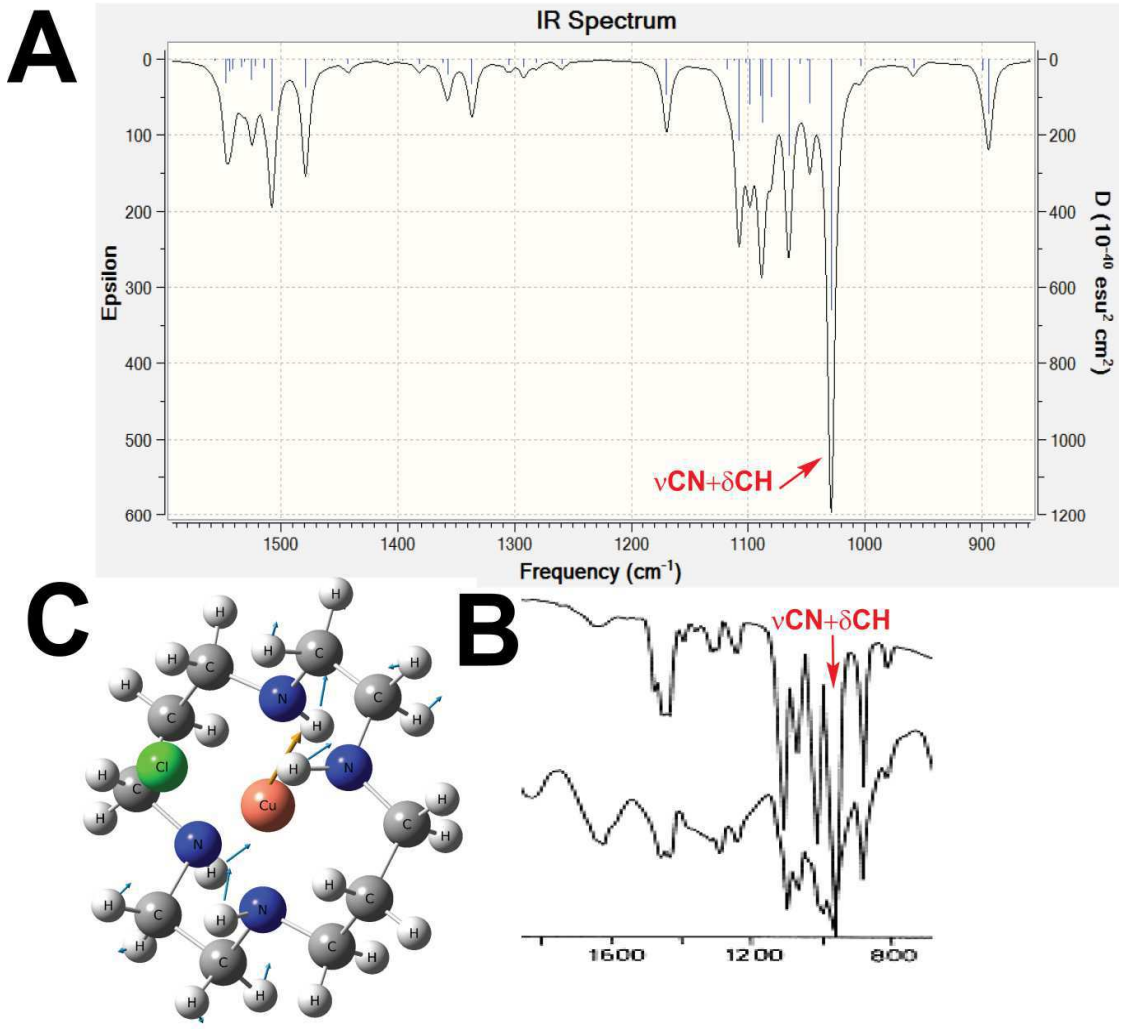

Figure 4.3.3: Comparison of (A) theoretical IR spectra of Cu-cyclam monochloride from DFT calculation and (B) experimental IR spectra of Cu-cyclam complex from Diaz *et al.*[160] near the region of prominent 1000 cm^{-1} to 1500 cm^{-1} (C) DFT generated vibration mode of νCN+δCH at 1028 cm^{-1} with dipole vector

As we can see in Figure 4.3.3 B when comparing the experimental IR spectra of (a) pure cyclam and (c) Cu-cyclam complex this signal at 1110 cm^{-1} which is the strongest one among all others shows major difference between pure cyclam and the Cu-cyclam complex. We compared this experimental IR analysis with our theoretical IR spectra and found that we too observe the strong signal but it was shifted to 1028 cm^{-1} (see Figure 4.3.3 A red arrow). This shift may be due to the fact that the Cu-cyclam complex used in our investigation has a chloride ion. However we analyzed the strong signal at 1028 cm^{-1} by visualizing the vibration modes graphically using GAUSSVIEW 5 program (see Figure 4.3.3 A red arrow) which confirmed the Cu-cyclam complexation. Shown in Figure 4.3.3 A is the expanded region between 1000 cm^{-1} and 1500 cm^{-1} of DFT generated IR

spectra of Cu-cyclam monochloride complex with red arrow indicating the strong signal at 1028 cm^{-1} which is the combined stretching and bending mode of CN and CH pair (νCN+δCH). It is compared to Figure 4.3.3 B, the expanded region of experimental IR spectra of Cu-cyclam complex by Diaz *et al.* with red arrow indicating the strong signal at 1110 cm^{-1}. Figure 4.3.3 C is a snap shot of the animation of the strong vibration mode at 1028 cm^{-1} in Cu-cyclam monochloride complex performed using DFT calculation. The vibration analysis reassures that the DFT optimization of Cu-cyclam complex had successfully reached the stationary point and hence the structure can be used for any further calculation.

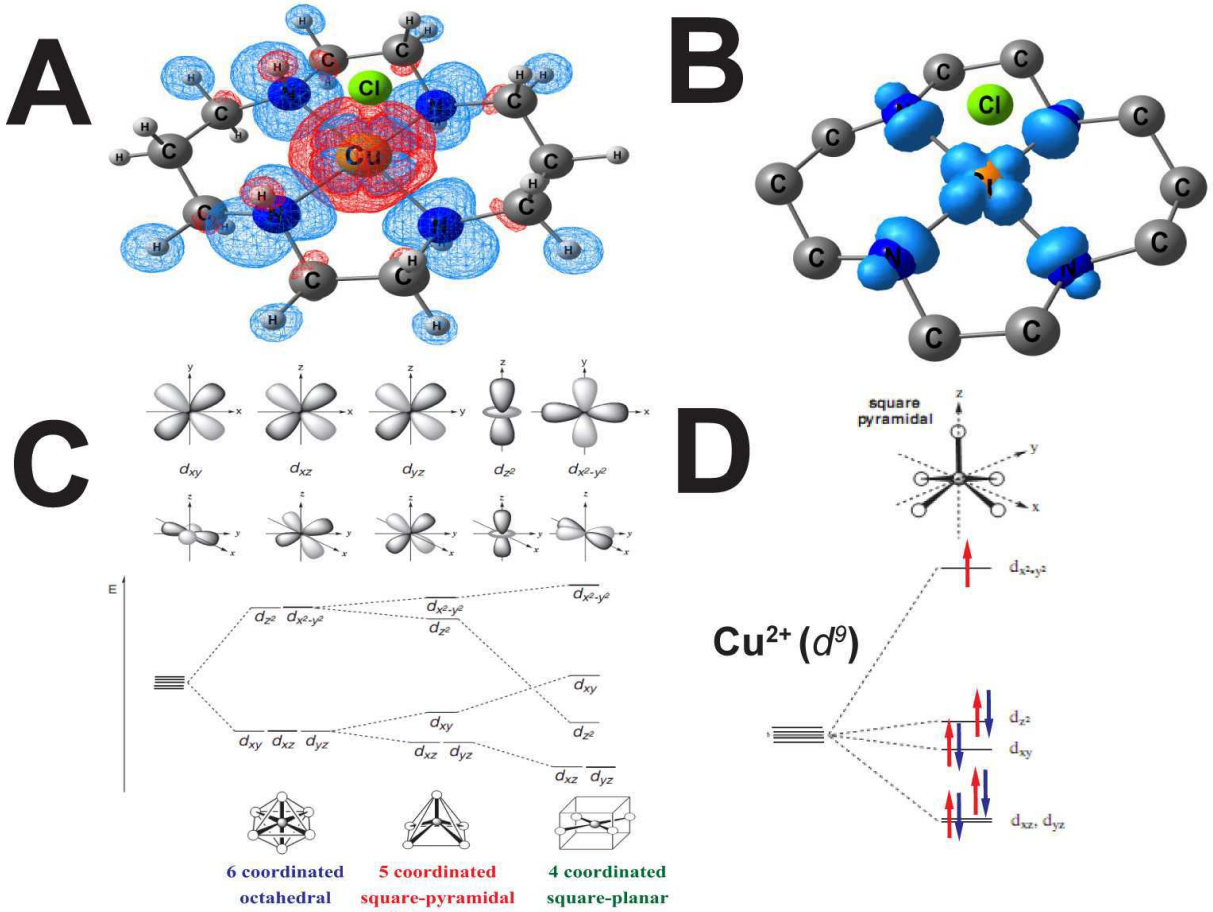

Figure 4.3.4: (A) Contour plot of spin density in Cu-cyclam monochloride complex (red=negative and blue=positive spin density with contour values ranging between ± 0.00045 au). (B) Alpha minus Beta orbitals contour plot resulting in $d_{x^2-y^2}$ type orbital in Cu-cyclam mono chloride complex (C) *d*-orbital energy levels in 6, 5 and 4 coordinated complexes. (D) Occupation of electrons in d-orbitals of Cu^{2+} ion in a 5-coordinated square pyramidal field.

According to the ligand field theory in five coordinated square pyramidal complexes (such as the one used in our investigation i.e. Cu-cyclam monochloride complex and one found in literature i.e. Cu-cyclam isothiocyanato complex) the *d*-sub orbitals of Cu^{2+} i.e. $d_{x^2-y^2}$ and d_{z^2} are higher in energy compared to other three *d*-sub-orbitals. This is crucial for the location of the unpaired electron and also to understand the spin density distribution on the entire molecule. We performed a molecular orbital analysis in GAUSSIAN 09 program by subjecting the DFT optimized Cu-cyclam monochloride complex to population analysis. The population analysis job POP maps all the molecular orbital of a molecule and the orbitals can be visualized in GAUSSVIEW 5 program. The population analysis was performed with same method of B3LYP at same basis set 6-311G in GAUSSIAN 09 program (command line *ub3lyp/6-311g gfinput pop=full*). Later the output was visualized using CHEMCRAFT graphic program.

Figure 4.3.4 A shows a contour plot of the unpaired electron spin density in Cu-cyclam mono chloride complex. Here the red color corresponds to negative and blue to positive spin density. For the sake of visibility of spin density especially on carbon atoms the contour levels were set to low values of +0.00045 au and -0.00045 au. Figure 4.3.4 B shows a contour plot of alpha minus the beta states plot which directly gives the shape of the orbital where the unpaired electron resides. It confirms that the unpaired electron partially resides in $d_{x^2-y^2}$ orbital type of the Cu atom. From crystal and ligand field theory it is clear that transition metal cations with d^9 valence shell electronic configuration under the influence of electrostatic field resulting from five coordinated square pyramidal geometry have *d*-orbital energy level separation as shown in Figure 4.3.4 C. The filling up of an electron into *d*-orbital in the case of Cu^{2+} ion under the influence of electrostatic field from such geometry is shown in Figure 4.3.4 D with $d_{x^2-y^2}$ having the unpaired electron. Our result from the DFT molecular orbital calculation and the predicted result from the ligand field theory are in good agreement confirming the location of the unpaired electron.

4.3.2 Assignment of ^{13}C solid state NMR signals in the paramagnetic Cu-cyclam complex from spin densities calculated using DFT calculation

The ^{13}C Hahn-echo spectra of Cu-cyclam monochloride complex shows four distinct signals with three of them being upfield shifted. Figure 4.3.5 shows the ^{13}C Hahn-echo spectra of Cu-cyclam monochloride complex with labeling of the signals.

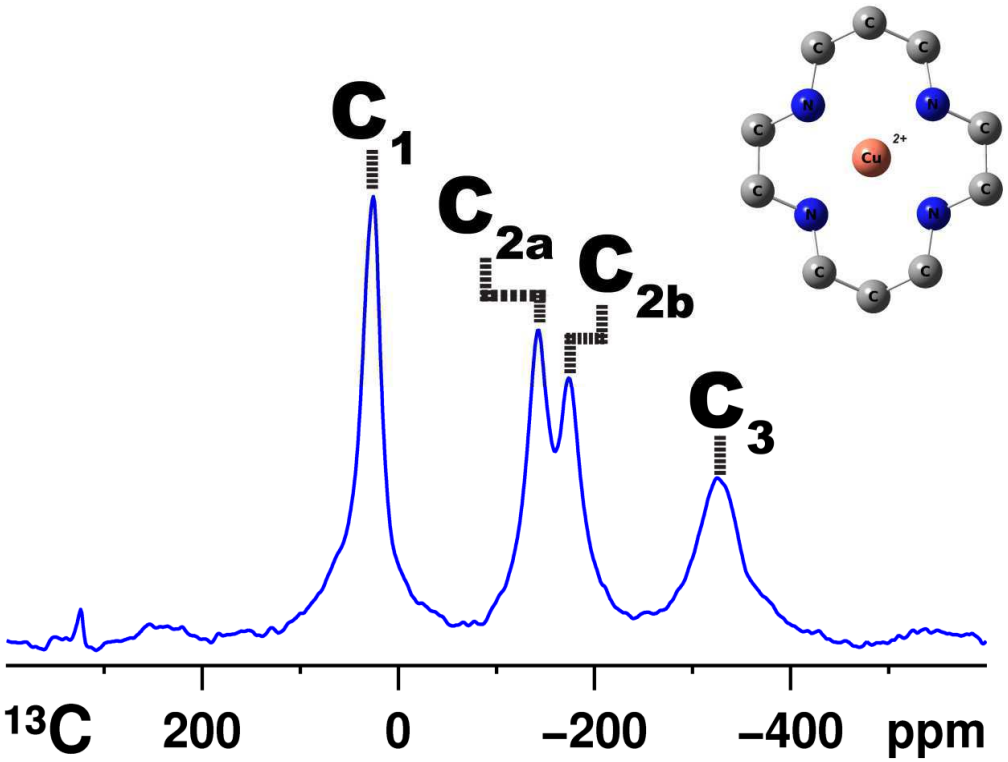

Figure 4.3.5: ^{13}C Hahn-echo spectra of Cu-cyclam monochloride complex.

Here the signal C_1 (26 ppm) is in the diamagnetic range (0-220 ppm) of carbon chemical shift, the upfield shifted convoluted signals at -143 ppm and -174 ppm is labeled as C_{2a} and C_{2b}. The fourth signal which is shift to extreme negative end of chemical shift scale at -326 ppm is labeled as C_3. The total shift of ^{13}C signal in the Figure 4.3.5 is the sum of diamagnetic part (chemical shift) and the paramagnetic part of the interactions. Fermi contact shifts are characteristic of unpaired electron spin density in a paramagnetic molecule. Using DFT calculated spin density and hence Fermi-contact shifts, we compare here with the experimental shifts and assign the NMR signal in paramagnetic complexes.

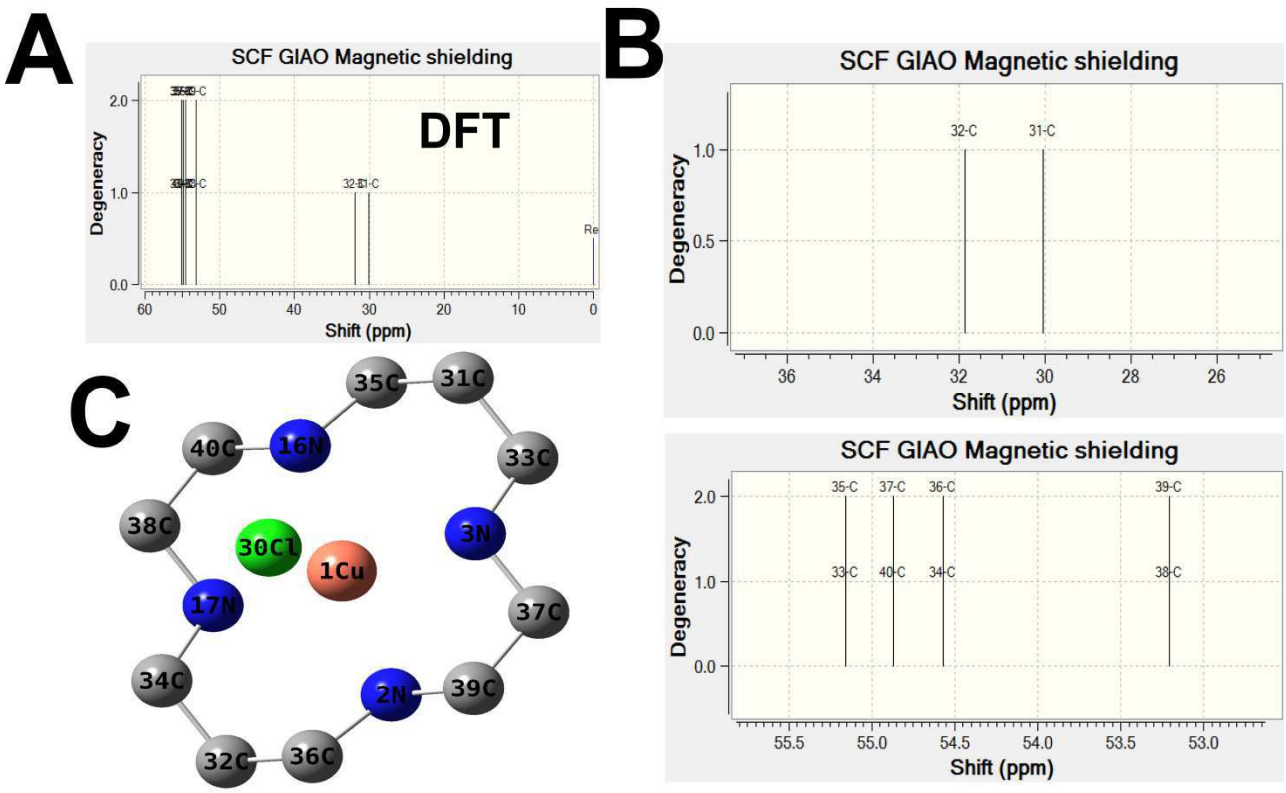

Figure 4.3.6: (A) DFT generated ^{13}C (diamagnetic part) NMR spectra of Cu-cyclam monochloride complex with (B) enlarged region between 20-40 ppm and 50-60 ppm. (C) Assignment of carbon site in Cu-cyclam.

The total theoretical shift is again the sum of diamagnetic part (chemical shift) and the paramagnetic part (Fermi contact shift) of the paramagnetic complex. We used NMR=GIAO job command in GAUSSIAN 09 to calculate the diamagnetic NMR chemical shift in Cu-cyclam monochloride complex. The geometry optimized Cu-cyclam monochloride complex structure was subject to NMR property calculation using gaussian induced atomic orbital (GIAO) option with B3LYP method at 6-311+G(2d,p) basis set (since the TMS used for chemical referencing is pre calculated at 6-311+G (2d,p) basis set in GAUSSVIEW 5). Figure 4.3.6 (A) shows the DFT generated ^{13}C NMR spectra of diamagnetic part of Cu-cyclam complex with assignment of the carbon-13 signals. The DFT calculated ^{13}C diamagnetic chemical shifts of Cu-cyclam monochloride complex is in good agreement with the experimental ^{13}C NMR chemical shift of diamagnetic zinc-cyclam dichloride complex observed by Alcock *et al.*[156]

Experimental ^{13}C shifts $^{ssNMR}\delta_{Total}$ [ppm]	**^{13}C chemical shift from DFT $^{DFT}\delta_O$ [ppm]**	**spin density (from DFT) ρ [au]**	**^{13}C Fermi-contact shift from DFT $^{DFT}\delta_{FC}$ [ppm]**	**Theoretical ^{13}C shift $^{DFT}\delta_{Total}$ [ppm]**	**Assignment of carbon sites (*see Figure 4.3.5*) in Cu-cyclam monochloride complex**
26 [C_1]	31	*-0.00006*	-6	25	C31
		-0.00003	-3	28	C32
-142 [C_{2a}]	55	*-0.00184*	-196	-141	C33, C35
-173 [C_{2b}]		*-0.00250*	-266	-212	C34, C36
-324 [C_3]	54	*-0.00332*	-354	-301	C38, C39
		-0.00380	-405	-350	C37, C40

Table 4.3.2: Comparison of experimental ^{13}C shift $^{ssNMR}\delta_{Total}$ from solid state NMR and theoretical ^{13}C shift $^{DFT}\delta_{Total}$ from DFT calculation, there by assignment of ^{13}C signals in paramagnetic Cu-cyclam monochloride complex

The unpaired electron spin density list generated at the end of geometry optimization of Cu-cyclam monochloride complex was inserted into Equation 2.7.22 and the ^{13}C theoretical Fermi-contact shift δ_{FC} was calculated. The calculated ^{13}C Fermi contact shifts were added to calculated diamagnetic shifts to obtain the total ^{13}C theoretical shift. Table 4.3.2 shows a comparison of carbon-13 total experimental shift $^{ssNMR}\delta_{Total}$ and total theoretical shift $^{DFT}\delta_{Total}$ in paramagnetic Cu-cyclam monochloride complex with assignment of carbon-13 signals. The theoretical shifts are in good agreement with the experimental shifts and the information was used to assign the signals to carbon sites. The β-carbons in the six-membered rings are furthest away from the Cu center and have a very small spin density, so that the chemical shift is dominating (C_1). The signal between -150 and -200 ppm is assigned to the four α-carbons, and the calculations even reproduce its splitting by an asymmetry between the two six-membered rings forming chair conformation[77] and allow therefore a tentative assignment of the two sub-peaks (C_{2a}, C_{2b} in Figure 4.3.5). One must however

acknowledge that cyclam is a flexible molecule existing in different conformations possessing more than one local energy minimum. With other computational approaches a conformation is obtained where it is the diagonal opposite α-carbons that have a similar distance to Cu and hyperfine shift.[8] In all cases an asymmetry is obtained by a binding of cyclam to only one Cl. Also the four carbons in the two five membered rings group to two sub-sites in the calculation, in the spectrum however they merge to a single broad peak C_3.

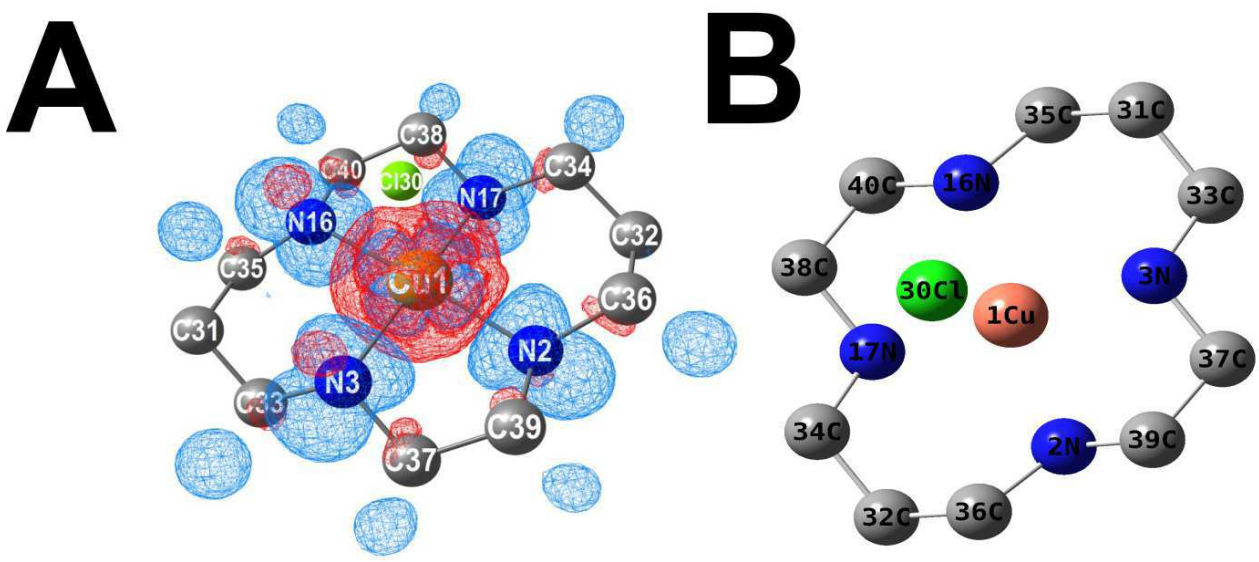

Figure 4.3.7: (A) Unpaired electron spin density distribution in Cu-cyclam complex (+0.00045 au (blue) -0.00045 au (red)). (B) Carbon site assignment for comparison of the data from Table 4.3.2.

4.3.3 Geometry optimization, Vibration frequency analysis and molecular orbital analysis of Ni-cyclam complex

We found several references in the literature pertaining to the XRD structures in case of Ni-cyclam dichloride complex. The paramagnetic Ni-cyclam complex studied is a very well known system in coordination chemistry.[62,170-172] There are numerous examples of research works on this system right from its interesting thermodynamic stability in terms of coordination,[155,161,173] application in various fields of material chemistry,[6-8] and usage in drugs and pharmaceutical research[10] etc. The X-ray analysis of Ni-cyclam dichloride was done for the first time by Bosnich *et al.* in 1965.[74] Later the XRD structure of this complex was refined by Ito *et al.* with not many differences in the XRD data

as compared to Bosnich *et al.* The X-ray data from these articles were used for comparison of the geometry of Ni-cyclam dichloride complex after DFT optimization.

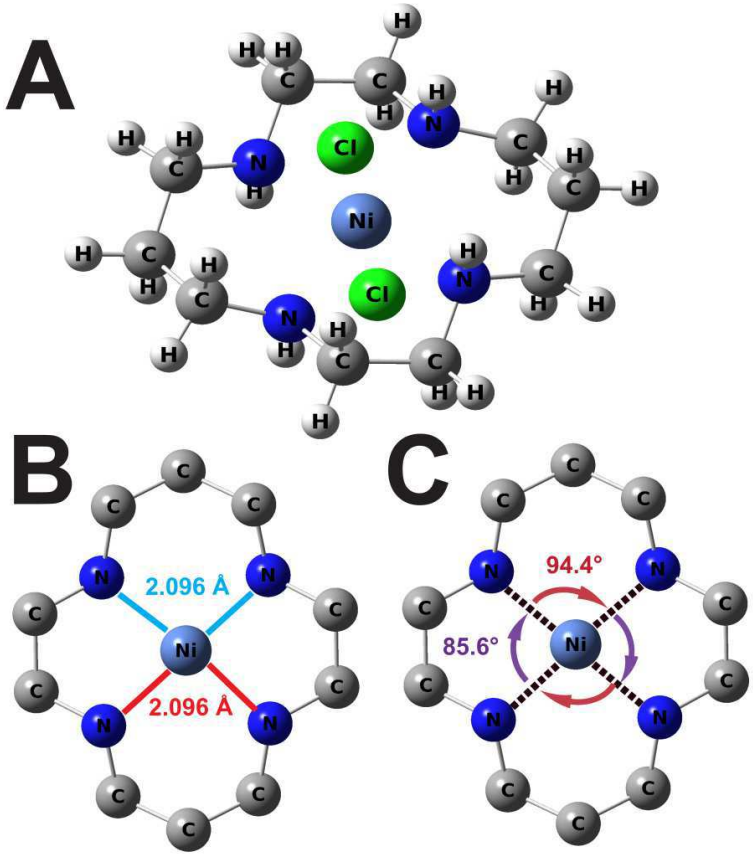

Figure 4.3.8: (A) DFT optimized Ni-cyclam dichloride structure with (B) Ni-N bond distances and (C) N-Ni-N bond angles.

The structure of Ni-cyclam dichloride complex was constructed in GAUSSVIEW 5 program and the structure was subject to geometry optimization by the same method as used in the case of Cu-cyclam complex i.e. at generalized gradient approximation (GGA) using hybrid potential B3LYP (unrestricted) with 6-311G basis set. Since the complex is paramagnetic with a triplet state, the degeneracy was changed from 1 to 3.

Shown in Figure 4.3.8 (A) is the DFT optimized structure of Ni-cyclam dichloride complex with (B) the Ni-N bond distances and N-Ni-N bond angles. The four nitrogen donor atoms forming complex bond with the nickel ion have equal bond distances of 2.096 Å. Furthermore the N-Ni-N bond angle in both six membered rings forming chair conformation is 94.4° and in both five membered rings is 85.6° which suggests that the Ni-cyclam complex is symmetric in geometry. Table 4.3.3 shows a

comparison of Ni-N bond distance and N-Ni-N bond angles of the DFT optimized Ni-cyclam complex with the X-ray data from Bosnich *et al.* and Ito *et al.* The N-Ni-N bond angle of the DFT optimized structure is in close agreement with the XRD data from both Bosnich and Ito *et al.*

Bond distance and bond angle	**DFT data of Ni-cyclamCl_2**	**X-ray data of the Ni-cyclam Cl_2**	
		Bosnich *et al.*	**Ito *et al.***
Ni-N	2.096	2.066	2.066
Ni-N`	2.096	2.050	2.067
N-Ni-N (6-membered ring)	94.40	94.30	94.70
N-Ni-N` (5-membered ring)	85.60	85.70	85.30

Table 4.3.3: Comparison of Ni-N bond distance and N-Ni-N bond angle of DFT optimized Ni-cyclam dichloride structure with the X-ray data of Ni-cyclam dichloride from Bosnich *et al.* and Ito *et al.*

However, the Ni-N bond distance calculated by DFT shows a small deviation of 0.025 Å with respect to XRD data shown in Figure 4.3.9 A and B reported by Bosnich *et al.* and Ito *et al.* respectively.

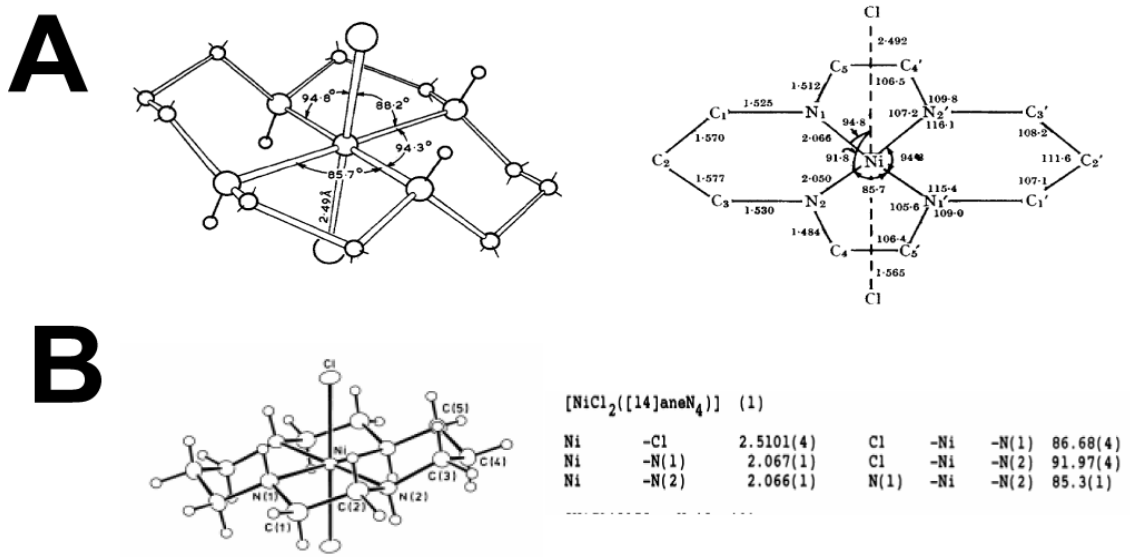

Figure 4.3.9: XRD structures of Ni-cyclam dichloride with bond angles and bond distances from (A) Bosnich *et al.*[174] and (B) Ito *et al.*[76]

The DFT optimized Ni-cyclam structure was subject to frequency calculation in GAUSSIAN 09 using same method (B3LYP) and same basis set (6-311G). We found that all the vibration modes generated by GAUSSIAN 09 calculation were positive suggesting that the energy of the structure had reached stationary state. Hence the structure is appropriate for further property calculation.

Figure 4.3.10 (A) shows the DFT generated IR spectra of Ni-cyclam dichloride compared with (B) experimental IR spectra of Ni-cyclam complex from Makowska-Janusik *et al.*[8] We also compared the data from the experimental IR analysis of Ni-cyclam dichloride complex by Bosnich *et al.* and found that the DFT IR data were in good agreement with the experimental data.

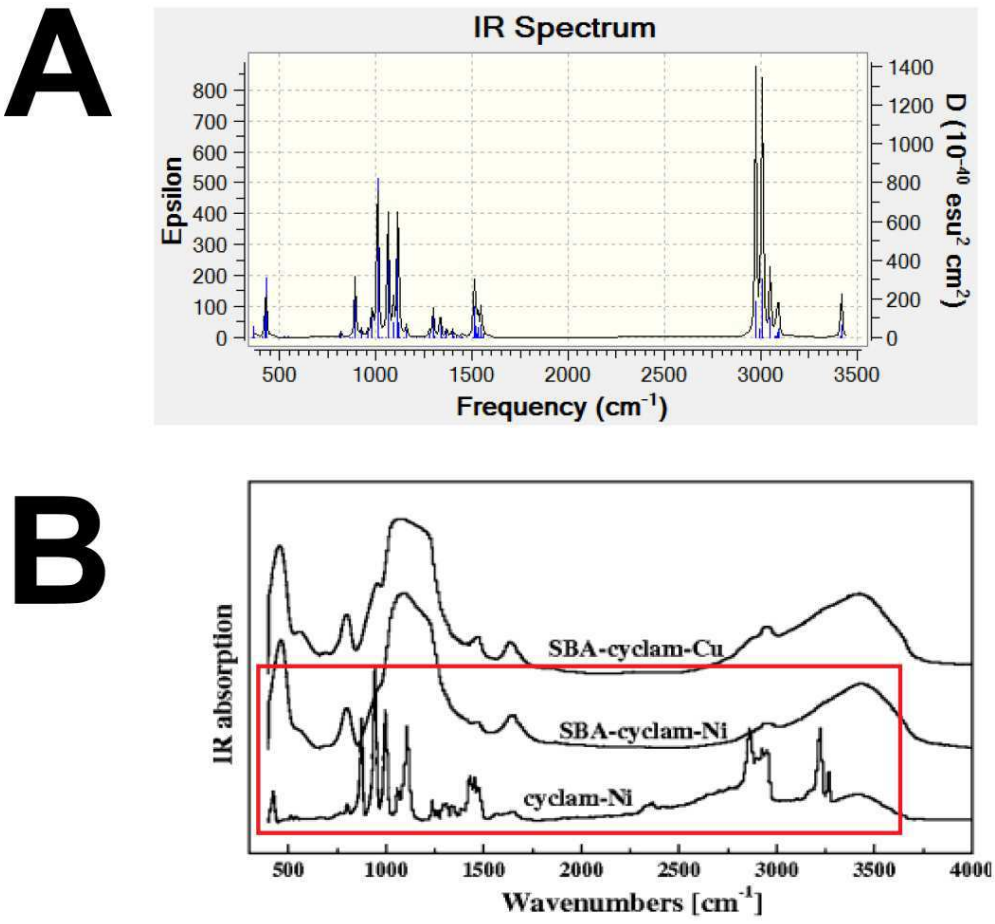

Figure 4.3.10: Comparison of (A) DFT generated IR spectra of Ni-cyclam dichloride with the (B) experimental IR spectra of Ni-cyclam complex used in the investigation of mesoporous silica materials functionalized with metal-cyclam complexes by Makowska-Janusik *et al.*[8]

Furthermore we performed molecular orbital analysis as similarly done in the case of Cu-cyclam monochloride complex. The optimized structure of Ni-cyclam dichloride complex was subject to

full population analysis (*ub3lyp/6-311g gfinput pop=full*) and the generated output was visualized with the program CHEMCRAFT.

Shown in Figure 4.3.11 A is a contour plot of unpaired electron spin density distribution in Ni-cyclam dichloride complex. The contour values are +0.0004 au (blue) to -0.0004 au (red). Figure 4.3.11 B is a contour plot showing alpha minus the beta molecular orbitals in Ni-cyclam complex. The plot directly provides information of the location of unpaired electron spins in the *d*-type orbitals. The shape of the orbital is equivalent to a convoluted $d_{x^2-y^2}$ and d_{z^2}orbital. From the crystal field and ligand field theory one can see that six coordinated octahedral type of systems have their d-orbital energy level split as shown in Figure 4.3.11 C. Furthermore under octahedral field

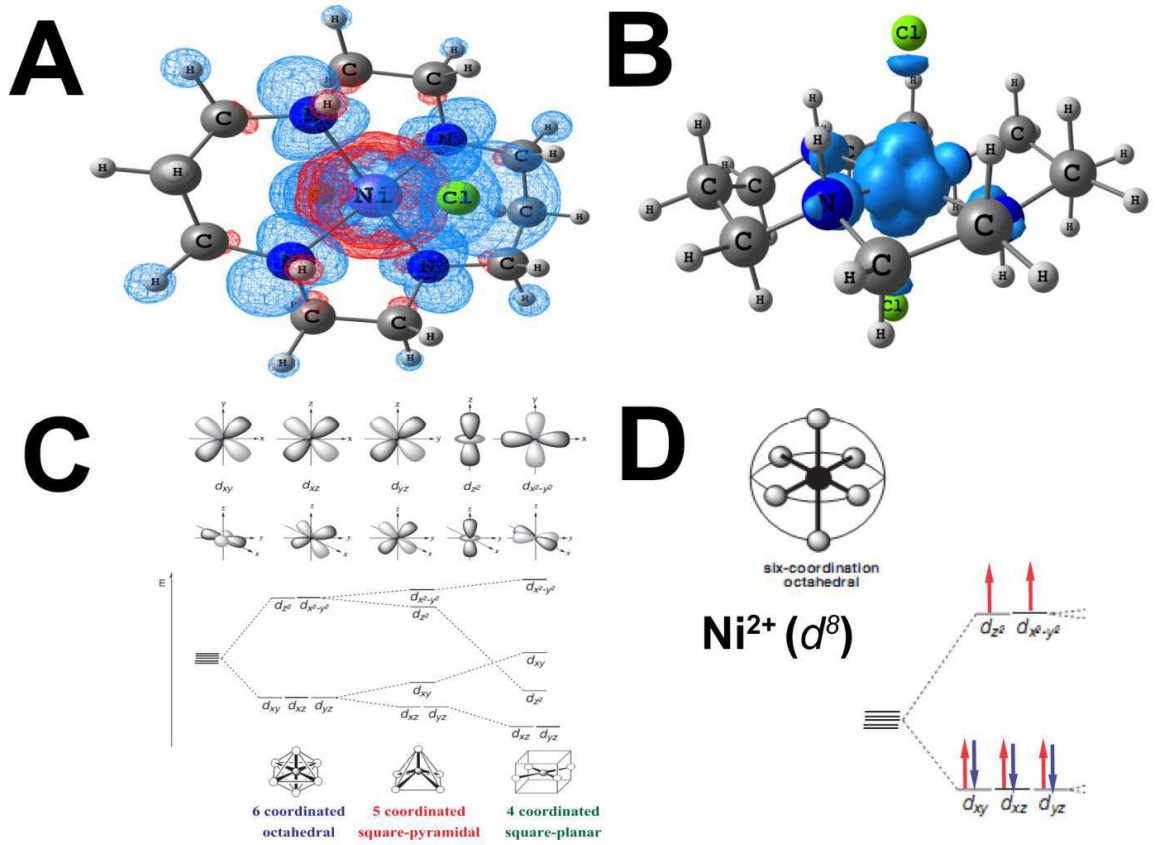

Figure 4.3.11: (A) Contour plot of total spin density in Ni-cyclam dichloride complex (red=negative and blue=positive spin density with contour value ranging between ± 0.0004 au). (B) Alpha minus Beta orbitals contour plot resulting in a shape which looks equivalent to convolution of $d_{x^2-y^2}$ and d_{z^2} type orbital in Ni-cyclam dichloride complex (C) *d*-orbital energy levels in 6, 5 and 4 coordinated complexes[163]. (D) Occupation of electrons in *d*-orbitals of Ni^{2+} ion in a 6-coordinated octahedral field.[163]

the Ni^{2+} with valence shell electronic configuration of d^8 has *d*-orbital energy levels as shown in Figure 4.3.11 D. The molecular orbital calculation from DFT is consistent with crystal field theory which predicts two unpaired electrons in Ni-cyclam dichloride complex.

4.3.4 Assignment of ^{13}C solid state NMR signals of the Ni-cyclam complex from spin densities calculated using DFT calculation

The ^{13}C Hahn-echo spectra of Ni-cyclam dichloride complex shows five distinct ^{13}C signals representing five carbon sites in the cyclam coordinating Ni^{2+} ion. The five signals are labeled with symbols as shown in Figure 4.3.12.

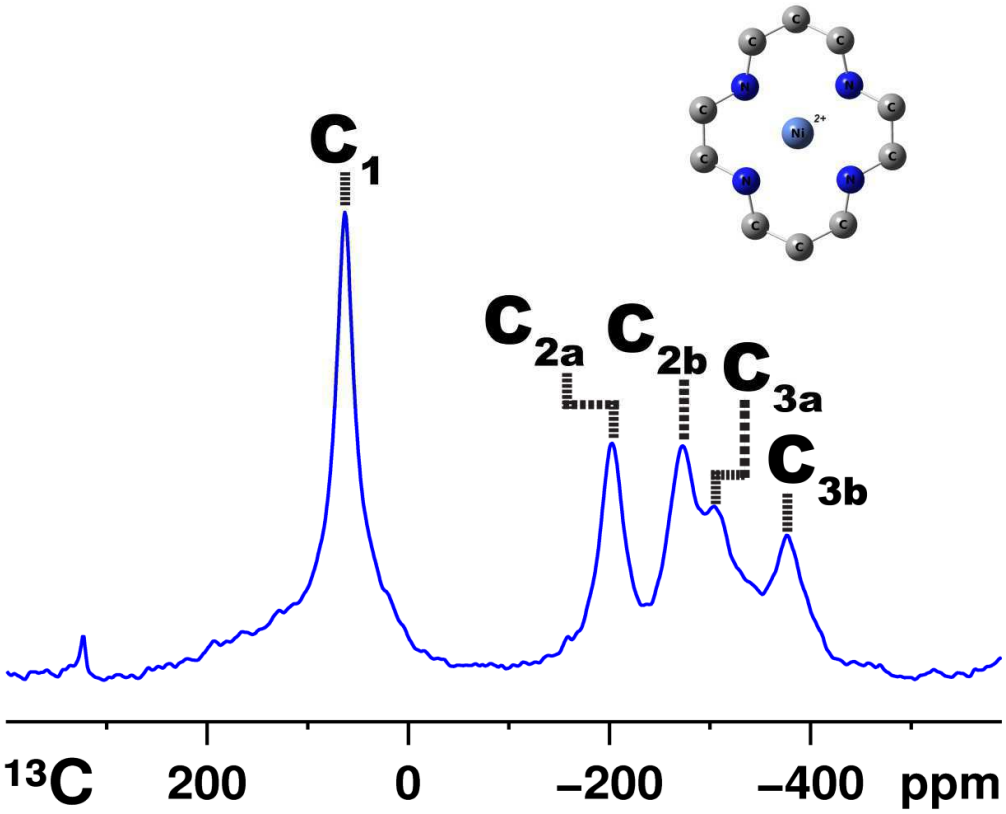

Figure 4.3.12: ^{13}C Hahn-echo spectra of Ni-cyclam dichloride complex with labeling of signals.

Here C_1 at 63 ppm is the only signal among five signals that is downfield shifted and found in the normal diamagnetic range. The four signals shifted up field are: C_{2a} at -202 ppm, C_{2b} at -276 ppm, C_{3a} at -303 ppm, and C_{3b} at -393 ppm. Due to the similarity in the intensity and signal shape the signals at -202 and -273 ppm are labeled C_{2a} and C_{2b} and similarly -303 ppm and -393 ppm as C_{3a} and C_{3b} respectively.

The diamagnetic part of the total shift of Ni-cyclam dichloride complex was calculated by subjecting the optimized structure to NMR=GIAO job in GAUSSIAN 09 using B3LYP method and 6-311+G(2d,p) basis set. The output of the NMR calculation was visualized using GAUSSVIEW program. Figure 4.3.13 shows the DFT generated ^{13}C NMR chemical shift in Ni-cyclam dichloride complex. The DFT generated carbon-13 NMR spectra showed three distinct signals similar to any

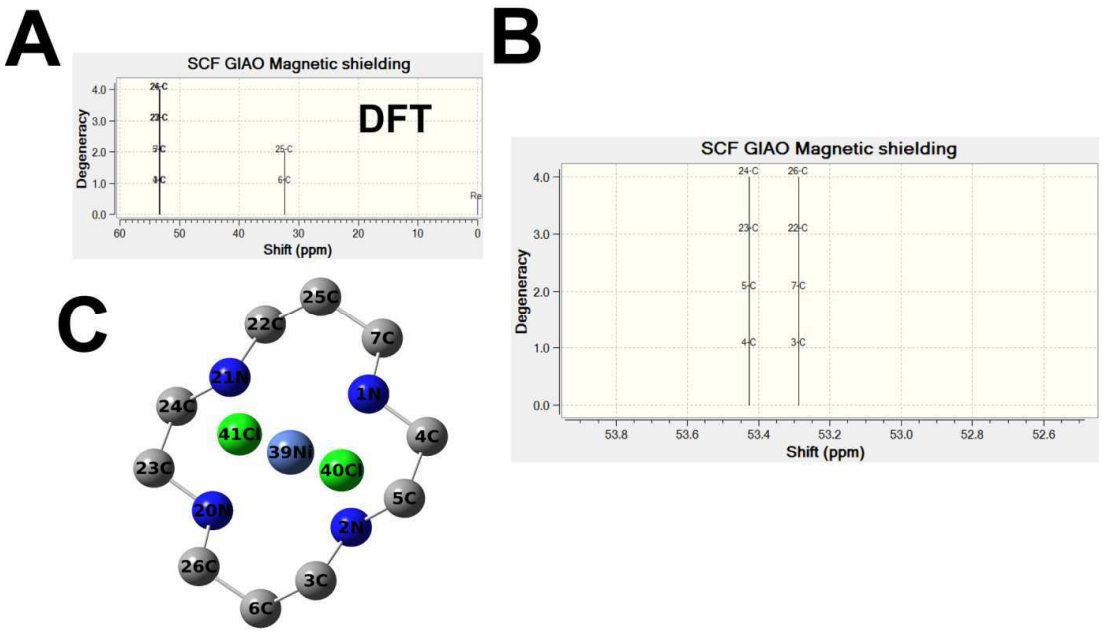

Figure 4.3.13: (A) DFT generated ^{13}C (diamagnetic part) NMR spectra of Ni-cyclam dichloride complex with (B) enlarged region between 50-60 ppm. (C) Assignment of carbon site in Ni-cyclam.

diamagnetic metal-cyclam complex or pure cyclam. This information was later used for calculating the total shift predicted by DFT calculation in paramagnetic Ni-cyclam dichloride complex.

Unpaired electron spin density from the Ni^{2+} ion is delocalized on to the nitrogen (donor atoms) and then distributed on to the carbon atoms through spin polarization. The spin density distribution (contour levels: +0.0003 au to -0.0003 au) on the entire molecule is shown in the Figure 4.3.14 A with positive spin density on the β-carbons C_6/C_{25} giving rise to positive Fermi contact shift. While the α-carbons C_3, C_{26}, C_7, and C_{22}, and γ-carbons C_4, C_{24}, C_5, and C_{23} feel the negative spin density at their respective nuclei giving rise to negative Fermi contact shifts. These spin densities generated by the DFT were inserted in Equation 2.7.22 and thereby Fermi contact shifts were obtained. The ^{13}C

Fermi contact shifts were added to the diamagnetic chemical shifts calculated using NMR job in GAUSSIAN to obtain the total theoretical shifts of paramagnetic Ni-cyclam dichloride complex.

Experimental ^{13}C shifts $^{ssNMR}\delta_{Total}$ [ppm]	**^{13}C chemical shift from DFT $^{DFT}\delta_{O}$ [ppm]**	**spin density (from DFT) ρ [au]**	**^{13}C Fermi-contact shift from DFT $^{DFT}\delta_{FC}$ [ppm]**	**Theoretical ^{13}C shift $^{DFT}\delta_{Total}$ [ppm]**	**Assignment of carbon sites (*see Figure 4.3.12*) in Ni-cyclam dichloride complex**
63 [C_1]	33	*0.00016*	22	55	C6, C25
-203 [C_{2a}]	53.3	*-0.0023*	-327	-273	C3, C26
-273 [C_{2b}]				-273	C7, C22
-305 [C_{3a}]	53.5	*-0.00297*	-422	-368	C5, C23
-377 [C_{3b}]				-368	C4, C24

Table 4.3.4: Comparison of experimental ^{13}C shift $^{ssNMR}\delta_{Total}$ from solid state NMR and theoretical ^{13}C shift $^{DFT}\delta_{Total}$ from DFT calculation, there by assignment of ^{13}C signals in paramagnetic Ni-cyclam dichloride complex

The total theoretical shifts are compared with the total experimental shifts (see Table 4.3.4) and the ^{13}C solid state NMR signal in Hahn-echo spectra were assigned to the respective carbon sites. The experimental ^{13}C shift of the β-carbons C_1 at 63 ppm is in good agreement with the DFT calculation which showed 50 ppm (C_6/C_{25}). But all the 4 α-carbons in the two six membered ring shows one common shift of -273 ppm in DFT calculation which were assigned to C_{2a} and C_{2b} signal in Hahn-echo at -203 and -273 ppm respectively. Similarly the 4 γ-carbons in the two five membered ring corresponding to C_{3a} and C_{3b} signal (at -305 and -377 ppm) in the Hahn-echo spectra showed a common shift of -368 ppm in the DFT calculation. However the DFT calculation was not able to resolve the asymmetry in the structure of Ni-cyclam dichloride which was depicted in ^{13}C Hahn-echo as five different sites.

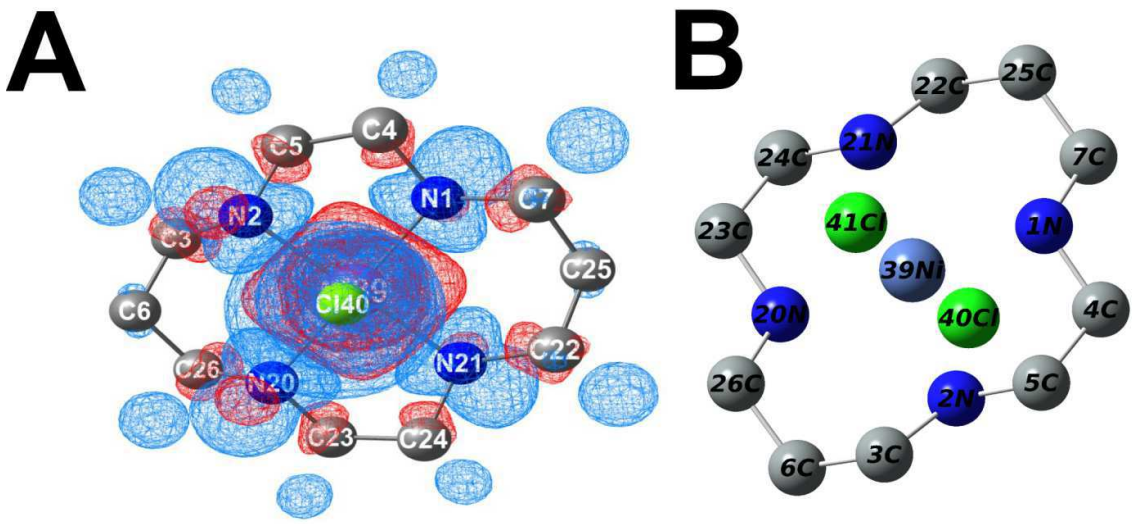

Figure 4.3.14: (A) Unpaired electron spin density distribution in Ni-cyclam complex (+0.0003 au (blue), -0.0003 au (red)). (B) Carbon site numbering for comparison of the data from Table 4.3.4.

4.4 Assignment of ^{1}H solid state NMR signals by ^{1}H-^{13}C dipolar INEPT, ^{1}H-^{13}C dipolar HSQC, ^{1}H-^{1}H correlation experiments and Karplus relation in paramagnetic Cu-cyclam monochloride complex

Sensitivity and resolution enhancement of ^{1}H and ^{13}C solid state NMR signals achieved using very-fast MAS technique in paramagnetic Cu-cyclam complex (see Figure 4.2.3 A and B) motivated us to try two dimensional solid state NMR experiments in order to obtain ^{1}H-^{13}C correlations and hence gain access to the information for ^{1}H assignment. Two dimensional heteronuclear experiments in NMR have two basic goals: (1) resolve the unresolved signals and (2) to obtain correlation between two nuclei. Normally in solid state NMR for ^{1}H-^{13}C heteronuclear 2D correlation one uses the heteronuclear correlation (HETCOR) experiment, which is an extension of one dimensional ^{13}C CP (cross polarization). Since as already shown, cross polarization technique is inefficient in the case of paramagnetic systems an alternative technique is needed to obtain ^{1}H-^{13}C correlations.

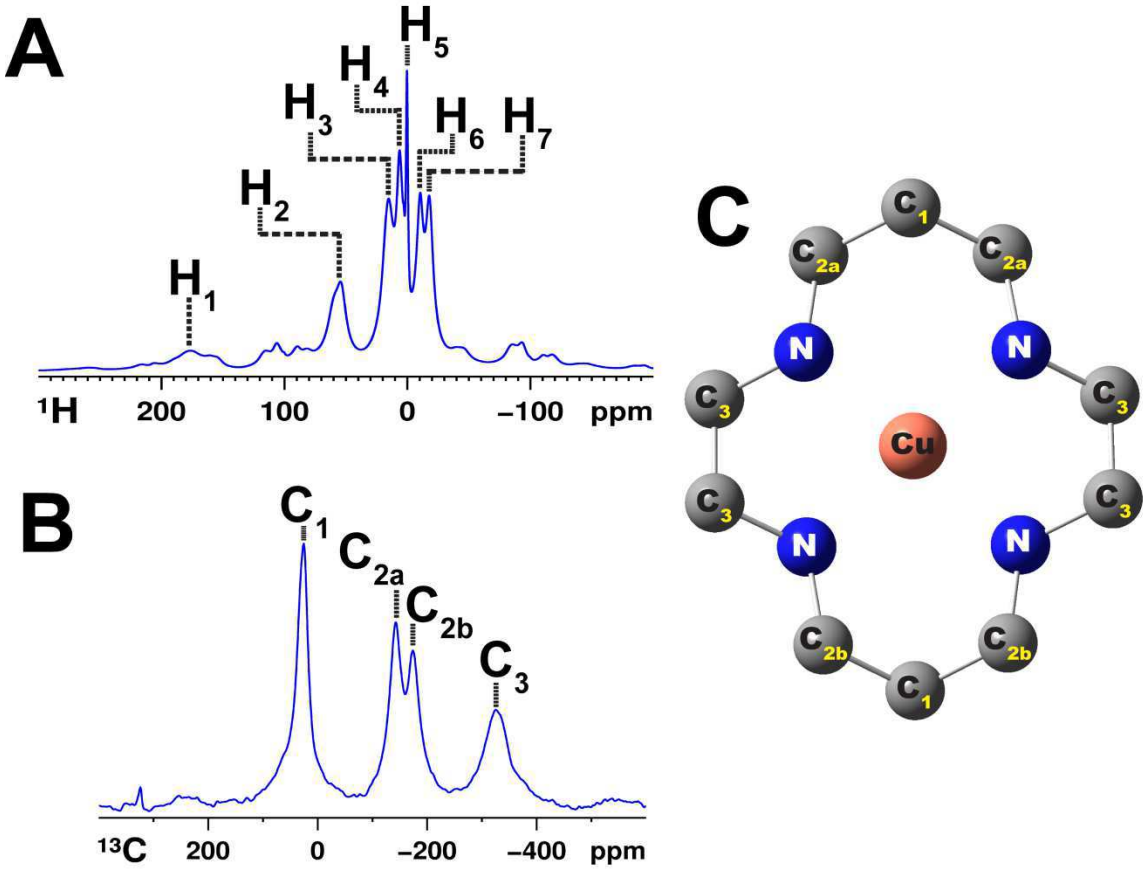

Figure 4.4.1: (A) ^{1}H and (B) ^{13}C Hahn-echo spectra of Cu-cyclam monochloride complex (C) with assignment of carbon signals based on DFT calculations.

We have used a dipolar INEPT pulse sequence to obtain ^{1}H-^{13}C correlation which is similar to the technique applied by Ishii *et al.*[60] in paramagnetic Cu(DL-alanine)$_2$ complex. Dipolar INEPT is coherent polarization technique introduced in diamagnetic systems for ^{13}C spectral editing by De Vita *et al.*[175] Later it was modified for ^{1}H-^{13}C correlation in paramagnetic complexes by Wickramasinghe *et al.*[59] The dipolar INEPT pulse sequence uses recoupling technique such as TEDOR (transferred-echo double resonance) block for polarization transfer. The dipolar coupling which is averaged during MAS is re-introduced back into the system by applying refocusing pulses at time intervals synchronized to MAS frequency ω_r. Several schemes of dipolar INEPT pulse sequence have been proposed by Ishii *et al.*[60] and Kervern *et al.*[61] but the pulse sequence adapted in our work is most similar to the one used in the work of Kervern *et al.*[61]

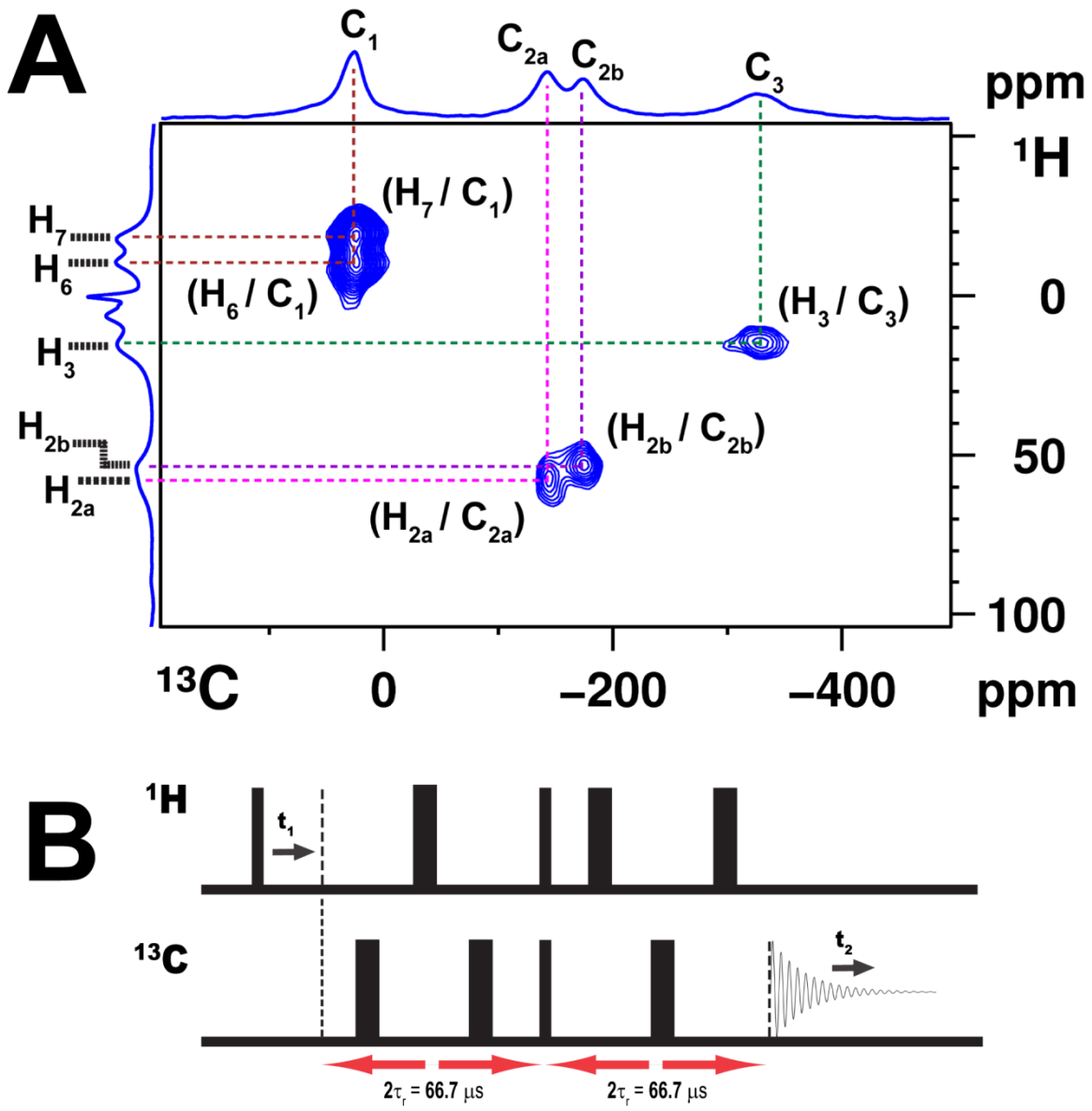

Figure 4.4.2: (A) ^{1}H-^{13}C 2D dipolar INEPT spectra of Cu-cyclam monochloride complex (B) with the pulse sequence.

Shown in Figure 4.4.2 A is the ^{1}H-^{13}C 2D dipolar INEPT spectrum of Cu-cyclam monochloride complex. We used a $2\tau_r$ transfer period (= 66.7 μs) during recoupling period as shown in Figure 4.4.2 B. The dipolar INEPT pulse sequence is similar to INEPT (Insensitive Nucleus Enhancement by Polarization Transfer)[84] experiment in solution state NMR. Only here the mode of polarization transfer is through dipolar coupling between ^{1}H and ^{13}C. The excitation pulse on ^{1}H creates ^{1}H coherence with its high polarization. The time period t_1 is set just after the excitation pulse on ^{1}H.This is later transferred to ^{13}C by a refocusing pulse which is on ^{1}H and ^{13}C for a period of time known as recoupling time τ_{rcpl} in TEDOR experiment. During this period the ^{1}H-^{13}C dipolar

coupling which is averaged spatially during MAS is reintroduced back into the system with the help of 180° pulses. The magnetization is refocused back to ^{1}H, and the ^{13}C signals are acquired. The Fourier transform of the signals stored during t_1 and t_2 produces a 2D plot providing the ^{1}H-^{13}C dipolar connectivity information.

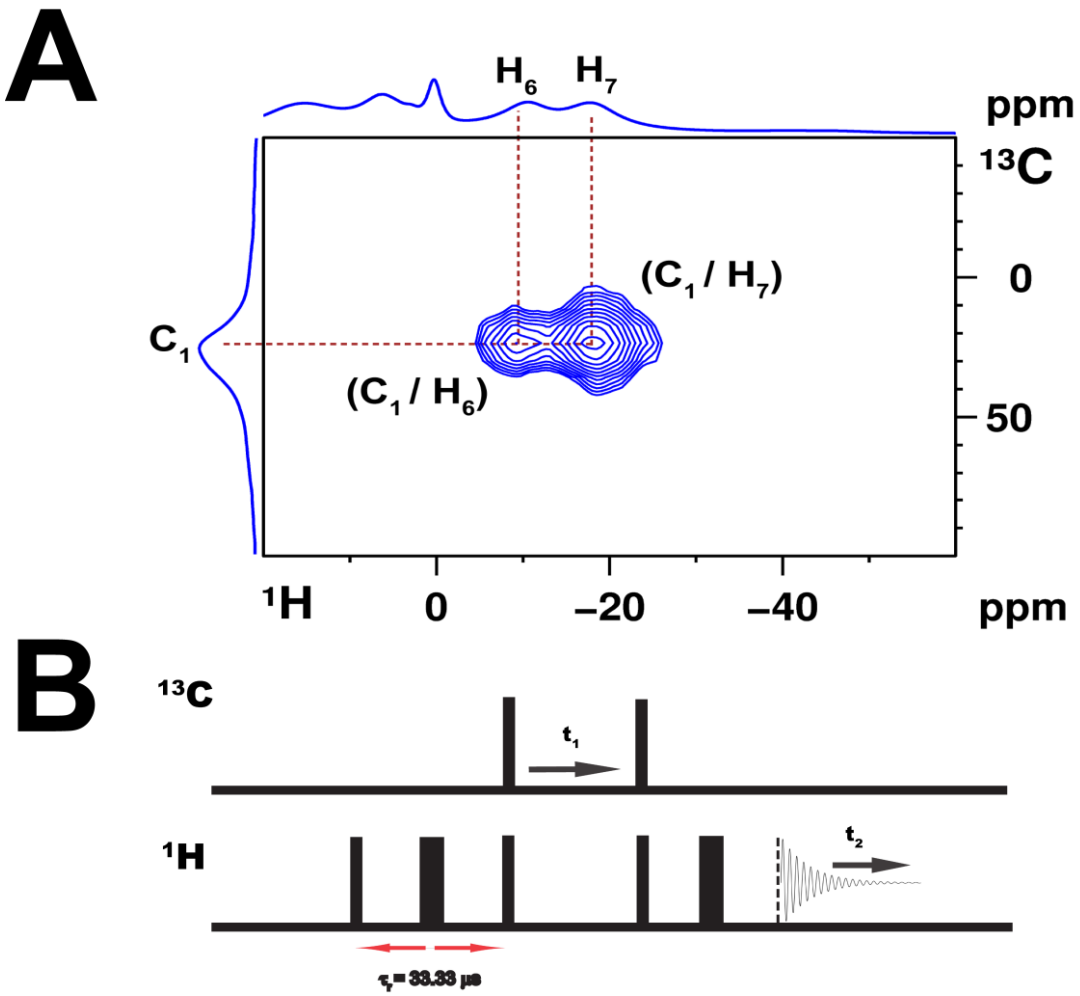

Figure 4.4.3: (A) ^{1}H-^{13}C 2D dipolar HSQC spectra of Cu-cyclam monochloride complex (B) with the pulse sequence.

All four signals in the ^{13}C dimension showed cross peaks to ^{1}H in the indirect dimension. The C_1 (26 ppm) signal arising from the carbon atom farthest from the Cu- center showed a cross peak to the upfield shifted ^{1}H signals H_6 (-10 ppm) and H_7 (-18 ppm). The H_2 signal at 55 ppm in one dimensional ^{1}H Hahn-echo (see Figure 4.4.1 A) is separated in the 2D dipolar INEPT showing two individual cross peaks to C_{2a} (-142 ppm) and C_{2b} (-173 ppm), respectively. This confirms that the H_2 signal is superposition of two signals H_{2a} (57 ppm) and H_{2b} (53 ppm) connected to two different

carbons C_{2a} and C_{2b}, respectively. The C_3 (-324 ppm) carbon signal arising from the carbon close to Cu- center shows a cross peak to H_3 (15 ppm) proton. The H_1 and the two signals in the diamagnetic region i.e. H_4 and H_5 (see Figure 4.4.1 A) showed no cross peak in the 2D dipolar INEPT spectra.

High sensitivity and resolution of ^{1}H Hahn-echo of paramagnetic Cu-cyclam monochloride complex achieved using VFMAS technique motivated us to try ^{1}H-^{13}C dipolar HSQC type of experiment with ^{1}H acquisition. Such an experiment gives sufficient ^{1}H resolution to resolve the two cross peaks in less experimental time. Shown in Figure 4.4.3 A is the ^{1}H -^{13}C dipolar HSQC spectra of C_1, H_6/H_7 of Cu-cyclam monochloride complex with ^{1}H acquisition. In comparison to the conventional HSQC in liquid state NMR which exploits *J*-coupling, the transfer times last only one rotor period (33.3 μs, thus shorter by two orders of magnitude) and the ^{13}C π pulses are omitted in order to allow recoupling of the ($1\times\omega_r$) modulated term of the dipolar Hamiltonian (Figure 4.4.3 B). This experiment however only works in the case of relatively slow relaxation of coherences, and therefore the other three cross peaks could not be observed. Critical are not only the relaxation during the transfer periods (there are two likewise in the dipolar INEPT), but in particular the evolution as antiphase type coherence including hydrogen suffers from very fast coherence loss.

4.4.1 Distinction of axial and equatorial protons by Karplus relation in Cu-cyclam complex.

As discussed in the previous unit metal-cyclam complexes show various configurations (Figure 4.1.1 C) in solution but in solids the trans-III type is retained.[10] Shown in Figure 4.4.4 A is the stable trans-III configuration of the Cu-cyclam complex. From our DFT calculation and some examples of XRD data from the literature we have confirmed that the Cu-cyclam monochloride complex used in our investigation shows stable trans-III type configuration. Furthermore there is a difference in the hyperfine shifts of axial and equatorial protons in the –CH_2 moiety of paramagnetic Cu-cyclam complex which follows Karplus relation.[86] The relation connects the hyperfine coupling with the dihedral angle θ of the dihedron Cu-N-C-H[50] (shown in Figure 4.4.5)

$$A = a\,cos^2\theta + b\,cos\theta + c \qquad \textbf{4.4.1}$$

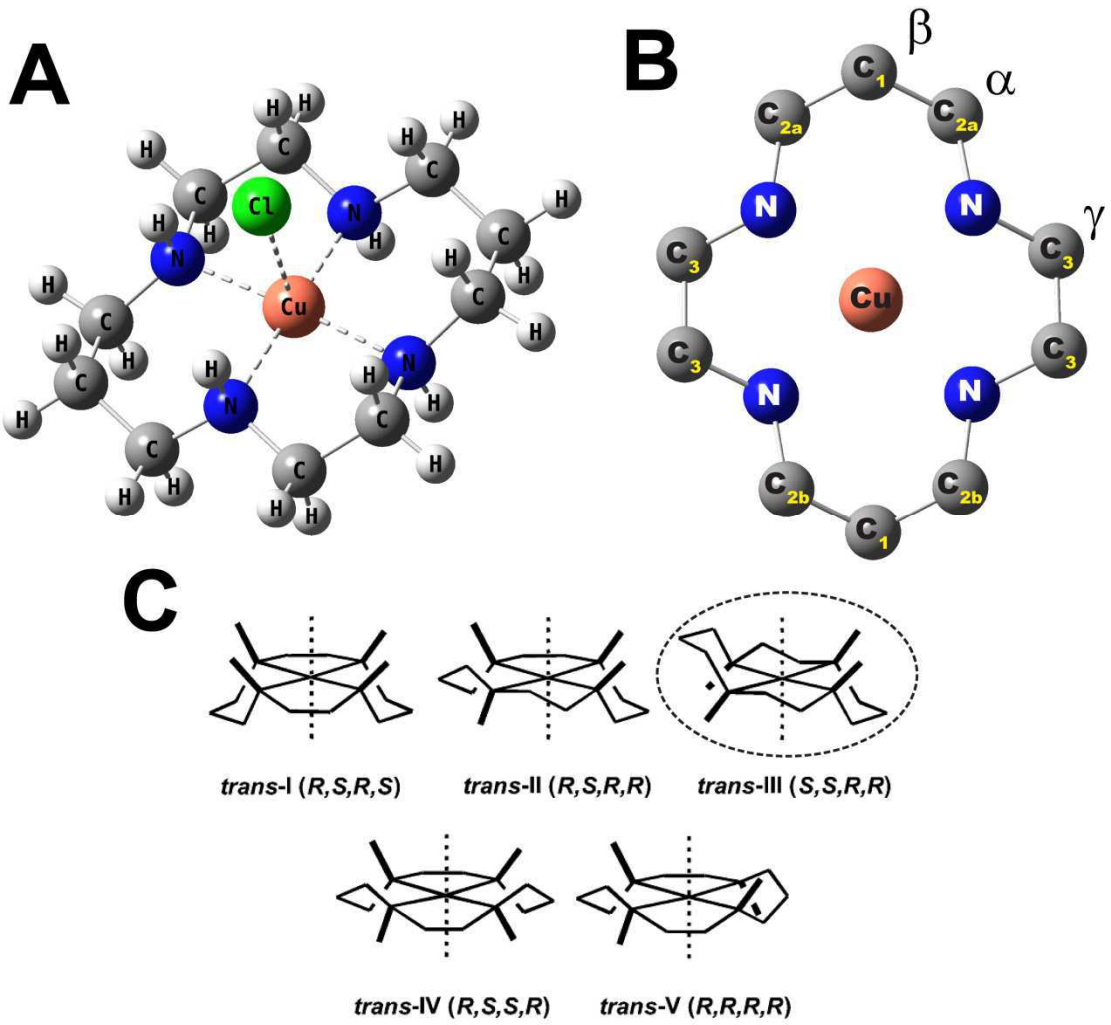

Figure 4.4.4: (A) DFT optimized Cu-cyclam complex structure with (B) ^{13}C signal assignment from DFT calculation and labeling of carbon sites adapted from Dei *et al.*[77] (C) Various configuration of metal-cyclam complex with stable trans-III highlighted.

As the coefficient $a >> b$ and c, the equatorial hydrogen atoms should in general display stronger hyperfine shifts. This has been witnessed in the ^{1}H solution state NMR of paramagnetic Ni-cyclam dichloride complex by Dei *et al.*[77] This work is supporting the assignment of ^{1}H in Ni-cyclam complex we have investigated which will be discussed later. Based on this relation we assign the proton signal (signal from the hydrogens attached to β-carbon atom) H_6 (-11 ppm) to be axial and H_7 (-18 ppm) to be equatorial. Similarly we expect that there is distinction of axial and equatorial ^{1}H signal arising from hydrogen attached to C_{2a}, C_{2b} (α-carbons) and C_3 (γ-carbons) carbons. The distinction of axial and equatorial proton signals based on Karplus relation is presented in the ^{1}H-^{13}C 2D dipolar INEPT spectra in Figure 4.4.6 by relabeling of ^{1}H signals.

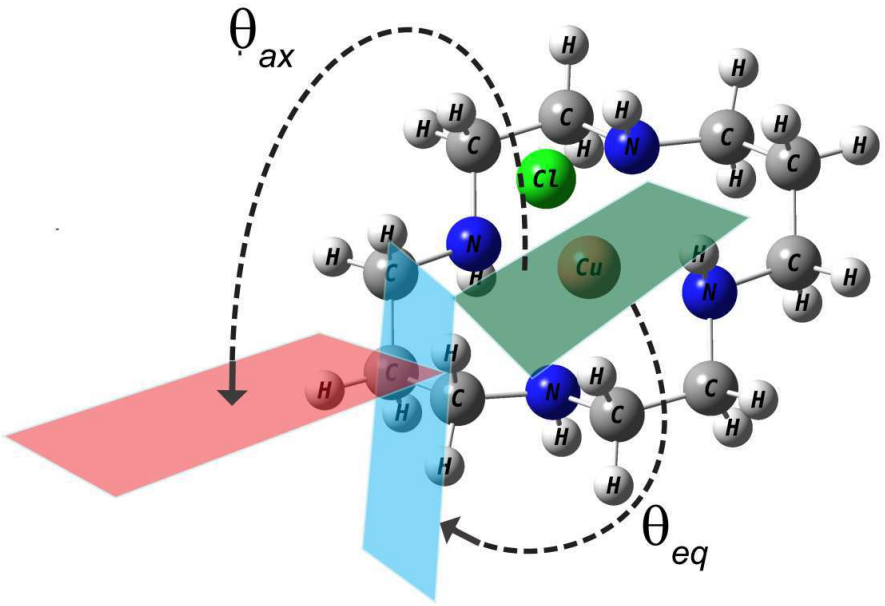

Figure 4.4.5: Dihedral angles: θ_{ax} between N-Cu-N plane and plane containing axial hydrogen in -CH_2 moiety and θ_{eq} between N-Cu-N plane and plane containing axial hydrogen in -CH_2 moiety

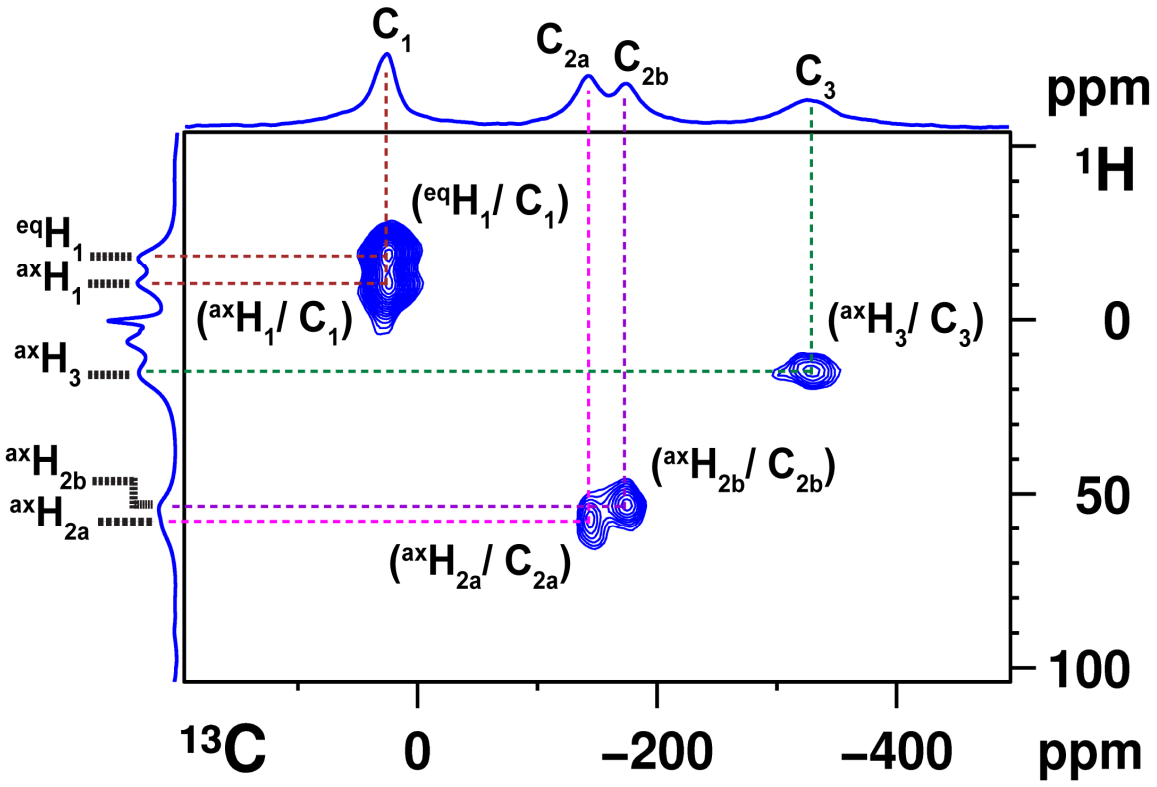

Figure 4.4.6: ^{1}H-^{13}C 2D dipolar INEPT spectra of paramagnetic Cu-cyclam monochloride complex with distinction of axial and equatorial proton signals based on Karplus relation.

4.4.2 Completion of ^{1}H assignment of paramagnetic Cu-cyclam monochloride complex by ^{1}H-^{1}H 2D correlation spectra

In liquid state NMR, ^{1}H-^{1}H correlation spectra as COSY, TOCSY and NOESY are the most frequently applied 2D experiments. In solid-state NMR, such spectroscopy is rarely possible due to signal broadening. With the better ^{1}H signal resolution in paramagnetic NMR, correlation spectra by means of the strong dipolar coupling should be possible as long as relaxation is not too fast with respect to ^{1}H-^{1}H magnetization transfer. We have applied a simple NOESY type sequence for transfer by the strong homonuclear dipolar couplings followed by a rotor synchronized echo sequence (Figure 4.4.7 B). The diamagnetic signals are suppressed by presaturation through

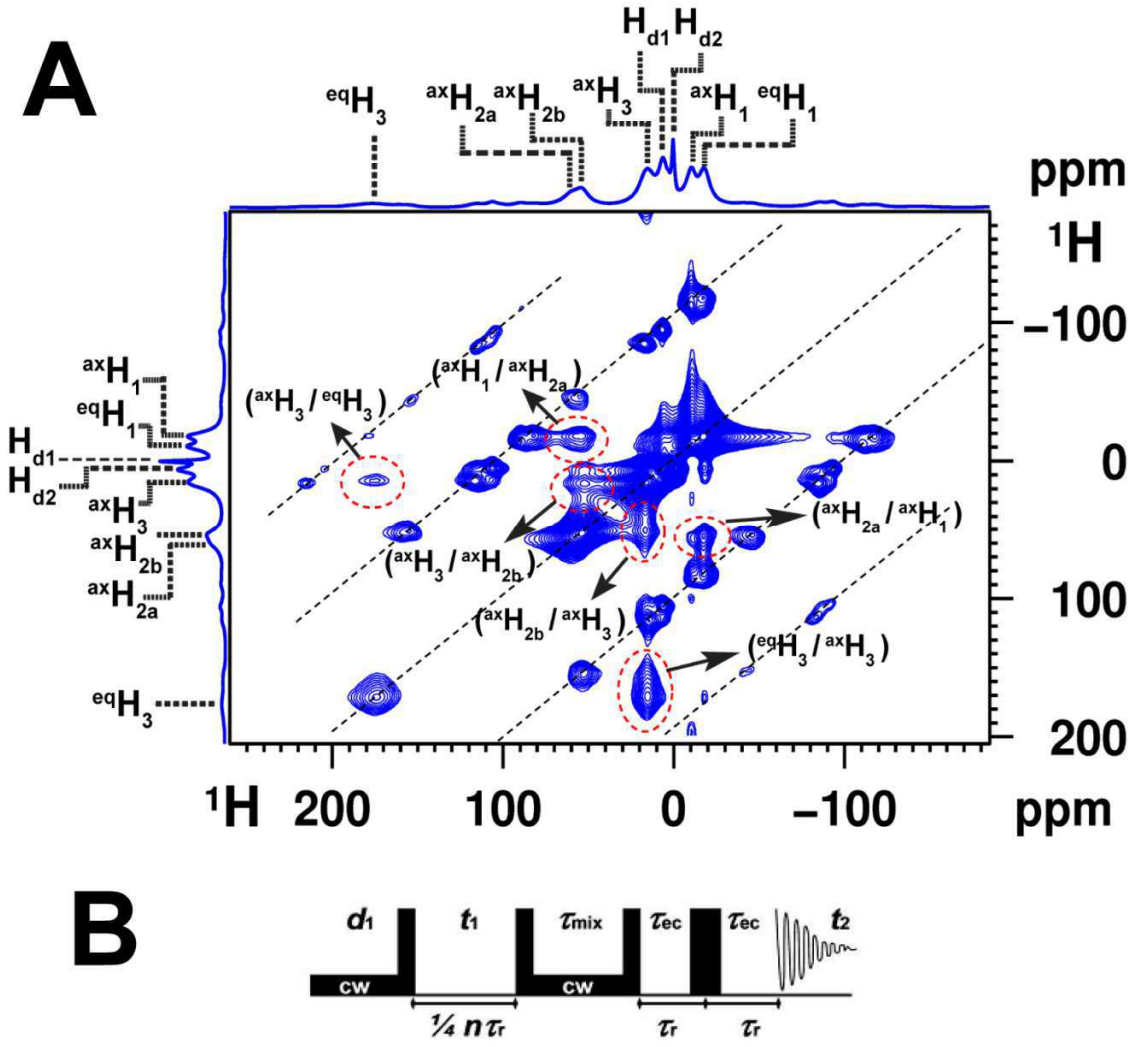

Figure 4.4.7: ^{1}H-^{13}C 2D dipolar INEPT spectra of paramagnetic Cu-cyclam monochloride complex with distinction of axial and equatorial proton signals based on Karplus relation.

continuous irradiation with 2.8 kHz during the interscan delay. Figure 4.4.7 A shows the spectrum for a mixing time τ_{mix} = 140 µs. In order to avoid too much overlap by spectral aliasing, the t_1 increments are reduced to ¼ of the rotation time (spectral width 120 kHz). The spectrum is dominated by diagonal and, due to spinning side bands, secondary diagonal peaks, but there are several cross peaks visible: $^{ax}H_{2b}$ correlates with $^{eq}H_1$, however not with $^{ax}H_1$, and $^{ax}H_{2a}$ with $^{ax}H_3$. Most interesting is the strong cross peak of the so far unassigned 177 ppm signal to H_3, indicating that it is the equatorial H_3. Cross peaks between $^{ax}H_1$ and $^{eq}H_1$, confirming that they are attached to the same carbon, are manifested only as shoulders of the diagonal peaks. There is however no indication of a cross peak between the signals of the two $^{ax}H_2$, even at longer mixing times. Although at the limit of resolution, one would at least expect a sign in the form of a broadening if the two different C_{2a} and C_{2b} were attached to the same C_1, as the distances between two axial H_2 would be about 2.5 Å. Its absence means that H_{2a} and H_{2b} are relatively far from each other, i.e. in

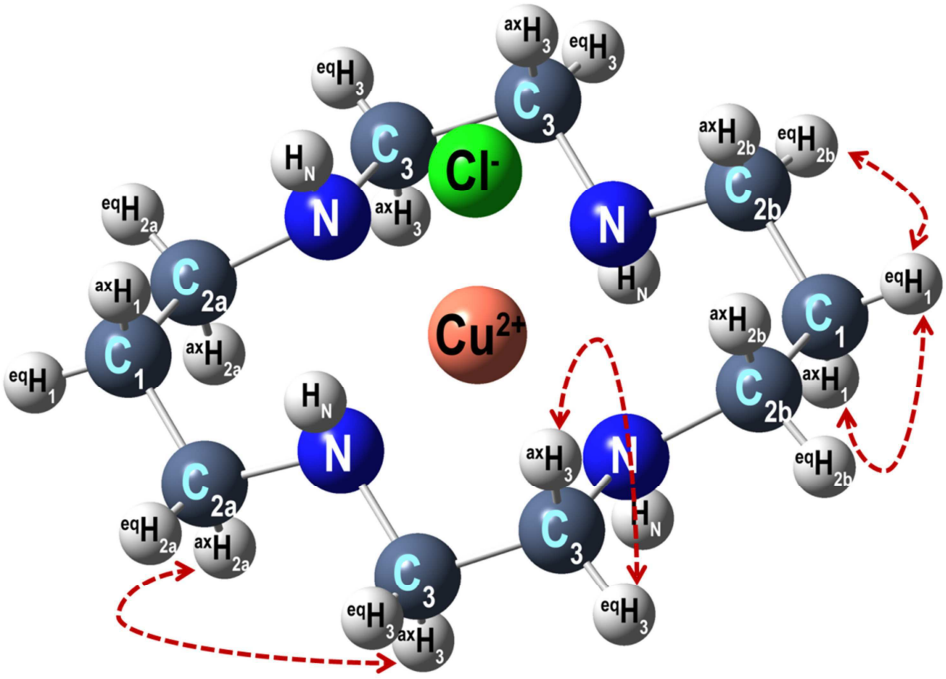

Figure 4.4.8: Conclusion of the assignment based on ^{1}H-^{1}H correlation experiment (arrows represent the dipolar connectivity)

different six-membered rings, as already concluded by the DFT calculations of the hyperfine shifts. When increasing the mixing time towards 1 ms, spin diffusion leads to mutual cross peaks of all peaks except the diamagnetic H_{d1} to H_{d2}. Figure 4.4.8 concludes the dipolar connectivities (without

symmetrical redundancies). The lacking ^{1}H signals could only be unambiguously identified with the help of a complementary spectrum of Cu-cyclam in $CHCl_3$ solution and variable temperature 1D ^{1}H solid state NMR (see unit 4.5 and 4.6). Here H_N has a negative shift due to spin polarization leading to a signal at -211 ppm, and the other signal at an extreme shift of 328 ppm must therefore be $^{eq}H_2$.

4.5 Comparison of study of ^{1}H NMR shifts from solid- and solution- state NMR with shifts from DFT calculation in paramagnetic Cu-cyclam monochloride complex.

In order to locate the missing signals ($^{eq}H_2$ and H_N) in ^{1}H Hahn-echo spectra of paramagnetic Cu-cyclam monochloride complex we tried to detect them in solution state NMR. A 1D ^{1}H Hahn echo was recorded for a solution containing Cu-cyclam monochloride complex dissolved in deuterated

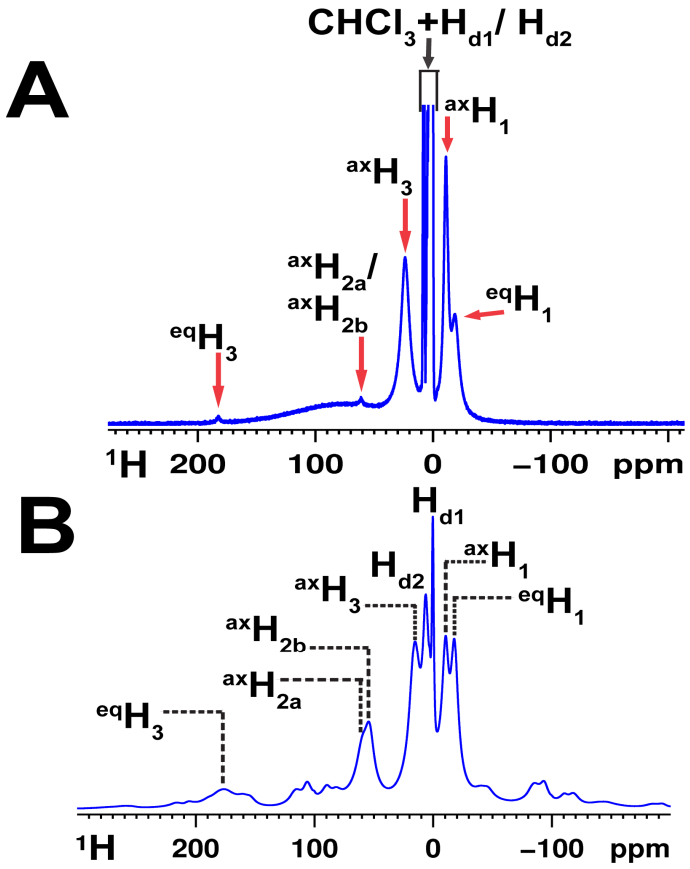

Figure 4.5.1: Comparison of the central region of solution and solid state ^{1}H Hahn-echo spectra of paramagnetic Cu-cyclam monochloride complex. Spectra processed with little line broadening (100 Hz) with which H_N and $^{eq}H_2$ are not detectable.

chloroform. Shown in Figure 4.5.1 is a comparison of (A) solution state ^{1}H NMR spectra of paramagnetic Cu-cyclam monochloride complex with the (B) solid state NMR ^{1}H Hahn-echo spectra. The ^{1}H signals in solution state spectra appear to be slightly shifted (+/- 2-3 ppm) relative to solid state spectra. This is obvious because the solid state spectrum is acquired at a sample temperature of about 58°C (RT + temperature rise from friction due to spinning). The 1D solution state ^{1}H NMR experiments were performed using a static solid state probe because the excitation bandwidth of a common liquid state probe head is too small. In solution state the sensitivity of the $^{ax}H_{2a}/^{ax}H_{2b}$ and $^{eq}H_3$ is relatively weak compared to other paramagnetic ^{1}H signals. Again, some

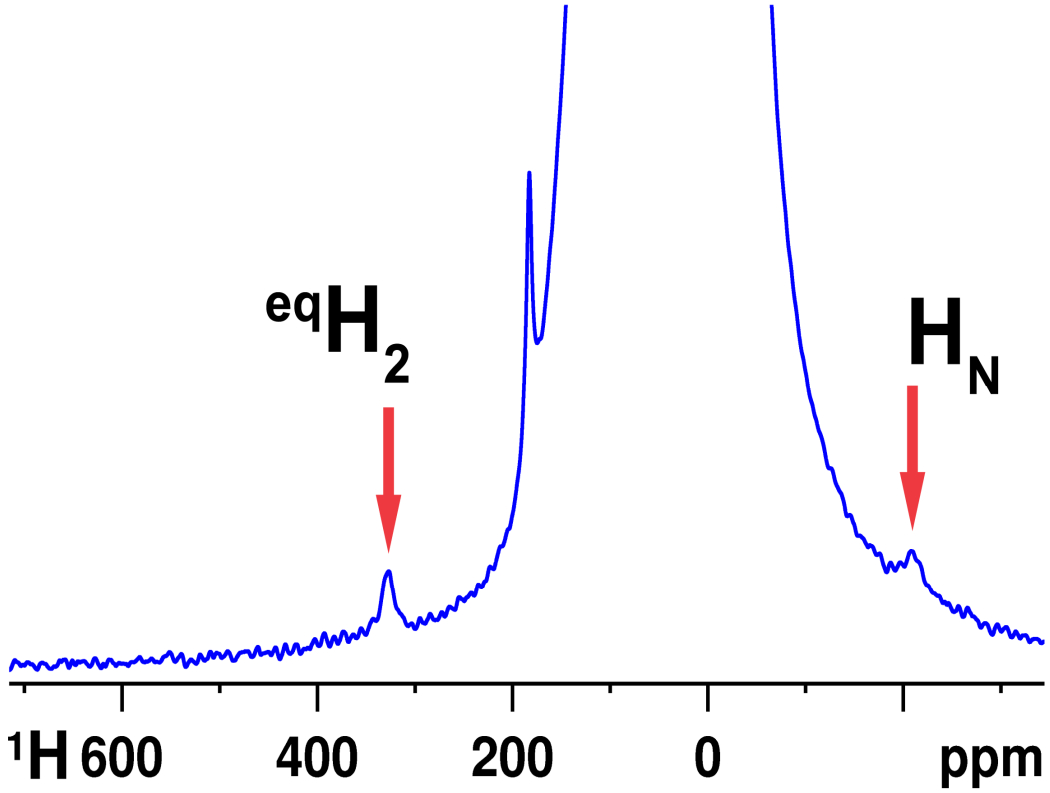

Figure 4.5.2: Identification of equatorial proton signals $^{eq}H_2$ (328 ppm) from hydrogen attached to α-carbon C_{2a}/C_{2b} and extremely up field shifted tertiary amide proton signal H_N (-211 ppm).

signals are found in the region of diamagnetic range (0-14 ppm) along with the solvent signal (chloroform 7.26 ppm). The equatorial proton signal $^{eq}H_2$ and tertiary amine proton signal H_N were located by processing with larger line broadening due to their fast relaxation. Figure 4.5.2 shows the region comprising $^{eq}H_2$ (328 ppm) and H_N (-200 ppm) processed with a broadening

Methods	^{1}H shifts in Cu-cyclam (Cl^-) [ppm] *(assignment from ^{1}H-^{1}H 2D correlation and Karplus relation)*						
	$^{eq}H_{2a}/^{eq}H_{2b}$	$^{eq}H_3$	$^{ax}H_{2a}/^{ax}H_{2b}$	$^{ax}H_3$	$^{ax}H_1$	$^{eq}H_1$	H_N
ssNMR	340*	176	58/54	15	-11	-18	-240*
Soln. NMR	328	183	61	24	-11	-18	-210
DFT	319/384	183/209	65/53	18	-8	-17.5	-200/-98

Table 4.5.1: Comparison of ^{1}H shifts from solid /solution NMR with shifts from DFT calculation (*identified by variable temperature solid state NMR, *see unit 4.6*)

by exponential window of 1000 Hz. Table 4.5.1 shows a comparison of ^{1}H shifts in solid and solution state with shifts from DFT calculation. We observe that the ^{1}H shifts from solid- and solution-state agree well with the shifts from DFT calculation. The shifts of $^{eq}H_{2a}$/ $^{eq}H_{2b}$ and $^{ax}H_{2a}$/ $^{ax}H_{2b}$ calculated by DFT shows two values due to the asymmetry in the structure and hence asymmetry in the spin distribution. This is crucial, since we observed two values of $^{ax}H_{2a}$/ $^{ax}H_{2b}$ in solid state NMR (2D dipolar INEPT see Figure 4.4.6). However, the correlation peaks corresponding to $^{eq}H_{2a}$/ $^{eq}H_{2b}$ were not seen in 2D dipolar INEPT. However, we observed a single signal of the equatorial proton $^{eq}H_2$ in 1D solution state ^{1}H NMR (see Figure 4.5.2). In liquids due to the motional averaging, the two asymmetric equatorial proton signals of H_2 merge to a single signal.

4.6 Identification of tertiary amine proton H_N and equatorial proton $^{eq}H_2$ signal using variable temperature solid state NMR experiment in paramagnetic Cu-cyclam monochloride complex

We know that NMR signals of paramagnetic samples are very sensitive to the temperature change and obey Curie's relation,

$$\delta_P = C\frac{B}{T} \qquad \textbf{4.6.1}$$

i.e. as the temperature T rises the NMR shifts of a paramagnetic sample δ_p tend to shift towards the diamagnetic region. The magnitude of the shift is stronger for signals arising from nucleus close to paramagnetic center. On the one hand tertiary amine proton signal is very hard to locate since it suffers from low sensitivity due to severe broadening (close to paramagnetic center). But on the other hand these signals can be relatively sensitive to the temperature compared to the other signals. We performed a variable temperature ^{1}H Hahn-echo with temperature interval of 10 K from 294 K to 244 K, and we observed the region of H_N and $^{eq}H_2$ (-210 ppm and 328 ppm as seen from solution state NMR and DFT). Shown in Figure 4.6.1 A is the variable temperature solid state NMR 1D ^{1}H Hahn-echo spectra of paramagnetic Cu-cyclam complex with region of (B) the equatorial proton signal H_2 and (C) the tertiary amine proton signal. The colored dotted lines indicate the Curie behavior of the signals as

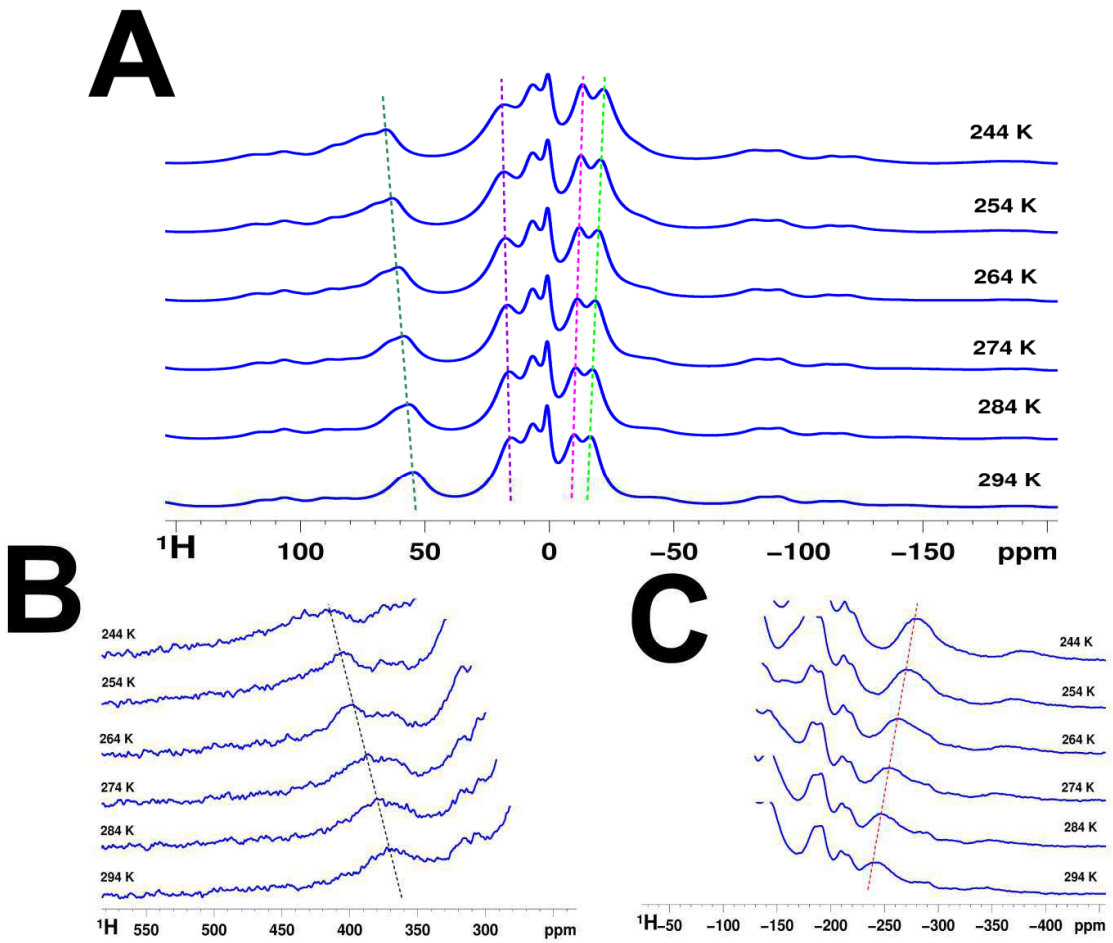

Figure 4.6.1: Identification of equatorial proton signals $^{eq}H_2$ arising from hydrogen attached to α-carbon C_{2a}/C_{2b}, and extremely upfield shifted tertiary amide proton signal H_N by variation of the temperature

temperature is lowered i.e. the signals move away from diamagnetic region. Strong dependence of the temperature over the shifts of signal $^{eq}H_2$ and H_N which have a rate of 10 ppm / 10 K suggests that they are not sidebands and must be real signals. Like this, the other two missing signals ($^{eq}H_2$ at 340 ppm and H_N at -240 ppm) in ^1H solid state spectra of paramagnetic Cu-cyclam monochloride complex could be identified.

4.7 Assignment of ^1H signals in solid paramagnetic Ni-cyclam dichloride complex by comparison with shifts from solution state NMR and DFT calculation

Paramagnetic Ni-cyclam dichloride complex investigated here presents a case of system with two unpaired electrons (electronic spin S = 1). Due to this the anisotropic part of the pseudocontact

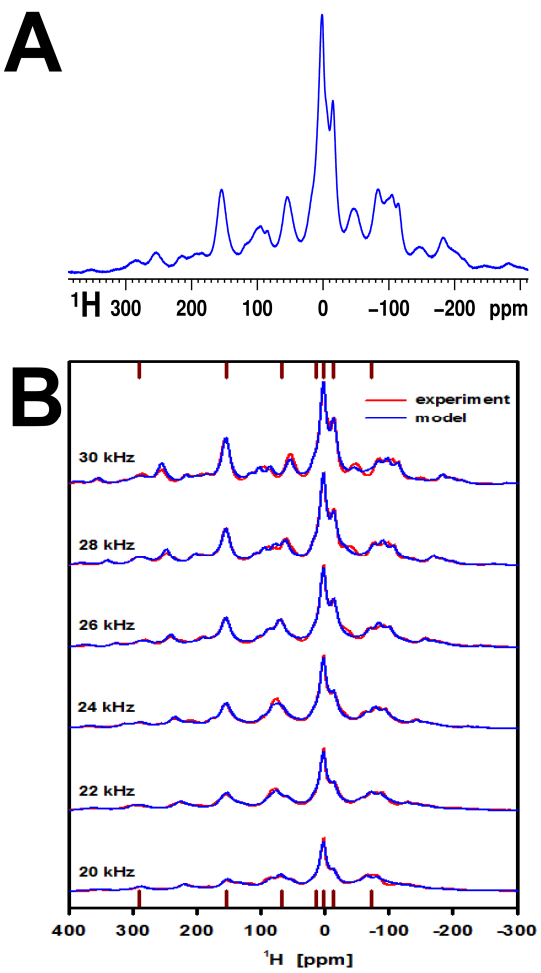

Figure 4.7.1: (A) ^1H Hahn-echo spectra of paramagnetic Ni-cyclam dichloride complex with 30 kHz MAS frequency. (B) Separation of isotropic signals from sidebands using variable MAS experiment deconvolution. The red dashes mark isotropic signals at 30 kHz.

contribution of the paramagnetic interaction is relatively large in magnitude compared to Cu-cyclam complex. This is quite evident from the ^{1}H and ^{13}C Hahn-echo spectra (see Figure 4.2.3 B) of Ni-cyclam complex which exhibits stronger anisotropy through spinning sidebands. On the one hand relatively large spectral dispersion is advantageous but on the other hand too many sidebands are serious hindrance for identification of the signals. For this we tried to separate isotropic signals from sidebands by a variation of the spinning frequency. This is a quite common test in solid state NMR to identify isotropic signals among sidebands. Since sidebands are a function of MAS frequency they shift with increase or decrease in the MAS speed which separates the isotropic signal from the sidebands. However, the isotropic signals too shift along with sidebands during variable spinning experiment since MAS produces heating due to friction and temperature rise influences the paramagnetic signals to shift (Curie's law, see Equation 4.6.1). We monitored the temperature using calibration curve of lead nitrate $Pb(NO_3)_2$ during variable spinning experiment. We have recorded 1D ^{1}H Hahn-echo of paramagnetic Ni-cyclam dichloride complex under variable MAS speeds of 20 kHz to 30 kHz in the interval of 2 kHz as shown in Figure 4.7.1 B. Using a joint deconvolution program written in MATLAB the data were fitted to obtain the isotropic ^{1}H shifts in paramagnetic Ni-cyclam dichloride complex as shown in Figure 4.7.1. Seven isotropic signals could be identified.

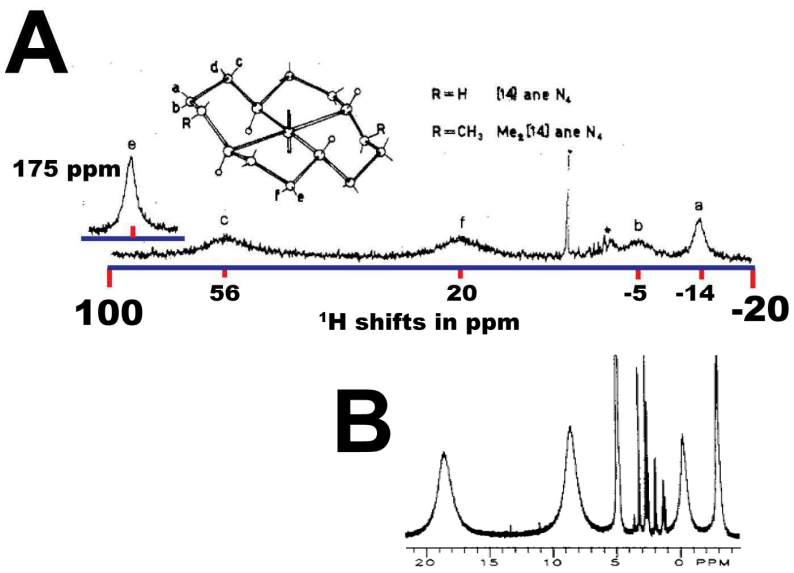

Figure 4.7.2: (A) Assignment of ^{1}H signals in solution based on Karplus relation by Dei *et al.*[77] and (B) solution ^{1}H spectra reported by Connolly *et al.*[78]

There are quite a number of examples of solution state ^{1}H NMR of paramagnetic Ni-cyclam dichloride complex in the literature. Figure 4.7.2 A shows the assignment of ^{1}H signals in paramagnetic Ni-cyclam dichloride complex by Dei *et al.*[77] Billo and Connolly[78] have shown that ^{1}H shifts of paramagnetic Ni-cyclam dichloride complex in solution are solvent dependent (DMSO > D_2O > $CHCl_3$) and extreme shifts are observed using chloroform.[78]

We have recorded a solution state ^{1}H NMR of paramagnetic Ni-cyclam dichloride complex in $CHCl_3$ as done for Cu-cyclam complex. Based on the Karplus relation and ^{1}H assignment from Dei *et al.*[77] we compared the ^{1}H shifts in solution state (Figure 4.7.3 A) and solid state NMR spectra (Figure 4.7.3 B) of Ni-cyclam complex and have assigned the ^{1}H signals in Hahn-echo spectra as shown in Figure 4.7.3.

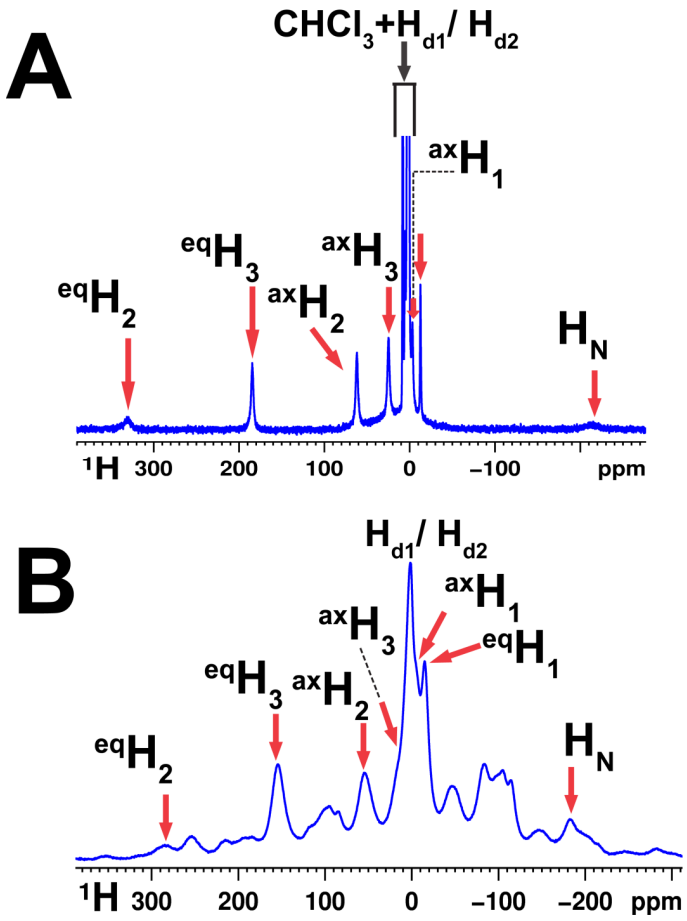

Figure 4.7.3: ^{1}H assignment in (B) solid state spectra of paramagnetic Ni-cyclam dichloride complex by comparing ^{1}H assignment in (A) solution state.

As done for Cu-cyclam complex, here too we have calculated the ^{1}H shifts in Ni-cyclam by DFT. Table 4.7.1 shows a comparison of ^{1}H shifts in solution- and solid-state with the shifts from DFT calculation in paramagnetic Ni-cyclam dichloride complex. The ^{1}H shifts from DFT are in good agreement with the ^{1}H shifts of all the seven signals from the solid state NMR.

Methods	^{1}H shifts in Ni-cyclamCl_2 [ppm]						
	$^{eq}H_2$	$^{eq}H_3$	$^{ax}H_2$	$^{ax}H_3$	$^{ax}H_1$	$^{eq}H_1$	H_N
Solids (330 K)	283	155	55	14	-5	-15	-182
Solution (300 K)	330	185	62	25	-4	-14	-215
DFT	258	149	53	18	-7	-14	-187

Table 4.7.1: Comparison of ^{1}H shifts from solid /solution NMR with shifts from DFT calculation

4.8 Ni-H distance measurement using anisotropy parameter Δ_{aniso} calculated by Herzfeld-Berger method in paramagnetic Ni-cyclam dichloride complex.

As explained in previous units the anisotropic part of pseudocontact interaction is relatively large in magnitude in Ni-cyclam compared to Cu-cyclam which is exhibited in terms of severe sidebands in ^{1}H Hahn-echo. On one hand this is serious hindrance to the assignment. On the other hand one can exploit this interaction in obtaining Ni-H distances by measuring anisotropic parameter Δ_{aniso} which is essentially the anisotropic part of the pseudocontact interaction (Δ_{PC}) in paramagnetic systems. For electron-nucleus dipolar interaction anisotropic parameter Δ_{aniso}

$$\Delta_{aniso} \approx \Delta_{PC} = \frac{4 g_e^2 \mu_0 \mu_B}{4\pi} \frac{S(S+1)}{3 k_B T} \frac{1}{r^3} \qquad \textbf{4.8.1}$$

where T is the temperature, k_B is Boltzmann's constant, B is the Bohr magneton, and g is the isotropic value of the electron g-tensor. By grouping all the physical constants we get,

$$\Delta_{PC} = \left(1.66 \times 10^{6}\right) \frac{S(S+1)}{3 k_B T} \frac{1}{r^3} \qquad \textbf{4.8.2}$$

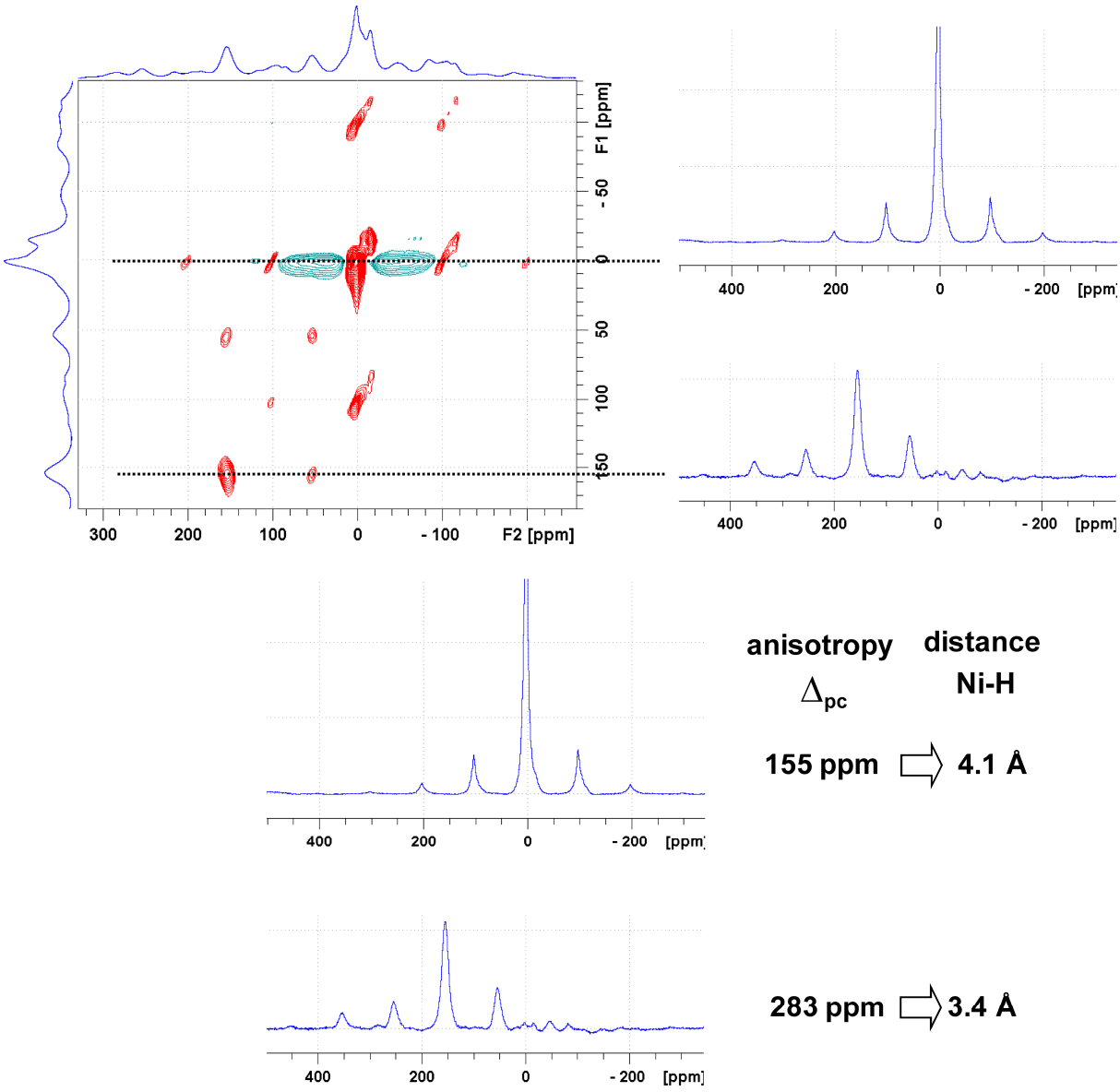

Figure 4.8.1: Extraction of ^{1}H sidebands from a pseudo 2D, to determine the anisotropy parameter Δ_{PC} and hence the Ni-H distances.

We have used a ^{1}H-^{1}H pseudo 2D spectrum to extract the spinning sidebands in order to separate spinning sideband pattern and for having good resolution (Figure 4.8.1). The patterns of $^{ax}H_3$ (14 ppm) and $^{eq}H_3$ (155 ppm) could be resolved without any perturbing overlap. The intensities of the sidebands were used to determine the anisotropy parameter Δ_{aniso} using the Herzfeld-Berger analysis. The anisotropy parameter Δ_{PC} was inserted into Equation 4.8.2 to extract Ni-H distance '*r*' in the paramagnetic Ni-cyclam dichloride complex. The anisotropy in the Ni-cyclam was about 155 ppm and 283 ppm for $^{ax}H_3$ and $^{eq}H_3$ respectively, corresponding to a Ni-H distance of 3.4 Å and 4.1 Å.

These distances were in good agreement with the distances from XRD (3.5 Å and 4.5 Å) reported by Ito *et al.*[76] and Bosnich *et al.*[74-75]

4.9 Metal-carbon distance measurement using solid state NMR relaxation rates in Cu-cyclam monochloride complex

In paramagnetic complexes the Fermi-contact interaction between unpaired electron(s) causes shifts and the dipolar interaction causes relaxation. The relaxation rates of nuclei close to a paramagnetic center depend in first approximation on the distance 'r' between nucleus and central atom and therefore in principle allow a measurement of this distance. According to the Solomon-Bloembergen-Morgan equation[50,88-89] the nuclear relaxation rates $R_{1,2}$

$$R_1 = \frac{2}{15}\left(\frac{\mu_0}{4\pi}\right)^2 \mu_B^2 g^2\gamma^2 S_e(S_e+1)\frac{1}{r^6}\left(\frac{3\tau_c}{1+\omega_n^2\tau_c^2}+\frac{7\tau_c}{1+\omega_e^2\tau_c^2}\right) \qquad \textbf{4.9.1}$$

$$R_2 = \frac{1}{15}\left(\frac{\mu_0}{4\pi}\right)^2 \mu_B^2 g^2\gamma^2 S_e(S_e+1)\frac{1}{r^6}\left(4\tau_c+\frac{3\tau_c}{1+\omega_n^2\tau_c^2}+\frac{13\tau_c}{1+\omega_e^2\tau_c^2}\right) \qquad \textbf{4.9.2}$$

are directly proportional to inverse of sixth power of metal-nucleus distance ($R_{1,2} \propto r^{-6}$) in a paramagnetic complex. Except 'r' and 'τ_c' all other terms are constant in Equation 4.9.1 and 4.9.2. The correlation time τ_c in the case of solids[176] is the electron relaxation time T^e which can be measured by electron paramagnetic resonance (EPR) spectroscopy. So here by knowing two experimental parameters i.e. nuclear relaxation rates $R_{1,2}$ and electron relaxation time T^e one can precisely measure the metal-nucleus (especially carbon) distance in a paramagnetic metal-organic complex. We know the copper-carbon distances from the X-ray diffraction and DFT calculations, and in the following we verify then by means of Equation 4.9.1 and 4.9.2.

To a first approximation we can have an idea of copper-carbon proximity by measuring the line widths of the four distinguishable ^{13}C signals in the ^{13}C Hahn-echo spectra of paramagnetic Cu-cyclam complex as shown in Figure 4.9.1 A. The line width of the ^{13}C signals directly provide the transverse relaxation rate R_2 (= $\pi *$ FWHH). The line width of C_1 (26 ppm) is 700 Hz which arises from the carbon at a distance (DFT) of 3.36 Å - 3.43 Å from Cu- center, similarly C_{2a} (-143 ppm)

and C_{2b} (-173 ppm) have 1-1.2 kHz arising from carbon at a distance of 2.99 Å - 3.08 Å and C_3 (-326 ppm) which experiences severe broadening of 3.5 kHz arises from the carbon which is at the closest distance of 2.85 Å - 2.89 Å. The DFT optimized copper-carbon distances ${}^{DFT}r_{Cu\text{-}C}$ of Cu-cyclam (see Figure 4.9.1 B) go as $C_1 > C_{2a} > C_{2b} > C_3$. The line widths of the respective carbon signals are in good agreement with the approximation. This motivated us to try measuring actual R_2 rates from solid state NMR experiment.

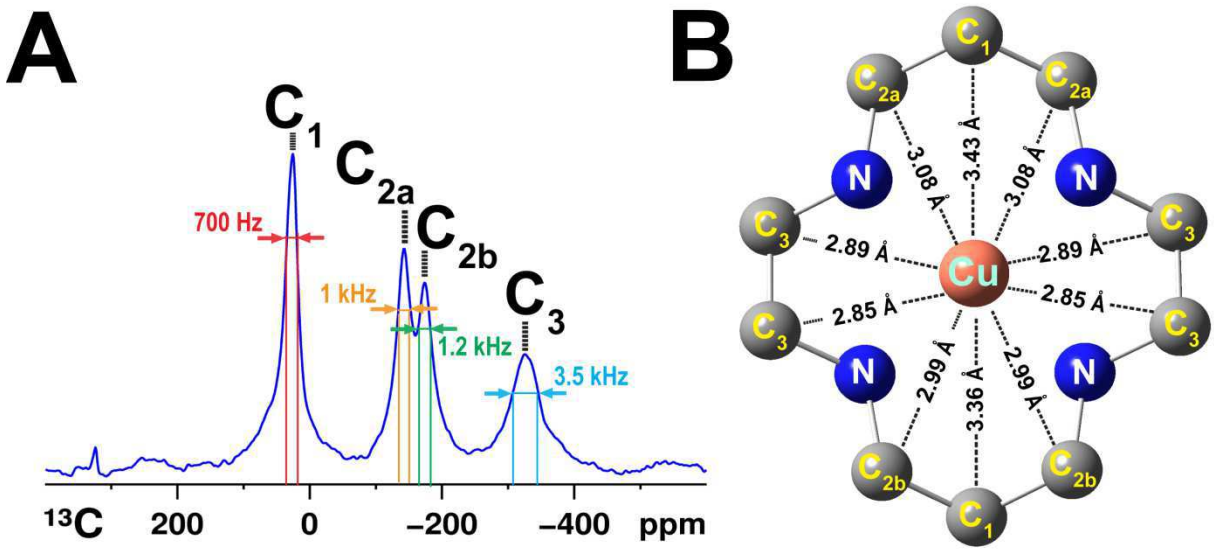

Figure 4.9.1: (A) Line widths of signals in ${}^{13}C$ Hahn echo spectra of paramagnetic Cu-cyclam monochloride complex. (B) Copper-carbon distance from DFT optimization in Cu-cyclam monochloride complex

We have used Carr-Purcell-Meiboom-Gill (CPMG)[91-92] pulse sequence to measure the transverse relaxation rates of the four distinguishable signals in ${}^{13}C$ Hahn-echo spectra. The CPMG pulse sequence shown in Figure 4.9.2 is a multiple spin-echo sequence. The pulse sequence starts with a excitation 90° pulse followed by τ_r-180-τ_r block which is repeated n times before the signal is acquired. The experiment is repeated with different values of n, and the decay of the signal intensities is determined. The signal intensity I_{xy} decreases with

$$I_{xy} = I_0\, e^{(-R_2 t)} \qquad \textbf{4.9.3}$$

where $t = n \times 2\tau_{echo}$. Only even values of n were used and the signals were acquired. Due to the low sensitivity of the signals the data processing was crucial. For larger n, the intensities could not be read out directly from the spectra for rates calculation without high experimental error. A fit

program written in MATLAB (*see* Appendix II) was used to extract intensities from the ^{13}C CPMG spectra. The peak positions and the line widths of the ^{13}C signals were determined by fitting the signals from a Hahn echo spectra with good signal to noise ratio (ns = 1024 K) to Lorentzian line shape.

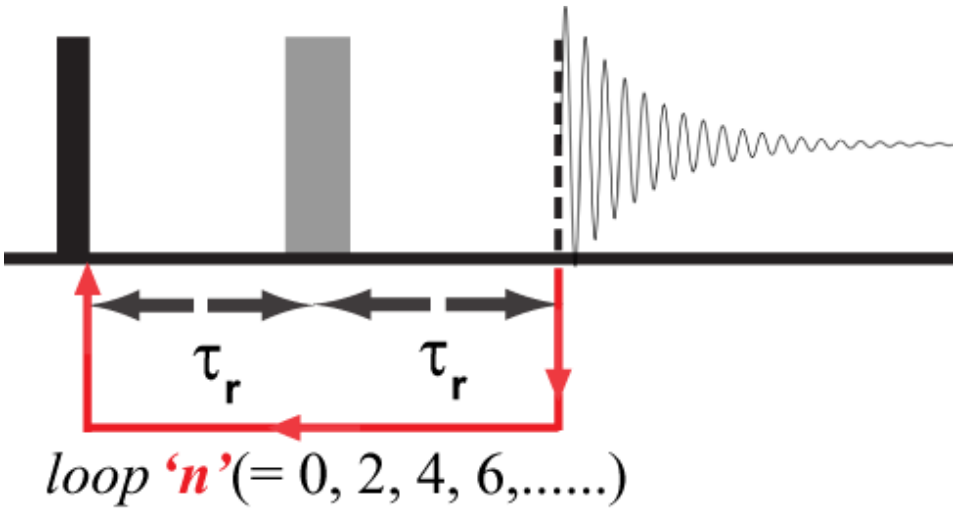

Figure 4.9.2: Carr-Purcell-Meiboom-Gill (CPMG) pulse sequence used for measuring transverse relaxation rate R_2.

Here rotor period τ_r = 33.33 μs

We had fixed peak position and line width of the signals, the only fit parameters remained were the intensities. These intensities which were obtained as output from the joint-fit program, are plotted as a function of CPMG delay T (= n×2×66.7 μs). Shown in Figure 4.9.3 are the decay curves of ^{13}C signals in paramagnetic Cu-cyclam monochloride complex. The experimental data points were fitted to the Equation 4.9.3 and the transverse relaxation rates of the ^{13}C signals were extracted.

In paramagnetic complexes the fluctuation of electron-nucleus dipolar interaction is the dominant source for nuclear relaxation. Apart from this several relaxation mechanisms such as Curie's relaxation, contact relaxation, relaxation due to chemical exchange can trigger the nuclear relaxation. Recently Kervern *et al.*[176] have shown that the Curie's relaxation is usually absent in paramagnetic solids. Furthermore contact relaxation mechanism only influences nucleus very close to paramagnetic centers such as the nitrogen donor atoms in Cu-cyclam complex and hence can be

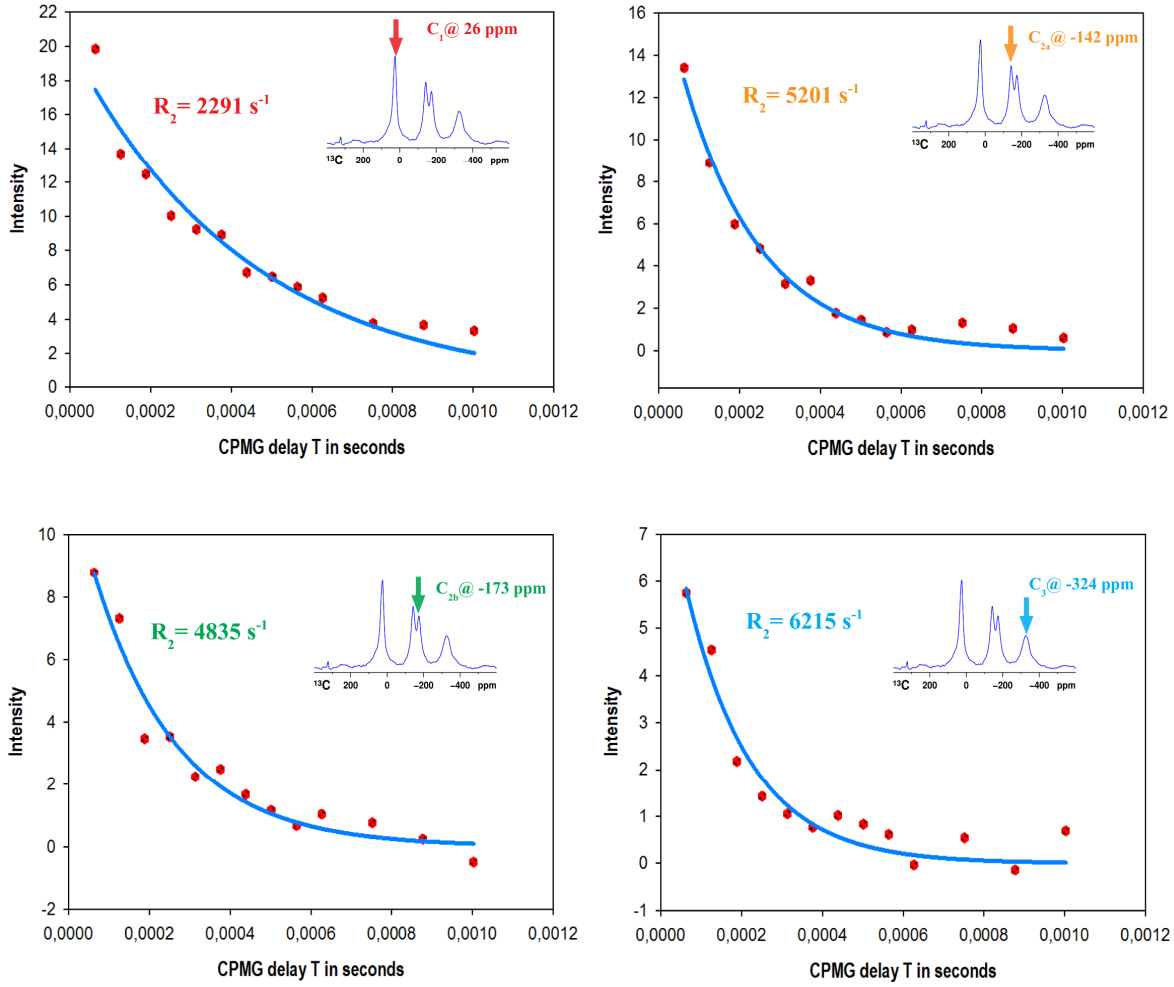

Figure 4.9.3: Plot of intensities (from MATLAB joint-fit output) versus the CPMG delay of ^{13}C signals in paramagnetic Cu-cyclam monochloride complex (red dots = experimental data and blue line = theoretical curve).

neglected in the case of carbon. The Cu-cyclam monochloride complex in solid form is a quite stable molecule and relaxation due to chemical exchange does not take place. Further the nuclear-nuclear dipolar relaxation has very small contribution. So here the dominant mechanism by which the ^{13}C nuclei can relax is due to the fluctuation of interaction caused by flipping of electron spin orientation described for the ensemble by the relaxation time,[50,177-178] $T^e_1 \approx T^e_2$.

In order to determine T^e, we use a room temperature solid state EPR experiment (*Courtesy:* Professor Abdelhadi Kassiba) for paramagnetic Cu-cyclam monochloride complex. Shown in Figure 4.9.4 is the first derivative EPR signal of paramagnetic Cu-cyclam monochloride complex.

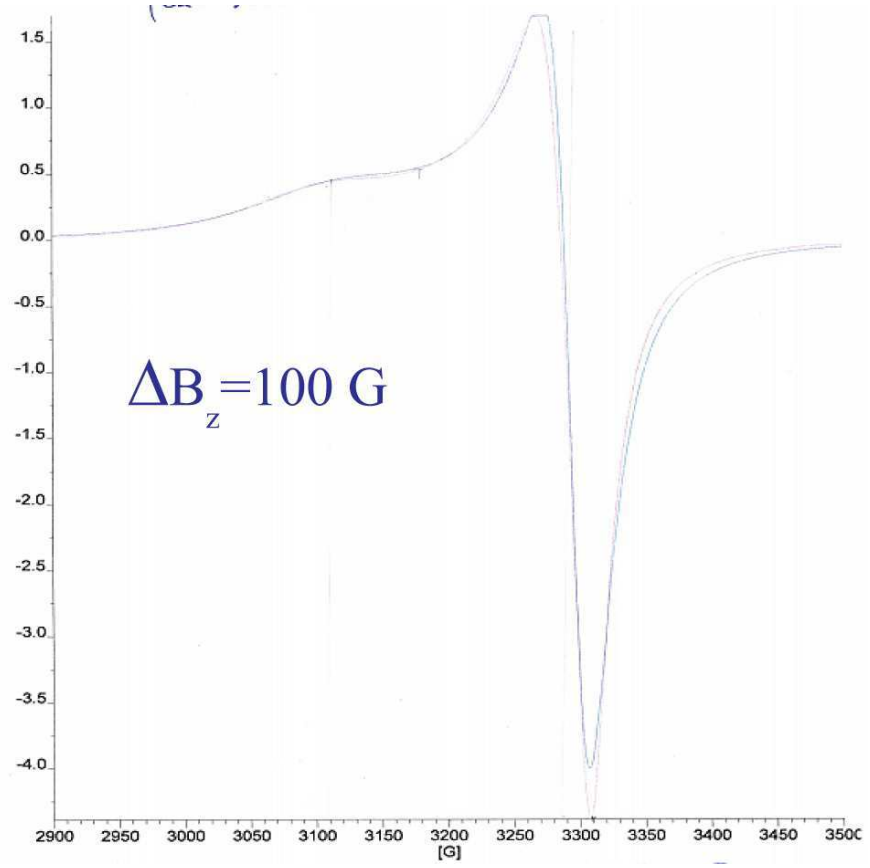

Figure 4.9.4: Solid state EPR spectra of paramagnetic Cu-cyclam monochloride complex recorded at room temperature. Line width ΔB = 100 G

The transverse relaxation rate of electron is given by[179]

$$(T_2^e)^{-1} = \frac{\sqrt{3}}{2}\frac{\mu_B}{\hbar}\hat{g}\,\Delta B \qquad \textbf{4.9.4}$$

We find ΔB = 100 G and the average Landé g factor,

$$\hat{g} = (g_{II} + 2g_{\perp})/3 = (2.180 + 2\times 2.055)/3 = 2.10 \qquad \textbf{4.9.5}$$

and thus $\tau_c \approx T^e_2$ = 0.6 ns. For the determination of the electronic relaxation times we have applied the simplest approach, which may in other cases not be appropriate: T^e_1 may not be approximated by T^e_2, and one might have to discriminate the dependence of R_2 on T^e_1 and T^e_2 in Equation 4.9.2 (see Eq. 3.17 in Ref. 174[178]). The electronic relaxation rate T^e_1 could be determined by power saturation techniques or, if a pulsed EPR spectrometer is available, a saturation recovery experiment. On the other hand there are arguments that T^e_2 alone represents the correct correlation time τ_c for the fluctuation of the dipolar interaction.[178] Furthermoremore, the EPR line width can contain other contributions than the actual relaxation T^e_2. Inhomogeneous broadening will certainly lead to a

misinterpretation, but homogeneous broadening effects will equally lead to nuclear spin relaxation. Wickramasinghe *et al.*[90] compare the electronic correlation time determined from nuclear relaxation with the coupling between the electronic spins of the metal centers of different molecular units rather than the actual T^e_2.

After subtraction of non-paramagnetic contribution of relaxation of estimated 100 Hz (mainly due to the ^{1}H-^{13}C dipolar interaction in CH_2) we obtain paramagnetic rates of the signal decays of 2000 s^{-1}-6000 s^{-1} as shown in Table 4.9.1. These rates along with electron correlation time τ_c (transverse electron relaxation time T^e_2) were inserted into Equation 4.9.2 to obtain copper-carbon distances of all the four carbon sites in paramagnetic Cu-cyclam monochloride complex.

Carbon sites	**^{13}C transverse relaxation rates from CPMG R_2 [s^{-1}]**	**Cu-carbon distances from solid state NMR rates r_{ssNMR} [Å]**	**Cu-carbon distances from XRD (Lu *et al.*)[67] r_{XRD} [Å]**
C_1	1990	3.42	3.34 / 3.35
C_{2a}	4540	2.98	2.99
C_{2b}	4900	2.94	3.01
C_3	5920	2.85	2.81 / 2.82

Table 4.9.1: Comparison of copper-carbon distances measured using solid state NMR and XRD

For the comparison with known distances we have used XRD distances of Cu-cyclam coordinating with isothiocyanato ligand of Lu *et al.*[67] since we have no XRD structure of the Cu-cyclam monochloride complex. Table 4.9.1 shows a comparison of copper-carbon distances measured using solid state NMR relaxation rates and the XRD distances of Cu-cyclam isothiocyanate complex by Lu *et al.*[67] We observe that the NMR relaxation distances match the XRD distances within a precision of 0.1 Å. The estimated experimental precision is in the same range. Figure 4.9.5 illustrates the final comparison of Cu-carbon distances measured using solid state NMR with XRD distances from the reference structure of Cu-cyclam isothiocyanate.

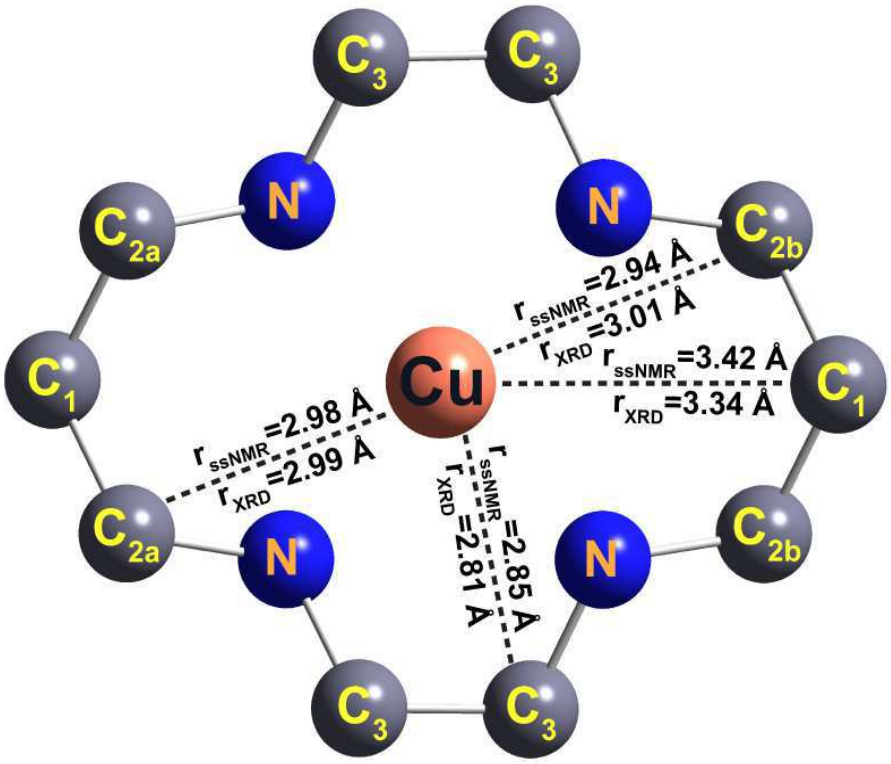

Figure 4.9.5: Comparison of copper-carbon distances measured using solid state NMR with XRD distances

The r^{-6} dependence of the relaxation rates implies both advantages and disadvantages for the measurement of distances. On the one hand it limits the range of application to a relatively thin shell the boundaries of which depend on the electronic spin and its relaxation properties. If the atom is too far, the nuclear relaxation is too weak compared to other relaxation contributions; if it is too close, the high R_2 implies extensive line broadening. If the signals are still detectable and

resolved, it will be preferable to determine the relaxation rate directly from the line width rather than by a CPMG experiment. Obviously, Cu(II) is one of the most appropriate paramagnetic centers for the described distance measurements, and for centers with higher spin and/or slower electronic relaxation rates the nuclear relaxation can be much faster.

On the other hand, the r^{-6} dependence allows for a relatively high precision of the distance, even if the relaxation rates themselves are affected by a poor S/N ratio and by other relaxation contributions which have to be estimated. The estimated precision of < 0.1 Å does not reach the level of X-ray diffraction or EXAFS, but compared to the latter technique the method has the advantage that the coordination shell is better resolved.

The specification of the experimental precision would have been better if there were an X-ray structure available. We have chosen Cu-cyclam coordinating isothiocyanate[67] for Table 4.9.1 because it is also five-coordinated and adopts the same square-pyramidal symmetry as found for Cu-cyclam coordinating Cl^- in DFT calculations. The Cu-C distances of Cu-cyclam coordinating $(ClO_4)_2$,[64] $CuCl_4$,[165] or Br_2[164] deviate maximally 0.15 Å from the tabulated X-ray distances, but in most cases not more than 0.02 Å. Our DFT calculations on Cu-cyclam(Cl) and those shown in Ref. 8 differ from these X-ray values by maximal 0.08 Å.[8]

We have determined these rates by means of saturation recovery and inversion recovery experiments. However, they are in the average about one order of magnitudes too low compared to the theory. The fact that the experimental rates are too low (rather than too high) obviously excludes the possibility that the discrepancy is due to additional relaxation contributions as internuclear dipolar or Fermi contact interaction. The latter is expected to be negligible anyway compared to the electron-dipolar relaxation.[50] Interestingly, the results appear to be consistent with the rates found by Wickramasinghe *et al.*[90] on $Cu(DL\text{-}Ala)_2$, a comparable system. The authors of this study did not directly determine the distances by Equation 4.9.1, but calibrated them with one single distance determined by X-ray diffraction. A reason for the unexpected low rates might be the approximation in defining '*r*' as the distance to the central atom rather than to the electron followed by integrating over the electron positions weighted by their probabilities. But also with this procedure one will expect that the corrected calculation will lead to higher rather than lower rates.

4.10 Conclusion

We have shown how to reach a nearly complete assignment of ^1H signals of Cu-cyclam by means of ^1H-^{13}C dipolar INEPT and a ^1H-^1H correlation experiment. Furthermoremore the general feasibility of a dipolar HSQC experiment is demonstrated. The bottleneck for the NMR analysis of paramagnetic systems is the need of DFT calculations for the prior assignment of the ^{13}C signals. The main result is the determination of metal-carbon distances with a precision of 0.1 Å by means of transverse relaxation (R_2) experiments. It remains to be understood why the more common R_1 experiment gives rates that are by far too low compared to the theory.

In the case of Ni-cyclam dichloride complex ^{13}C signals assignment was done using spin densities calculated by DFT. However the split in the upfield shifted ^{13}C signals could not be reproduced by DFT. Paramagnetic Ni-cyclam dichloride complex presents a case with two unpaired electrons (evident from MO calculation by DFT) in the system, i.e., the total electronic spin of the complex is one (S=1) and exhibits faster nuclear relaxation relative to Cu-cyclam complex (which is a spin ½ system). This caused serious problems in the ^{1}H-^{13}C 2D dipolar INEPT experiment of Ni-cyclam complex. Loss of coherence due to fast relaxation and overlap of sidebands made ^{1}H assignment impossible. The ^{1}H signals in Ni-cyclam complex could only be assigned by comparison with DFT calculation and solution state NMR. Furthermore we have shown how one can measure Ni-H distance using the anisotropic parameter in Ni-cyclam complex.

Chapter 5: Paramagnetic metal-acetylacetonate complexes

"At the heart of science is an essential balance between two seemingly contradictory attitudes: openness to new ideas, no matter how bizarre or counterintuitive they may be, and the most ruthless skeptical scrutiny of all ideas, old and new. This is how deep truths are winnowed from deep nonsense.

- Carl Sagan

5.1 Introduction

Metal-acetylacetonate complexes attract various fields of material chemistry due to their unusual properties.[180] Due to their fair solubility in some of the organic solvents they provide an easy means of carrying metal ions into some important classes of industrial materials such as rubbers, plastics, lubricant oils, gasoline etc. One of the important uses of these systems is that they are good catalysts. Especially they are recommended as catalysts for oxidation of hydrocarbons, for polymerization of unsaturated hydrocarbons and of silicone monomers.[181] Also their usage as drying agents in linseed oil and accelerators for vulcanization of rubbers illustrates the catalytic properties.[182] The utility of metal acetylacetonate complexes as combustion promoters in jet fuels is particularly noteworthy.[183] Metal acetylacetonate complexes with transition metal ions as metal centers exhibit paramagnetism. The *d*-block transition metal ions such as Cu^{2+}, Ni^{2+}, Cr^{3+}, VO^{2+}, Co^{2+} etc. bind to the acetyl acetone ligand to form stable paramagnetic metal-acetylacetonate complexes. Due to the presence of the unpaired electron(s) these complexes exhibit paramagnetic behavior. Some of these paramagnetic metal-acetylacetonate complexes are used as relaxation agent in magnetic resonance imaging (MRI).[184]

We have investigated some of these transition metal-acetylacetonate complexes that are paramagnetic using solid state NMR spectroscopy. The methodology established for paramagnetic metal-cyclam complexes using VFMAS technique in solid state NMR motivated us to make a test on paramagnetic metal-acetylacetonate complexes. Here in this unit we have investigated paramagnetic Cu(II)-, Ni(II)- and VO(IV)-acetylacetonate complexes using solid state NMR in combination with density functional theory (DFT) calculations.

In yesteryears there were some early attempts to interpret the ^{1}H NMR (solution state) spectra of paramagnetic transition metal-acetylacetonate complexes by Eaton *et al.*[185] The authors in reference No. 181[185] have performed thorough analysis of solution state NMR of some of the transition metal (Ti, Mo, Cr, V, Co, Fe, Ru and Mn)-acetylacetonate complexes. But have failed to observed in the case of Cu(II) and VO(IV)- acetylacetonate complexes due to sever shift from Fermi-contact interaction. However they have managed to make some conclusion concerning the metal-ligand interaction and the effect of it on NMR spectra along with primitive methods of molecular orbital calculations which is appreciable and very much of our interest.

Here in this chapter we apply the developed techniques in solid state NMR of paramagnetic metal-organic complexes to paramagnetic metal-acetylacetonate complexes. We show here the differences between the 1D ^{1}H and ^{13}C solid state NMR spectra of paramagnetic Copper-, Nickel- and Vanadyl-acetylacetonate complexes based on the coordination of metal-ligand, the geometry of the complex and the configuration of the unpaired electron molecular orbital. Later we assign the severely shifted (due to Fermi-contact interaction) ^{13}C spectra of the Copper and Vanadyl-acetylacetonate complexes using spin densities calculated using DFT calculation. Also we discuss some similarities and differences seen in the ^{13}C spectra of Copper and Vanadyl complexes due to their valence electronic configuration. Later we discuss the complexity observed in ^{13}C spectra of paramagnetic Nickel-acetylacetonate complex. The assignment of ^{1}H signals in Copper and Vanadyl complexes is performed using ^{1}H-^{13}C 2D dipolar INEPT spectra.

Our work mainly focuses on developing methods in solid sate NMR for paramagnetic metal-organics complexes in combination with quantum chemical methods. We have successfully accomplished this in the case of metal-cyclam complexes. In this chapter we apply the developed methods on different systems in terms of metal-ligand coordination with different donor atoms forming different geometry i.e. we have seen how one can apply this method on six coordinated octahedral and five coordinated square pyramidal complexes. Here we apply the solid state NMR method in combination with DFT calculation to square planar and square pyramidal type complexes of metal-acetylacetonate complexes that are paramagnetic.

5.1.1 Chemical structure, metal-ligand coordination and significance of paramagnetic Copper-, Nickel-, and Vanadyl-acetylacetonate complexes

Acetyl acetone is an organic compound which exists in two tautomeric forms (enol and keto) as shown in Figure 5.1.1. The most stable tautomer is a diketone formally named pentane-2,4-dione. This compound is the precursor to the acetylacetonate (acac), a common bidentate ligand. The acetylacetonate anion, $acac^-$, forms complexes with many transition metal ions. A general method of

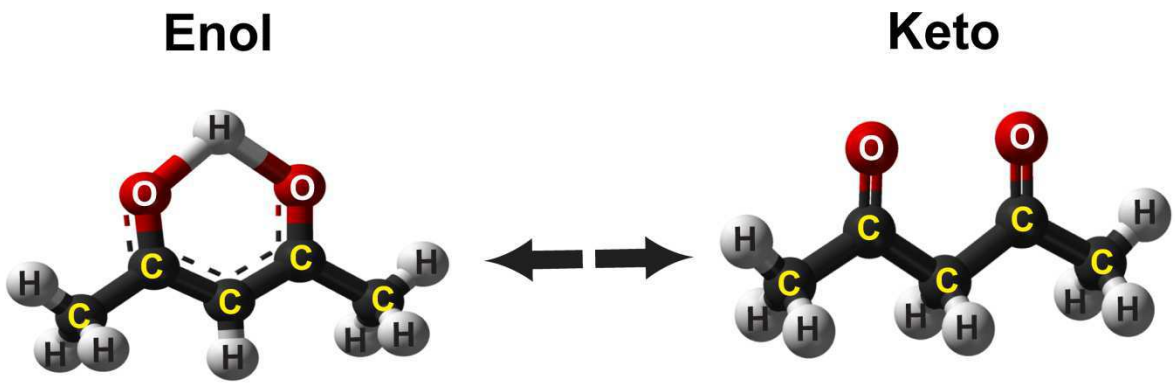

Figure 5.1.1: Tautomeric forms (Enol and Keto) of acetyl acetone (pentane-2,4-dione) compound

synthesis is to react the metal ion with acetyl acetone in the presence of a base (B) i.e.

$$M^{n+} + n\ (acacH) \leftrightarrow M(acac)_n + n\ BH^+ \qquad \textbf{5.1}$$

which assists the removal of a proton from acetyl acetone and shifts the equilibrium in favor of the complex. Both oxygen atoms bind to the metal to form a six-membered chelate ring. In some cases the chelate effect is so strong that no added base is needed to form the complex. Since the metal complex carries no electrical charge, it is soluble in non-polar organic solvents.

With *d*-block transition metal ions such as Cu^{2+}, Ni^{2+}, VO^{2+}, Cr^{3+}, Mn^{2+}, Co^{2+} etc. as metal center, the acac ligand forms stable paramagnetic metal-organic complex as shown in Figure 5.1.2. The geometry of the final complex depends on the type of coordination (metal coordination number). The paramagnetic-diamagnetic behavior exclusively depends on the geometry of the final complex. We have investigated Copper-, Nickel- and Vanadyl-acetylacetonate complexes which exhibit paramagnetism using solid state NMR in combination with DFT calculations.

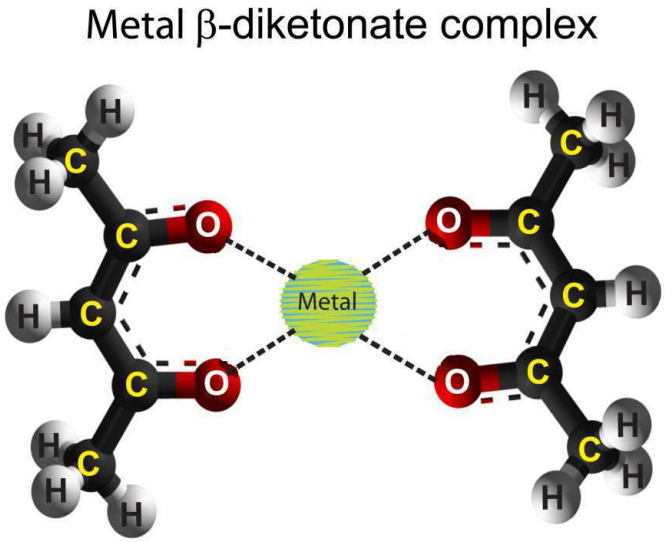

Figure 5.1.2: Structure of metal-acetylacetonate (metal- β-diketonate) complex

The paramagnetic metal-acetylacetonate complexes used in our investigation are Cu-acac, VO-acac and Ni-acac with four coordinate square-planar, five coordinate square-pyramidal, and six coordinated octahedral in geometry respectively. We have found XRD structures in literature for

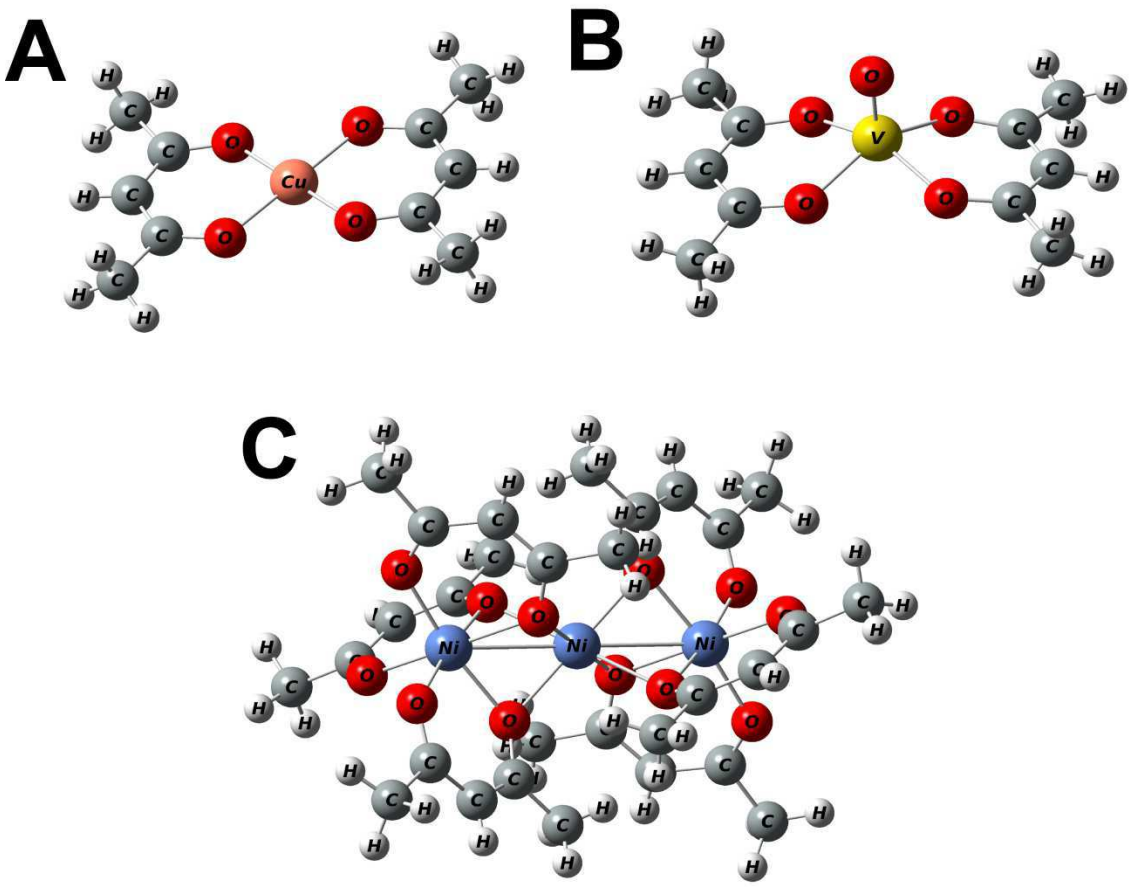

Figure 5.1.3: XRD structures of (A) $Cu(acac)_2$, (B) $VO(acac)_2$, and $Ni(acac)_2$

comparison of the distances and other structural information for $Cu(acac)_2$,[186-189] $VO(acac)_2$,[190-191] and $Ni(acac)_2$.[192-193] Figure 5.1.3 demonstrates the XRD crystal structure of (A) $Cu(acac)_2$ from Berry *et al.*,[189] (B) $VO(acac)_2$ from Hon *et al.*,[194] and (C) $Ni(acac)_2$ from Bullen *et al.*[192]

As explained in the previous chapter the final geometry of the metal-ligand coordination decides the paramagnetic-diamagnetic behavior of the paramagnetic metal-organic complexes. From crystal and ligand field theory it is seen that in case of transition metal-complexes the *d*-orbital degeneracy are lifted by the electrostatic interaction of the strong field ligand with the metal cation. Figure 5.1.4 shows the energy level separation of the five *d*-orbitals in transition metals when encountered with strong field ligand forming four coordinated square planar, five coordinated square pyramidal and six coordinated octahedral type of complexes.

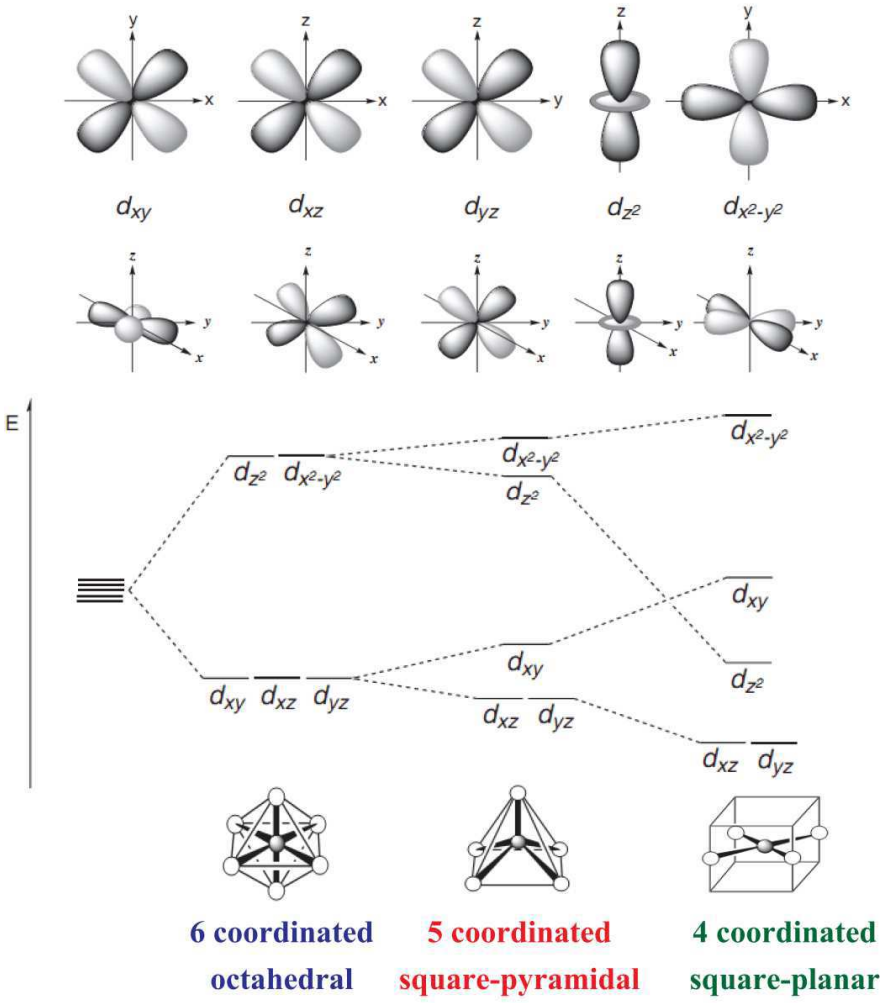

Figure 5.1.4: Energy levels of five *d*-orbitals of transition metals in four-, five- and six- coordinated metal-complexes

The location of unpaired electron in the transition metal ion d-orbital is crucial to understand paramagnetic behavior exhibited by these metal-organic complexes. Also it is our firm interest to understand since the unpaired electron spin density distribution over the molecule directly influences the ^{1}H and ^{13}C solid state NMR spectra through large hyperfine shifts (Fermi-contact shifts). As performed previously for the paramagnetic metal-cyclam complexes we calculate these spin density by DFT calculation. Later we also perform molecular orbital analysis to understand the unpaired electron molecular orbital in paramagnetic Cu- and VO-acetylacetonate complexes

5.1.2 One dimensional ^{1}H and ^{13}C NMR of diamagnetic acetyl acetone ligand and metal-acetylacetonate complex.

The total NMR shift of particular nuclei in any paramagnetic metal-organic complex is a sum of diamagnetic and paramagnetic part. The diamagnetic part of NMR shift contains information of chemical groups present in the organic arm of the metal-organic complex and is severely masked by the large hyperfine shifts (especially Fermi-contact shifts) in a paramagnetic complex. During our investigation of paramagnetic metal-acetylacetonate complexes using solid state NMR it was necessary to have an idea of ^{1}H and ^{13}C chemical shift range in a diamagnetic system. So here we show the one dimensional ^{1}H and ^{13}C NMR (in solution and solids) of acetyl acetone ligand and Zinc-acetylacetonate complex (diamagnetic) found in database and some literature.

As seen before in unit 5.1.1 the acetyl acetone compound exhibits two tautomeric forms, evidently ^{1}H and ^{13}C NMR (solution) which are shown in Figure 5.1.5 A and B depicts the presence of enol and keto forms. The ^{1}H NMR (in $CDCl_3$) on acac compound shows (**a**) methine group C-^{1}H at 5.5 ppm in enol form, (**c**) C-$^{1}H_2$ at 3.6 ppm in keto form and methyl protons C-$^{1}H_3$ are found at (**d**) 2.2 ppm in keto and (**e**) 2 ppm in enol forms. Furthermore in ^{13}C NMR the methyl group ^{13}C-H_3 is found at (**3**) 31 ppm in keto form and (**6**) 25 ppm in enol form, methine group ^{13}C-H in enol form at (**2**) 59 ppm, ^{13}C-H_2 in keto form at (**5**) 100 ppm and carbonyl group ^{13}C=O at (**1**) 202 ppm and (**4**) 191 ppm in keto and enol form respectively We compared the ^{13}C solution state NMR shifts from database (see Figure 5.1.5 B) with the solid state ^{13}C CPMAS data of acac in Al_2O_3 by Claramunt *et al.*[195] shown in Figure 5.1.6 and found that the shifts were quite reasonably in match.

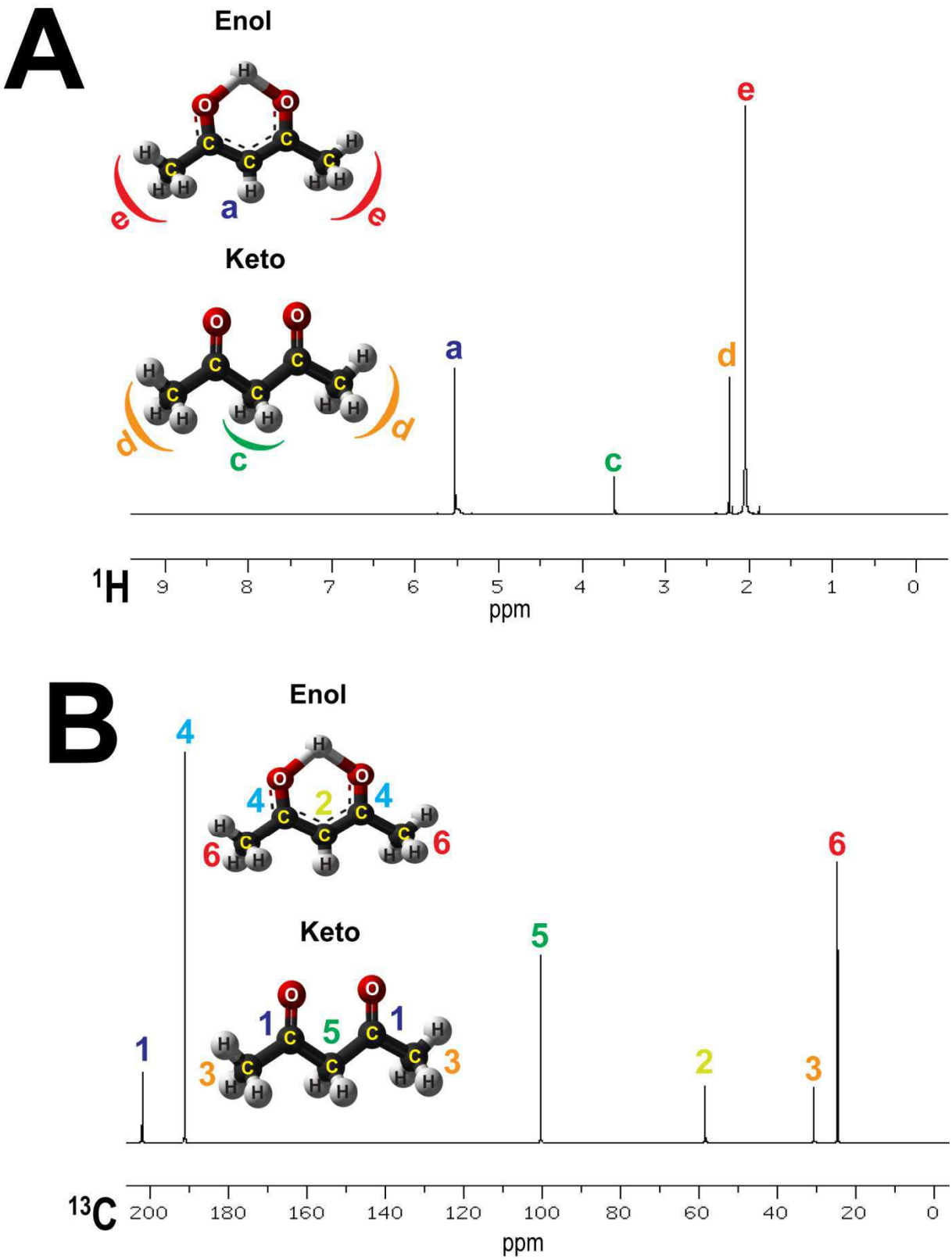

Figure 5.1.5: Solution state 1D (A) ^{1}H and (B) ^{13}C NMR spectra of acetyl acetone compound in $CDCl_3$ (from Japanese NMR database SDBS No: ^{1}H NMR: 1030HSP-46-239, ^{13}C NMR: 1030CDS-04-041)

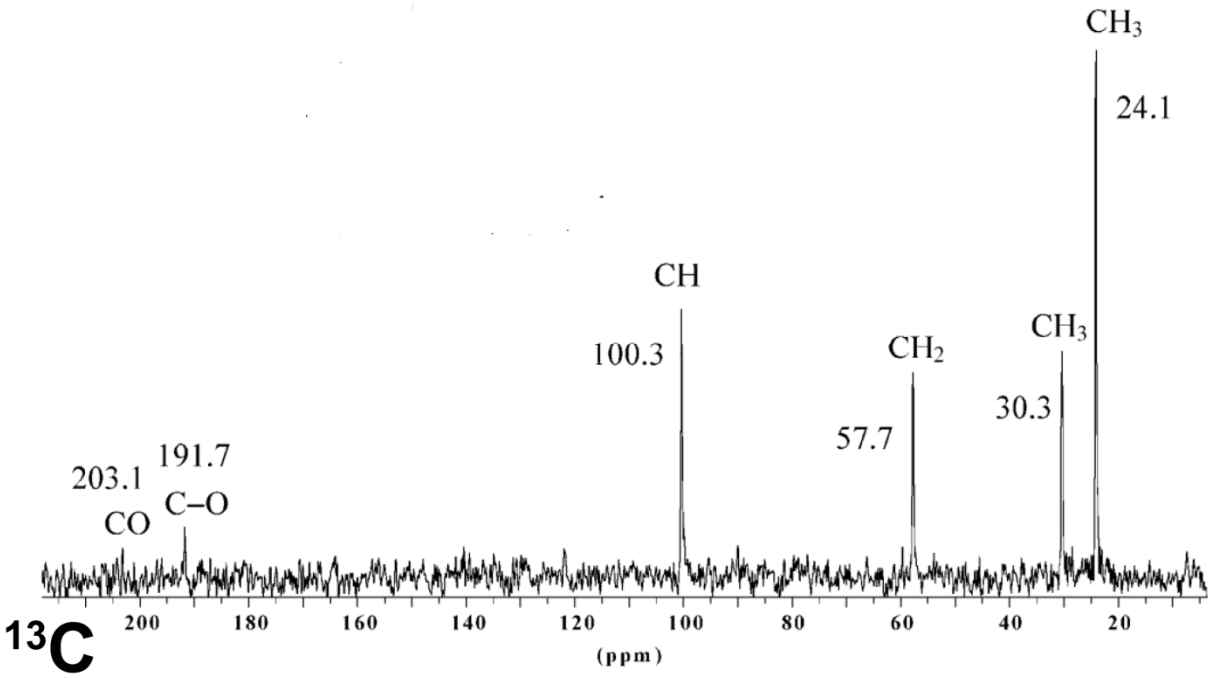

Figure 5.1.6: 1D ^{13}C CPMAS spectra of acetyl acetone compound in Al_2O_3 matrix from Claramunt *et al.*[195]

Since our investigation on paramagnetic metal-acetylacetonate complexes have no complication of tautomerization of acetylacetonate ligand the keto and enol forms seen through NMR chemical shifts was not so much crucial. Nevertheless we compared these shifts (especially the data of ^{13}C CPMAS spectra of Claramunt *et al.*) with the ^{13}C shifts in ^{13}C CPMAS spectra of diamagnetic Zinc-acetylacetonate (trimer) complex by Takegoshi *et al.*[196] and found that the shifts were quite consistent there too (carbonyl carbon $^{13}C{=}O$ at 188-199 ppm, methine carbon ^{13}C-H at 99-103 ppm and methyl carbon ^{13}C-H_3 at 27-30 ppm).

5.2 One dimension ^{1}H and ^{13}C solid state NMR studies of paramagnetic metal-acetylacetonate complexes

Investigation of solid state NMR of paramagnetic metal-acetylacetonate complexes were done by one dimensional ^{1}H and ^{13}C studies. The solid state NMR methodology established on paramagnetic metal-cyclam complexes were implemented on paramagnetic metal-acetylacetonate complexes. The very fast MAS (VFMAS 30 kHz) technique was used here in acquiring 1D ^{1}H and ^{13}C Hahn-echo for paramagnetic Copper-, Vanadyl- and Nickel-acetylacetonate complexes. Here in this unit we

understand the range of ^{1}H and ^{13}C shifts in paramagnetic metal-acetylacetonate complexes through one dimensional solid state NMR studies.

5.2.1 Comparative studies of one dimension ^{1}H and ^{13}C solid state NMR in copper-, nickel-, and vanadyl-acetylacetonate complexes

Figure 5.2.1 demonstrates 1D (A) ^{1}H and (B) ^{13}C spectra of paramagnetic Copper-, Vanadyl-, and Nickel-acetylacetonate complex. Two signals of methyl and methine group are expected in ^{1}H Hahn

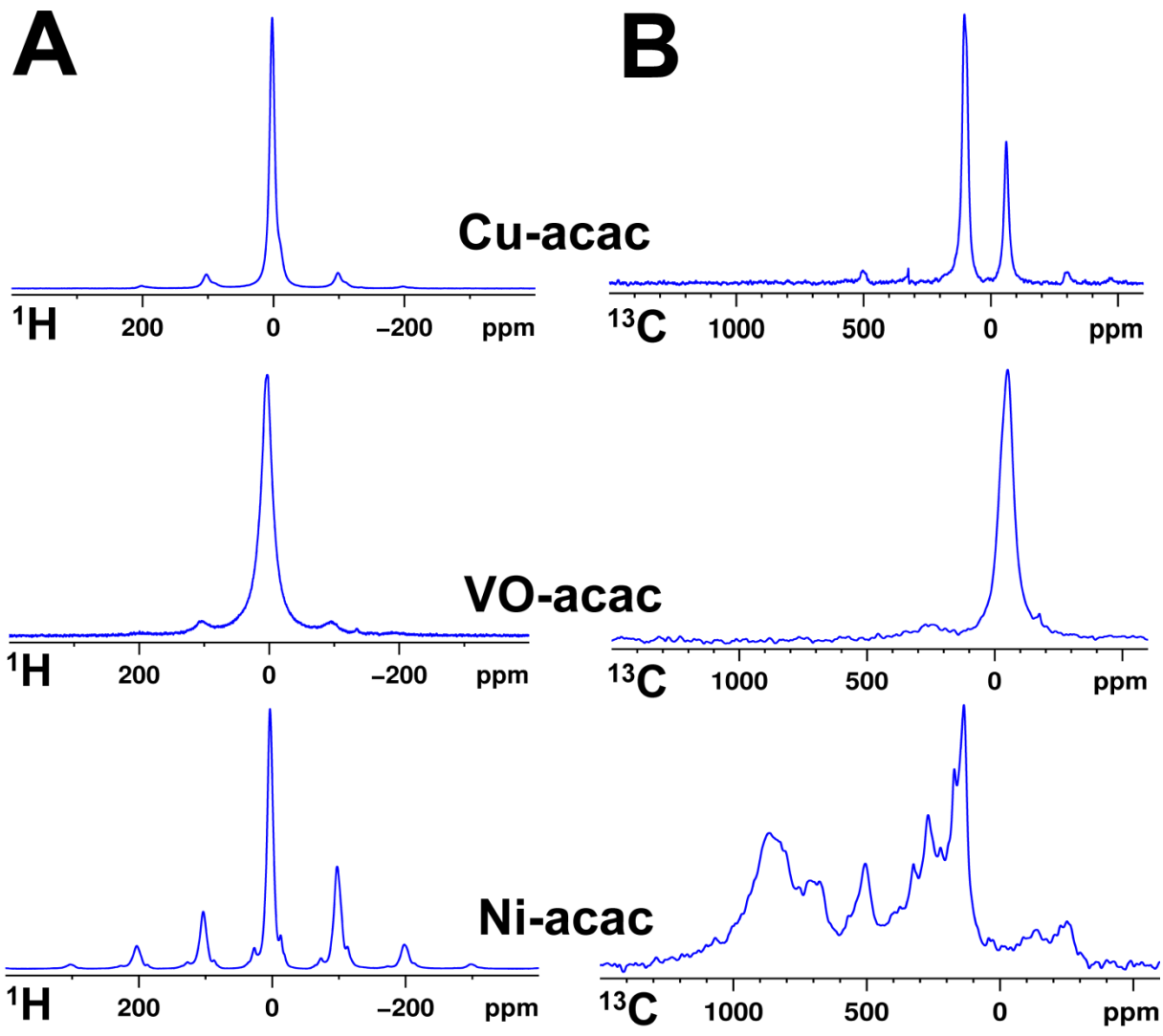

Figure 5.2.1: (A) ^{1}H and (B) ^{13}C Hahn-echo spectra of paramagnetic Cu-, VO-, and Ni-acetylacetonate complexes

-echo spectra whereas three signals of methyl, carbonyl and methine group are expected in ^{13}C Hahn echo spectra of paramagnetic metal-acetylacetonate complexes. The ^{1}H Hahn-echo of Cu-acac shows two signals: a sharp intense signal in the diamagnetic range (2.2 ppm) and an upfield shifted

broad peak at -10 ppm which is 7 times less intense than the sharp peak and is submerged at the foot of the sharp peak. Similarly in ^{13}C Hahn-echo spectra of Cu-acac two signals are seen, one in the diamagnetic region at 100 ppm and another peak at -61 ppm which is up field shifted. The up field shifted peak is twice less intense compared to the peak at 100 ppm, also the peak at 100 ppm seems to have more than one signal and hence looks quite broad compared to up field shifted peak.

In the case of ^{1}H Hahn-echo of VO-acac complex we observed a single signal at 4.3 ppm which is in diamagnetic range but severely broadened. The ^{13}C Hahn-echo shows two signals; one at 350 ppm which is severely broadened and is almost in the noise level (was identifiable with a strong exponential window function). Another signal is found at -65 ppm which is also severely broadened but is almost 6 times intense than the downfield shifted signal. Here too the upfield shifted ^{13}C signal at -65 ppm seems to have more than one signal similar to one seen in Cu-acac complex.

The ^{1}H and ^{13}C Hahn-echo spectra of Ni-acac in contrast show too many signals spread over -10 to +30 ppm and -100 to 1500 ppm respectively with lot of sidebands overlapping the signals and hence it is complex to understand. A lot more sidebands are seen in ^{1}H and ^{13}C Hahn-echo of Ni-acac as compared to Hahn-echo spectra of Cu- and VO-acac complex. This is quite obvious due to the fact that the hyperfine interaction in Ni-acac complex exhibits stronger anisotropy due to the presence of two unpaired electrons relative to Cu- and VO-acac system which have one unpaired electron in the valence shell of metal ion (Cu^{2+}- d^9, VO^{2+}- d^1). Furthermore the ^{13}C Hahn-echo spectrum exhibits larger spectral dispersion of almost 1600 ppm relative to Cu-acac (300 ppm) and VO-acac (700 ppm) complex. The complexity seen in ^{13}C Hahn-echo spectra of Ni-acac may be attributed to the formation of Ni-acac trimers i.e. $[Ni(acac)_2]_3$ in solid state as reported by Bullen *et al.* from X-ray crystallographic studies.[192,197]

The one dimensional ^{1}H and ^{13}C Hahn-echo spectra of paramagnetic Cu-, VO- and Ni-acac complexes clearly show strong features of hyperfine interaction through large shifts (Fermi-contact) and signal broadening. The assignment of these signals with conventional techniques is impossible. We proceed with DFT calculation in order to obtain unpaired electron spin density for assignment of ^{13}C signals as performed on paramagnetic metal-cyclam complexes.

5.3 Assignment of ^{13}C signals using spin densities calculated by DFT calculation in paramagnetic copper- and vanadyl-acetylacetonate complexes

In this unit we show some results of DFT analysis of paramagnetic metal-acetylacetonate complexes and thereby use the DFT results to assign ^{13}C signals in solid state NMR Hahn-echo spectra of paramagnetic metal-acetylacetonate complexes. As seen in last unit large Fermi-contact shifts in paramagnetic metal-acetylacetonate complexes mask the ^{1}H and ^{13}C diamagnetic chemical shift which is rich in chemical group information. Fermi contact shifts are characteristics of unpaired electron spin density. If one has the idea of these spin densities then one can calculate the Fermi contact shifts from Equation 2.7.22. We have used the same methods in DFT analysis on paramagnetic metal-acetylacetonate complexes as done on paramagnetic metal-cyclam complex.

Due to severe complex structure exhibited by Ni-acac complex (evidently seen in ^{13}C Hahn-echo spectra), we have chosen only Cu- and VO-acac for the DFT analysis. Both Cu- and VO-acac complexes are paramagnetic with electronic spin ½ system (S = ½). But the unpaired molecular orbital configuration is different due to the electronic configuration of the Cu- and VO metal ions and different geometry exhibited by the complex. This directly influences the unpaired electron spin density distribution on the molecule and hence ^{1}H and ^{13}C NMR shifts. We have investigated this by molecular orbital analysis using DFT calculation in this unit.

5.3.1 Geometry optimization, vibration frequency and molecular orbital analysis of paramagnetic Copper-acetylacetonate complex

Geometry optimization of the Cu-acac complex was done using B3LYP potential with unrestricted mode in GAUSSIAN 09. The structure of Cu-acac was constructed using GAUSSVIEW 5.0 and the optimization job was tested (command *#P opt ub3lyp/6-311G*).

Since the optimization of Cu-acac with 6-311G basis set failed to reach single point (evidently seen as negative vibration frequency modes in the results of frequency calculation) we made changes in selecting basis sets. We have found some examples in literature for geometry optimization of transition metal complexes such as works of Bühl *et al.*[145] and Kervern *et al.*[61] We have used

Wachters-f basis set on heavy atom i.e. Cu, 6-31G(d) on hydrogen atoms and 6-311G(d) on rest of the atoms. After optimization, the structure was checked for negative vibration frequencies (evidence for transition states or false energy minima) by running a FREQ job with the same level of theory and basis sets described for optimization, and we found no negative frequencies.

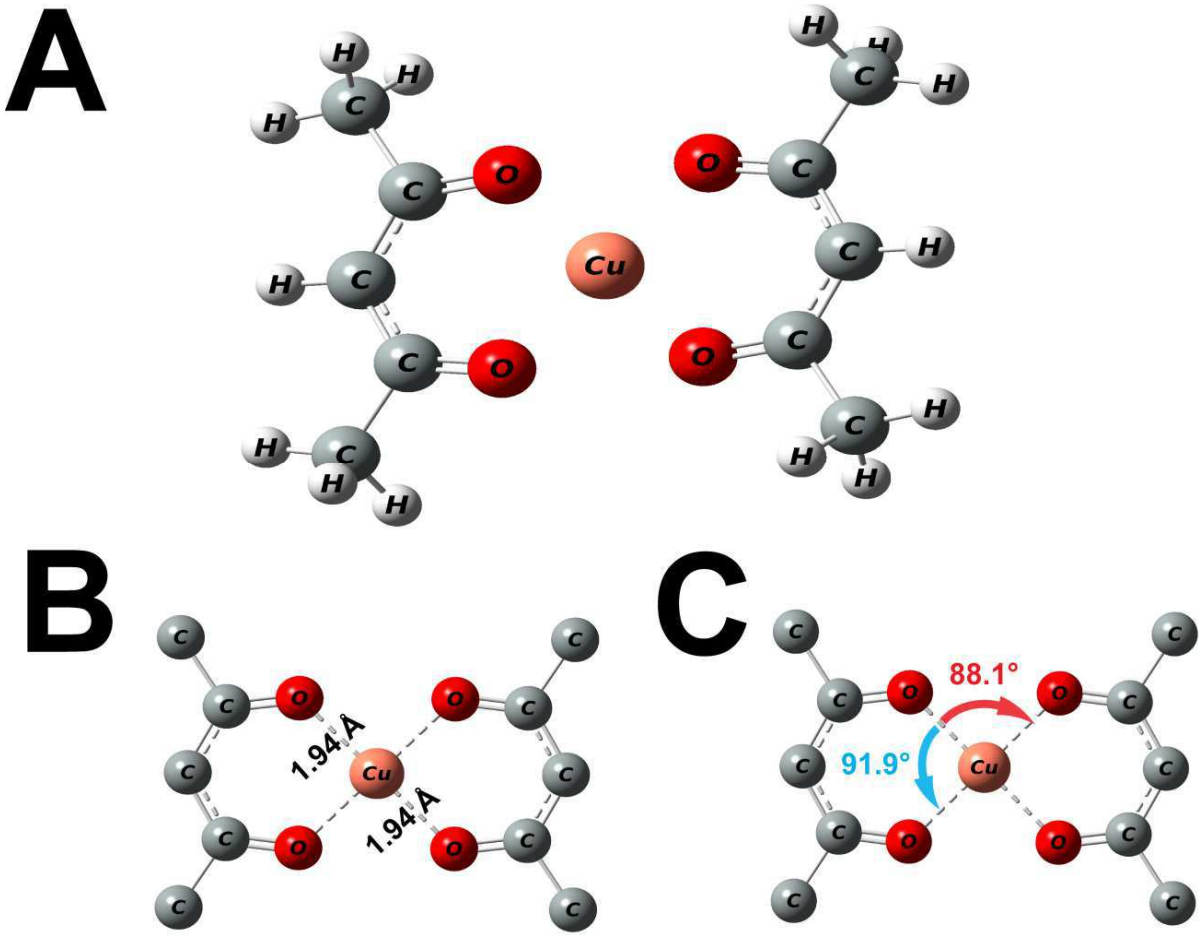

Figure 5.3.1: (A) DFT optimized Copper-acetylacetonate structure with (B) Cu-O bond distance and (C) O-Cu-O bond angles.

We have compared the structural parameters such as O-Cu-O bond angle and Cu-O bond distances of Cu-acac with the four reference structures from XRD of Cu-acac i.e. Lingafelter *et al.*,[198] Starikova *et al.*,[187] Lebrun *et al.*,[188] and Berry *et al.* [189] found in the literature. Table 5.3.1 shows the comparison of the bond angles and bond distances in DFT optimized Cu-acac structure with the XRD data from the references. The DFT bond angle and bond distances of Cu-acac are in good agreement (with 2° and 0.2 Å precision) with the experimental XRD data.

Bond distance and bond angle	DFT data of Cu-(acac)$_2$	X-ray data of the Cu-(acac)$_2$ complex			
		Lingafelter *et al.*[186]	Starikova *et al.*[187]	LeBrun *et al.*[188]	Berry *et al.*[189]
Cu-O	1.942	1.92	1.91	1.912	1.945
Cu-O`	1.942	1.92	1.93	1.914	1.945
O-Cu-O`	91.9	93.6	95	93.2	93.0

Table 5.3.1: Comparison of Cu-O bond distance and O-Cu-O` bond angle from DFT optimized Cu-(acac)$_2$ structure with the XRD data of Cu-(acac)$_2$ from literature.

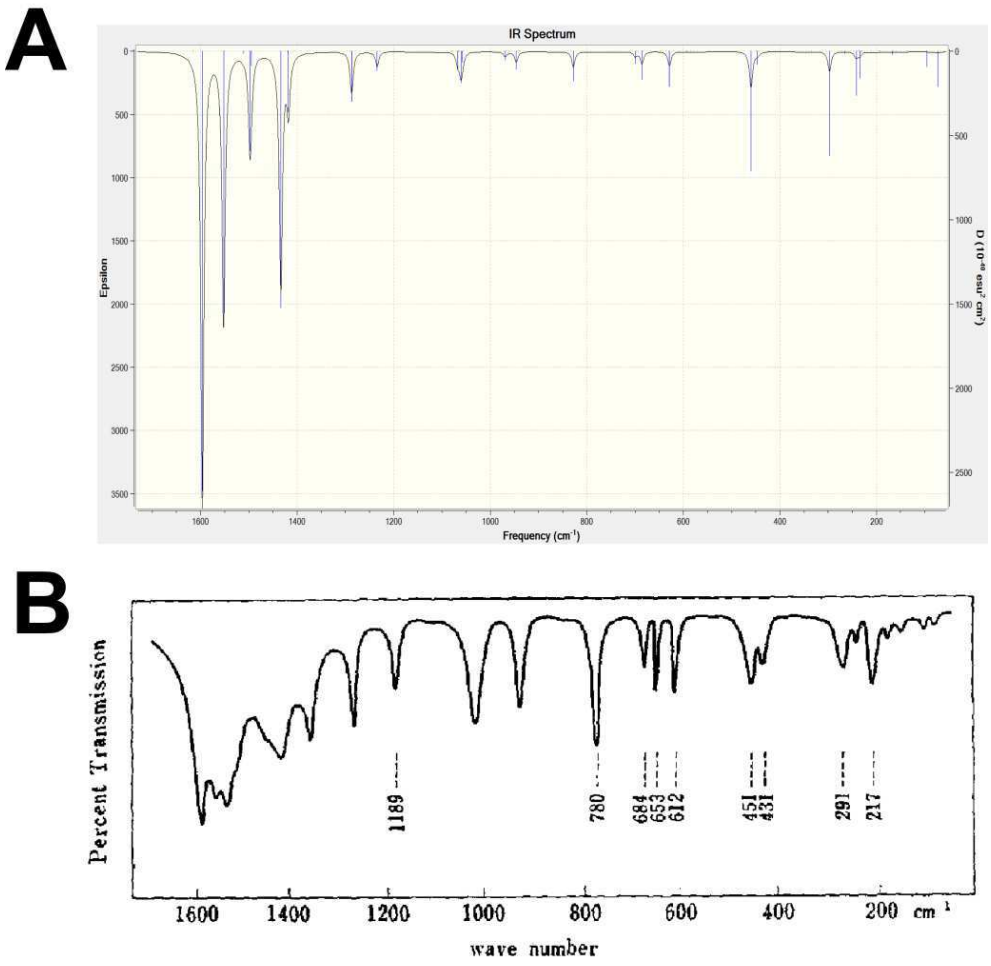

Figure 5.3.2: Comparison of (A) DFT generated IR spectra with the (B) experimental IR spectra[199] of paramagnetic Cu[acac]$_2$ complex.

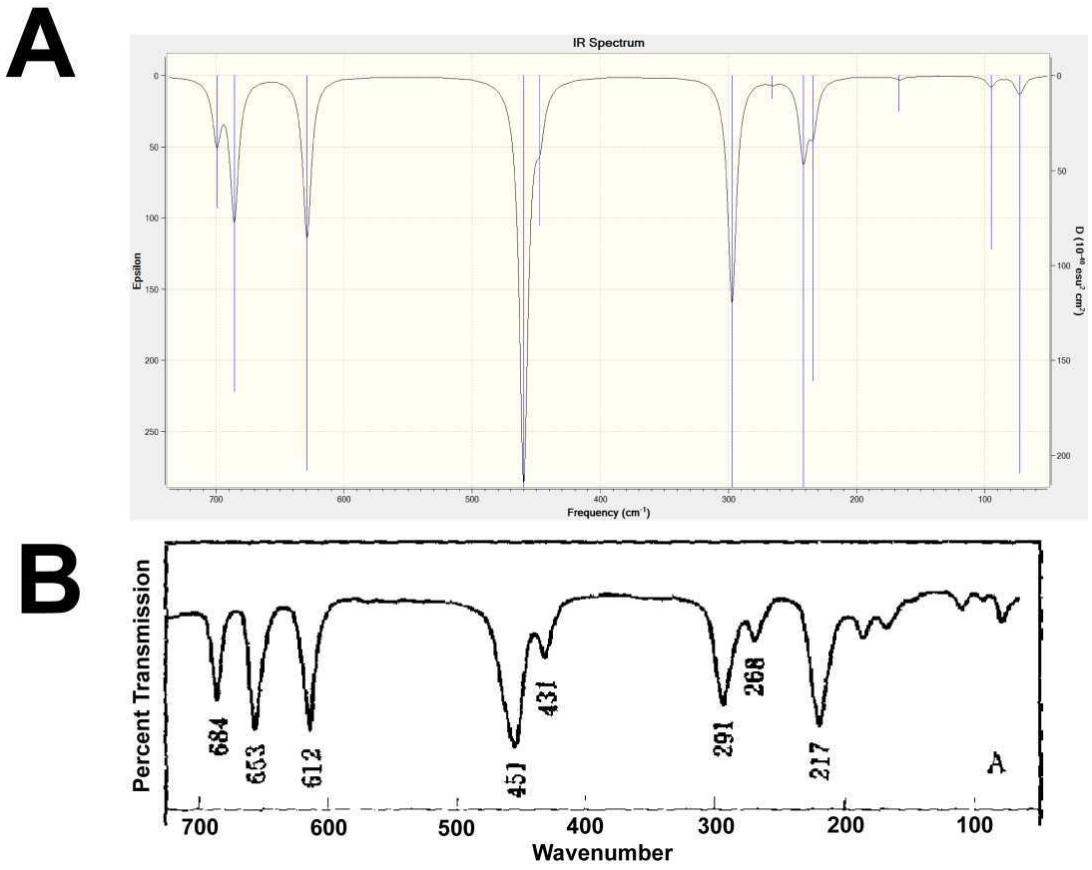

Figure 5.3.3: Comparison of (A) DFT generated IR spectra with the (B) experimental IR[199] of paramagnetic $Cu[acac]_2$ complex in the Far-IR region (100-700 cm^{-1}).

Figure 5.3.2 shows a comparison of DFT generated IR spectra with experimental IR spectra of paramagnetic Cu-acac complex from Mikami *et al.*[199] The significant IR frequency range of 200 cm^{-1} to 1600 cm^{-1} is compared and it is seen that our DFT generated IR is in well agreement with the experiment IR spectra of Cu-acac from Mikami *et al.*[199]

Mikami *et al.*[199] have performed a vibration frequency analysis on transition metal acetylacetonate complexes. The two intense bands at 1577 and 1529 cm^{-1} are assigned to C=O and C-C stretching modes of the chelate rings. These two frequencies are sensitive to the central metal ion and are subject of discussion on the coordination of the metal with the oxygen (ligand donor atoms). Figure 5.3.4 shows DFT analysis of these two vibration bands in paramagnetic Cu-acac complexes i.e. (A) C=O stretching mode at 1596 cm^{-1} and (B) C-C stretching mode at 1552 cm^{-1} which are in

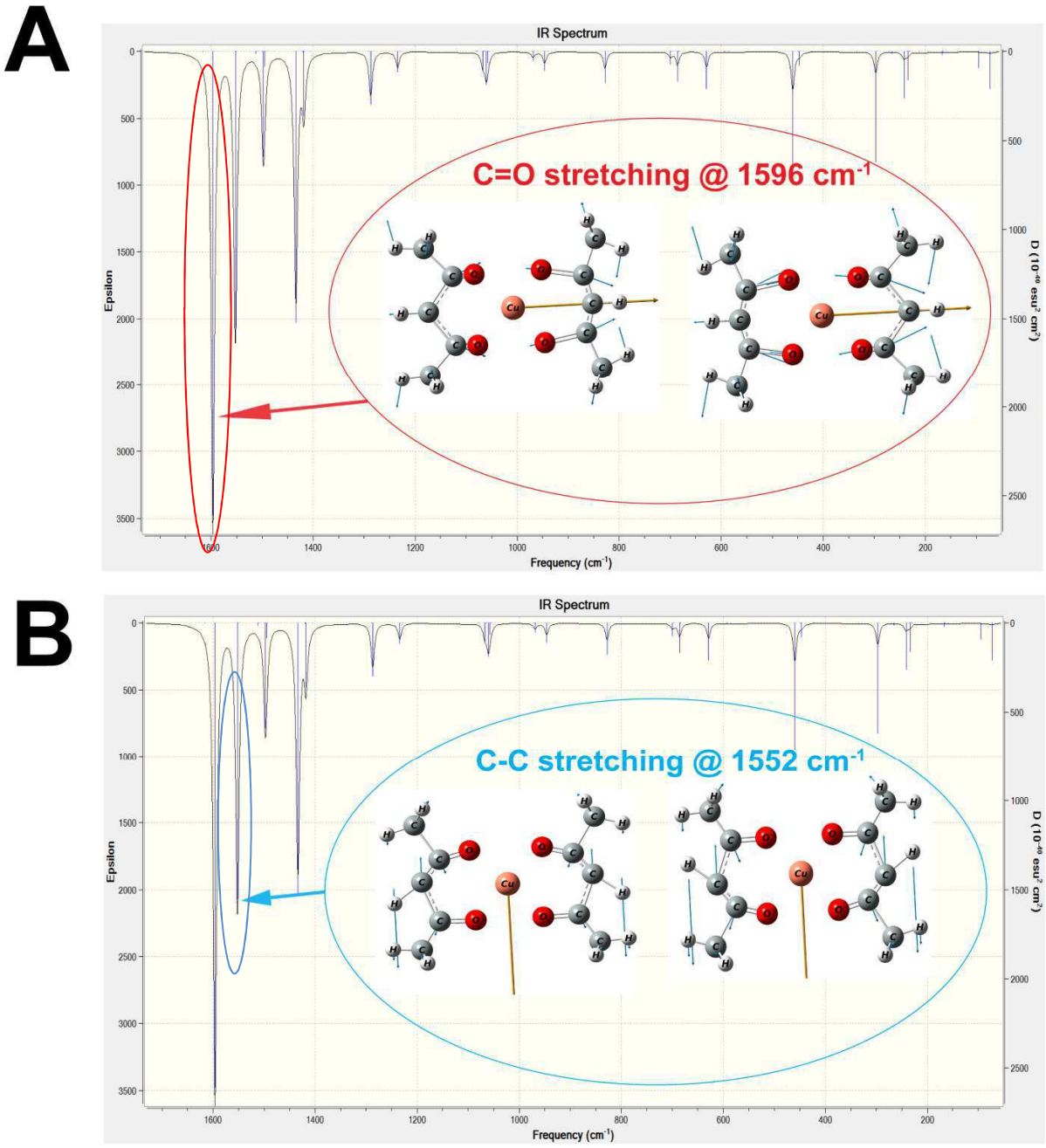

Figure 5.3.4: Two prominent IR frequencies: (A) 1596 cm^{-1} assigned to C=O stretching (see vector representation in the inlet) and (B) 1552 cm^{-1} assigned to C-C stretching (see vector representation in the inlet) are from C-C and C-O stretching in the chelate ring. (expt. IR spectra reported by Mikami *et al.*[199])

good agreement with the assignment of experimental IR bands (1577 and 1529 cm^{-1}) by Mikami *et al.*[199] The inlet of Figure 5.3.4 A and B shows animation snapshot of C=O and C-C stretching modes (from GAUSSVIEW 5 program) respectively in the chelate ring confirming the experimental IR results of Mikami *et al.*[199] The above analysis confirms that the DFT optimized structure of Cu-acac complex is stable and can be safely used for any other property calculation using DFT methods.

We used the DFT optimized Cu-acac structure to perform molecular orbital (MO) analysis to understand the unpaired electron spin density distribution over the molecule. The optimized structure of Cu-acac was subject to full population analysis in GAUSSIAN 09 using the same level of theory and basis set. The output of the population analysis was analyzed using CHEMCRAFT program. Figure 5.3.5 A shows contour plot of unpaired electron spin density with contour levels ranging from +0.00055 au (blue) to -0.00055 au (red) in paramagnetic Cu-acac complex calculated using DFT method. Furthermore the total alpha molecular orbitals were subtracted

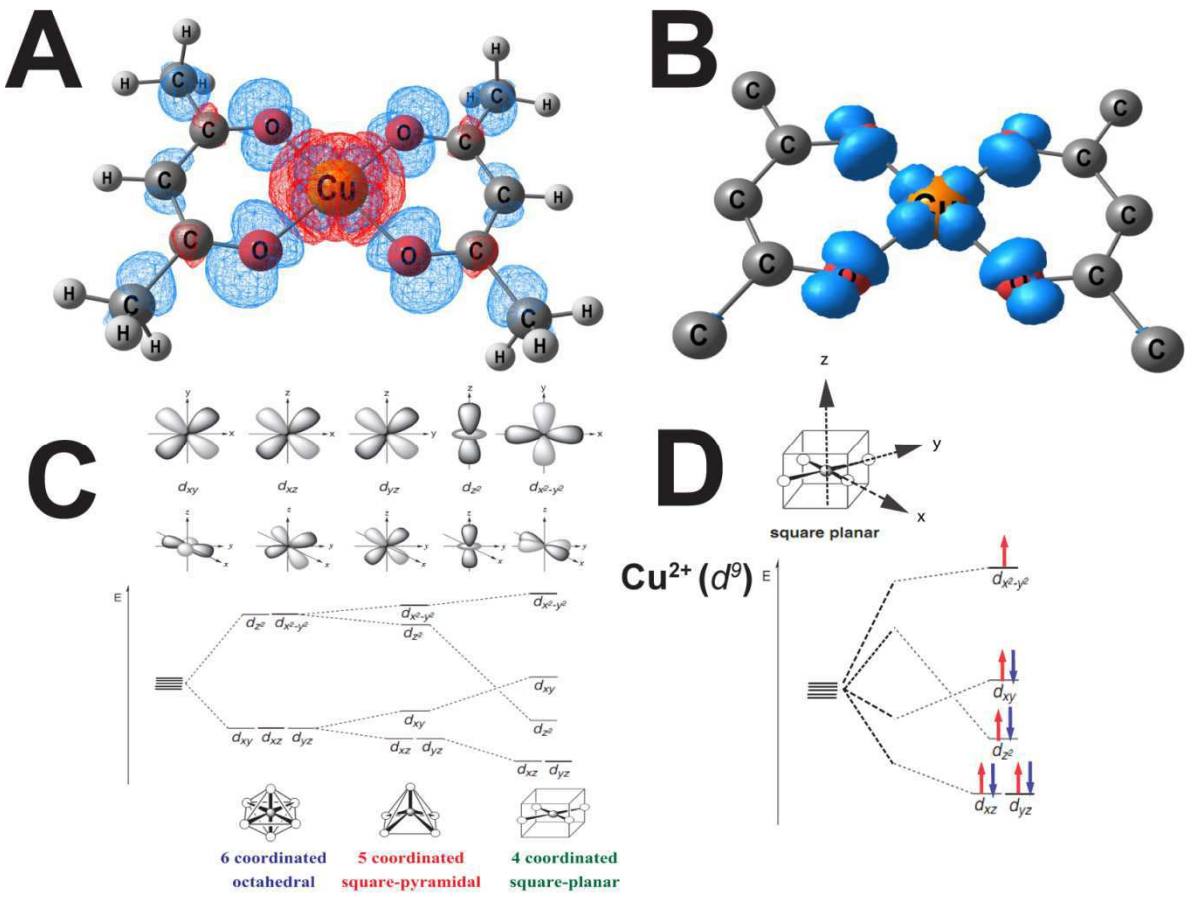

Figure 5.3.5: (A) Contour plot of spin density in Copper-acetylacetonate complex (red=negative and blue=positive spin density with contour value ranging between ± 0.00055 au). (B) Alpha minus Beta orbitals contour plot resulting in $d_{x^2-y^2}$ type orbital in Cu-acac complex (C) d-orbital energy levels in 6, 5 and 4 coordinated complexes. (D) Occupation of electrons in *d*-orbitals of Cu^{2+} ion in a 4-coordinated square planar field.

with the total beta molecular orbitals in Cu-acac which directly gives the location of unpaired electron in the molecular orbital of Cu^{2+} ion. Figure 5.3.5 B shows a contour plot of α - β orbital in Cu-acac complex. The shape of the molecular orbital resembles the $d_{x^2-y^2}$ orbital. These results

from DFT are in agreement with the crystal and ligand field theory which predicts that in four coordinated square planar complexes the *d*-orbital degeneracy is lifted by the ligand-metal interaction shown in Figure 5.3.5 C with unpaired electron occupation in Cu^{2+} (d^9) ion's highest occupied molecular orbital (HOMO) orbital i.e. $d_{x^2-y^2}$.

5.3.2 Assignment of ^{13}C solid state NMR signals using spin densities calculated from DFT calculation in paramagnetic Copper-acetylacetonate complex

We used the unpaired electron spin density in Cu-acac complex to assign ^{13}C Hahn-echo spectra of paramagnetic Cu-acac complex. Shown in Figure 5.3.6 is the ^{13}C Hahn-echo spectra of paramagnetic Cu-acac complex, the signal in diamagnetic region at 100 ppm is labeled preliminarily as C_1 and the upfield shifted signal at -61 ppm is labeled as C_2.

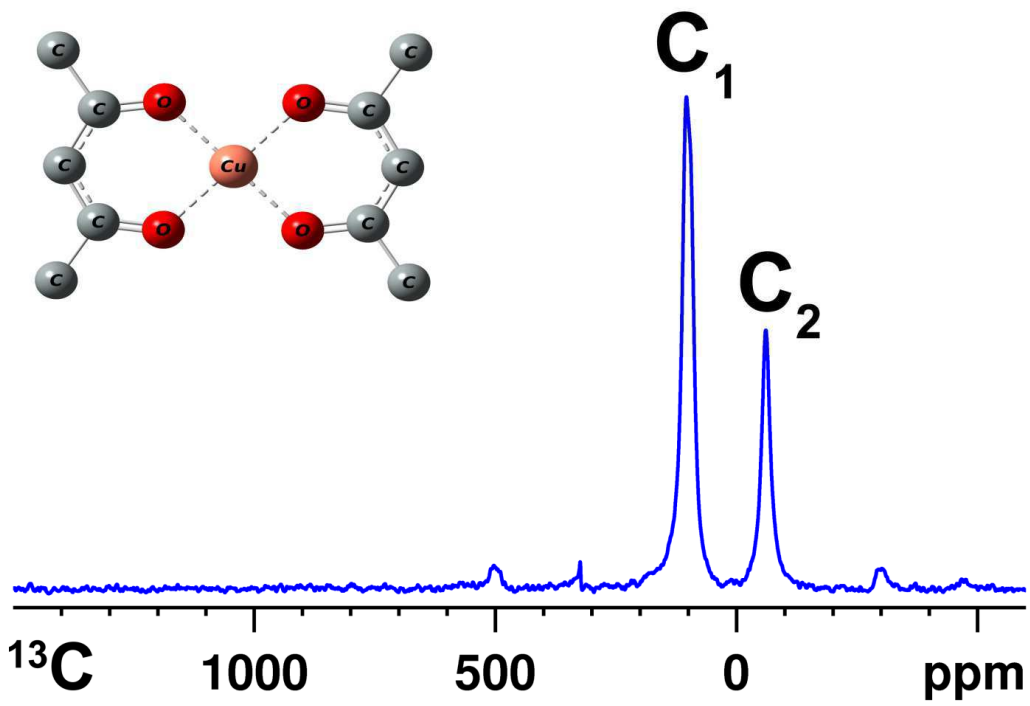

Figure 5.3.6: ^{13}C Hahn-echo spectra of Cu-cyclam monochloride complex with labeling of signals.

The total NMR shift of a nucleus in paramagnetic complex is a sum of paramagnetic and diamagnetic contribution. The diamagnetic part of the shift for Cu-acac complex was calculated theoretically by subjecting the DFT optimized Cu-acac structure to NMR=GIAO job using B3LYP

level of theory and with 6-311+G(2d,p) basis set. The outputs of the NMR shifts were analyzed using GAUSSVIEW 5 program. Figure 5.3.7 (A) shows the DFT generated ^{13}C NMR spectra of Cu-acac complex with (B) signal assignment with respect to carbon site.

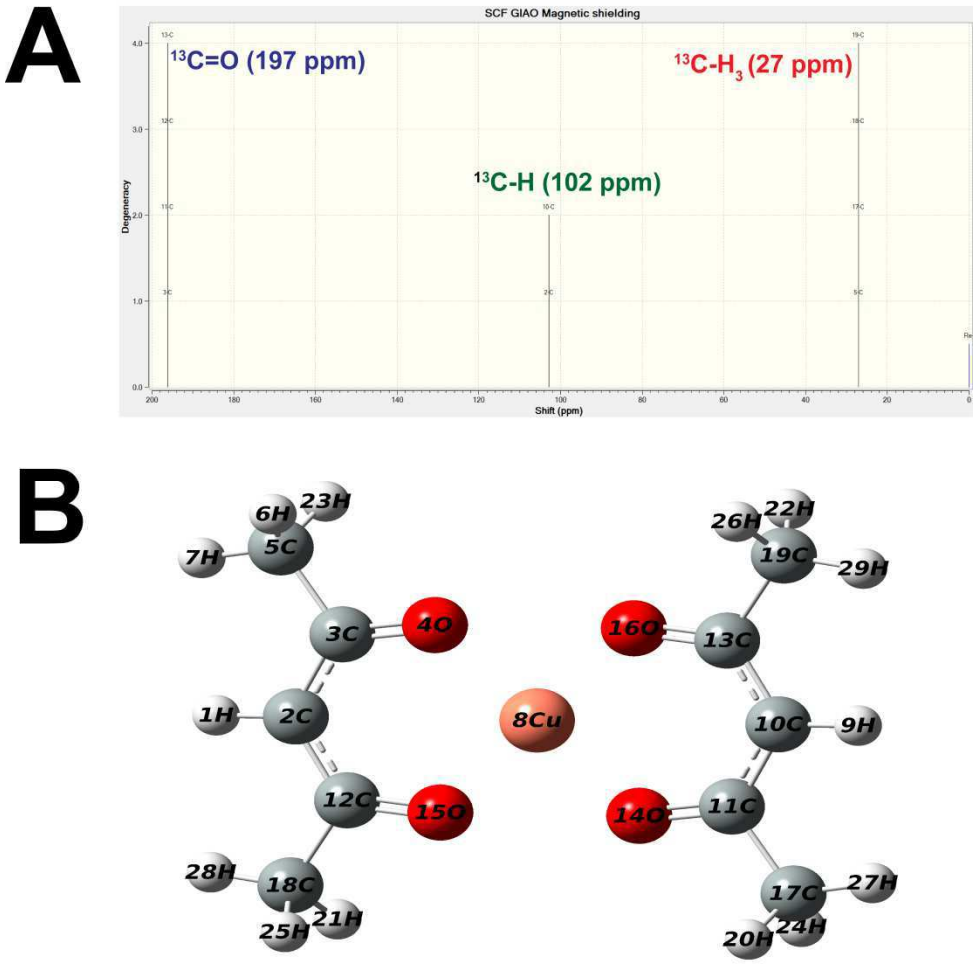

Figure 5.3.7: (A) DFT generated ^{13}C (diamagnetic part) NMR spectra of paramagnetic Cu-acac complex with (B) assignment of ^{13}C signals to respective carbon site.

These ^{13}C NMR (diamagnetic) chemical shifts were compared to experimental ^{13}C shifts of diamagnetic Zinc-acac complex from ^{13}C CPMAS by Takegoshi *et al.*[196] and we found that the DFT calculated shifts were in good agreement with experimental shifts.

The unpaired electron spin density generated by optimization job in GAUSSIAN 09 was inserted in Equation 2.7.22 to get ^{13}C Fermi-contact shifts in paramagnetic Copper-acetylacetonate complex. Later these shifts were added to DFT calculated diamagnetic chemical shift to get the total shift of

^{13}C from DFT $^{DFT}\delta_{Total}$. Table 5.3.2 compares the ^{13}C total shift observed using solid state NMR and those calculated by DFT.

^{13}C group	**Spin density ρ [au]**	**^{13}C Fermi-contact shifts $^{DFT}\delta_{FC}$ [ppm]**	**^{13}C chemical shifts (DFT) $^{DFT}\delta_{0}$ [ppm]**	**^{13}C total shift from DFT $^{DFT}\delta_{Total}$ [ppm]**	**^{13}C total shift from ssNMR $^{ssNMR}\delta_{Total}$ [ppm]**	**^{13}C site assignment (see Figure 5.3.8 B)**
Carbonyl ^{13}C=O	-0.00086	-92	196	105	100 (C_1)	C2, C10
Methine ^{13}C-H	-0.00148	-158	103	-55	-61 (C_2)	C3, C11, C12, C13
Methyl ^{13}C-H_3	0.01023	1089	27	1116	-	C5, C17 C18, C19

Table 5.3.3: Comparison of ^{13}C total shift observed using solid state NMR with the shifts calculated using DFT method in paramagnetic Copper-acetylacetonate complex ('-' means not detectable).

The two ^{13}C signals C_1 at 100 ppm and C_2 at -61 ppm are assigned to carbonyl carbon (^{13}C=O) and methine carbon (^{13}C-H) in paramagnetic Cu-acac complex as per DFT calculation. Figure 5.3.8 (A) shows unpaired electron spin density distribution on Cu-acac molecule. The square planar electrostatic field from the acetylacetonate ligand lifts the degeneracy in the energy of the d-orbitals of the Cu^{2+} ion such that the d^9 electronic configuration of the Cu^{2+} ion leaves the $d_{x^2-y^2}$ (see Figure 5.3.8 B) sub-orbital with one unpaired electron. Furthermore this huge spin density from the metal ion is transferred to oxygen donor atoms in the ligand through spin delocalization mechanism. Furthermore the positive spin density on the oxygen is transferred to carbonyl carbon through spin polarization mechanism creating negative spin density of -0.00086 au on the same. Hence we see a negative Fermi-contact shift of -92 ppm on carbonyl carbons from DFT calculation. As a result the far shifted carbonyl carbon (^{13}C=O) signals at 196 ppm in diamagnetic complex is seen at 100 ppm in ^{13}C Hahn-echo spectra of paramagnetic Cu-acac complex which agrees well with the DFT shift of the same (105 ppm). Furthermore this negative spin density on carbonyl carbon is transferred to

methine carbons through spin polarization and we see a huge negative spin density of -0.00148 au leading to a Fermi-contact shift of -158 ppm. As a result we observed an upfield shifted signal at -61 ppm in ^{13}C Hahn-echo spectra which is assigned to methine carbon (^{13}C-H) from DFT calculation which shows a total shift of -55 ppm.

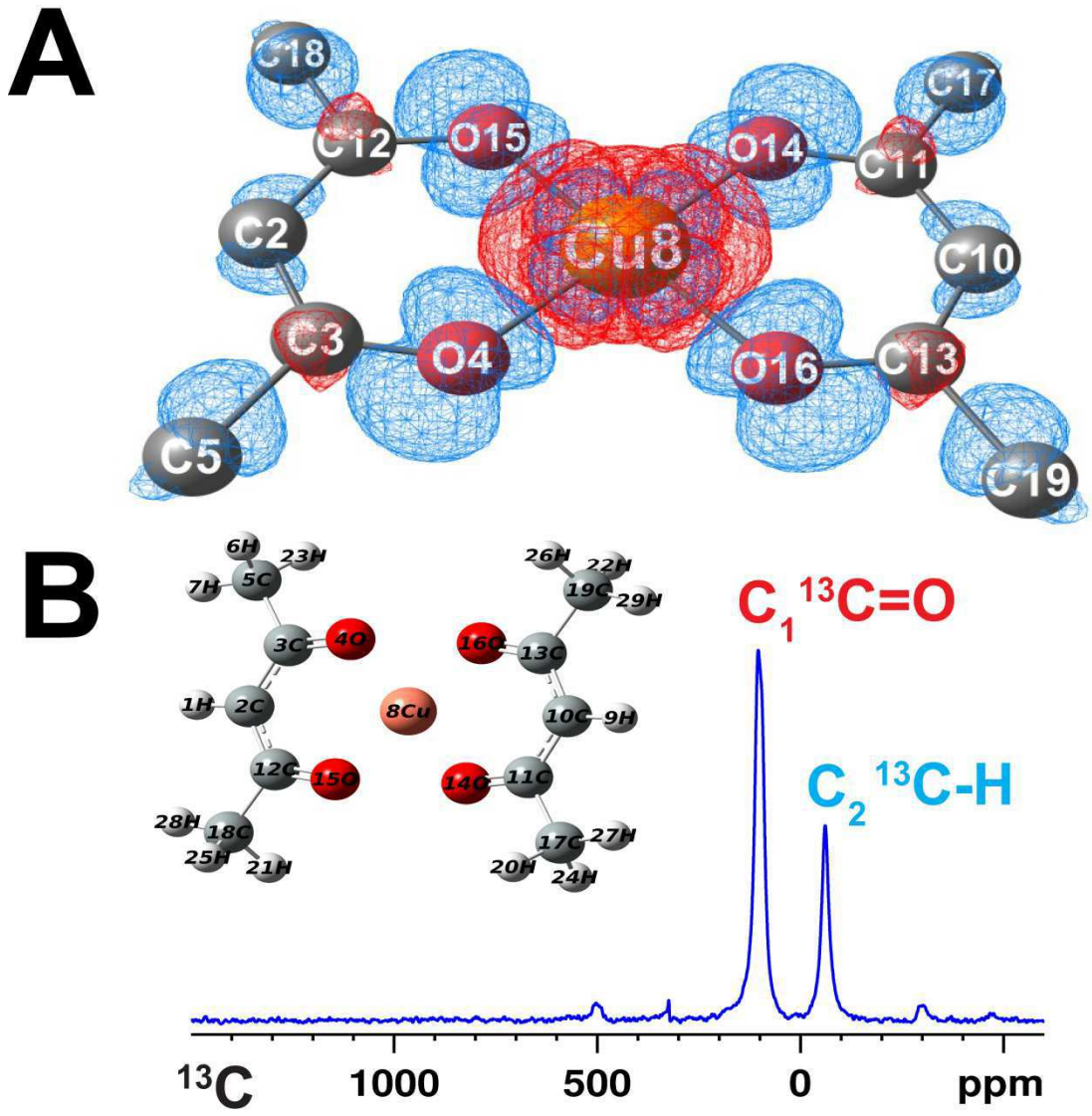

Figure 5.3.8: (A) Unpaired electron spin density distribution over Cu-acac complex from DFT generated contour plot with contour levels ranging from -0.00055 au (red) to +0.00055 au (blue). (B) ^{13}C signal assignment in solid state NMR ^{13}C Hahn-echo spectra of paramagnetic Copper-acetylacetonate complex

The methyl carbons experience huge amount of spin density due to spin polarization from carbonyl carbons and hence we see a severe downfield shift of 1116 ppm from DFT calculation. However we were not able to detect methyl carbon in Cu-acac complex even after shifting the offset to downfield

owing that the resonance is away from the excitation range. This may be due to the fact that the distance (inter-molecular) of methyl carbon to the Cu^{2+} in the neighboring molecular unit is very close leading to fast relaxation and causing severe broadening making it to be undetectable in solid state NMR Hahn-echo experiment.

5.3.3 Geometry optimization, vibration frequency and molecular orbital analysis of paramagnetic Vanadyl-acetylacetonate complex

The geometry optimization of the Vanadyl acetylacetonate complex were equally performed at B3LYP level of theory using 6-311G basis set under unrestricted mode. Figure 5.3.9 (A) shows the DFT optimized structure of VO-acac complex

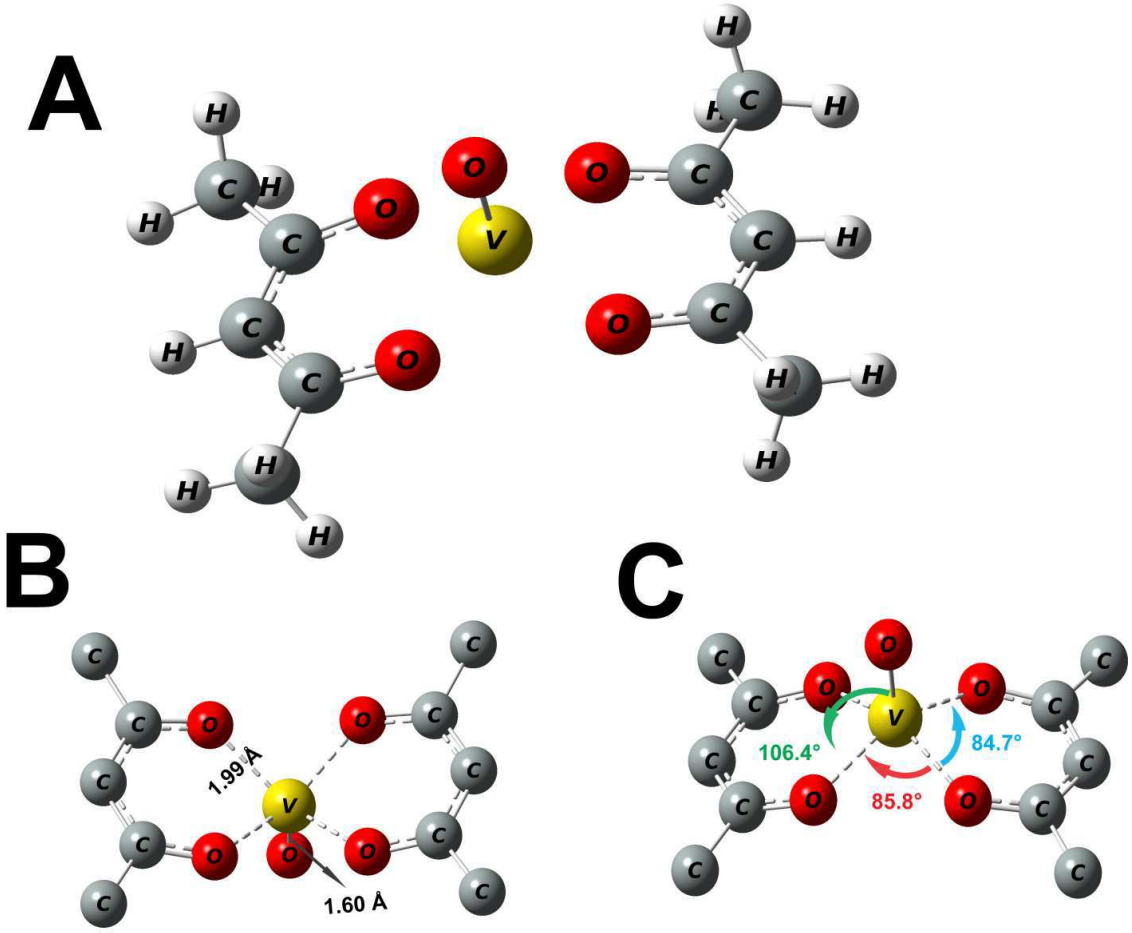

Figure 5.3.9: (A) DFT optimized Vanadyl-acetylacetonate structure. (B) V-O bond distance and (C) O-V-O bond angles in DFT optimized VO-acac structure.

with (B) V-O bond distance and (C) O-V-O bond angles. For the sake of comparison of the DFT optimized distances and angles in VO-acac, we have used the XRD data of Dodge *et al.*[190] and Hon *et al.*[194] found in the literature. Table 5.3.4 compares the V-O bond angles and O-V-O bond angles of DFT optimized structure with the XRD data from references.

Bond distance and bond angle	**DFT data of VO-(acac)$_2$**	**X-ray data of the VO-(acac)$_2$ complex**	
		Dodge *et al.*[190] (Ref. No. 180)	**Hon *et al.*[194] (Ref. No. 184)**
V-O **V-O`**	1.942 1.942	1.96 1.97	1.95 1.96
V-O``(oxygen above the plane of chelate)	1.60	1.56	1.56
O-V-O **O-V-O`**	84.7° 85.8°	83.5° 87.2°	83.8° 87.5°
Angle between V=O to plane of the chelate ring	106.4°	106.3°	106.3°

Table 5.3.4: Comparison of DFT optimized V-O bond distances and O-V-O bond angles with the XRD data from references of Dodge *et al.* and Hon *et al.*

The V-O bond distances and O-V-O bond angles of the DFT optimized structure of VO-acac complex is in good agreement with the XRD data of VO-acac reported by both Dodge *et al.*[190] and Hon *et al.*[194]

Furthermore we show here some results from the vibration analysis of DFT optimized VO-acac structure. Figure 5.3.10 shows a comparison of (A) DFT generated IR spectra (0-3000 cm^{-1}) with the (B) experimental IR spectra (obtained from the database) of paramagnetic Vanadyl-acetylacetonate complex. The comparison of DFT generated IR data and the experimental IR data

(from database) in the range of 0-3000 cm^{-1} of paramagnetic VO-acac complex shows that the values were in good agreement. Especially in the region between 1000 cm^{-1} to 1600 cm^{-1} which contains the characteristic IR bands resulting from C=O and C-C stretching modes (see Figure 5.3.4 A and B of Cu-acac), well agrees with the experimental IR data. The two intense IR bands: 1567

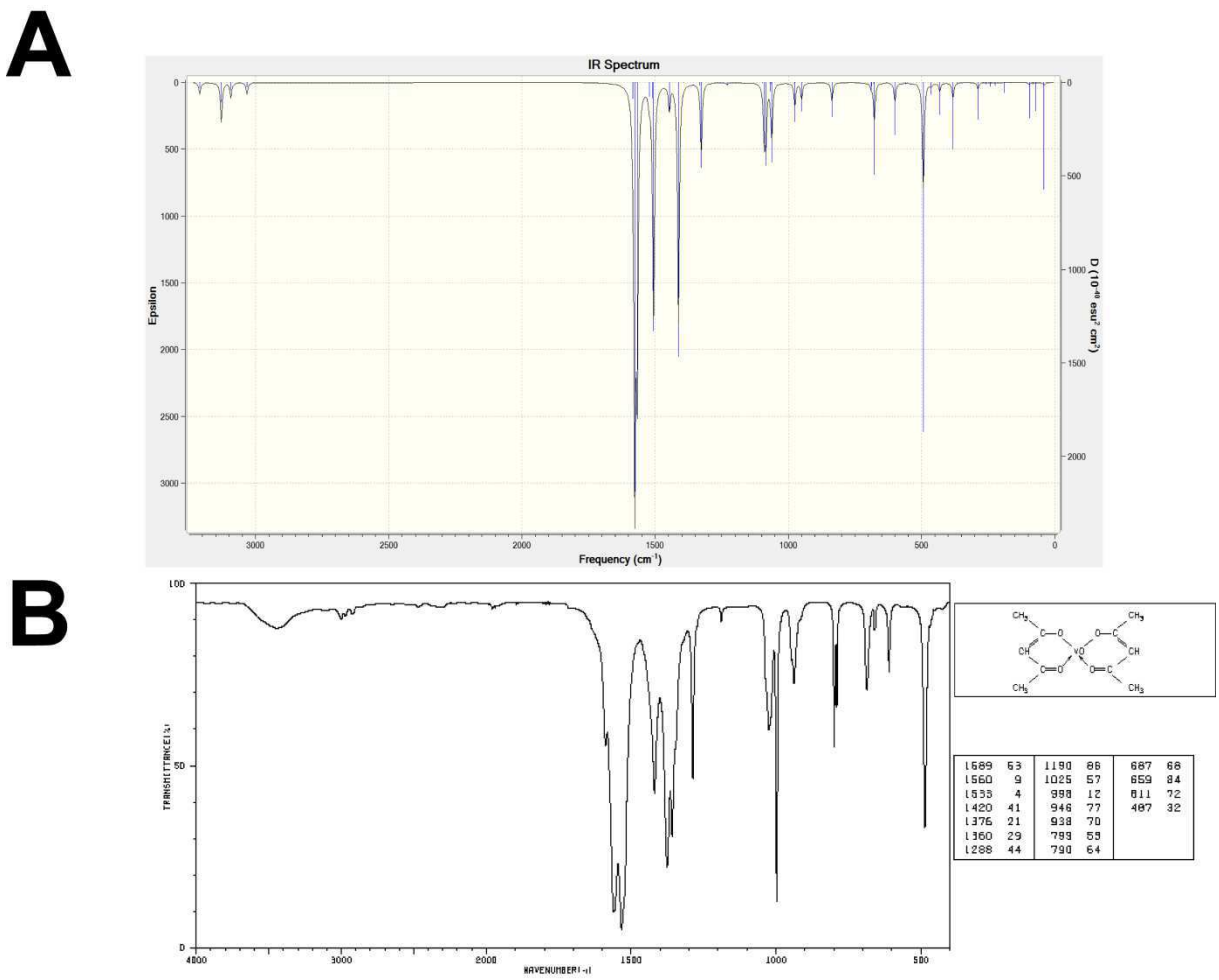

Figure 5.3.10: Comparison of (A) DFT generated IR spectra with the (B) experimental IR spectra (from Japanese database SDBS No. 4158) of paramagnetic VO-acac complex (with tables showing prominent IR bands and VO-acac structure).

cm^{-1} and 1576 cm^{-1} in DFT generated IR spectra speaks about the metal ion coordinating with the oxygen atoms in the ligand.

The DFT optimized VO-acac structure was subjected to full population analysis in GAUSSIAN 09 program at the same level of theory (uB3LYP) and same basis set (6-311G) for molecular orbital analysis. Figure 5.3.11 A shows the unpaired electron spin density distribution (contour levels (blue) +0.00055 au to (red) -0.00055 au) on the paramagnetic VO-acac molecule. The total alpha

molecular orbitals were subtracted from the total beta molecular orbitals for identification of the unpaired electron molecular orbital shown in Figure 5.3.11 B. From crystal field theory we see that

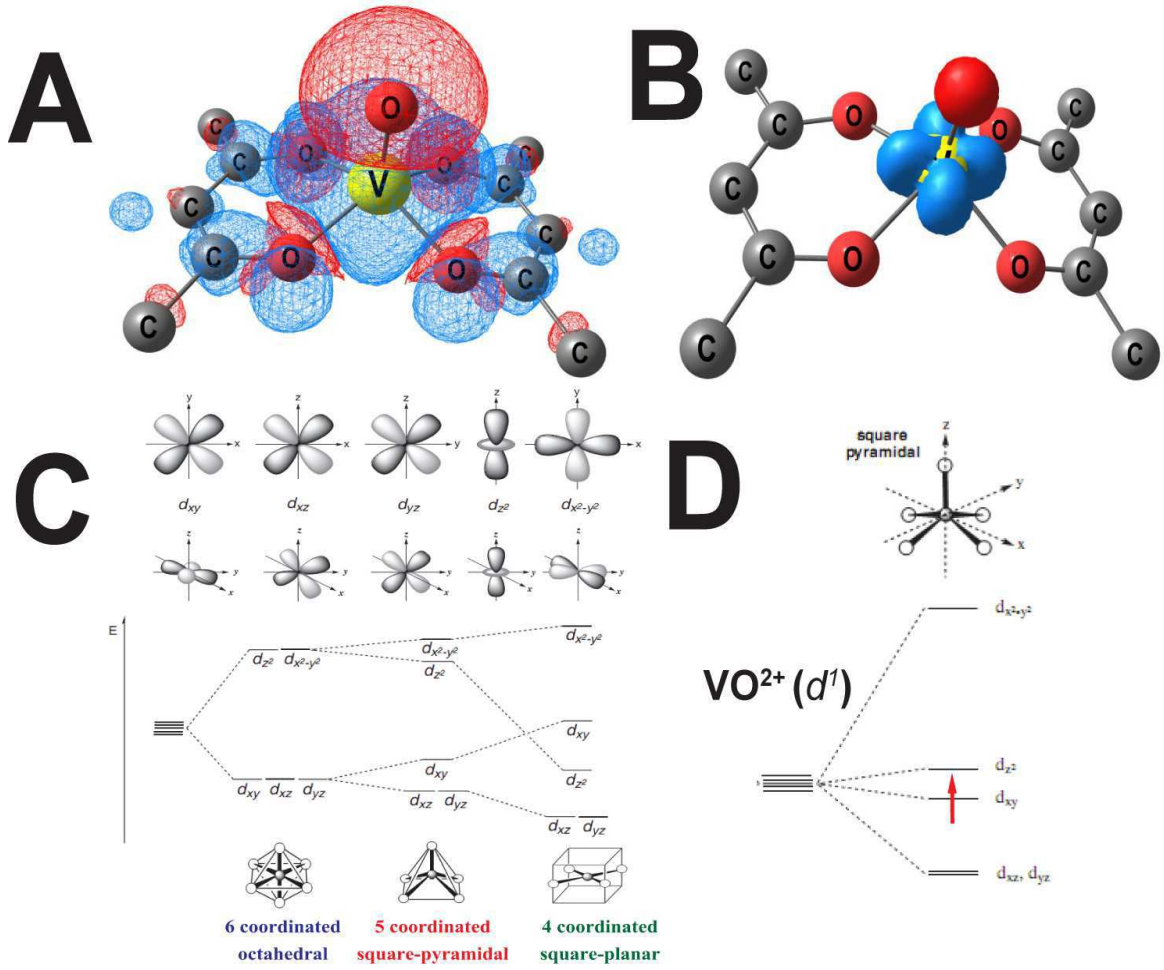

Figure 5.3.11: (A) Contour plot of spin density in Vanadyl-acetylacetonate complex (red=negative and blue=positive spin density with contour value ranging between ± 0.00055 au). (B) Alpha minus Beta orbitals contour plot resulting in d_{xy} orbital in VO-acac complex (C) d-orbital energy levels in 6, 5 and 4 coordinated complexes. (D) Occupation of electrons in *d*-orbitals of VO^{2+} ion in a 5-coordinated square-pyramidal field from CFT.

in five coordinated square pyramidal complexes the energy level configuration of the *d*-sub orbitals of the metal ion will be as shown in Figure 5.3.12 C. The square pyramidal field induced on VO^{2+} ion will influence the unpaired electron in the d^1 to occupy d_{xy} orbital as shown in Figure 5.3.12 D. The DFT generated unpaired electron molecular orbital of VO^{2+} ion by subtracting the total α - β orbitals from DFT calculation shown in Figure 5.3.11 B evidently resembles the d_{xy} orbital of Vanadyl ion.

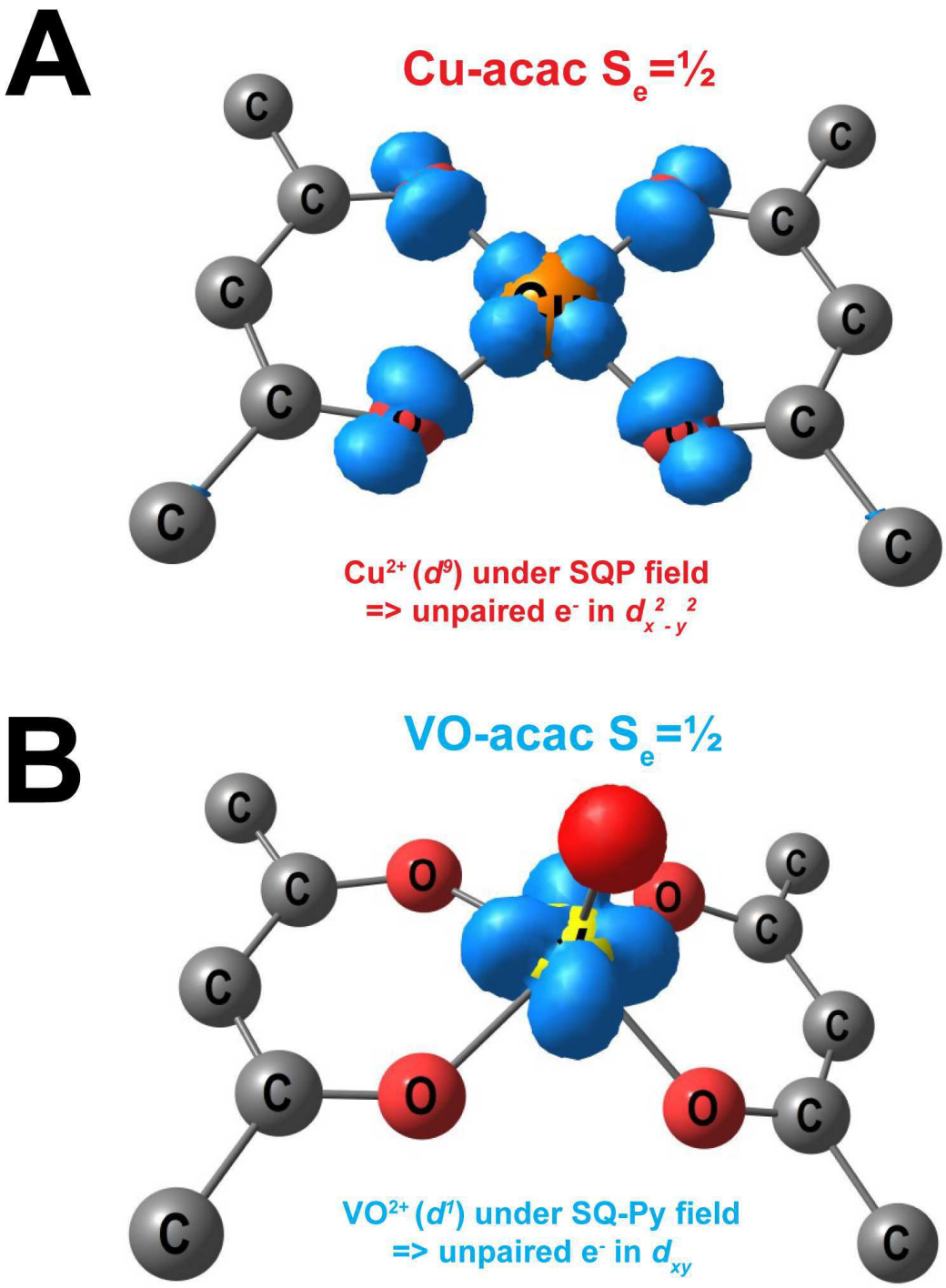

Figure 5.3.12: Comparison of alpha minus beta orbitals (α-β) of (A) Cu-acac complex with (B) VO-acac complex from DFT molecular orbital calculations.

Both Cu-acac and VO-acac complexes exhibit paramagnetic behavior due to the presence of one unpaired electron. However, due to the difference in the valence shell electron configuration of Cu^{2+} (d^9) and VO^{2+} (d^1) ions the location of the unpaired electron in the *d*-orbital is also different. Figure 5.3.12 demonstrates a comparison of location of molecular orbital in (A) Copper-acetylacetonate

complex and (B) Vanadyl-acetylacetonate complex calculated using molecular orbital calculation from DFT. The square planar field leaves Cu^{2+} ion with one unpaired electron in $d_{x^2-y^2}$ and similarly the square pyramidal environment leaves the VO^{2+} ion with one unpaired electron in the d_{xy} orbital. This also influences the spin density distribution mechanisms in Cu- and VO- acac complexes and hence also influences the ^{1}H and ^{13}C shifts in NMR. This is *Iso*-valence shell electronic configuration i.e. two complexes having same number of unpaired electron but in different orbitals is evidently seen through NMR shifts which is discussed in the immediate unit.

5.3.4 Assignment of ^{13}C solid state NMR signals using spin densities calculated from DFT calculation in paramagnetic Vanadyl-acetylacetonate complex

Figure 5.3.13 shows preliminary labeling of the ^{13}C signals in Hah-echo spectra of paramagnetic Vanadyl-acetylacetonate complex. The two signals C_1 at 350 ppm and C_2 at -70 ppm cannot be identified by conventional NMR assignment methods. The Fermi-contact shifts which are due to the hyperfine interaction masks the diamagnetic chemical shifts (rich of chemical group information) and makes signals assignment extremely difficult.

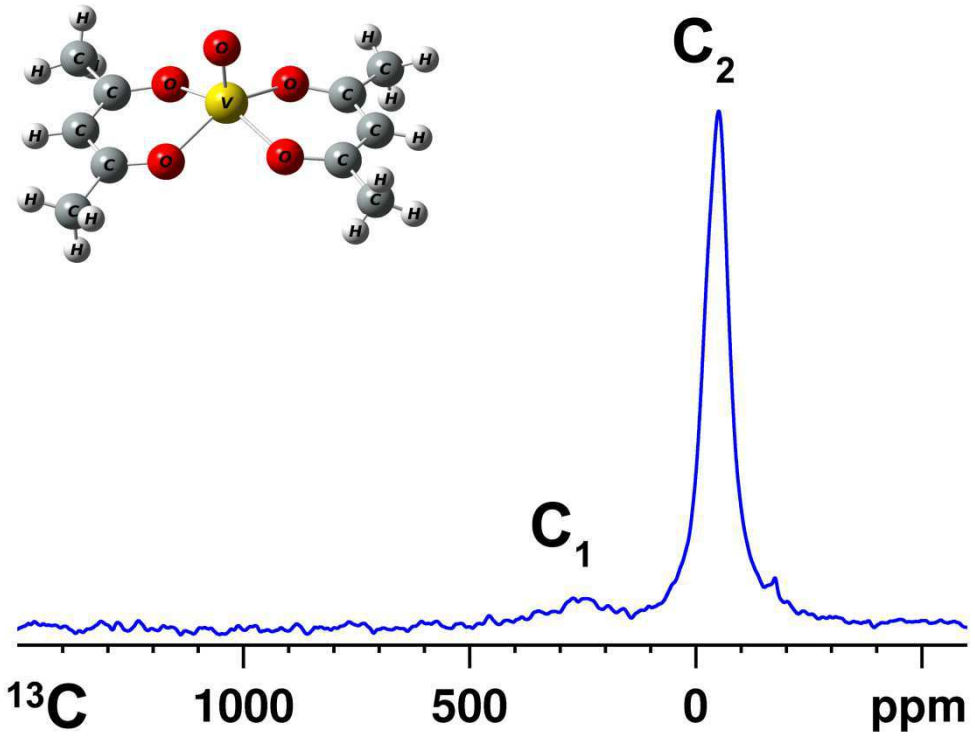

Figure 5.3.13: ^{13}C Hahn-echo spectra of Vanadyl acetylacetonate complex with labeling of signals.

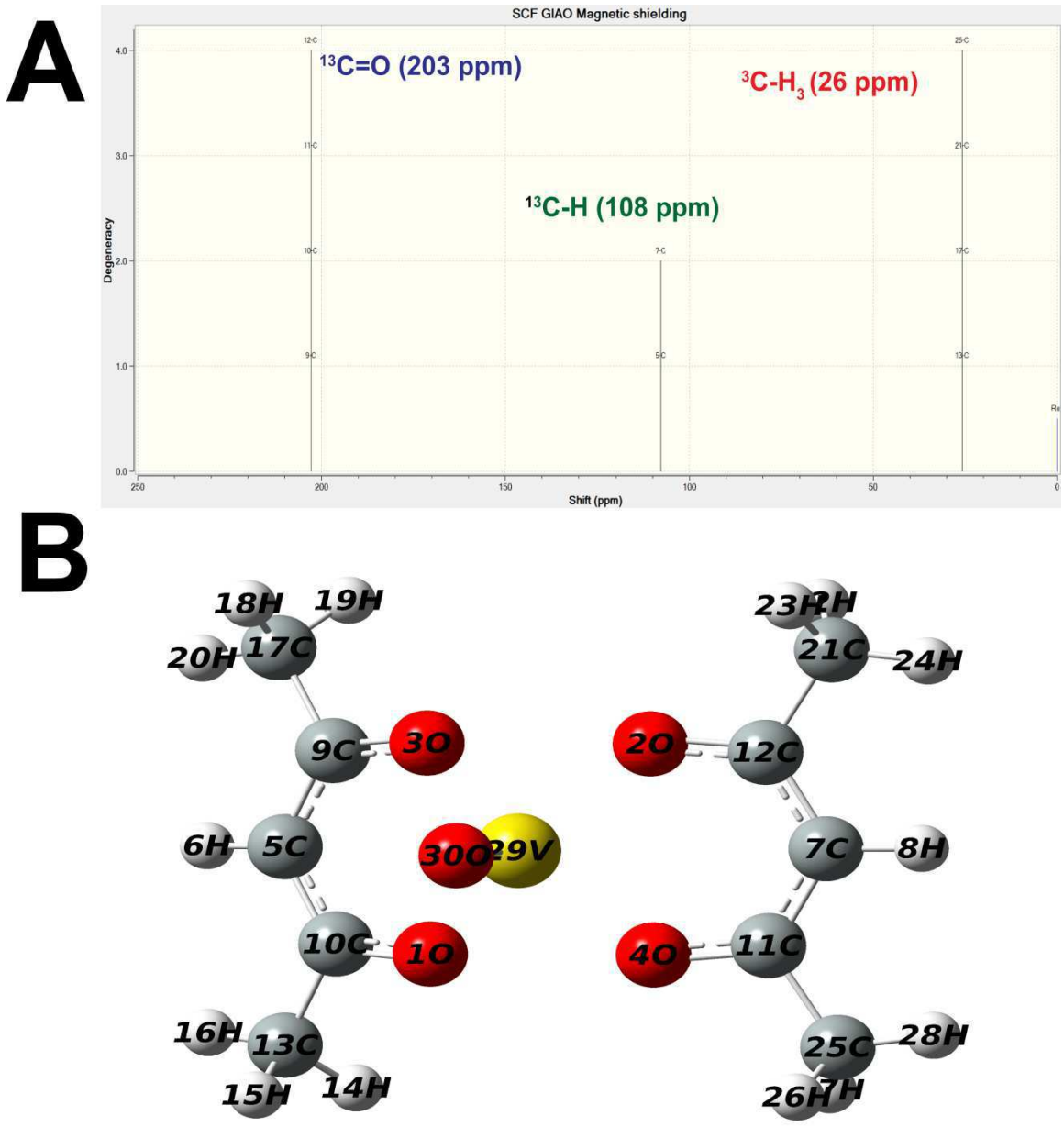

Figure 5.3.14: (A) DFT generated ^{13}C (diamagnetic part) NMR spectra of paramagnetic Cu-acac complex with (B) assignment of ^{13}C signals to respective carbon site.

Figure 5.3.14 shows (A) DFT generated ^{13}C NMR spectra (diamagnetic part) of paramagnetic VO-acac complex with (B) the assignment of carbon sites. We compared the DFT generated ^{13}C NMR chemical shifts and assignment of paramagnetic VO-acac with the experimental data of diamagnetic complex of Zinc-acetylacetonate complex from Takegoshi *et al.*[196] and observed that the values and assignment were consistent.

Unpaired electron spin density on carbon atoms in paramagnetic VO-acac complex generated by DFT optimization were inserted in Equation 2.7.22 to obtain ^{13}C Fermi-contact shifts. The ^{13}C total

shifts DFT $^{DFT}\delta_{Total}$ in paramagnetic VO-acac complex where compared with the total shift of ^{13}C from solid state $^{ssNMR}\delta_{Total}$ NMR Hahn-echo and the ^{13}C signals were assigned as shown in Table 5.3.5.

^{13}C group	**Spin density ρ [au]**	**^{13}C Fermi-contact shifts $^{DFT}\delta_{FC}$ [ppm]**	**^{13}C chemical shifts (DFT) $^{DFT}\delta_{0}$ [ppm]**	**^{13}C total shift from DFT $^{DFT}\delta_{Total}$ [ppm]**	**^{13}C total shift from ssNMR $^{ssNMR}\delta_{Total}$ [ppm]**	**^{13}C site assignment (see Figure. 5.3.17 B)**
Carbonyl $^{13}C=O$	0.00475	506	203	709	-	C9, C10 C11, C12
Methine $^{13}C-H$	0.00269	286	108	394	250 (C_1)	C7, C5
Methyl $^{13}C-H_3$	-0.00074	-79	26	-53	-51 (C_2)	C13, C17 C21, C25

Table 5.3.5: Comparison of ^{13}C total shift observed from solid state NMR with the shifts calculated using DFT in paramagnetic Vanadyl-acetylacetonate complex with assignment of the signals respective to the carbon sites.

The calculated ^{13}C shifts from DFT are in well agreement with the experimental solid state NMR shifts. Figure 5.3.15 shows (A) unpaired electron spin density distribution on the entire molecule of paramagnetic VO-acac complex with contour levels ranging from +0.0055 au (blue) to -0.0055 au with (B) ^{13}C assignment of signals in Hahn-echo spectra with respect to carbon sites (for comparison of values in the Table 5.3.5). From the Figure 5.3.15 A, we can understand the unpaired electron density distribution mechanism; here we see that the positive spin density from the dxy orbital of Vanadyl ion is transferred on to the oxygen (donor atoms) in the ligand through spin polarization mechanism creating a huge negative spin density on the same. Furthermore this negative spin density is transferred onto the carbonyl carbon atoms through spin polarization resulting in large positive spin density. Thus the Fermi contact shifts for the carbonyl carbons are positive and hence we see from DFT calculation an upfield shifted signal for it. Since the carbonyl

resonances are away from the excitation range, we tried to shift the offset in the solid state NMR Hahn-echo experiment. But we did not observe any signal even after repeating for large number of

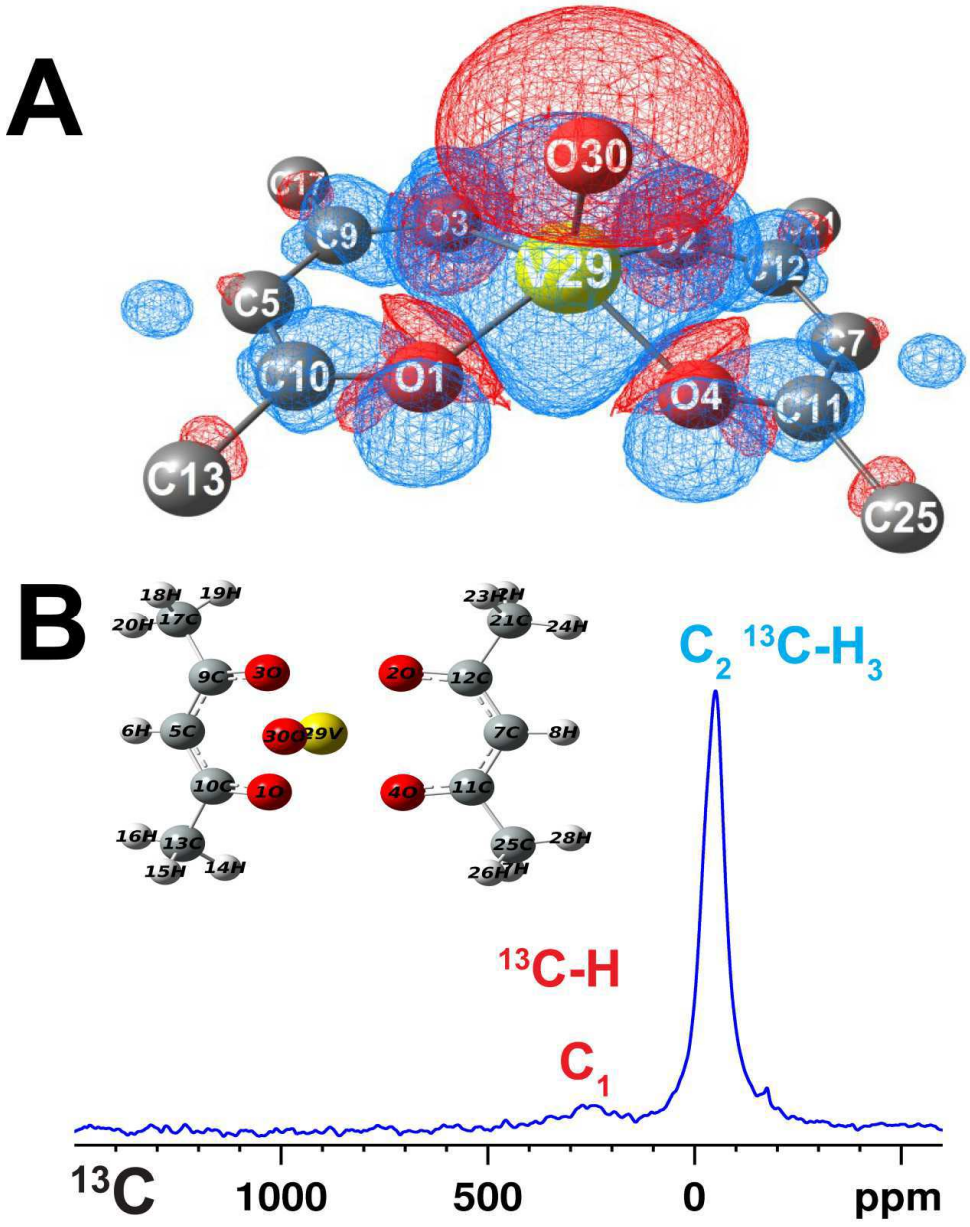

Figure 5.3.15: (A) Unpaired electron spin density distribution over VO-acac complex from DFT generated contour plot with contour levels ranging from -0.00055 au (red) to +0.00055 au (blue). (B) ^{13}C signal assignment in solid state NMR ^{13}C Hahn-echo spectra of paramagnetic Vanadyl-acetylacetonate complex

scans. This may be due to the fact that carbonyl group is too close to the paramagnetic center (2.83 Å) and suffers from too much broadening due to paramagnetic relaxation. Furthermore the positive spin density is transferred to methine carbon through spin delocalization and hence we see a positive spin density (and hence positive Fermi contact shift). The methyl carbons experience negative spin

density due to spin polarization from methine carbon and hence we observe a negative Fermi contact shift.

Even though Cu-acac and VO-acac demonstrate an example of paramagnetic complex with spin one half, they are distinguished based on the unpaired electron molecular orbital configuration. The Cu^{2+} with valence shell electron configuration of d^9 has unpaired electron in the $d_{x^2-y^2}$ orbital, whereas VO^{2+} with d^1 has an unpaired electron in the d_{xy} orbital. This is evidently seen when we compare the ^{13}C Hahn-echo spectra of paramagnetic Cu-acac and VO-acac complexes, which is a direct influence of unpaired electron spin density distribution. To be more specific the symmetry of the unpaired molecular orbital in VO-acac and Cu-acac is such that the mechanism by which the Cu^{2+} ion distributes the unpaired electron spins over Cu-acac molecule, is exactly the opposite mechanism the VO^{2+} ion distributes on its chelate ligand. So as shown in Figure 5.3.12 (A) in Cu-acac the $d_{x^2-y^2}$ molecular orbital will face the ligand donor atoms and (B) in VO-acac the d_{xy} molecular orbital will face the donor atoms.

5.4 Assignment of ^1H solid state NMR signals by ^1H-^{13}C 2D dipolar INEPT experiment in paramagnetic Copper-, Vanadyl-acetylacetonate complexes

For assignment of ^1H signals in solid state NMR Hahn-echo spectra of paramagnetic Cu-acac and VO-acac complexes we have used a ^1H-^{13}C 2D dipolar INEPT experiment. The transfer of polarization from ^1H to ^{13}C was done in two rotor period ($2\tau_r$ = 2×33.33 = 66.66 μs). The assignment of the cross peaks in the 2D dipolar INEPT spectra was done with the help of the already assigned ^{13}C signal from DFT.

Shown in Figure 5.4.1 is a ^1H-^{13}C 2D dipolar INEPT spectra of paramagnetic Copper-acetylacetonate complex. We observed one intense cross peak between upfield shifted methine carbon C_2 (-51 ppm) and an upfield shifted ^1H signal H_2 at -10 ppm indicating that H_2 is a methine proton. And a relatively (10 times less) less intense cross peak between carbonyl carbon C_{1b} (92 ppm) and the ^1H signal H_1 in the diamagnetic region at 4 ppm is observed. The broad ^1H signal in diamagnetic region (4 ppm) might be methyl protons. This cross peak between carbonyl carbon and methyl proton (suspected) is unexpected but since we use dipolar coupling between ^1H and ^{13}C in

solid state NMR experiments this cross peak is not completely meaningless. Because protons arising from methyl carbons can be close to carbonyl carbons in space (3.2 Å in Cu-acac from XRD) and hence one can expect a correlation peak between $^{13}C{=}O$ and $^{1}H_3$-C.

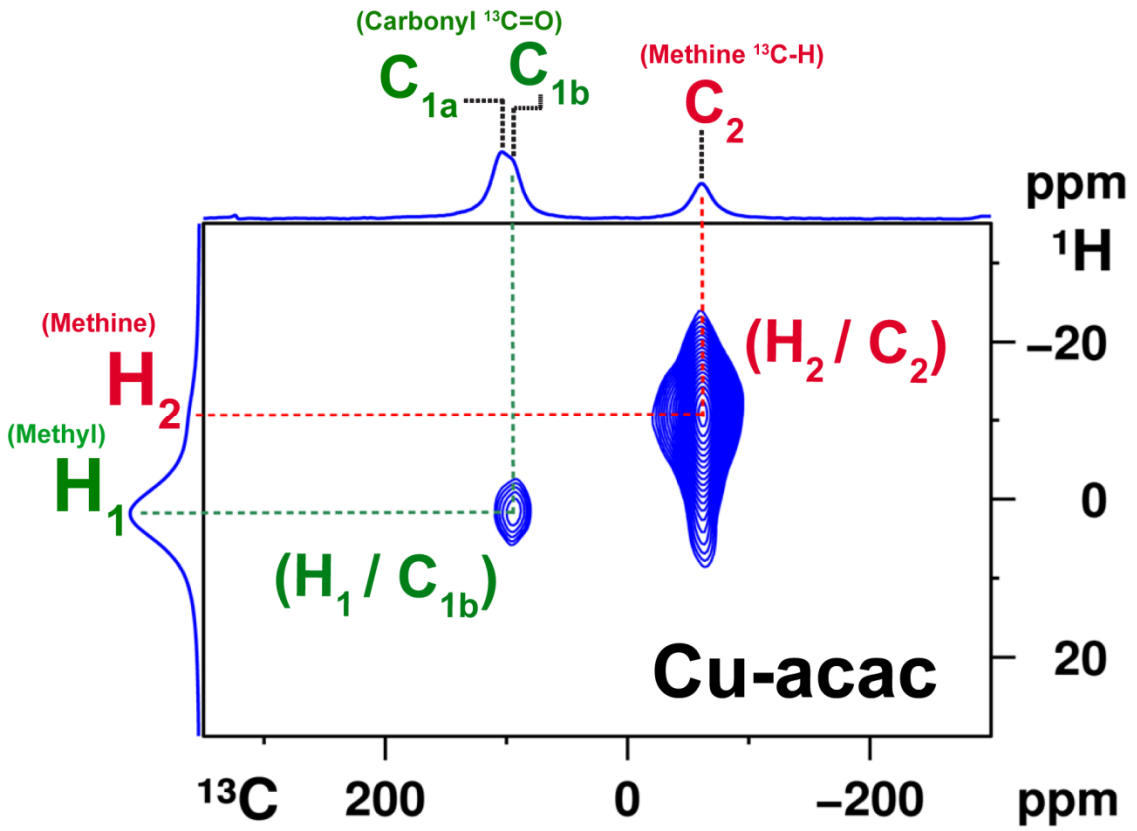

Figure 5.4.1: ^{1}H-^{13}C 2D dipolar INEPT spectra of paramagnetic Copper-acetylacetonate complex

This cross peak manifests the XRD distances that the carbonyl carbons are closer to the methyl protons of the immediately neighboring Cu-acac molecular unit. Also an interesting point to be notices is that the two signals which were overlapping in the ^{13}C Hahn-echo were well resolved in the 2D dipolar INEPT spectra (C_{1a} at 109 ppm C_{1b} at 92 ppm). However since we were not able to observe the methyl carbons in 1D Hahn-echo we tried shifting offset in 2D experiment as well and were unsuccessful in observing any cross peak even after repeating for large number of scans.

Figure 5.4.2 shows a ^{1}H-^{13}C 2D dipolar INEPT spectra of paramagnetic Vanadyl acetylacetonate complex. Here we observe only one cross peak between methyl carbon C_{2a} and the broad ^{1}H signal H_2 at 3 ppm. Here too we see that the two ^{13}C signals which were overlapping in 1D were well resolved in the 2D spectra and hence we label this signal as C_{2a} (-45 ppm). The methine carbon at C_1

at 250 ppm gave no cross peak since the sensitivity of this signal was already extremely low in 1D. Furthermore we tried to shift the offset and repeat the experiment with more number of scans to search the missing carbonyl carbon and were unsuccessful in locating it. Again the fact that the carbonyl carbons are too close paramagnetic center makes them undetectable.

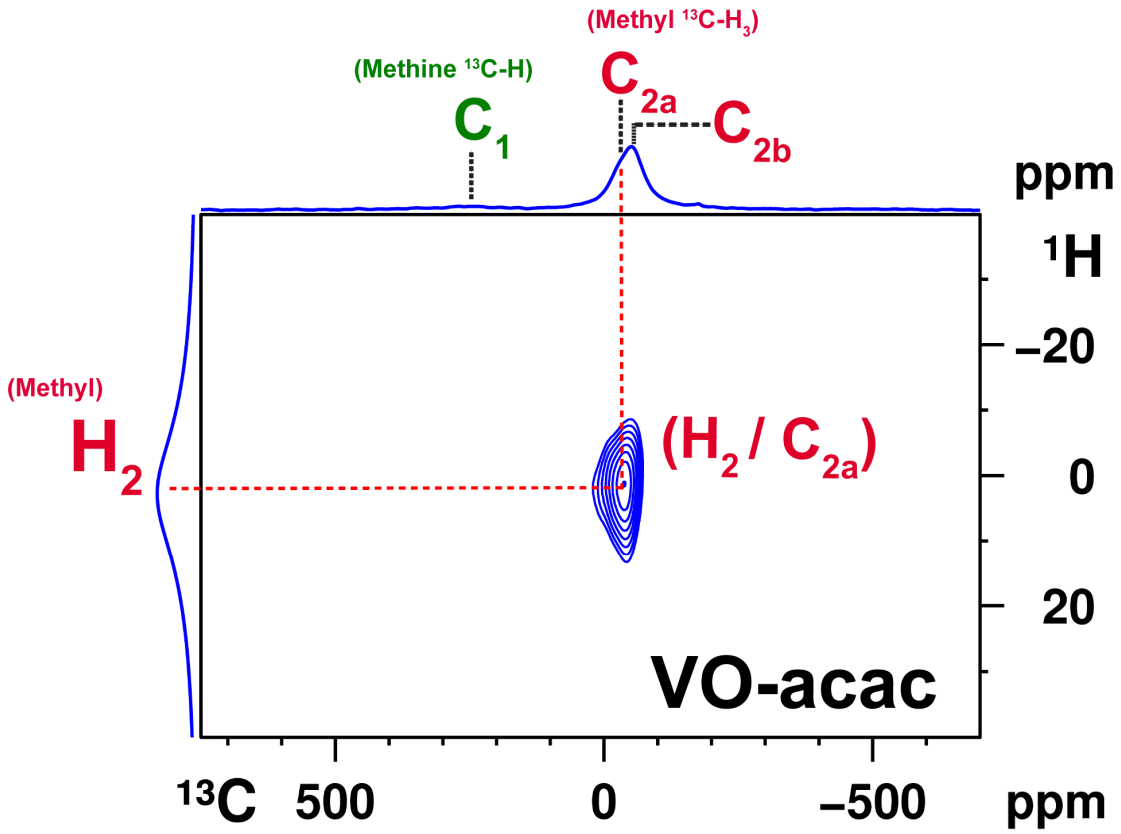

Figure 5.4.2: ^{1}H-^{13}C 2D dipolar INEPT spectra of paramagnetic Copper-acetylacetonate complex

With the Figure 5.4.3 showing ^{1}H signal assignment in paramagnetic Cu-acac and VO-acac complex the assignment of the ^{1}H and ^{13}C signals observed are completed.

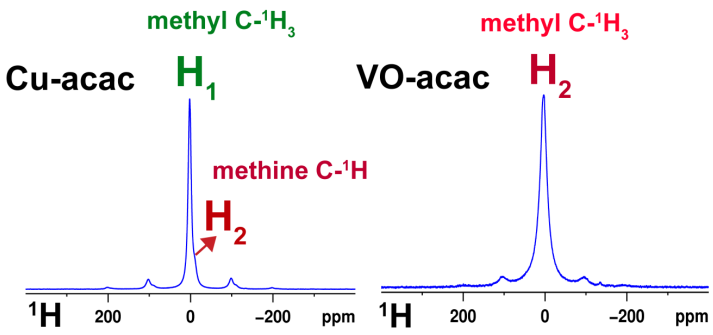

Figure 5.4.3: Proton assignment in Cu- and VO-acac complex from ^{1}H-^{13}C 2D dipolar INEPT experiment

5.5 Conclusion

With the methodology developed in solid state NMR for paramagnetic metal-organic complexes using paramagnetic metal-cyclam complexes as model system, here we have extended the method by apply it on another type of paramagnetic metal-organic complex. With the help of DFT calculation not only we have assigned the ^{13}C signals but also we have shown how one can understand the unpaired electron spin density distribution in such as Cu-acac and VO-acac complex which are spin one half systems but with different molecular orbital configuration. For ^{1}H assignment we have successfully used the ^{1}H-^{13}C 2D dipolar INEPT experiment.

However it is was difficult to understand more complex ^{13}C Hahn-echo spectra of Ni-acac complex. With more advance methods in DFT there might be a possibility of assigning ^{13}C signals.

SECTION II

PARAMAGNETIC METAL-INORGANIC SYSTEMS

Chapter 6: Paramagnetic alkaline metal-copper pyrophosphate systems

"Anyone who thinks science is trying to make human life easier or more pleasant is utterly mistaken."

- Albert Einstein

6.1 Introduction

The anions of pyrophosphoric acid ($H_4P_2O_7$) are generally called pyrophosphates $[P_2O_7]^{4-}$. They are very important in biochemistry and often encountered with the abbreviation PP_i during the hydrolysis of adenosine tri-phosphate (ATP) to adenosine mono-phosphate (AMP). Pyrophosphates find importance in Inorganic chemistry as well; they form stable metal pyrophosphates with transition metal ions such as copper, nickel and cobalt. Furthermore, these transition metal-pyrophosphates combine with alkali metal ions such as Li^{2+}, Na^{2+} and K^{2+} and form stable alkaline transition metal-pyrophosphates which exhibit paramagnetism. Alkali metal-copper pyrophosphates have wide range of applications as prospective materials in technology, viz. in electronic devices, as solid electrolytes, ceramics, solid state lasers and magnetic materials. We have investigated some of these alkali metal-copper pyrophosphates with ^{31}P solid state NMR. Phosphorus is well suited for NMR studies due to the 100 % natural abundance of the NMR active spin ½ nuclei ^{31}P, an isotope of phosphorus.

The very fast MAS technique which is used in the investigation of 1D ^{1}H and ^{13}C solid state NMR of paramagnetic metal-organic complexes is also applied here for 1D ^{31}P studies in paramagnetic alkali metal (Na^{2+}, K^{2+}, and Li^{2+})-copper pyrophosphates. Due to the hyperfine interaction the normal diamagnetic range of ^{31}P [+250 ppm to -200 ppm] is masked by large Fermi contact shifts of thousands of ppm range in alkali metal-cooper pyrophosphates. We have used a simple Hahn-echo experiment for acquiring 1D ^{31}P in these paramagnetic alkali metal-copper pyrophosphates. Later, the idea of copper-carbon distance measurement using solid state NMR relaxation rates (from Solomon's rate equation) which is successfully implemented in paramagnetic Cu-cyclam complex

was tested here to measure copper-phosphorus distances in paramagnetic alkali metal-copper pyrophosphates.

6.1.1 Structure of sodium, potassium, and lithium ion-copper pyrophosphates

We have investigated three alkali metal-copper pyrophosphates which are paramagnetic using solid state NMR. We have found few literature references for the crystal structure of sodium, potassium and lithium ion-copper pyrophosphates. Shown in Figure 6.1.1 are the crystal structures of (A) sodium-copper pyrophosphate ($Na_2CuP_2O_7$) reported by Erragh *et al.*,[93] (B) potassium-copper pyrophosphate ($K_2CuP_2O_7$) reported by ElMaadi *et al.*,[94] and (C) lithium-copper pyrophosphate ($Li_2CuP_2O_7$) reported by Gopalakrishna *et al.*[95]

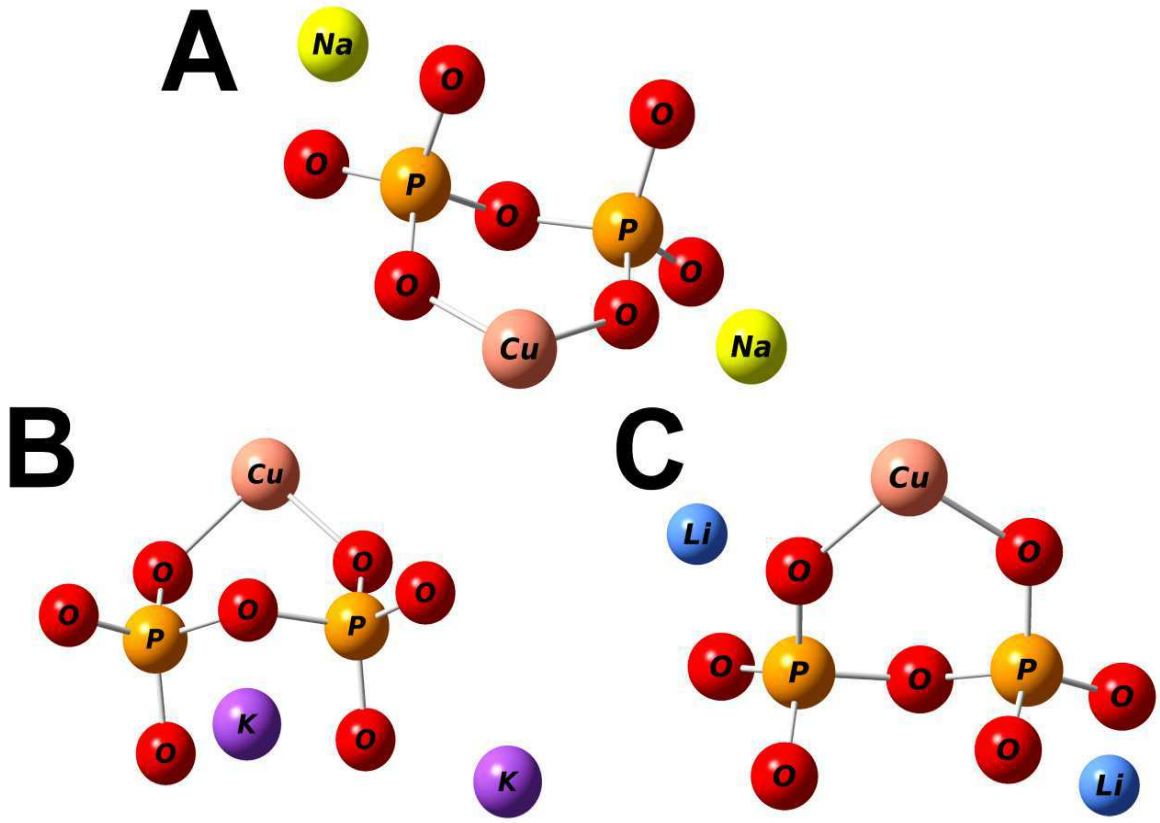

Figure 6.1.1: Crystal structure of (A) sodium-copper pyrophosphate ($Na_2CuP_2O_7$) reported by Erragh *et al.*,[93] (B) potassium-copper pyrophosphate ($K_2CuP_2O_7$) reported by ElMaadi *et al.*,[94] and (C) lithium-copper pyrophosphate ($Li_2CuP_2O_7$) reported by Gopalakrishna *et al.*[95]

The sodium-copper pyrophosphates and lithium-copper pyrophosphates are monoclinic systems and the potassium-copper pyrophosphate is an orthorhombic crystallographic system.

6.2 One dimension ^{31}P solid state NMR studies of paramagnetic sodium-, potassium- and lithium-copper pyrophosphates.

With the help of very fast MAS technique we were able to acquire 1D ^{31}P Hahn-echo spectra of paramagnetic alkali metal-copper pyrophosphates as shown in Figure 6.1.2. When compared to the

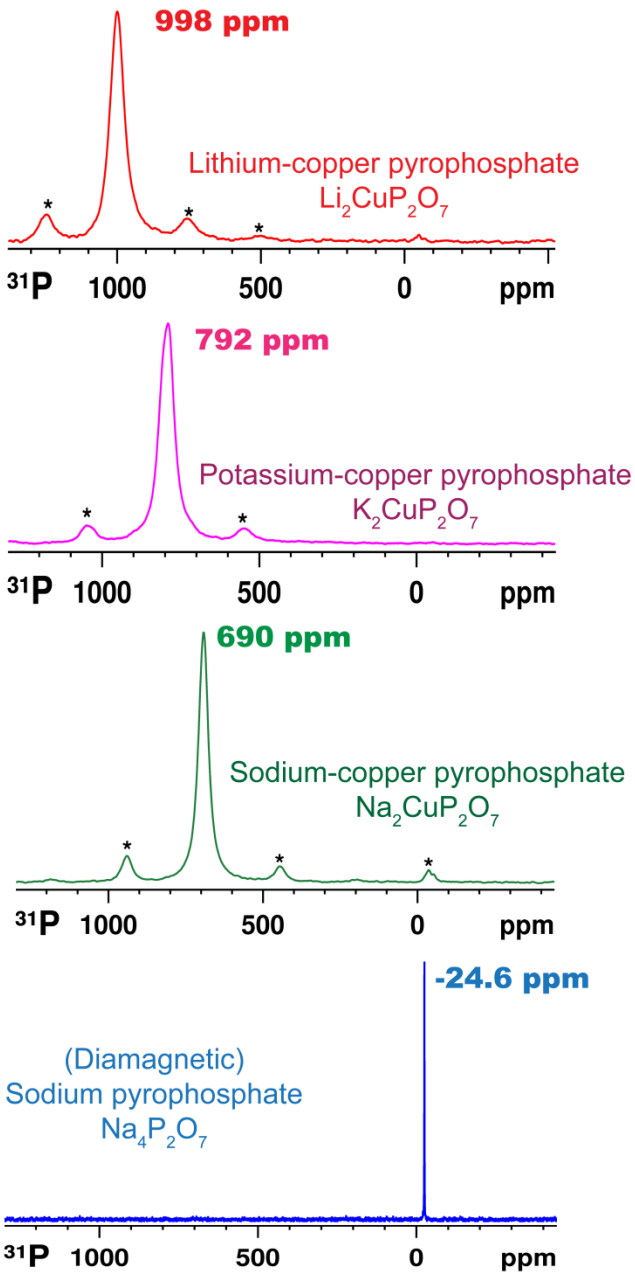

Figure 6.1.2: Comparison of ^{31}P Hahn-echo spectra of paramagnetic sodium-copper pyrophosphate ($Na_2CuP_2O_7$), potassium-copper pyrophosphate ($K_2CuP_2O_7$), lithium-copper pyrophosphate ($Li_2CuP_2O_7$), and diamagnetic sodium pyrophosphate ($Na_4P_2O_7$).

signal of ^{31}P at -24.6 ppm in diamagnetic sodium-pyrophosphate, the ^{31}P signal in alkali metal-copper pyrophosphates are severely shifted ($Na_2CuP_2O_7$ – 690 ppm, $K_2CuP_2O_7$ – 792 ppm, and $Li_2CuP_2O_7$ – 998 ppm) due to Fermi-contact interaction. However all the three alkali metal-copper pyrophosphates show a single ^{31}P signal in Hahn-echo indicating single symmetric site of phosphorus. This is consistent with the crystal structure[93-95] of the all the three alkali metal-copper pyrophosphates. As usual we see the signal is broadened due to electron-nucleus dipolar interaction compared to the diamagnetic signal of ^{31}P in sodium pyrophosphate.

6.3 Copper-phosphorus distances from ^{31}P relaxation rates measured using solid state NMR in paramagnetic sodium-, potassium- and lithium-copper pyrophosphates.

With some success in the copper-carbon distance measurement method using solid state NMR relaxation rates in the Cu-cyclam complex that we have developed, we test here the general feasibility of this method for paramagnetic metal-inorganic system of alkali metal-copper pyrophosphates.

We have measured ^{31}P transverse relaxation rates of the three alkali metal-copper pyrophosphates and the diamagnetic sodium pyrophosphate using CPMG[91-92] experiment from solid state NMR. The plot of intensity of the ^{31}P signals versus the CPMG delay gives the decay curves for sodium-, potassium-, and lithium-copper pyrophosphates (Figure 6.1.3). The CPMG decay curves of the three alkali metal-copper pyrophosphates were fitted to the exponential decay model (Equation 4.9.3) to obtain the transverse relaxation rates R_2 of the ^{31}P signals. We have subtracted other contributions of relaxation (essentially ^{31}P-^{31}P dipolar coupling) from these rates using rates from the diamagnetic reference of sodium-pyrophosphate. The determination of electron relaxation time T^e using EPR experiment was not straightforward for paramagnetic alkali metal-copper pyrophosphates. We could therefore only do a test of the general applicability. We have used electronic relaxation time T^e of Cu-cyclam (0.6 ns) to calculate expected rates from XRD distances. This is of course a very rough approximation, but it showed that the experimental rates are in the same order of magnitude (some thousand per second) as the predicted ones. The experimental rates and the expected rates from

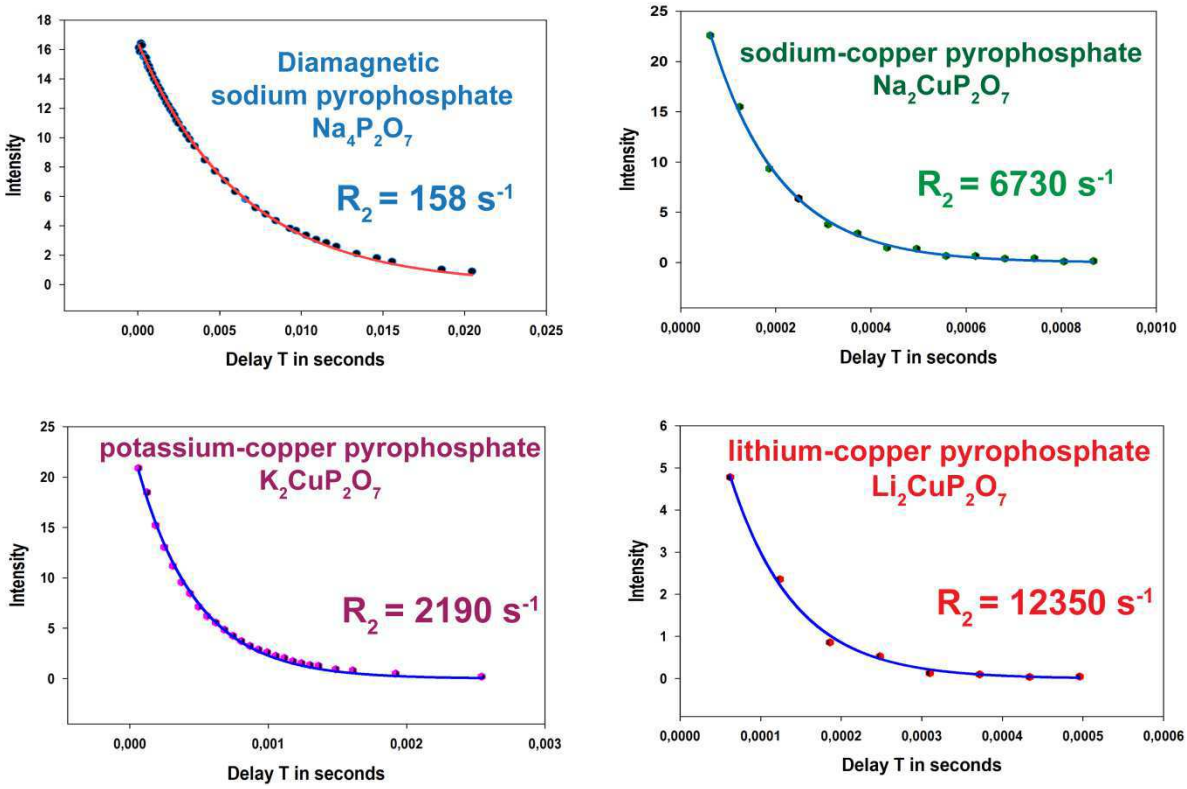

Figure 6.1.3: Comparison of ^{31}P R_2 decay curves from CPMG experiment in paramagnetic sodium-copper pyrophosphate ($Na_2CuP_2O_7$), potassium-copper pyrophosphate ($K_2CuP_2O_7$), lithium-copper pyrophosphate ($Li_2CuP_2O_7$), and diamagnetic sodium pyrophosphate ($Na_4P_2O_7$).

$$R_2 = \frac{1}{15}\left(\frac{\mu_0}{4\pi}\right)^2 \mu_B^2 g^2 \gamma^2 S_e(S_e+1)\frac{1}{r^6}\left(4\tau_c + \frac{3\tau_c}{1+\omega_n^2\tau_c^2} + \frac{13\tau_c}{1+\omega_e^2\tau_c^2}\right) \qquad \textbf{6.3.1}$$

Alkali metal-copper pyrophosphates	^{31}P transverse relaxation rates R_2 from CPMG [s^{-1}]	Expected ^{31}P R_2 rates from XRD distances [s^{-1}]	Copper-phosphorus distances from XRD[93-95] [Å]
$Li_2CuP_2O_7$	12350	9412 / 7339	3.07 / 3.20
$K_2CuP_2O_7$	2190	8221 / 7478	3.14 / 3.19
$Na_2CuP_2O_7$	6730	9558 / 7339	3.06 / 3.20

Table 6.3.1: Comparison of ^{31}P transverse relaxation rate R_2 from: CPMG and expected rates R_2 using XRD distances, in paramagnetic sodium-copper pyrophosphate ($Na_2CuP_2O_7$), potassium-copper pyrophosphate ($K_2CuP_2O_7$), lithium-copper pyrophosphate ($Li_2CuP_2O_7$).

XRD (copper-phosphorus) distance[93-95] were compared (Table 6.3.1). The lithium-copper pyrophosphates were four times larger compared to the expected rates from XRD. However the measured rates and the expected rates were in same order of magnitude for all the three alkaline metal-copper pyrophosphates. From Solomon's rate equation we see that except electron correlation time 'τ_c' and electron-nucleus distance '*r*' rest of them are constant. So the variation in the measured rates indicate that the electron relaxation time T^e is different for the all the three alkaline metal-copper pyrophosphates. The determination of the electronic relaxation time from EPR experiment is not straightforward for these systems, and more advanced methods in EPR will have to be applied.

Chapter 7: Conclusion

"When I examine myself and my methods of thought, I come to the conclusion that the gift of fantasy has meant more to me than any talent for abstract, positive thinking."

- Albert Einstein

The main aim of the thesis was to develop methods in solid state NMR of paramagnetic metal - organic and –inorganic systems in combination with electron paramagnetic resonance spectroscopy (EPR) and density functional theory (DFT) calculations.

We have used paramagnetic copper- and nickel-cyclam and paramagnetic copper–, vanadyl- and nickel-acetylacetonate complexes as model systems in the case of metal-organic part of investigation. In the paramagnetic metal-inorganic system part, we have investigated three alkaline metal (Li^{2+}, K^{2+} and Na^{2+})-copper pyrophosphates using solid state NMR.

Using very fast MAS (30 kHz) we have observed that the paramagnetic Cu- and Ni-cyclam complexes showed drastic enhancement of sensitivity and resolution of ^{1}H and ^{13}C solid state NMR signals. Even though with one pulse experiment one gains optimal intensity, a Hahn-echo experiment was preferred for both ^{1}H and even ^{13}C nuclei to avoid spurious signals from the probe and baseline distortion. We compared the ^{13}C CPMAS spectra of both Cu- and Ni-cyclam complexes with Hahn-echo spectra and found that Hahn-echo was more efficient than CP. The ^{1}H and ^{13}C spectra of Cu- and Ni-cyclam complexes showed clear signs of paramagnetic (Fermi-contact) interactions with signals spreading over large range i.e. almost 200 ppm for ^{1}H (-18 ppm to +173 ppm) and 450 ppm for ^{13}C (+30 ppm to -420 ppm). Assignment of such broad and largely shifted signals is difficult using conventional assignment techniques and one has to rely on quantum chemical calculations such as density functional theory (DFT) for ^{1}H and especially for ^{13}C.

We have used Gaussian 09[83] program to perform DFT calculations on our model systems. The spin densities of ^{13}C for paramagnetic metal-cyclam complexes were obtained after a geometry optimization of the structures and checking for false minima using frequency calculation using hybrid DFT methods such as B3LYP.[151,168] The diamagnetic part of the total shift was theoretically

calculated used DFT methods in G09 using NMR property calculation. With total shift from theoretical calculations in hand we were able to assign ^{13}C solid state NMR signals in both Cu- and Ni-cyclam complexes. Even though the calculations were done for structures in an isolated gaseous state approximation the theoretical shifts were in good agreement with the experimental shifts.

For assignment of ^{1}H solid state NMR signals especially for Cu-cyclam complex a 2D version of dipolar INEPT experiment similar to the one by Kervern *et al.*[61] were used. Dipolar INEPT is a coherent polarization transfer technique similar to INEPT[84] using dipolar rather than *J*-coupling. The MAS averaged dipolar coupling is reintroduced into the systems by using a TEDOR[85] type dipolar recoupling sequence. Since the pulse sequence is rotor-synchronized a very short transfer time ($2\tau_r$ = 66.7 μs) was used. We were successful in identifying the correlation peaks in ^{1}H-^{13}C 2D dipolar INEPT spectra of Cu-cyclam complex. The good resolution in ^{1}H spectra of Cu-cyclam complex motivated us to try a ^{1}H-^{13}C dipolar HSQC with ^{1}H acquisition. We were successful in having two correlation peaks. However the ^{1}H-^{13}C cross peaks originating from carbons too close to the Cu center suffered from severe loss of coherence and hence no cross peaks were observed. But we would like to emphasize that the ^{1}H-^{13}C dipolar HSQC spectra with ^{1}H acquisition obtained in paramagnetic Cu-cyclam complex is unique and one of a kind.

A very well resolved ^{1}H solid state NMR spectrum observed in Cu-cyclam complex motivated us to try some homonuclear correlation type of experiment similar to Correlation spectroscopy (COSY) and Nuclear Overhauser spectroscopy (NOESY) in solution state NMR. The pulse sequence is similar to NOESY with a very short mixing time (~150 μs) and a presaturation pulse during interscan delay and mixing time to avoid evolution of diamagnetic residual signals which covered the signals of interest. Several cross peaks were observed. These cross peaks gave us the dipolar connectivity information between protons which was used for finalizing the ^{1}H assignment in Cu-cyclam complex. The solid state NMR ^{1}H-^{1}H correlation experiment in paramagnetic Cu-cyclam complex can be considered as unique and one of a kind since the technique used is very simple unlike for ^{1}H NMR in diamagnetic solids where a ^{1}H-^{1}H correlation spectra are in most cases not possible.[167] Additional information, in particular for the distinction between equatorial and axial hydrogens, came from a Karplus-type relation for contact shifts.[50,86]

For Ni-cyclam complex, the dipolar INEPT experiment only gave few cross peaks. The reasons for this might lie on the one hand in faster coherence loss due to relaxation on the other hand in interference of the anisotropic interactions, because the t_1 increments had to be set to a fourth ($0.25\,\tau_r$ = 8.33 μs) or eighth ($0.125\,\tau_r$ = 4.17 μs) of a rotor period. Both problems could be overcome by ultrafast MAS (ν_r = 60 kHz). Faster spinning would allow reducing relaxation losses because all the pulse sequence parts that are limited by synchronization could be shortened to one half of the length. Furthermore the spectral width can be doubled without compromising the MAS frequency. The stronger anisotropy in Ni-cyclam due to the presence of two unpaired electron showed furthermore a lot of sidebands. The identification of the ^{1}H signals in 2D experiment for Ni-cyclam was relatively difficult compared to Cu-cyclam. However, we observed that the 2D methods developed for paramagnetic complexes were efficient for complexes with one unpaired electron such as Cu-cyclam complex. Despite some unsuccessful results for Ni-cyclam, we were able to assign the ^{1}H signals by comparing a solution state NMR spectra performed in this work and from the work of Dei *et al.*[77] and Billo *et al.*[66,78].

One of the important and main goals of the thesis was to determine metal-carbon distances using relaxation rates. In paramagnetic metal-organic complexes the carbon-13 relaxation caused by dipolar interaction between the unpaired electron and the nucleus depends on the distance of the carbon atoms to the central metal ion. Hence these rates in principle contain structural information as seen from Solomon's rate equation.[50,87-89] We used Carr Purcell Meiboom Gill (CPMG)[91-92] pulse sequence to measure spin-spin relaxation rate R_2 of ^{13}C signals in Cu-cyclam complex. In our case, electron-nucleus dipolar interaction is the dominant mechanism by which nucleus relaxes. In a solid, the correlation time τ_c in Solomon's rate equation can often be approximated by the electron relaxation time T^e for our system. We have measured the electron relaxation time T^e in Cu-cyclam complex by EPR. The ^{13}C nuclear relaxation rates R_2 and the electron relaxation time T^e were inserted in the Solomon's rate equation and the carbon-copper distances in Cu-cyclam complex were determined. We compared these distances with the X-ray distances of Cu-cyclam SCN^- complex and found that the distances were in good agreement with accuracy of 0.1 Å. This method of determining metal-nucleus distance from nuclear relaxation rate is quite precise since $R_{1,2} \propto 1/r^6$

itself demonstrates how the nuclear relaxation rates are sensitive to the metal-nucleus distance. However, Cu-carbon distances using spin-lattice relaxation rates R_1 showed large deviation from the XRD distances in Cu-cyclam complex. A similar problem seems to have been encountered in the work by another group (Wickramasinghe *et al*).[90] The conclusion is that it is better to measure R_2 rather than R_1. The reason however remains to be understood.

In the second part of our investigation on paramagnetic metal-organic complexes we have investigated paramagnetic copper-, vanadyl-, and nickel- acetylacetonate complexes using the same methods established for paramagnetic metal-cyclam complex. One dimensional ^{1}H and ^{13}C solid state NMR Hahn-echo served as basic solid state NMR experiments for the investigation. The assignment of ^{13}C signals in $Cu[acac]_2$ and $VO[acac]_2$ was done using the spin density from DFT calculation. The presence of one unpaired electron in: $d_{x^2-y^2}$ orbital in Cu^{2+} ion (with valence shell electronic configuration d^9) and d_{xy} orbital in VO^{2+} ion (with valence shell electronic configuration of d^1) led to completely different contact shifts, as consistently seen in both the experimental ^{13}C spectra and the DFT calculations. However, due to complex trimerization in Ni-acac which was reflected in the ^{13}C Hahn-echo spectra the ^{13}C assignment from DFT calculation was not straightforward. The spectra showed at least 6 different carbon signals. Furthermore for assignment of ^{1}H signals a 2D dipolar INEPT experiment was used (as done before for Cu-cyclam complex) for Cu-acac and VO-acac complexes.

Some of the interesting and successful results seen in solid state NMR of paramagnetic metal-organic systems motivated us to extend the solid state NMR investigation on metal-inorganic systems. Here phosphorus isotope ^{31}P was the subject of NMR interest in alkali metal (Li^{2+}, K^{2+} and Na^{2+}]-copper pyrophosphate systems. Due to the presence of paramagnetic metal ion of copper we observed severely shifted phosphorus signals up to 1000 ppm beyond the diamagnetic range (250 ppm to -200 ppm) in all the three alkali metal-copper pyrophosphates.

We tried to test the feasibility of method of determining copper-nucleus distances using relaxation rates in these alkali metal-copper pyrophosphates as done for paramagnetic Cu-cyclam complex. The electronic relaxation time could not be easily determined for the alkaline metal-copper

pyrophosphates as for Cu-cyclam. Therefore only a rough estimation was possible, which show that the transverse relaxation rates R_2 were in correct order of magnitude, while the R1 rates were again much too low. For the future, we will need to establish a technique to measure the electronic relaxation times, for example by saturation curves. Furthermore, the R_1 problem demands for a theoretical explanation.

The experiments developed within this thesis were not applicable to all systems because the relaxation during the pulse sequences was too fast. Faster spinning with up to 60 kHz, technically now possible with 1.3 mm probes, not only improves the suppression of the anisotropic interactions, but also allow a reduction of the duration of the pulse sequences by a factor of 2, thus reducing the relaxation losses during the experiment.

References:

(1) Tanaka, K.; Toda, F. *Chemical Reviews* **2000**, *100*, 1025.

(2) Tatsuma, T.; Watanabe, T. *Analytical Chemistry* **1991**, *63*, 1580.

(3) Okuda, J.; Wakai, J.; Sode, K. *Analytical Letters* **2002**, *35*, 1465.

(4) Ju, H.; Liu, S.; Ge, B.; Lisdat, F.; Scheller, F. W. *Electroanalysis* **2002**, *14*, 141.

(5) Thordarson, P.; Marquis, A.; Crossley, M. J. *Organic & Biomolecular Chemistry* **2003**, *1*, 1216.

(6) Kassiba, A.; Makowska-Janusik, M.; Alauzun, J.; Kafrouni, W.; Mehdi, A.; Reyé, C.; Corriu, R. J.; Gibaud, A. *Journal of Physics and Chemistry of Solids* **2006**, *67*, 875.

(7) Laskowski, L.; et al. *Journal of Physics: Condensed Matter* **2009**, *21*, 076004.

(8) Makowska-Janusik, M.; Kassiba, A.; Errien, N.; Mehdi, A. *Journal of Inorganic and Organometallic Polymers and Materials* **2010**, *20*, 761.

(9) Bertini, I., Gray, H. B., Lippard, S. J. and Valentine, J. S. *University Science Books, Mill Valley, California* **1994**.

(10) Liang, X.; Sadler, P. J. *Chemical Society Reviews* **2004**, *33*, 246.

(11) Williams, D. B., and C. Barry Carter *2nd ed., New York: Springer, 2010, 1st ed. New York: Plenum Press,* **2010**.

(12) Klinowski, J. *Annual Review of Materials Science* **1988**, *18*, 189.

(13) Tongyin, Y.; Mingming, G. *Progress in Polymer Science* **1990**, *15*, 825.

(14) Lesage, A. *Physical Chemistry Chemical Physics* **2009**, *11*, 6876.

(15) Ashbrook, S. E. *Physical Chemistry Chemical Physics* **2009**, *11*, 6892.

(16) Hanna, J. V.; Smith, M. E. *Solid State Nuclear Magnetic Resonance* **2010**, *38*, 1.

(17) Ishii, Y.; Wickramasinghe, N. P.; Chimon, S. *Journal of the American Chemical Society* **2003**, *125*, 3438.

(18) Duer, M. J. *Blackwell Science, Oxford* **2004**.

(19) Hunger, M.; Wang, W. In *Handbook of Heterogeneous Catalysis*; Wiley-VCH Verlag GmbH & Co. KGaA: 2008.

(20) Koch, B.; Vogel, M. *Solid State Nuclear Magnetic Resonance* **2008**, *34*, 37.

(21) Hain, H.; Scheuermann, M.; Heinzmann, R.; Wünsche, L.; Hahn, H.; Indris, S. *Solid State Nuclear Magnetic Resonance* **2012**, *42*, 9.

(22) Kuhn, A.; Kunze, M.; Sreeraj, P.; Wiemhöfer, H. D.; Thangadurai, V.; Wilkening, M.; Heitjans, P. *Solid State Nuclear Magnetic Resonance* **2012**, *42*, 2.

(23) Mali, G.; Rangus, M.; Sirisopanaporn, C.; Dominko, R. *Solid State Nuclear Magnetic Resonance* **2012**, *42*, 33.

(24) Bakhmutov, V. I. *Chemical Reviews* **2010**, *111*, 530.

(25) Fung, B. M.; Khitrin, A. K.; Ermolaev, K. *Journal of Magnetic Resonance* **2000**, *142*, 97.

(26) Fung, B. M. *Progress in Nuclear Magnetic Resonance Spectroscopy* **2002**, *41*, 171.
(27) Dong, R. Y. In *Annual Reports on NMR Spectroscopy*; Webb, G. A., Ed.; Academic Press: 2004; Vol. Volume 53, p 67.
(28) Schnell, I. *Progress in Nuclear Magnetic Resonance Spectroscopy* **2004**, *45*, 145.
(29) Lesot, P.; Courtieu, J. *Progress in Nuclear Magnetic Resonance Spectroscopy* **2009**, *55*, 128.
(30) Schmidt-Rohr, K., Spiess, H. W. *Academic Press, London* **1994**.
(31) Aguiar, P. M.; Katz, M. J.; Leznoff, D. B.; Kroeker, S. *Physical Chemistry Chemical Physics* **2009**, *11*, 6925.
(32) Steger, T. R.; Schaefer, J.; Stejskal, E. O.; McKay, R. A.; Sefcik, M. D. *Annals of the New York Academy of Sciences* **1981**, *371*, 106.
(33) Peter Puls, S.; Eckert, H. *Physical Chemistry Chemical Physics* **2007**, *9*, 3992.
(34) Hiet, J.; Deschamps, M.; Pellerin, N.; Fayon, F.; Massiot, D. *Physical Chemistry Chemical Physics* **2009**, *11*, 6935.
(35) Wong, A.; Howes, A. P.; Parkinson, B.; Anupold, T.; Samoson, A.; Holland, D.; Dupree, R. *Physical Chemistry Chemical Physics* **2009**, *11*, 7061.
(36) Hayashi, S. In *Annual Reports on NMR Spectroscopy*; Ando, I., Webb, G. A., Eds.; Academic Press: 1994; Vol. Volume 28, p 29.
(37) Sehlleier, Y. H.; Verhoeven, A.; Jansen, M. *Zeitschrift für anorganische und allgemeine Chemie* **2012**, n/a.
(38) Smith, S. O.; Peersen, O. B. *Annual Review of Biophysics and Biomolecular Structure* **1992**, *21*, 25.
(39) Cross, T. A.; Opella, S. J. *Current Opinion in Structural Biology* **1994**, *4*, 574.
(40) de Groot, H. J. M. *Current Opinion in Structural Biology* **2000**, *10*, 593.
(41) Kamihira, M.; Vosegaard, T.; Mason, A. J.; Straus, S. K.; Nielsen, N. C.; Watts, A. *Journal of Structural Biology* **2005**, *149*, 7.
(42) Geppi, M.; Mollica, G.; Borsacchi, S.; Veracini, C. A. *Applied Spectroscopy Reviews* **2008**, *43*, 202.
(43) McConnell, H. M.; Robertson, R. E. *The Journal of Chemical Physics* **1958**, *29*, 1361.
(44) Liu, K.; Ryan, D.; Nakanishi, K.; McDermott, A. *Journal of the American Chemical Society* **1995**, *117*, 6897.
(45) Chacko, V. P.; Ganapathy, S.; Bryant, R. G. *Journal of the American Chemical Society* **1983**, *105*, 5491.
(46) Ganapathy, S.; Bryant, R. G. *Journal of Magnetic Resonance (1969)* **1986**, *70*, 149.
(47) Willans, M. J.; Sears, D. N.; Wasylishen, R. E. *Journal of Magnetic Resonance* **2008**, *191*, 31.

(48) Smernik, R. J.; Oades, J. M. *J. Environ. Qual.* **2002**, *31*, 414.
(49) La Mar, G. N., Horrocks, W.D., Holm H. R. *Academic Press, New York* **1973**.
(50) Bertini, I., Luchinat, C. and Parigi, G. *Coord. Chem. Rev.* **1996**, *150*.
(51) Bertini, I., Luchinat, C. and Parigi, G. *Current Methods in Inorganic Chemistry* **2001**, *2*.
(52) Banci, L.; Luchinat, C. *Inorganica Chimica Acta* **1998**, *275–276*, 373.
(53) Banci, L.; Bertini, I.; Bren, K. L.; Cremonini, M. A.; Gray, H. B.; Luchinat, C.; Turano, P. *Journal of Biological Inorganic Chemistry* **1996**, *1*, 117.
(54) Kosen, P. A. In *Methods in Enzymology*; Norman, J. O., Thomas, L. J., Eds.; Academic Press: 1989; Vol. Volume 177, p 86.
(55) Respondek, M.; Madl, T.; Göbl, C.; Golser, R.; Zangger, K. *Journal of the American Chemical Society* **2007**, *129*, 5228.
(56) Dittmer, J.; Thøgersen, L.; Underhaug, J.; Bertelsen, K.; Vosegaard, T.; Pedersen, J. M.; Schiøtt, B.; Tajkhorshid, E.; Skrydstrup, T.; Nielsen, N. C. *The Journal of Physical Chemistry B* **2009**, *113*, 6928.
(57) Brough, A. R.; Grey, C. P.; Dobson, C. M. *Journal of the American Chemical Society* **1993**, *115*, 7318.
(58) Clayton, A. N.; Dobson, C. M.; Grey, C. P. *Journal of the Chemical Society, Chemical Communications* **1990**, 72.
(59) Wickramasinghe, N. P.; Shaibat, M.; Ishii, Y. *Journal of the American Chemical Society* **2005**, *127*, 5796.
(60) Wickramasinghe, N. P.; Ishii, Y. *Journal of Magnetic Resonance* **2006**, *181*, 233.
(61) Kervern, G.; Pintacuda, G.; Zhang, Y.; Oldfield, E.; Roukoss, C.; Kuntz, E.; Herdtweck, E.; Basset, J.-M.; Cadars, S.; Lesage, A.; Copéret, C.; Emsley, L. *Journal of the American Chemical Society* **2006**, *128*, 13545.
(62) Barefield, E. K. *Inorganic Chemistry* **1972**, *11*, 2273.
(63) Barefield, E. K.; Wagner, F. *Inorganic Chemistry* **1973**, *12*, 2435.
(64) Tasker, P. A.; Sklar, L. *Journal of Chemical Crystallography* **1975**, *5*, 329.
(65) Chan, P.-K.; Poon, C.-K. *Journal of the Chemical Society, Dalton Transactions* **1976**, 858.
(66) Joseph Billo, E.; Connolly, P. J.; Sardella, D. J.; Jasinski, J. P.; Butcher, R. J. *Inorganica Chimica Acta* **1995**, *230*, 19.
(67) Lu, T.-H.; Tahirov, T. H.; Liu, Y.-L.; Chung, C.-S.; Huang, C.-C.; Hong, Y.-S. *Acta Crystallographica Section C* **1996**, *52*, 1093.
(68) De Buysser, K.; Herman, G. G.; Bruneel, E.; Hoste, S.; Van Driessche, I. *Chemical Physics* **2005**, *315*, 286.
(69) So, H.; Jung, H.; Choy, J.-H.; Belford, R. L. *The Journal of Physical Chemistry B* **2005**, *109*, 3324.

(70) De Buysser K., H. G. G., Bruneel E., Hoste S., Van Driessche I. *MEASUREMENT SCIENCE REVIEW* **2005**, *5*, 30.
(71) Kent Barefield, E. *Coordination Chemistry Reviews* **2010**, *254*, 1607.
(72) Schols, D.; Esté, J. A.; Henson, G.; De Clercq, E. *Antiviral Research* **1997**, *35*, 147.
(73) Xu, P.; Yu, H.; Li, X. *Analytical Chemistry* **2011**, *83*, 3448.
(74) Bosnich, B.; Mason, R.; Pauling, P. J.; Robertson, G. B.; Tobe, M. L. *Chemical Communications (London)* **1965**, 97.
(75) Bosnich, B.; Tobe, M. L.; Webb, G. A. *Inorganic Chemistry* **1965**, *4*, 1109.
(76) Tasuku Ito, M. K. a. H. I. *Bulletin of the Chemical Society of Japan* **1984**, *57*, 2641.
(77) Dei, A. *Inorganic Chemistry* **1979**, *18*, 891.
(78) Connolly, P. J.; Billo, E. J. *Inorganic Chemistry* **1987**, *26*, 3224.
(79) Wilkens, S. J.; Xia, B.; Weinhold, F.; Markley, J. L.; Westler, W. M. *Journal of the American Chemical Society* **1998**, *120*, 4806.
(80) Wilkens, S. J.; Xia, B.; Volkman, B. F.; Weinhold, F.; Markley, J. L.; Westler, W. M. *The Journal of Physical Chemistry B* **1998**, *102*, 8300.
(81) Zhang, Y.; Sun, H.; Oldfield, E. *Journal of the American Chemical Society* **2005**, *127*, 3652.
(82) Mao, J.; Zhang, Y.; Oldfield, E. *Journal of the American Chemical Society* **2002**, *124*, 13911.
(83) Gaussian 09, R. A., Frisch, M. J.; Trucks, G. W.; Schlegel, H. B.; Scuseria, G. E.; Robb, M. A.; Cheeseman, J. R.; Scalmani, G.; Barone, V.; Mennucci, B.; Petersson, G. A.; Nakatsuji, H.; Caricato, M.; Li, X.; Hratchian, H. P.; Izmaylov, A. F.; Bloino, J.; Zheng, G.; Sonnenberg, J. L.; Hada, M.; Ehara, M.; Toyota, K.; Fukuda, R.; Hasegawa, J.; Ishida, M.; Nakajima, T.; Honda, Y.; Kitao, O.; Nakai, H.; Vreven, T.; Montgomery, Jr., J. A.; Peralta, J. E.; Ogliaro, F.; Bearpark, M.; Heyd, J. J.; Brothers, E.; Kudin, K. N.; Staroverov, V. N.; Kobayashi, R.; Normand, J.; Raghavachari, K.; Rendell, A.; Burant, J. C.; Iyengar, S. S.; Tomasi, J.; Cossi, M.; Rega, N.; Millam, J. M.; Klene, M.; Knox, J. E.; Cross, J. B.; Bakken, V.; Adamo, C.; Jaramillo, J.; Gomperts, R.; Stratmann, R. E.; Yazyev, O.; Austin, A. J.; Cammi, R.; Pomelli, C.; Ochterski, J. W.; Martin, R. L.; Morokuma, K.; Zakrzewski, V. G.; Voth, G. A.; Salvador, P.; Dannenberg, J. J.; Dapprich, S.; Daniels, A. D.; Farkas, Ö.; Foresman, J. B.; Ortiz, J. V.; Cioslowski, J.; Fox, D. J. *Gaussian, Inc., Wallingford CT, .* **2009**.
(84) Morris, G. A.; Freeman, R. *Journal of the American Chemical Society* **1979**, *101*, 760.
(85) Hing, A. W.; Vega, S.; Schaefer, J. *Journal of Magnetic Resonance (1969)* **1992**, *96*, 205.
(86) Karplus, M. *Journal of the American Chemical Society* **1963**, *85*, 2870.
(87) Solomon, I. *Physical Review* **1955**, *99*, 559.
(88) Koenig, S. H. *Journal of Magnetic Resonance (1969)* **1978**, *31*, 1.

(89) Konig, S. H. *Journal of Magnetic Resonance (1969)* **1982**, *47*, 441.
(90) Wickramasinghe, N. P.; Shaibat, M. A.; Jones, C. R.; Casabianca, L. B.; de Dios, A. C.; Harwood, J. S.; Ishii, Y. *The Journal of Chemical Physics* **2008**, *128*, 052210.
(91) Carr, H. Y.; Purcell, E. M. *Physical Review* **1954**, *94*, 630.
(92) Meiboom, S.; Gill, D. *Review of Scientific Instruments* **1958**, *29*, 688.
(93) Erragh, F.; Boukhari, A.; Abraham, F.; Elouadi, B. *Journal of Solid State Chemistry* **1995**, *120*, 23.
(94) ElMaadi, A.; Boukhari, A.; Holt, E. M. *Journal of Alloys and Compounds* **1995**, *223*, 13.
(95) Gopalakrishna, G. S.; Mahesh, M. J.; Ashamanjari, K. G.; Prasad, J. S. *Materials Research Bulletin* **2008**, *43*, 1171.
(96) Rabi, I. I.; Zacharias, J. R.; Millman, S.; Kusch, P. *Physical Review* **1938**, *53*, 318.
(97) Purcell, E. M.; Torrey, H. C.; Pound, R. V. *Physical Review* **1946**, *69*, 37.
(98) Bloch, F.; Hansen, W. W.; Packard, M. *Physical Review* **1946**, *70*, 474.
(99) Bloch, F. *Physical Review* **1946**, *70*, 460.
(100) Bloch, F.; Hansen, W. W.; Packard, M. *Physical Review* **1946**, *69*, 127.
(101) Ernst, R. R.; Anderson, W. A. *Review of Scientific Instruments* **1966**, *37*, 93.
(102) Hahn, E. L. *Physical Review* **1950**, *80*, 580.
(103) Proctor, W. G.; Yu, F. C. *Physical Review* **1950**, *77*, 717.
(104) Dickinson, W. C. *Physical Review* **1950**, *77*, 736.
(105) Meyer, L. H.; Saika, A.; Gutowsky, H. S. *Journal of the American Chemical Society* **1953**, *75*, 4567.
(106) Levine, S. G. *Journal of Chemical Education* **2001**, *78*, 133.
(107) Nagaoka, S.-i. *Journal of Chemical Education* **2007**, *84*, 801.
(108) Gutowsky, H. S.; McCall, D. W.; Slichter, C. P. *Physical Review* **1951**, *84*, 589.
(109) Hahn, E. L.; Maxwell, D. E. *Physical Review* **1951**, *84*, 1246.
(110) Ramsey, N. F.; Purcell, E. M. *Physical Review* **1952**, *85*, 143.
(111) Smith, M. *Pergamon Publications* **2002**, *6*.
(112) Castellani, F.; van Rossum, B.; Diehl, A.; Schubert, M.; Rehbein, K.; Oschkinat, H. *Nature* **2002**, *420*, 98.
(113) Jaroniec, C. P.; MacPhee, C. E.; Bajaj, V. S.; McMahon, M. T.; Dobson, C. M.; Griffin, R. G. *Proceedings of the National Academy of Sciences of the United States of America* **2004**, *101*, 711.
(114) Andrew, E. R.; Bradbury, A.; Eades, R. G. *Nature* **1958**, *182*, 1659.
(115) Andrew, E. R.; Bradbury, A.; Eades, R. G. *Nature* **1959**, *183*, 1802.
(116) Andrew, E. R.; Bradbury, A.; Eades, R. G.; Jenks, G. J. *Nature* **1960**, *188*, 1096.
(117) Andrew, E. R.; Eades, R. G. *Discussions of the Faraday Society* **1962**, *34*, 38.

(118) Pines, A.; Gibby, M. G.; Waugh, J. S. *The Journal of Chemical Physics* **1973**, *59*, 569.
(119) Bennett, A. E.; Rienstra, C. M.; Auger, M.; Lakshmi, K. V.; Griffin, R. G. *The Journal of Chemical Physics* **1995**, *103*, 6951.
(120) Bork, V.; Gullion, T.; Hing, A.; Schaefer, J. *Journal of Magnetic Resonance (1969)* **1990**, *88*, 523.
(121) Shore, S. E.; Ansermet, J.-P.; Slichter, C. P.; Sinfelt, J. H. *Physical Review Letters* **1987**, *58*, 953.
(122) Pan, Y.; Gullion, T.; Schaefer, J. *Journal of Magnetic Resonance (1969)* **1990**, *90*, 330.
(123) Fyfe, C. A.; Wong-Moon, K. C.; Huang, Y.; Grondey, H. *Journal of the American Chemical Society* **1995**, *117*, 10397.
(124) Elena, B.; Lesage, A.; Steuernagel, S.; Böckmann, A.; Emsley, L. *Journal of the American Chemical Society* **2005**, *127*, 17296.
(125) Saalwächter, K.; Graf, R.; Spiess, H. W. *Journal of Magnetic Resonance* **2001**, *148*, 398.
(126) Saalwächter, K.; Graf, R.; Spiess, H. W. *Journal of Magnetic Resonance* **1999**, *140*, 471.
(127) Saalwächter, K.; Schnell, I. *Solid State Nuclear Magnetic Resonance* **2002**, *22*, 154.
(128) Saalwachter, K.; Spiess, H. W. *The Journal of Chemical Physics* **2001**, *114*, 5707.
(129) Lowe, I. J. *Physical Review Letters* **1959**, *2*, 285.
(130) Hartmann, S. R.; Hahn, E. L. *Physical Review* **1962**, *128*, 2042.
(131) Stejskal, E. O.; Schaefer, J.; Waugh, J. S. *Journal of Magnetic Resonance (1969)* **1977**, *28*, 105.
(132) Metz, G.; Wu, X. L.; Smith, S. O. *Journal of Magnetic Resonance, Series A* **1994**, *110*, 219.
(133) Anderson, W. A.; Freeman, R. *The Journal of Chemical Physics* **1962**, *37*, 85.
(134) Bloom, A. L.; Shoolery, J. N. *Physical Review* **1955**, *97*, 1261.
(135) Ernst, R. R., Bodenhausen, G., and Wokaun, A. *Oxford Univ. Press, London/New York* **1987**.
(136) Ernst, M. *Journal of Magnetic Resonance* **2003**, *162*, 1.
(137) Ernst, M.; Samoson, A.; Meier, B. H. *Chemical Physics Letters* **2001**, *348*, 293.
(138) Levitt, M. H.; Freeman, R. *Journal of Magnetic Resonance (1969)* **1981**, *43*, 502.
(139) Shaka, A. J.; Freeman, R. *Journal of Magnetic Resonance (1969)* **1983**, *55*, 487.
(140) Gullion, T.; Schaefer, J. *Journal of Magnetic Resonance (1969)* **1989**, *81*, 196.
(141) Laws, D. D.; Bitter, H.-M. L.; Jerschow, A. *Angewandte Chemie International Edition* **2002**, *41*, 3096.
(142) Parr, R. G. *Density-Functional Theory of Atoms and Molecules*; Oxford University Press, USA, 1994.
(143) Kohn, W.; Sham, L. J. *Physical Review* **1965**, *140*, A1133.
(144) Rastrelli, F.; Bagno, A. *Chemistry – A European Journal* **2009**, *15*, 7990.

(145) Bühl, M.; Kabrede, H. *Journal of Chemical Theory and Computation* **2006**, *2*, 1282.
(146) Bertini, I.; Emsley, L.; Lelli, M.; Luchinat, C.; Mao, J.; Pintacuda, G. *Journal of the American Chemical Society* **2010**, *132*, 5558.
(147) Hrobarik, P.; Reviakine, R.; Arbuznikov, A. V.; Malkina, O. L.; Malkin, V. G.; Kohler, F. H.; Kaupp, M. *The Journal of Chemical Physics* **2007**, *126*, 024107.
(148) Adam, K. R.; Atkinson, I. M.; Lindoy, L. F. *Inorganic Chemistry* **1997**, *36*, 480.
(149) Carlier, D.; eacute; trier, M.; Grey, C. P.; Delmas, C.; Ceder, G. *Physical Review B* **2003**, *67*, 174103.
(150) Becke, A. D. *The Journal of Chemical Physics* **1986**, *85*, 7184.
(151) Perdew, J. P. *Physical Review Letters* **1985**, *55*, 1665.
(152) Lindoy, L. F. *The Chemistry of Macrocyclic Ligand Complexes*; Cambridge University Press, 1990.
(153) Zagal, J. H.; Dodelet, J. P.; Bedioui, F. *N4-Macrocyclic Metal Complexes*; Springer, 2006.
(154) Evers, A.; Hancock, R. D. *Inorganica Chimica Acta* **1989**, *160*, 245.
(155) Kotek, J.; Lubal, P.; Hermann, P.; Císařová, I.; Lukeš, I.; Godula, T.; Svobodová, I.; Táborský, P.; Havel, J. *Chemistry – A European Journal* **2003**, *9*, 233.
(156) Alcock, N. W.; Berry, A.; Moore, P. *Acta Crystallographica Section C* **1992**, *48*, 16.
(157) Hunter, T. M.; McNae, I. W.; Liang, X.; Bella, J.; Parsons, S.; Walkinshaw, M. D.; Sadler, P. J. *Proceedings of the National Academy of Sciences of the United States of America* **2005**, *102*, 2288.
(158) Silversides, J. D.; Allan, C. C.; Archibald, S. J. *Dalton Trans.* **2007**, 971.
(159) Smith, S. V. *Journal of Inorganic Biochemistry* **2004**, *98*, 1874.
(160) Diaz F, G.; Clavijo C, R. E.; Campos-Vallette, M. M.; Saavedra S, M.; Diez, S.; Muñoz, R. *Vibrational Spectroscopy* **1997**, *15*, 201.
(161) Izatt, R. M.; Pawlak, K.; Bradshaw, J. S.; Bruening, R. L. *Chemical Reviews* **1995**, *95*, 2529.
(162) Whimp, P. O.; Bailey, M. F.; Curtis, N. F. *Journal of the Chemical Society A: Inorganic, Physical, Theoretical* **1970**, 1956.
(163) Lawrance, G. A. *Introduction to Coordination Chemistry*; John Wiley & Sons, 2010.
(164) Chen, X.; Long, G.; Willett, R. D.; Hawks, T.; Molnar, S.; Brewer, K. *Acta Crystallographica Section C* **1996**, *52*, 1924.
(165) Wang, Z.; Willett, R. D.; Molnar, S.; Brewer, K. J. *Acta Crystallographica Section C* **1996**, *52*, 581.
(166) Prasad, L.; Nyburg, S. C.; McAuley, A. *Acta Crystallographica Section C* **1987**, *43*, 1038.
(167) Vinogradov, E.; Madhu, P.; Vega, S.; Klinowski, J., Ed.; Springer Berlin / Heidelberg: 2005; Vol. 246, p 33.

(168) Becke, A. D. *The Journal of Chemical Physics* **1988**, *88*, 1053.
(169) Davidson, E. R.; Feller, D. *Chemical Reviews* **1986**, *86*, 681.
(170) Lovecchio, F. V.; Gore, E. S.; Busch, D. H. *Journal of the American Chemical Society* **1974**, *96*, 3109.
(171) Fabbrizzi, L.; Micheloni, M.; Paoletti, P. *Journal of the Chemical Society, Dalton Transactions* **1980**, 134.
(172) Churchard, A. J.; Cyranski, M. K.; Dobrzycki, L.; Budzianowski, A.; Grochala, W. *Energy & Environmental Science* **2010**, *3*, 1973.
(173) Zagal, J.; Páez, M.; Silva, J.; Zagal, J. H., Bedioui, F., Dodelet, J.-P., Eds.; Springer New York: 2006, p 41.
(174) Bosnich, B.; Poon, C. K.; Tobe, M. L. *Inorganic Chemistry* **1965**, *4*, 1102.
(175) De Vita, E.; Frydman, L. *Journal of Magnetic Resonance* **2001**, *148*, 327.
(176) Kervern, G.; Steuernagel, S.; Engelke, F.; Pintacuda, G.; Emsley, L. *Journal of the American Chemical Society* **2007**, *129*, 14118.
(177) Connick, R. E.; Fiat, D. *The Journal of Chemical Physics* **1966**, *44*, 4103.
(178) Reuben, J.; Reed, G. H.; Cohn, M. *The Journal of Chemical Physics* **1970**, *52*, 1617.
(179) Kemple, M. D.; Stapleton, H. J. *Physical Review B* **1972**, *5*, 1668.
(180) Lamprey, H. *Annals of the New York Academy of Sciences* **1960**, *88*, 519.
(181) Petrie, R. D. S. *United States Patent 2644840* **1953**.
(182) Chovin, P. *Rubber Chemistry and Technology* **1945**, *18*, 607.
(183) Bellinger, F.; Friedman, H. B.; Bauer, W. H.; Eastes, J. W.; Bull, W. C. *Industrial & Engineering Chemistry* **1948**, *40*, 1320.
(184) Val M. Runge, J. A. C. *United States Patent 4615879* **1986**.
(185) Eaton, D. R. *Journal of the American Chemical Society* **1965**, *87*, 3097.
(186) Lingafelter, E. C.; Braun, R. L. *Journal of the American Chemical Society* **1966**, *88*, 2951.
(187) Z. A. Starikova, E. A. S. *Zhumal Strukturnoi Khimii* **1969**, *10*, 290.
(188) Lebrun, P. C.; Lyon, W. D.; Kuska, H. A. *Journal of Chemical Crystallography* **1986**, *16*, 889.
(189) Berry, G., Callon, G., Gowans, B., Low, J. N. & Smith, R. *Private communication to the Cambridge Crystallographic Data Centre* **2004**.
(190) Dodge, R. P.; Templeton, D. H.; Zalkin, A. *The Journal of Chemical Physics* **1961**, *35*, 55.
(191) Hoshino, M.; Sekine, A.; Uekusa, H.; Ohashi, Y. *Chemistry Letters* **2005**, *34*, 1228.
(192) Bullen, G. J.; Mason, R.; Pauling, P. *Nature* **1961**, *189*, 291.
(193) Montgomery, H.; Lingafelter, E. C. *Acta Crystallographica* **1964**, *17*, 1481.
(194) Hon, P.-K.; Belford, R. L.; Pfluger, C. E. *The Journal of Chemical Physics* **1965**, *43*, 3111.

(195) Claramunt, R. M.; López, C.; Lott, S.; Santa María, M. D.; Alkorta, I.; Elguero, J. *Helvetica Chimica Acta* **2005**, *88*, 1931.

(196) Takegoshi, K.; Schenk, K. J.; McDowell, C. A. *Inorganic Chemistry* **1987**, *26*, 2552.

(197) Bullen, G. J. *Nature* **1956**, *177*, 537.

(198) Lingafelter, E. C. *Coordination Chemistry Reviews* **1966**, *1*, 151.

(199) Mikami, M.; Nakagawa, I.; Shimanouchi, T. *Spectrochimica Acta Part A: Molecular Spectroscopy* **1967**, *23*, 1037.

APPENDIX

APPENDIX I: NMR pulse programs

I.1: One pulse

```
1 ze
2 30m
  d1
  p1 ph1
  go=2 ph31
  30m mc #0 to 2 F0(zd)
exit


ph1=0 2 2 0 1 3 3 1
ph31=0 2 2 0 1 3 3 1
```

I.2. Hahn-echo

```
1 ze
2 10m
# ifdef dec
  d1 do:f2
# else
  d1
# endif /* dec */
(p1 pl1 ph1):f1
# ifdef dec
d6 cpds2:f2
# else
d6
# endif /* dec */
(p2 ph2):f1
go=2 ph31
# ifdef dec
1m do:f2
# endif /* dec */
10m mc #0 to 2 F1QF(id0)
exit

ph0=0
ph1=0 1 2 3
ph2=0 0 0 0 1 1 1 1 2 2 2 2 3 3 3 3
ph30=0
ph31=0 3 2 1 2 1 0 3
```

I.3: CP MAS

```
1 ze
2 d1 do:f2
1u fq=cnst21:f2
(p3 pl12 ph1):f2
(p15 pl1 ph2):f1 (p15:sp0ph10):f2
1u cpds2:f2
go=2 ph31
1m do:f2
wr #0
HaltAcqu, 1m
exit

ph0= 0
ph1= 1 3
ph2= 0 0 2 2 1 1 3 3
ph10= 0
ph31= 0 2 2 0 1 3 3 1
```

I.4: Inversion recovery

```
1 ze
2 30m
d1
p2 ph1
d7
p1 ph2
d6
p2 ph22
go=2 ph31
30m mc #0 to 2 F0(zd)
exit


ph1 =0 2
ph2 =0 0 2 2 3 3 1 1
ph22=0 0 0 0 0 0 0 0
     1 1 1 1 1 1 1 1
     2 2 2 2 2 2 2 2
     3 3 3 3 3 3 3 3
ph31=0 0 2 2 1 1 3 3
     2 2 0 0 3 3 1 1
```

I.5: Saturation recovery

```
1 ze
2 30m
  d1
3 d20
  (p1 pl1 ph4):f1
  lo to 3 times l20
;  p2 ph1
  d7
  p1 ph2
  d6
  p2 ph22
  go=2 ph31
  30m mc #0 to 2 F0(zd)
exit


ph2=0 2 1 3
ph22=1 3 2 0
     2 0 3 1
     3 1 0 2
     0 2 1 3
ph4=1
ph31=0 2 1 3
     2 0 3 1
```

I.6: CPMG

```
1 ze
2 30m
d1
p1 ph1
3 d20
p2 ph2
d20
lo to 3 times l4
d21
p2 ph2
;d21
go=2 ph31
30m mc #0 to 2 F0(zd)
exit


ph1=0 0 2 2 1 1 3 3
ph2=1 3 1 3 0 2 0 2
ph31=0 0 2 2 1 1 3 3
```

I.7: 2D dipolar INEPT

```
"d6=1s/cnst31"
"d15=d6-p3*2/3.14-d14-p2-p4/2"
"d16=p3*2/3.14+d14+p2/2-p4/2-p2/2"
"d17=d6-p4/2-d16-p2-p1/2"
"d18=p3*2/3.14+d14+p2/2-p1/2-p4/2"
"d19=d6-p1/2-d18-p4-p2/2"
"d20=p1/2+d18+p4/2-p2/2-p4/2"
"d21=d6-p2/2-d20-p4-de"

1 ze
2 10m
3 d1
(p11 pl11 ph20):f1
 d25
 (p11 pl11 ph21):f1
 d26
 (p11 pl11 ph22):f1
 d27
 (p3 pl2 ph1):f2
 d0
 d14
 (p2 pl1 ph10):f1
 d15
 (p4 pl2 ph6):f2
 d16
 (p2 pl1 ph11):f1
 d17
 (center (p1 pl1 ph2):f1 (p3 pl2 ph2):f2)
 d18
 (p4 pl2 ph12):f2
 d19
 (p2 pl1 ph3):f1
 d20
 (p4 pl2 ph13):f2
 d21
 ;(p3 pl2 ph7):f2
go=2 ph31 ;acquire
1m
10m mc #0 to 2 F1PH(ip1,id0)
exit                    ;exit

ph1 =0 1 2 3
ph2 =1 2 3 0
ph3 =0 0 0 0 1 1 1 1 2 2 2 2 3 3 3 3
ph6 =0
ph7 =0
ph10=0
ph11=2
ph12=0
ph13=2
ph20=0
ph21=1
ph22=0
ph31=1 2 3 0 3 0 1 2 1 2 3 0 3 0 1 2
```

I.8: 2D dipolar HSQC

```
"d6=1s/cnst31"
"d14=d6/2-p1/2-p2/2"
"d15=d6/2-p2/2-p3/2"
"d16=d6/2-p2/2"
1 ze
2 10m
3 d1

 (p1 pl1 ph1):f1
 d14
 (p2 pl1 ph21):f1                ;1H 180
 d15
 (center (p1 pl1 ph3):f1 (p3 pl2 ph6):f2 )

 d0

 (center (p1 pl1 ph4):f1 (p3 pl2 ph7):f2 )
 d15
 (p2 pl1 ph21):f1      ;1H 180
 d16

 go=2 ph31
          ;acquire
 1m
 10m mc #0 to 2 F1PH(ip6,id0)

exit                    ;exit


ph1 =0
ph21=0
ph3 =1
ph6 =0 2
ph7 =0 0 2 2
ph4 =1
ph31=0 2 2 0

;ph1 =0
;ph2 =0
;ph3 =1
;ph4 =1
;ph6 =0 2
;ph7 =0; 0 0 0 2 2 2 2
;ph8=0 0 2 2
;ph10=0 0 0 0 0 0 0 0 2 2 2 2 2 2 2 2
;ph20=0
;ph21=1
;ph22=2
;ph23=3
;ph31=0 2 0 2; 2 0 2 0
```

I.9: 2D ^{1}H-^{1}H correlation

```
"d11=30m"
"d12=20u"
"d13=4u"


"d0=in0/2-p1*4/3.1416"


1 ze
2 d11
3 d12 pl9:f1
 d1 cw:f1 ph29
 d13 do:f1
 d12 pl1:f1
 p1 ph1
 d0
 p1 ph2
 d12 pl9:f1
 d8 cw:f1
 d13 do:f1
 d12 pl1:f1
 p1 ph3
 d6
 p2 ph4
 go=2 ph31
 d11 mc #0 to 2 F1PH(ip1 & ip29, id0)
exit


ph1 =0 2
ph2 =0 0 0 0 0 0 0 0 2 2 2 2 2 2 2 2
ph3 =0 0 2 2 1 1 3 3
ph4 =1 1 3 3 2 2 0 0 1 1 3 3 2 2 0 0 3 3 1
1 0 0 2 2 3 3 1 1 0 0 2 2
ph29=0
ph31=0 2 2 0 1 3 3 1 2 0 0 2 3 1 1 3 0 2
2 0 1 3 3 1 2 0 0 2 3 1 1 3
```

APPENDIX II: Joint-fit program (MATLAB)

1. simfit.m

```
clear all;

global wobs;
global spekt;
%spekt(:,1)=wobs.*0;
%spekt(:,2)=wobs.*0;
global nsp;
global npk;
global npt;
global nsb;
global npt;
global disb;
global model;
global nullen;
global idxl;
global idxr;
% reihenfolge   w0(nsp,npk),    ebenso  gam, I
%               spekt(nsp,nx)           model
% input randparameter
inputfile=input('name of input file [siminput.xls] ','s');
if isempty(inputfile)
   inputfile='siminput.xls';
end
fitoderplot=input('(f)it or only (p)lot with initial parameters [fit] ','s');
if isempty(fitoderplot)
   fitoderplot='f';
end
[inputnum,inputtxt]=xlsread(inputfile);
%nsp=xlsread(inputfile,'A1:A1');
nsp=inputnum(1,1)
modus=char(inputtxt(2,1))
spename=char(inputtxt(3,1))
parname=char(inputtxt(4,1))
npk=inputnum(5,1)
groeo=inputnum(6,1)
nsb=inputnum(7,1)
bf=inputnum(8,1)
mas=inputnum(9,1)
tolfun=inputnum(10,1)
if isnan(tolfun)
   tolfun=[]
end
maxfunevals=inputnum(11,1)
if isnan(maxfunevals)
   maxfunevals=[]
end
maxiter=inputnum(12,1)
```

```
if isnan(maxiter)
   maxiter=[]
end
%wobs=xlsread('simspectra.xls','A1:A11895');
spexls=xlsread(spename);
wobs=spexls(:,1);
for isp=1:nsp
   spekt(:,isp)=spexls(:,isp+1)./groeo;
end
parxls=xlsread(parname);
%%%% basic calcs
% points per spinning sideband
dwHz=(wobs(1)-wobs(2))*bf
disb=double(int32(mas/dwHz))
%number of points
[npt, dummy]=size(spekt);
nullen=zeros(npt,1);    %for sidebands
for isb=1:nsb
   shift=disb*isb;
   idxl(:,isb)=mod((0:(3*npt)-1)-shift, (3*npt))+1;
   idxr(:,isb)=mod((0:(3*npt)-1)+shift, (3*npt))+1;
end
%%%%%%%%%%%%%%%%%%%%
options = optimset('TolFun',tolfun,'MaxFunEvals',maxfunevals,'MaxIter',maxiter)
if modus == 'wsgsiu'
   %fit w0 simult, gam simult, I indep
   global sb;
   w0=parxls(1,:);
   gam=parxls(2,:);
   sb=parxls(3,:);
   I=parxls(4:3+nsp,:);
   pars=[w0(1,:); gam(1,:); I];
   if fitoderplot == 'f'
      parsopt=fminsearch(@simerrfunctwsgsiu,pars,options)
      save('simput.dat', 'parsopt','-ASCII');
   else
      simerrfunctwsgsiu(pars)
   end

elseif modus == 'wfgsiu'
   % w0 fix, gam simult, I indep
   global w0;
   global sb;
   w0=parxls(1,:);
   gam=parxls(2,:);
   sb=parxls(3,:);
   I=parxls(4:3+nsp,:);
   pars=[gam(1,:); I];
   if fitoderplot == 'f'
      parsopt=fminsearch(@simerrfunctwfgsiu,pars,options)
      save('simput.dat', 'parsopt','-ASCII');
   else
      simerrfunctwfgsiu(pars)
```

```
   end
elseif modus == 'wfgfiu'
   % w0 fix, gam fix, I indep
   global w0;
   global gam;
   global sb;
   w0=parxls(1,:);
   gam=parxls(2,:);
   sb=parxls(3,:);
   I=parxls(4:3+nsp,:);
   pars=[I];
   if fitoderplot == 'f'
      parsopt=fminsearch(@simerrfunctwfgfiu,pars,options)
      save('simput.dat', 'parsopt','-ASCII');
   else
      simerrfunctwfgfiu(pars)
   end
end
save('model.dat', 'model','-ASCII');
for isp=1:nsp
   figure
   plot(wobs,spekt(:,isp),wobs,model(:,isp))
end
%plot(wobs,spekt(:,1),wobs,model(:,1))
%figure
%plot(wobs,spekt(:,2),wobs,model(:,2))
```

2. simerrfunctwfgfiu.m

```
function err = simerrfunctwfgfiu(pars)
global wobs;
global yobs;
global nsp;
global npk;
global npt;
global nsb;
global disb;
global spekt;
global model;
global w0;
global gam;
global sb;
global nullen;
global idxl;
global idxr;
%w0=pars(1,:)   %  peaks
%gam=pars(2,:)  % peaks
I=pars(1:0+nsp,:);    %  spectra, peaks
I=abs(I);
% reihenfolge   w0(npk),    ebenso  gam
% reihenfolge   I(nsp,npk) I
```

```
%              spekt(nsp,nx)          model

model=0.*wobs;
err=0;
for isp=1:nsp
   model(:,isp)=0;
   for ipk=1:npk
      % Lorentzian with FWHH=gam, max=I*1:
      vgam2= 0.25 .*gam(ipk).^2;
      peak=I(isp,ipk) .* vgam2 ./ ((wobs-w0(ipk)).^2 + vgam2);
      model(:,isp)=model(:,isp)+peak;
      % add sidebands
      tmp=[nullen;peak;nullen];
      for isb=1:nsb
         % circshift too slow-> ausgeschrieben, indexing-schleife
         % (=limitierender faktor) vorgezogen in main (s.o., s. circshift.m):
         tmp1=tmp(idxl(:,isb));
         tmp2=tmp1(npt+1:2*npt);
         peaksbr=tmp2.*(sb(ipk).^isb);
         tmp1=tmp(idxr(:,isb));
         tmp2=tmp1(npt+1:2*npt);
         peaksbl=tmp2.*(sb(ipk).^isb);
         model(:,isp)=model(:,isp)+peaksbr+peaksbl;
      end
   end
   err = err+norm(model(:,isp)-spekt(:,isp));
end
% test: show during fit
```

3. simerrfunctwfgsiu.m

```
function err = simerrfunctwsgfiu(pars)
global wobs;
global yobs;
global nsp;
global npk;
global nsb;
global npt;
global disb;
global spekt;
global model;
global w0;
global sb;
global nullen;
global idxl;
global idxr;
%w0=pars(1,:)   %  peaks
gam=pars(1,:);  % peaks
I=pars(2:1+nsp,:);    %  spectra, peaks
% reihenfolge   w0(npk),    ebenso  gam
% reihenfolge   I(nsp,npk) I
%              spekt(nsp,nx)          model
```

```
model=0.*wobs;
err=0;

for isp=1:nsp
   model(:,isp)=0;
   for ipk=1:npk
      % Gaussian:
      %peak=I(isp,ipk).*exp(-(w0(ipk)-wobs).^2/(2*(gam(ipk)).^2));
      % Lorentzian with Int=I*1 , FWHH=gam, max=2/(pi*gam):
      %peak=I(isp,ipk) .* (1/pi) .* 0.5 .* gam(ipk) ./ ((wobs-w0(ipk)).^2 + 0.25.*gam(ipk).^2);
      % Lorentzian with FWHH=gam, max=I*1:
      vgam2= 0.25 .*gam(ipk).^2;
      peak=I(isp,ipk) .* vgam2 ./ ((wobs-w0(ipk)).^2 + vgam2);
      model(:,isp)=model(:,isp)+peak;
      % add sidebands
      tmp=[nullen;peak;nullen];
      for isb=1:nsb
         % circshift too slow-> ausgeschrieben, indexing-schleife
         % (=limitierender faktor) vorgezogen in main (s.o., s. circshift.m):
         tmp1=tmp(idxl(:,isb));
         tmp2=tmp1(npt+1:2*npt);
         peaksbr=tmp2.*(sb(ipk).^isb);
         tmp1=tmp(idxr(:,isb));
         tmp2=tmp1(npt+1:2*npt);
         peaksbl=tmp2.*(sb(ipk).^isb);
         model(:,isp)=model(:,isp)+peaksbr+peaksbl;
      end
   end
   err = err+norm(model(:,isp)-spekt(:,isp));
end
% test: show during fit
%model
%pars
%err
% test: plot on interrupt
%plot(wobs,spekt(:,1),wobs,model(:,1))
```

4. simerrfunctwsgsiu.m

```
function err = simerrfunctwsgsiu(pars)
global wobs;
global yobs;
global nsp;
global npk;
global npt;
global nsb;
global disb;
global spekt;
global model;
global sb;
global nullen;
global idxl;
```

```
global idxr;
w0=pars(1,:)   %  peaks
gam=pars(2,:)  % peaks
I=pars(3:2+nsp,:);    %  spectra, peaks
% reihenfolge   w0(npk),    ebenso  gam
% reihenfolge   I(nsp,npk) I
%               spekt(nsp,nx)          model
model=0.*wobs;
err=0;
for isp=1:nsp
   model(:,isp)=0;
   for ipk=1:npk
            % Lorentzian with FWHH=gam, max=I*1:
      vgam2= 0.25 .*gam(ipk).^2;
      peak=I(isp,ipk) .* vgam2 ./ ((wobs-w0(ipk)).^2 + vgam2);
      model(:,isp)=model(:,isp)+peak;
      % add sidebands
      tmp=[nullen;peak;nullen];
      for isb=1:nsb
         % circshift too slow-> ausgeschrieben, indexing-schleife
         % (=limitierender faktor) vorgezogen in main (s.o., s. circshift.m):
         tmp1=tmp(idxl(:,isb));
         tmp2=tmp1(npt+1:2*npt);
         peaksbr=tmp2.*(sb(ipk).^isb);
         tmp1=tmp(idxr(:,isb));
         tmp2=tmp1(npt+1:2*npt);
         peaksbl=tmp2.*(sb(ipk).^isb);
         model(:,isp)=model(:,isp)+peaksbr+peaksbl;
      end
   end
   err = err+norm(model(:,isp)-spekt(:,isp));
end
% test: show during fit
%model
%pars
%err
% test: plot on interrupt
%plot(wobs,spekt(:,1),wobs,model(:,1))
```

APPENDIX III: Coordinates of DFT optimized structures

1. Copper(II)-cyclam monochloride ($C_{10}H_{24}N_4CuCl$)

#P opt ub3lyp/6311G

Cu	-0.001700	0.000000	-0.254200
N	-1.326200	-1.517400	-0.659600
N	1.396000	-1.490600	0.009600
H	-1.407900	-1.636100	-1.670800
H	1.405400	-1.477000	1.035700
H	3.403100	-2.145000	-0.211800
H	2.745000	-1.272100	-1.592000
H	-0.821100	-2.699600	0.996200
H	-1.204700	-3.652900	-0.446800
H	0.922200	-2.854700	-1.524300
H	1.276800	-3.632800	0.017500
H	4.473200	-0.000000	-0.262700
H	3.413100	-0.000000	1.123800
H	-3.332500	-2.144800	-0.340300
H	-2.598300	-1.222300	0.979700
N	1.396000	1.490500	0.009700
N	-1.326200	1.517400	-0.659600
H	1.405400	1.477000	1.035700
H	-1.407900	1.636100	-1.670800
H	-3.332500	2.144800	-0.340200
H	-2.598200	1.222300	0.979700
H	0.922200	2.854600	-1.524300
H	1.276900	3.632800	0.017500
H	-0.821100	2.699600	0.996200
H	-1.204600	3.652900	-0.446900
H	-4.391000	0.000000	-0.336200
H	-3.352800	0.000000	-1.736600
H	3.403100	2.144900	-0.211800
H	2.745100	1.272100	-1.592000
C	3.421000	-0.000000	0.029200
C	-3.341900	0.000000	-0.639500
C	2.786600	-1.288400	-0.500600
C	-2.704300	1.282000	-0.102600
C	2.786700	1.288400	-0.500600
C	-2.704400	-1.282000	-0.102700
C	0.780600	-2.776300	-0.444300
C	-0.697500	2.756700	-0.084300
C	-0.697500	-2.756700	-0.084300
C	0.780600	2.776200	-0.444300
Cl	-0.253400	-0.000000	2.378900

2. Nickel(II)-cyclam dichloride ($C_{10}H_{24}N_4NiCl_2$)

#P opt ub3lyp/6311G

N	-0.343800	1.382100	1.538000
N	0.343800	-1.382100	1.538000
C	-0.182500	-2.754600	1.297500
C	0.182500	0.743000	2.777600
C	-0.182500	-0.743000	2.777600
C	0.361200	-3.370700	0.000000
C	0.182500	2.754600	1.297500
H	-1.364500	1.398300	1.569700
H	1.364500	-1.398300	1.569700
H	0.073200	-3.405300	2.143200
H	-1.268500	-2.679100	1.245000
H	1.265900	0.864400	2.768500
H	-0.210500	1.228500	3.677300
H	-1.265900	-0.864400	2.768500
H	0.210500	-1.228500	3.677300
H	0.088800	-4.429700	0.000000
H	1.456800	-3.340000	0.000000
H	-0.073200	3.405300	2.143200
H	1.268500	2.679100	1.245000
N	0.343800	-1.382100	-1.538000
N	-0.343800	1.382100	-1.538000
C	0.182500	2.754600	-1.297500
C	-0.182500	-0.743000	-2.777600
C	0.182500	0.743000	-2.777600
C	-0.361200	3.370700	0.000000
C	-0.182500	-2.754600	-1.297500
H	1.364500	-1.398300	-1.569700
H	-1.364500	1.398300	-1.569700
H	-0.073200	3.405300	-2.143200
H	1.268500	2.679100	-1.245000
H	-1.265900	-0.864400	-2.768500
H	0.210500	-1.228500	-3.677300
H	1.265900	0.864400	-2.768500
H	-0.210500	1.228500	-3.677300
H	-0.088800	4.429700	0.000000
H	-1.456800	3.340000	0.000000
H	0.073200	-3.405300	-2.143200
H	-1.268500	-2.679100	-1.245000
Ni	0.000000	0.000000	0.000000
Cl	2.576100	0.360600	0.000000
Cl	-2.576100	-0.360600	0.000000

3. Copper(II)-acetylacetonate ($C_{10}H_{14}O_4Cu$)

#P opt ub3lyp/6311G(d) extrabasis (Wacters-f on Cu, 631G(d) on H)

```
H       -4.356400    0.000000    0.000000
C       -3.274600    0.000000    0.000000
C       -2.611800    1.235700    0.000000
O       -1.349900    1.395600    0.000000
C       -3.414900    2.516300    0.000000
H       -3.147700    3.110300    0.878300
H       -4.490900    2.340200    0.000000
C       -2.611800   -1.235700    0.000000
O       -1.349900   -1.395600    0.000000
C       -3.414900   -2.516300    0.000000
H       -3.147700   -3.110300   -0.878300
H       -3.147700    3.110300   -0.878300
H       -3.147700   -3.110300    0.878300
H       -4.490900   -2.340200    0.000000
Cu       0.000000    0.000000    0.000000
H        4.356400    0.000000    0.000000
C        3.274600    0.000000    0.000000
C        2.611800   -1.235700    0.000000
C        2.611800    1.235700    0.000000
O        1.349900   -1.395600    0.000000
O        1.349900    1.395600    0.000000
C        3.414900   -2.516300    0.000000
C        3.414900    2.516300    0.000000
H        3.147700   -3.110300    0.878300
H        3.147700    3.110300   -0.878300
H        3.147700   -3.110300   -0.878300
H        3.147700    3.110300    0.878300
H        4.490900   -2.340200    0.000000
H        4.490900    2.340200    0.000000
```

3.Vanadyl(II)-acetylacetonate ($C_{10}H_{14}O_5V$)

#P opt ub3lyp/6311G

O	-1.342800	1.357000	-0.006800
O	1.342800	1.357000	-0.006800
C	0.000000	3.287100	-0.397300
H	0.000000	4.341200	-0.626600
C	1.229900	2.628400	-0.275400
C	-1.229900	2.628400	-0.275400
C	-2.529000	3.358500	-0.471100
H	-3.102300	2.875900	-1.264600
H	-3.126000	3.286600	0.440000
H	-2.382100	4.407300	-0.720500
C	2.529000	3.358500	-0.471100
H	3.126000	3.286600	0.440000
H	3.102300	2.875900	-1.264600
H	2.382100	4.407300	-0.720500
O	1.342800	-1.357000	-0.006800
O	-1.342800	-1.357000	-0.006800
C	0.000000	-3.287100	-0.397300
H	0.000000	-4.341200	-0.626600
C	-1.229900	-2.628400	-0.275400
C	1.229900	-2.628400	-0.275400
C	2.529000	-3.358500	-0.471100
H	3.102300	-2.875900	-1.264600
H	3.126000	-3.286600	0.440000
H	2.382100	-4.407300	-0.720500
C	-2.529000	-3.358500	-0.471100
H	-3.126000	-3.286600	0.440000
H	-3.102300	-2.875900	-1.264600
H	-2.382100	-4.407300	-0.720500
V	0.000000	0.000000	0.568100
O	0.000000	0.000000	2.158700